# Investigating seismic anisotropy in Ireland from shear wave splitting and surface wave tomography

Gulten POLAT

The thesis submitted to University College Dublin in fulfilment of

the requirements for the degree of

DOCTOR OF PHILOSOPHY




UCD School of Geological Sciences, University College Dublin,

Dublin, Ireland

*Head of School*: Prof. Stephen Daly

SUPERVISED BY:

Prof. Chris Bean, *University College Dublin, Dublin, Ireland*

Prof. Peter Readman and Prof. Brian O'Reilly, *Dublin Institute for Advanced Studies, Ireland*

March 2014

To my dear brother Ramazan Polat

# Declaration

I hereby declare that I am the sole author of this document. I authorise the National University of Ireland to lend this document to other institutions or individuals for the purpose of scholarly research. I further authorise the National University of Ireland to reproduce this document by photocopying or other means, in total or part, at the request of other institutions or individuals for the purpose of research.

Gulten POLAT.

# Summary

The main goals of my Ph.D. thesis are to investigate crustal and mantle anisotropy beneath Ireland by using surface wave tomography and shear wave splitting methods and to increase the understanding of anisotropy within the crust and upper mantle beneath Ireland and the D" layer by generation and analysis of the shear wave velocity profile and modelling. Previous studies were primarily carried out in southern Ireland. However, for the first time, these methods have been applied to the whole of Ireland in this project.

Shear-wave splitting analysis has been carried out on teleseismic data acquired by 40 temporary and 2 permanent broadband stations mainly from 2006 to 2011 in Ireland. It is found that there were two major event clusters: one from East Asia and the other from South America. A significant change in fast polarisation direction was observed between the results from these two event clusters which have nearly opposite back azimuths. This clearly suggests that there is a clear variation in fast polarization directions with back-azimuth. The results show that there are fundamentally different origins for the observed anisotropy beneath Ireland. In contrast, no significant difference in delay time is found for the two event clusters, and for both clusters the average delay time is greater than 1 s. The averaged fast polarization directions from the East Asian events are approximately aligned with Caledonian/Variscan trends but with some significant scatter, particularly in central Ireland. However, the averaged fast polarization directions from the South American events are fairly uniform and show N-S orientations. For this cluster there is not strong alignment of the fast polarization direction with either Caledonian and Variscan structural trends.

Rapid spatial variations in splitting parameters from the East Asian events are observed at the stations located in central Ireland. This suggests that the contribution of crustal anisotropy to teleseismic shear wave splitting is quite high and the observed anisotropy beneath central Ireland is probably related to fabrics within deep crustal rocks that preserve a record of deformation during and after the continental collisions.

Some events in the East Asian cluster were found to give discrepant SKS-SKKS splitting results. These may be related to anisotropy in the D" layer or other lower mantle effects including core-mantle boundary topography. It was not possible to draw definite conclusions in this

regard from the South American events as there were too few SKS-SKKS pairs in the data so far collected.

In addition, to determine the distribution of anisotropy with depth, phase velocities of seismic surface waves were measured. An inter-station technique was used to measure the dispersion curves of fundamental mode Rayleigh waves and those of Love waves along 43 and 21 interstation paths, respectively. The observed isotropic phase-velocity heterogeneity reflects moderate crustal thickness and seismic velocity variations across Ireland. Anisotropy of Rayleigh waves at 10-20 s periods shows a NE-SW fast-propagation direction and is the largest (up to 2%) at a 15 s period, at which Rayleigh waves sample primarily the middle and lower crust. The NE-SW trend of the deep-crustal anisotropic fabric is parallel to tectonic trends, in particular the Iapetus Suture Zone, which indicates that suture-parallel flow in the middle and lower crust accommodated the continental collision.

The average shear wave-crustal velocity model obtained from combining Rayleigh phase velocity measurements with those of Love wave for Ireland is broadly consistent with the velocity models from controlled source experiement wide-angle results, showing evidence for crustal layers with slightly varying Moho depths. The results suggest that the VARNET profiles are representative of the whole Irish crust. Rapid changes in vertical and lateral shear-speed structure in the whole Irish crust are not observed. The slight variations in shear velocity reflect moderate variations in crustal thickness and radial anisotropy. The absence of rapid changes of anisotropy with depth indicates that there is no change in anisotropic symmetry orientation. The averaged radial anisotropy of Ireland in the crust and uppermost mantle is slightly higher than the global average; it is slightly greater than 2%. Variations in the amount of the observed radial anisotropy within the upper crust to lower crust are small and very smooth. Radial anisotropy indicative of horizontal fabric in the crust and uppermost mantle is preferred by the data collected in this study. This is a robust observation and consistently indicates horizontally oriented fabric due to the alignment of intrinsically anisotropic minerals in the crust and uppermost mantle beneath Ireland.

# Acknowledgements

Foremost, I would like to express my sincere gratitude to my advisors Peter Readman, Chris Bean and Brian O'Reilly for the continuous support of my Ph.D. study and research, for their patience, motivation, enthusiasm, and immense knowledge. Their guidance helped me during all the time of research and writing of this thesis. I could not have imagined having better advisors and mentors for my Ph.D. study. It is always pleasure to be one of their students and work with them.

Besides my advisors, my special appreciation goes to Sergei Lebedev for guiding me through the thesis and for encouragement, insightful comments, and hard questions. Also, I would like to thank Sergei for generously providing me with surface wave tomography program. My sincere thanks also goes to Franz Hauser for his valuable scientific help. I am grateful to Prof. Nurcan M. Ozel and Prof. Niyazi Turkelli from KOERI (Bogazici University Kandilli Observatory and Earthquake Research Institute) for enlightening me the first glance of research. My special appreciation goes to my teachers, Prof. Hikmet Ucisik, Hurmuz Telceker from Bogazici University and Esen Arpat for their invaluable support to my thesis. I want to thank my teachers, Ayla Korucu and Salih Zeki Dinler for their unflagging encouragement throughout my graduate school career.

I would also like to thank Science Foundation Ireland (Research Frontiers Programme grant no. 07/RFP/GEOF758) and the Dublin Institute for Advanced Studies for providing generous financial support throughout my study. Special thanks to Clare Horan, Gerry Wallace, Louise Quigley for assistance in fieldwork and data management. I also thank the Irish Agriculture and

Food Development Authority for their help in finding sites for our stations and the landowners who generously provided them.

I would like to thank my best friend, Seda Yelkenci and Hilary O'Donnell for their immense support and help during my stay in Dublin. Last but not least, I would like to thank my family, my mom Seringul, my brother Orhan and my sisters Bahar and Akgul Polat for supporting me with full faith during my life time.

# Table of Contents

**1. Introduction** **1**
1.1. The structure of this thesis . . . . . 2

**2. Geological and geophysical background** **4**
2.1. Tectonic and geological background . . . . . 4
2.1.1. Caledonian Orogeny . . . . . 4
2.1.2. Variscan deformation . . . . . 11
2.2. Geophysical background . . . . . 12
2.2.1. Seismic results . . . . . 12
2.2.2. Gravity results . . . . . 22
2.2.3. Magnetotelluric (MT) results . . . . . 23
2.3. Summary of geophysical results . . . . . 23
2.4. Instrumentation . . . . . 25
2.4.1. Seismometers . . . . . 25
2.4.2. Instrument responses . . . . . 28
2.4.3. Data recorders . . . . . 31

**3. Seismic anisotropy, shear wave splitting and surface wave tomography** **34**
3.1. Hooke's Law . . . . . 34
3.2. Isotropic media . . . . . 35
3.3. Seismic anisotropy . . . . . 36
3.3.1. Origin of anisotropy . . . . . 37
3.3.2. Structural origins of anisotropy . . . . . 42
3.3.3. Seismic anisotropy and plate tectonics . . . . . 56
3.4. Shear wave splitting and surface wave tomography . . . . . 60
3.4.1. Shear wave splitting . . . . . 60
3.4.2. Surface wave tomography . . . . . 71
3.5. Review of anisotropy studies in the North Atlantic region, UK and Ireland . . . 85

**4. Shear-wave splitting analysis** **94**
4.1. Irish Seismological Upper Mantle Experiment . . . . . 94
4.1.1. Overview . . . . . 94
4.1.2. Site selection and permission . . . . . 95
4.1.3. Event selection . . . . . 98
4.1.4. Data processing . . . . . 99
4.1.5. Global earthquake distribution . . . . . 101
4.1.6. Routine shear wave splitting analysis . . . . . 103
4.2. Shear-wave splitting results . . . . . 119
4.2.1. General results . . . . . 119
4.2.2. Examples from results . . . . . 136
4.3. Concluding remarks and discussion . . . . . 144

**5. Surface wave tomography for azimuthal anisotropy** **146**
5.1. Data . . . . . 146
5.2. Interstation phase velocity measurements . . . . . 148
5.2.1. Phase velocity maps . . . . . 153
5.3. Azimuthal anisotropy . . . . . 155
5.4. Summary and discussion . . . . . 161

**6. Surface wave tomography for Radial anisotropy and Shear velocity profile** **164**
6.1. Data . . . . . 164
6.2. Love-wave phase velocity dispersion measurements . . . . . 166
6.2.1. Love wave phase velocity maps . . . . . 171
6.3. Love-wave anisotropy . . . . . 173
6.3.1. Radially anisotropic shear velocity profile . . . . . 177

**7. Discussion on localization of anisotropy in depth** **182**
7.1. Possible scenarios for origins of the anisotropy beneath Ireland . . . . . 182
7.1.1. Lithospheric anisotropy . . . . . 183
7.1.2. Asthenospheric anisotropy . . . . . 189
7.2. Seismic anisotropy models . . . . . 191
7.2.1. Two-layer anisotropy model . . . . . 192
7.2.2. Lateral variation and depth of seismic anisotropy from Fresnel zone arguments . . . . . 197
7.3. Seismic anisotropy in the lower mantle . . . . . 202
7.3.1. SKS-SKKS splitting discrepancies . . . . . 202
7.3.2. Comparison of SKS-SKKS waveform splitting . . . . . 217

7.3.3. The estimation of the depth of anisotropy using spatial coherency of shear-waves plitting parameters . . . . . 219

**8. Summary and conclusions** **223**
8.1. Summary and conclusions . . . . . 223
8.2. Future work . . . . . 226

**Appendices** **257**

**A. Glossary, annotation and symmetry system in seismic anisotropy** **258**
A.1. Glossary . . . . . 258
A.2. Anisotropic symmetry systems . . . . . 262
A.3. Elastic stiffness tensor . . . . . 263
A.3.1. Notation . . . . . 263
A.3.2. Isotropic case . . . . . 264
A.3.3. Orthorhombic case . . . . . 265
A.3.4. Hexagonal case . . . . . 265

**B. List of stations used in this study** **269**

**C. Summary of data loggers and sensors deployed at ISLE, ISUME and IA stations** **271**

**D. Complete list of results from shear wave splitting measurements at all Irish stations from 01/01/2003 to 31/09/2011** **273**

**E. Summary of results** **300**

**F. Averaged shear-wave splitting results** **302**

**G. Program to average shear-wave splitting measurements** **309**

**H. List of publications** **314**
H.1. Journals . . . . . 314
H.2. Conference proceedings . . . . . 314

# List of Figures

2.1. Simple geological map of Ireland . . . . . 6
2.2. Map of the Iapetus Ocean during the Caradoc (c. 455 Ma) . . . . . 7
2.3. Showing tectonic evolution of the Caledonian orogenic cycle . . . . . 8
2.4. Map of locations of Acadian and other Late Caledonian tectonic features and granite plutons . . . . . 10
2.5. The conducted experiments for Ireland from 1969-1999 . . . . . 13
2.6. P and S wave velocity models for VARNET line A . . . . . 16
2.7. P and S wave velocity models for VARNET line B . . . . . 17
2.8. Illustrating Silica content of Ireland . . . . . 18
2.9. Map of Ireland with smoothed LAB topography . . . . . 19
2.10. Shear-wave splitting results from the ISLE project . . . . . 21
2.11. Map of the Bouguer anomaly for Ireland . . . . . 22
2.12. The 3-component broadband seismometers . . . . . 26
2.13. The required equipments for a Nanometrics Trillium 120PA seismometer . . . 27
2.14. The differences between the response curves for different instruments . . . . . 29
2.15. Instrument responses of the 3-component broadband seismometers . . . . . 30
2.16. Earth Data logger (EDL) digital recorder . . . . . 32
2.17. Newer Earth Data logger (EDL) digital recorder . . . . . 33
2.18. Quanterra Q380 data logger. . . . . 33

3.1. Possible origins of anisotropy . . . . . 37
3.2. Complete representation of stresses on a block . . . . . 39
3.3. Four mechanisms of seismic anisotropy . . . . . 41
3.4. Conceptual model for P- and S-wave propagation in foliated lower crust and upper mantle rocks . . . . . 44
3.5. The simplified petrology and seismic anisotropy of the Earth's mantle and core 45
3.6. Conceptual model for the major physical and chemical variations in the Earth's mantle . . . . . 46
3.7. The seismic anisotropy of single crystals in the upper mantle minerals . . . . . 49
3.8. Illustrating the relationship between horizontal mantle flow and the resulting azimuthal anisotropy for different olivine fabric types . . . . . 50

3.9. Indicating possible mechanisms for D” anisotropy . . . . . 52
3.10. Example for measuring seismic anisotropy in the D” layer . . . . . 55
3.11. Model of seismic anisotropy beneath the Aegean subduction zone . . . . . 57
3.12. Model of seismic anisotropy beneath the East African Rift System . . . . . 58
3.13. An illustration of Shear wave splitting . . . . . 61
3.14. Schematic map of ray paths . . . . . 62
3.15. T-X curves of teleseismic phases . . . . . 63
3.16. Sketch of the particle motion of surface waves . . . . . 72
3.17. Example of dispersion of a surface wave packet . . . . . 74
3.18. Calculated dispersion curves for Love and Rayleigh waves . . . . . 74
3.19. Cartoon indicating the effects of transverse isotropy due to layering . . . . . 78
3.20. An example S-velocity profile (left-hand panel) and example parametrization (right-hand panel) . . . . . 85
3.21. Topography and bathymetry of the North Atlantic region . . . . . 88
3.22. S-wave velocity azimuthal anisotropy in the North Atlantic region for 110 and 210 km depth . . . . . 89
3.23. Horizontal component of LPO directions of the regional flow model in the North Atlantic region . . . . . 90
3.24. Splitting results across Iceland . . . . . 91
3.25. Illustrating splitting measurements from the UK and Ireland . . . . . 93

4.1. The location map for all the used seismic stations . . . . . 95
4.2. Examples of selected sites for the used stations . . . . . 97
4.3. Schematic map of ray paths . . . . . 98
4.4. T-X curves of teleseismic phases . . . . . 98
4.5. The distribution of the initial selected events . . . . . 101
4.6. The histogram distributions of the initial selected events . . . . . 102
4.7. Detecting seismic phases on unfiltered and filtered waveforms . . . . . 104
4.8. An example of high quality raw and windowed SKS seismogram . . . . . 105
4.9. Determining window sizes of the teleseismic noisy event for small time window 109
4.10. Determining window sizes of the teleseismic noisy event for medium time window 110
4.11. Determining window sizes of the teleseismic noisy event for large time window 111
4.12. Example of a high quality shear wave splitting measurement . . . . . 115
4.13. Example of a medium quality shear wave splitting measurement . . . . . 116
4.14. Example of a low quality shear wave splitting measurement . . . . . 117
4.15. Example of a null quality shear wave splitting measurement . . . . . 118
4.16. The distribution and histograms of the final events selected for shear-wave splitting analysis from 01/01/2003 to 31/09/2011 . . . . . 120

4.17. The Quality and Phase histogram distribution of the events used in the study for splitting analysis . . . 121
4.18. Individual SKS and SKKS splitting measurements from the East Asian and the South American event clusters for each station used in this study . . . 122
4.19. Individual SKS and SKKS splitting measurements from events with back azimuths in the range of 90-180$^0$ and 270-360$^0$ . . . 123
4.20. Individual SKS and SKKS splitting measurements from the East Asian event cluster for each station used in this study . . . 124
4.21. Individual SKS and SKKS splitting measurements from the South American event cluster for each station used in this study . . . 125
4.22. Summary of averaged splitting results across Ireland . . . 127
4.23. The averaged SKS splitting parameters . . . 130
4.24. The averaged SKKS splitting parameters . . . 131
4.25. High quality SKS and SKKS measurements . . . 134
4.26. Variations of high quality SKS and SKKS measurements from the EA cluster in back-azimuth . . . 135
4.27. The histograms of the determined measurements at D23 (top) and D16 (bottom) stations . . . 137
4.28. The quality distribution of the final used events for splitting analysis . . . 138
4.29. The distribution of SKS and SKKS measurements at stations D23 and D16 . . . 139
4.30. Plots of individual splitting measurements at D34 . . . 141
4.31. All measurements are plotted at true epicentral distance and back-azimuths . . . 142
4.32. Shear wave splitting parameters as a function of the incidence angle at D34 . . . 143

5.1. Seismic stations and inter-station path coverage for Rayleigh-wave tomography 147
5.2. An example of inter-station path coverage for Rayleigh-wave tomography with great circles between the epicentres and the stations . . . 148
5.3. An example for the determination of the phase velocity using the two-station method . . . 150
5.4. Example of biased estimates of the phase velocity measurements for the station pair D36-P07 . . . 151
5.5. Indicating examples of phase-velocity measurements . . . 152
5.6. Rayleigh wave phase velocity anomaly maps . . . 154
5.7. Tomographic maps of Rayleigh-wave phase velocities at different periods . . . 158
5.8. Produced models for showing the effect of smoothing at 15-s period . . . 159
5.9. Test inversions for a 15-s period . . . 160

6.1. Seismic stations and inter-station path coverage for Love-wave tomography . . . 165

6.2. Example of inter-station path coverage for Love-wave tomography with great circles between the epicentres and the stations . . . . . 166
6.3. An example of the determination of the phase velocity of Love wave using the two-station method . . . . . 169
6.4. Examples of phase-velocity measurements of Love wave . . . . . 170
6.5. Final Love wave phase velocity anomaly maps . . . . . 172
6.6. Tomographic maps of Love-wave phase velocities including $4\Psi$ anisotropy at periods of 12-30 s . . . . . 176
6.7. The final preferred radially anisotropic S-velocity profile . . . . . 181

7.1. The averaged SKS splitting parameters . . . . . 185
7.2. Averaged LPO directions for a depth of 175 km in the North Atlantic region . . 188
7.3. Shear wave splitting in oner and two−layer media . . . . . 191
7.4. Two-layer model for DSB station . . . . . 193
7.5. Two-layer model for VAL station . . . . . 194
7.6. Shear wave splitting parameters as a function of the incidence angle at stations D23, DSB and VAL . . . . . 196
7.7. Schematic illustration of the Fresnel zone as a function of depth for SKS phases 198
7.8. The local map of exit points of SKS and SKKS phases at stations DSB and VAL 200
7.9. Showing the regional exit points of SKS (circles) and SKKS (squares) phases at stations DSB and VAL . . . . . 201
7.10. Example raypaths for the core phases SKS, SKKS and PKS . . . . . 203
7.11. Indicating map of the individual SKS splitting results with SKS/SKKS and without SKS/SKKS pairs . . . . . 205
7.12. Showing map of the individual SKKS splitting results with SKS/SKKS and without SKS/SKKS pairs . . . . . 206
7.13. The map of discrepant SKS/SKKS pair stations . . . . . 207
7.14. Example of showing discrepancies between SKS and SKKS pairs . . . . . 207
7.15. Showing the examined waveforms of the SKS and SKKS phases . . . . . 208
7.16. Indicating the particle motion of discrepant SKS/SKKS pairs . . . . . 209
7.17. Examples of non discrepant SKS-SKKS pairs's particle motion . . . . . 210
7.18. Demostrating the location of exit points for SKS (circle) and SKKS (squares) phases from the EA cluster at the Core-Mantle Boundary (CMB) . . . . . 215
7.19. Showing the location of exit points at the Core-Mantle Boundary (CMB) for SKS (circle) and SKKS (squares) phases obtained from the SA cluster . . . . . 216
7.20. The map shows the plate motions on the global scale . . . . . 216
7.21. The map shows the exit points of normal and anomalous pairs at D" . . . . . 217
7.22. The sketch of SKS and SKKS ray paths at the distances of $90-135^0$ . . . . . 218

7.23. A comparison of waveform splitting of SKS and SKKS . . . . . 219
7.24. The optimal depth of the source ofanisotropy using spatial coherency of teleseismic splitting parameters . . . . . 222

A.1. Summary of common symmetry systems . . . . . 262

# List of Tables

5.1. Variance reductions for 15s period . . . . . 157

F.1. Summary of average SKS splitting parameters obtained from medium and high quality measurements at the permanent and temporary seismic stations for all events from back-azimuth range of $0 - 90^0$ . . . . . 302
F.2. Summary of average SKKS splitting parameters obtained from medium and high quality measurements at the permanent and temporary seismic stations for all events from back-azimuth range of $0 - 90^0$ . . . . . 303
F.3. Summary of average SKS+SKKS splitting parameters obtained from medium and high quality measurements at the permanent and temporary seismic stations for all events from back-azimuth range of $0 - 90^0$ . . . . . 304
F.4. Summary of average SKS splitting parameters obtained from medium and high quality measurements at the permanent and temporary seismic stations for all events from back-azimuth range of $180 - 270^0$ . . . . . 305
F.5. Summary of average SKKS splitting parameters obtained from medium and high quality measurements at the permanent and temporary seismic stations for all events from back-azimuth range of $180 - 270^0$ . . . . . 306
F.6. Summary of average SKS+SKKS splitting parameters obtained from medium and high quality measurements at the permanent and temporary seismic stations for all events from back-azimuth range of $180 - 270^0$ . . . . . 306
F.7. Summary of average SKS+SKKS splitting parameters obtained from medium and high quality measurements at the permanent and temporary seismic stations for all events from back-azimuth range from $0 - 90^0$ and $180 - 270^0$ . . . . . 307

# 1. Introduction

Knowledge of present-day and past dynamical processes taking place within the Earth is crucial to understand the interior of the Earth and how it has evolved through time. Although many observations of deformational processes in the upper crust are obtained from geology, our knowledge about mantle deformation is limited because it is derived from indirect observations coming chiefly from seismic waves that pass through the mantle and that are recorded at the surface. In particular, significant aspects of mantle dynamics that remain poorly understood include what controls the patterns of mantle flow, how this flow interacts with the surface plates, and how the lithospheric mantle is deformed as a result of plate boundary interactions. Shear and normal tractions are related to both large-scale plate motions and local mantle dynamics, and influence strongly upper mantle lithosphere dynamics. This suggests that anisotropy is a common property of the Earth's crust and the upper mantle related to the strain field of the medium and geodynamics. Therefore, seismic anisotropy is becoming increasingly significant as an aid to understand the Earth's tectonic evolution, especially to relate mantle flow to surface tectonics.

The aims of this Ph.D. thesis are to investigate crustal and mantle anisotropy beneath Ireland by using surface wave tomography and shear wave splitting methods and to increase the understanding of anisotropy within the crust, upper mantle and D" layer by generation and analysis of shear velocity profile and modelling.

## 1.1. The structure of this thesis

A geological overview of Ireland is given in chapter 2, in particular the early history of the Iapetus Ocean and the Caledonian orogenic cycle. In chapter 2 previous geological and geophysical studies are also described. Additionally, this chapter includes detailed information about seismometers and data recorders used in this study.

A comprehensive review of the basic theory of seismic anisotropy with some seismological observations is presented in chapter 3. Crustal, upper mantle and D" layer anisotropic minerals are described and discussed, as well as azimuthal and radial anisotropy and the relationship between anisotropy and tectonic processes. Besides, Shear Wave Splitting (SWS) and Surface Wave Tomograpy (SWT) methods are described in detail.

In chapter 4, the complete description of teleseismic data acquisition, processing and the analysis steps for the SWS method are given. For this part of the study, we obtained data from two permanent (DSB and VAL) and 40 temporary broadband stations deployed in Ireland during the Irish Seismological Lithospheric Experiment (ISLE), Irish Seismological Upper Mantle Experiment (ISUME) and Ireland Array (IA) projects. Technical information about the ISUME, the ISLE and the IA stations are provided in Appendices B and C. Finally, the results of the SWS analysis and a brief discussion of the results are presented at the end of the chapter. A more detailed discussion of the results from the SWS analysis is given in chapter 7.

Chapter 5 describes Rayleigh wave analysis and inversion procedure, including data selection, cross-correlation analysis, model parameterization, and inversion incorporating a variety of prior constraints. This chapter also includes a complete description about how to measure phase velocities from fundamental mode Rayleigh waves and then how to convert the phase-velocity data to make phase-velocity maps including azimuthal anisotropy.

Chapter 6 describes the measurements of Love wave phase velocities between pairs of seismic stations in Ireland. Additionally, this chapter includes the crustal shear wave velocity structure and radial anisotropy obtained from the results from Rayleigh and Love wave phase velocity analysis using inversion through different regularization parameters. The crustal models finally

obtained from the inversion are presented in the last part of this chapter. Based on variations in radial anisotropy, new constraints on the crustal structure throughout the study area are also suggested.

Detailed discussions on the results from SWS and SWT are presented in chapter 7. This chapter aims to particularly constrain the depth ranges of observed anisotropy. This chapter also includes modelling of shear-wave splitting and further analysis of the source of polarization anisotropy due to the discrepancies between SKS and SKKS measurements.

The thesis concludes with a summary of the work and the main conclusions drawn from the shear-wave splitting observations, modelling and surface wave tomography for azimuthal and radial anisotropy. Also, some suggestions for further studies are given in chapter 8.

# 2. Geological and geophysical background

The main purpose of this chapter is to summarize the most significant tectonic and geological features of Ireland. Previous geophysical studies conducted in the area are also described. At the end of this chapter, the information about the seismic recording instruments deployed during the ISLE, ISUME and IA projects are presented.

## 2.1. Tectonic and geological background

Geological observations from the study area show that Ireland has a rather complicated geology. The tectonic framework of Ireland has mainly been formed by the Caledonian (440 Ma) and Variscan orogenies (380 Ma). On the geological map of Ireland (Fig. 2.1), geological formations spanning from Proterozoic to Recent times, with Phanerozoic rocks forming the largest proportion, are exposed. Details of the above mentioned main tectonic processes are presented in turn in the following sections.

### 2.1.1. Caledonian Orogeny

The Caledonian Orogeny was one of the significant orogenies which formed the supercontinent Pangaea in the Late Paleozoic era. Between 650 and 550 million years ago (in the Ediacaran period), the smaller continents of Laurentia (containing the future north-east section of North

America), Baltica and Siberia had separated from Gondwana to move northward towards the equator (Fig. 2.2). In this process, the Iapetus Ocean between Gondwana, Baltica and Laurentia opened. Subsequent closure of this ocean resulted in the Caledonian Orogeny. Recently, many studies (e.g., *Woodcock and Strachan*, 2000) have shown that the Caledonian Orogeny was responsible for consolidating most of the British and Irish crust into the present pattern of fault-bounded blocks or terranes. Trace of Caledonian Orogeny can be broadly observed from East Greenland, through Ireland, Scotland to western Scandinavia (Norway). The Orogeny, which occurred during Ordovician and Early Silurian times, resulted from a triple-plate continental collision of Laurentia (North American craton), Baltica (part of the Fennoscandian shield), and Eastern Avalonia (a micro-plate of Gondwana) (e.g., *Woodcock and Strachan*, 2000). The Iapetus Suture Zone (ISZ) is a tectonic boundary resulting from the continential collision between the Laurentia and the Avalonia continents during the Early Devonian (400 Ma) closure of the Iapetus Ocean (Fig. 2.1). It is expressed in the Southern Uplands of Scotland, across the islands of Ireland and Newfoundland, and into the Appalachians of North America.

The ISZ stretches from the Shannon Estuary across central Ireland towards the Scottish Highlands (Fig. 2.1) (*Woodcock and Strachan,* 2000). Prior to the collision, Eastern Avalonia was separated from Laurentia by the Iapetus Ocean, and from Baltica by the Tornquist Sea (e.g., *Soper and Woodcock*, 1990). Significant strike-slip and transpressional movement during closure of the Iapetus Ocean along the Laurentia-Eastern Avalonia suture persisted to Late Silurian times (e.g., *Ford et al.*, 1992). *Lowe and Jacob* (1989) demostrated that the middle crust beneath the Irish Midlands was deformed in a 60 km wide zone, and this wide deformation zone is suggested as the site of the oceanic closure and continent-continent collision suture zone. During late Caledonian Orogeny, two main orogenic phases developed, termed the Grampian Orogeny from the Early to Middle Ordovician (475-460 Ma) and the Acadian Orogeny from the Early Devonian (405 Ma) (Fig. 2.3).

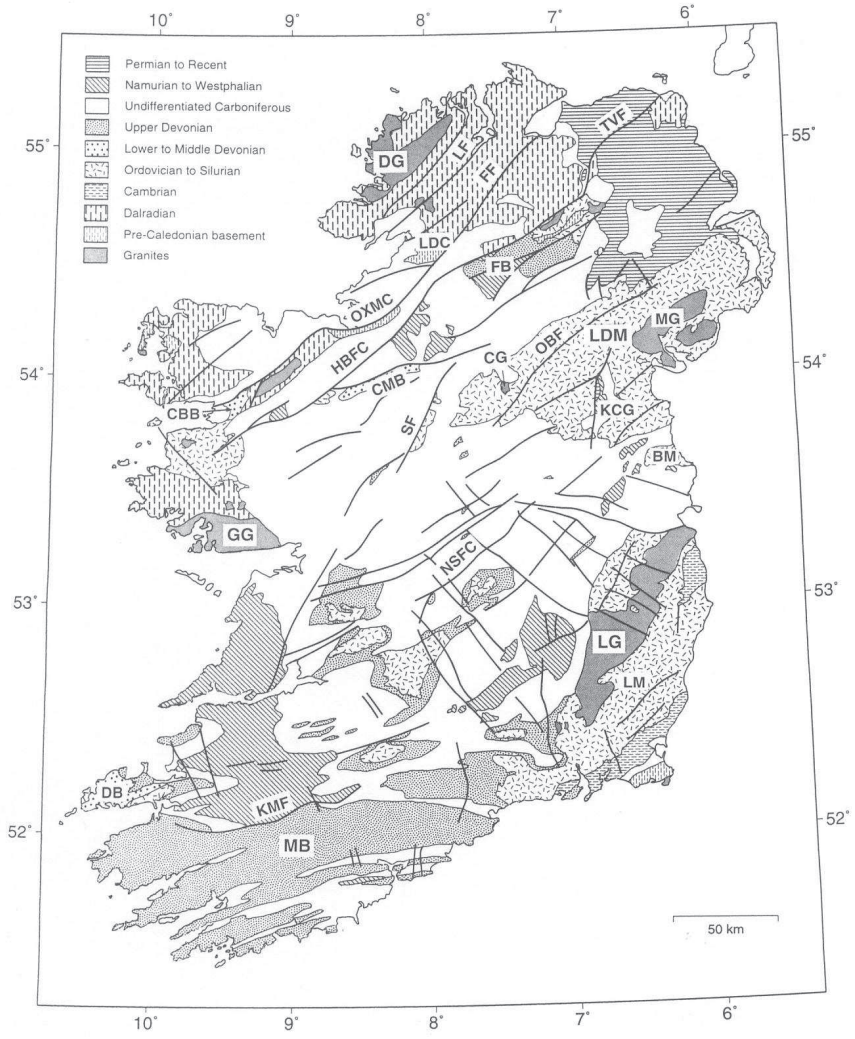



Figure 2.1.: Simplified geological map of Ireland (from *Readman et al.*, 1997). Abbreviations: Caledonian granites: CG, Crossdoney Granite; DG, Donegal Granite; GG, Galway Granite; LG, Leinster Granite; MG, Mourne Granite. Pre-Caledonian basement complexes: LDC, Lough Derg complex; OXMC, Ox Mountain complex. Lower Palaeozoic massifs: BM, Balbriggan Massif; LM, Leinster Massif; LDM, Longford-Down Massif. Devonian blocks: CBB, Clew Bay block; CMB, Curlew Mountains block; DB, Dingle block; FB, Fintona block. Main faults: FF, Foyle Fault; ISZ, Iapetus Suture Zone; HBFC, Highland Boundary Fault complex; KMF, Killarney-Mallow Fault; LF, Leannan Fault; OBF, Orlock Bridge Fault; NSFC, Navan-Silvermines Fault complex; SF, Strokes town Fault; TVF, Tow Valley Fault. Other features: Kingscourt graben, KCG; Munster Basin, MB.

Although the Caledonian Orogeny (440-430 Ma) resulting from the collision between Laurentia and Avalonia was a major Phanerozoic tectonic event that occurred in eastern North America and western Europe, and culminated in Late Silurian to Early Devonian periods with the closure of the Iapetus Ocean along the Iapetus Suture Zone (ISZ) (e.g., *Windley*, 1995; *Dewey and Mange*, 1999), the Orogeny did not end up until the Late Carboniferous at the end of the European Variscan Orogenic cycle (*Woodcock and Strachan*, 2000).

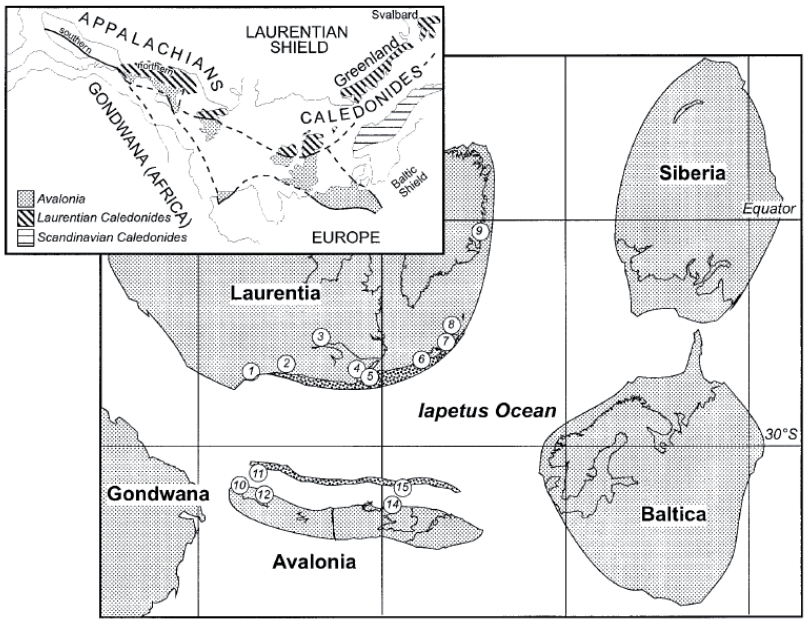



Figure 2.2.: Map of the Iapetus Ocean during the Caradoc (c. 455 Ma). Two arcs are shown diagrammatically: In reality, they each may have been composited with several subduction zones, distinct in time and place (from *McKerrow et al.*, 2000).

The majority of the crust of central Ireland was formed and modified during the Caledonian Orogeny. Geologic studies (e.g., *Soper et al.*, 1992; *Chew and Stillman*, 2009; *Chew*, 2009) ascertained that the early Palaeozoic oblique closure of the Iapetus Ocean particularly influenced the development of upper crustal structure within a region of large-scale sinistral transpression. The strong influence of this collision between Laurentia and Eastern Avalonia is still preserved in Ireland's rock record (*Windley*, 1995). Today the near-surface bedrock of the main part of Ireland consists mainly of the sediments of Carboniferous, Devonian and Silurian to Ordovician ages.

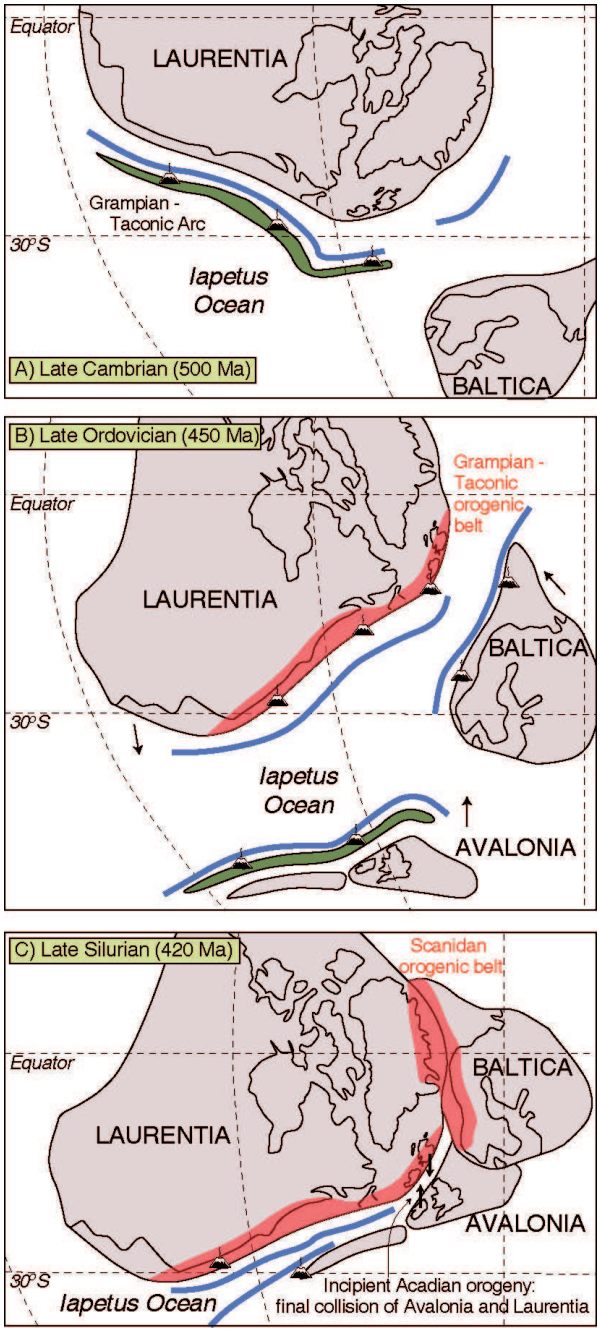



Figure 2.3.: Schematic tectonic evolution of the Caledonian orogenic cycle (the closure of the Iapetus Ocean), showing major orogenic events (e.g. the Grampian and Acadian). Volcanic arcs are shown in green; trenches are shown in blue and volcanoes indicate the polarity of subduction; collisional orogens are shown in red. A) South-directed subduction creates a volcanic arc within the Iapetus Ocean outboard of Laurentia. B) This arc collides with Laurentia causing the Grampian Orogeny, and north-directed subduction under Laurentia begins, contemporaneous with south-directed subduction beneath Avalonia. C) The Iapetus Ocean has been nearly closed. The "head-on" collision of Baltica and Laurentia causes the Scandian Orogeny, while the highly oblique collision between Laurentia and Avalonia causes the Acadian Orogeny (from *Chew and Stillman*, 2009).

**1) Grampian Orogeny**

*Lambert and McKerrow* (1976) recognised that the Dalradian sequences of the Scottish Highlands had undergone polyphase deformation and metamorphism during the Ordovician. This phase of orogenic activity clearly predated the post-Silurian deformation, namely "Caledonian", which is seen elsewhere in Britain and Ireland. They coined the term "Grampian Orogeny" for this Ordovician tectonic event. More recently, the Grampian Orogeny has been widely regarded as having resulted from the collision of Laurentia with an oceanic arc during the Arenig (*Dewey and Shackleton*, 1984) (Fig. 2.3). It is broadly equivalent to the Taconic Orogeny of the Appalachians and the Humberian Orogeny of western Newfoundland (*Dewey and Shackleton*, 1984; *van Staal et al.*, 1998; *Dewey and Mange*, 1999; *McKerrow et al.*, 2000).

During the Grampian Orogeny, the Dalradian rocks of Ireland and Scotland experienced multiple episodes of deformation. Each deformation event produced its own characteristic folds, schistosities and lineations, resulting in a complex cumulative set of structures. In Ireland, the Dalradian outcrop is fragmented into five inliers: NW Mayo, Donegal and the Sperrin Mountains, the Central Ox Mountains, Connemara, and NE Antrim. Moreover, subduction of Iapetus under the Laurentian margin is believed to have continued on into the Silurian (*van Staal et al.*, 1998), with large amounts of material being shed from the uplifting orogen into thick accretionary prisms such as the Southern Upland and Longford-Down belts (*Hutchison and Oliver*, 1998).

**2) Acadian Orogeny**

Acadian deformation resulting from the Acadian Orogeny in Britain and Ireland is temporally coincident (Mid-Devonian) with copious granitic melt production and magmatism within the crust (*Woodcock et al.*, 1988). The Acadian Orogeny was produced by the convergence of a small continental landmass called the Avalonia island arc at an active margin on the northeastern portion of the Laurentia plate (Fig. 2.4). However, the convergence of the Avalonia island arc created and reactivated numerous faults in the region and caused older rocks to be deformed and metamorphosed. Avalonia islands gradually accreted onto the eastern margin of the Laurentia

plate and created magmatic activity which can be found in scattered outcrop belts along the parts of Newfoundland and much of the coastal region of New England from Connecticut to northern Maine. Convergence of the Taconic and Avalonia tectonic plates were early stages of the formation of a supercontinent called Pangea. The final process, termed the Alleghanian Orogeny, occurred when the African and North American plates collided producing the final tectonic stresses attributed to the formation of the Appalachians.

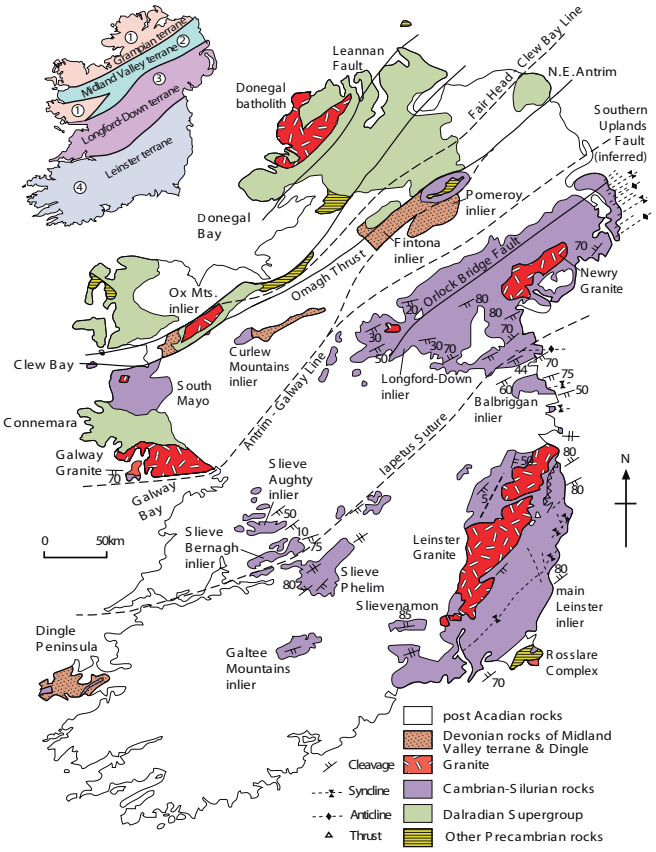



Figure 2.4.: Map of Ireland showing locations of Acadian and other Late Caledonian tectonic features and granitic plutons. This figure also shows the four informally termed terranes (taken from *Chew and Stillman*, 2009).

As a result of this, Avalon added the land lying under the coastal plain province to the edge of the continental shelf in the Mid-Atlantic region of North America. Large volumes of volcanic rocks and younger Iapetus Ocean sediments were accreted onto the North American margin as the land masses converged forming a band of younger terrane between the older North American and Avalonian terranes. Avalonian tectonic plate converged on Laurentia obliquely from the

northeast. The Laurentian coast had irregularities that the Avalonia island arc hit the hardest which resulted in a ragged type of mountain building that began in the north and migrated to the south through time as the Iapetus Ocean closed from northeast to southwest in direction.

### 2.1.2. Variscan deformation

Geological remains of the later Variscan Orogeny and deformation such as faults and nappes that resulted from the collision of Laurussia and Gondwanaland (Devonian to Permian) are observed in the southern part of Ireland (*Windley*, 1995; *Holland*, 2001). The beginning of the Variscan orogenic cycle from the Mid to Late Devonian produced sedimentary basins in Ireland that continued into the early Carboniferous (*Sevastopulo and Jackson*, 2009).

As a consequence, a significant deformation episode developed in southern Ireland. The Variscan faults (Killarney-Mallow fault zone in Fig. 2.1) are oriented mainly in an east−west direction, due to the north−south compressional forces that acted during the Variscan Orogeny (*Graham*, 2001). The Variscan deformation extends from Ireland into Great Britain and eastwards as far as Germany (*Matte*, 1986). The "Variscan Front" follows the KMF (Fig. 2.1), has been postulated as a continuous frontal thrust to the Variscan Orogeny of NW Europe, and also as a local frontal thrust to the fold belt in southern Ireland, and is widely considered as a major tectonic boundary (e.g., *Ford et al.*, 1992). However, its structure is still unknown and debatable. Similarly nappes that resulted from the collision of Laurussia and Gondwanaland (Devonian to Permian) are observed in the southern part of Ireland and in England (*Windley*, 1995; *Holland*, 2001).

**A) Post-Variscan**

Besides the widespread manifestations of Caledonian and Variscan orogenies, major sedimentary basins of younger ages (250-60 Ma) around Ireland and Britain were formed, most probably associated with the opening of the North Atlantic (*Naylor and Shannon*, 1982). According to a study of *O'Reilly and Readman* (2003), multiphase rifting episodes during the early to late Mesozoic era are mainly responsible for the development of sedimantary basins.

The basins comprise a global assemblage distributed across the entire North Atlantic region from eastern North America to the European Platform. This assemblage of basins has as its centre the region around and to the west of Ireland where tectonic re-activation of a strong NE-SW trending Caledonian basement fabric partly controlled the siting of the basins. In particular, *Shannon* (1991) demostrated that a variety of ensialic Mesozoic and Cenozoic sedimentary basins surround Ireland. Three main periods of basin development occurred. The first, in the Permo-Triassic, produced a series of small rift basins which nucleated along reactivated, generally Caledonian, structures. The second, in the Mid- and Late Jurassic, represents a period of crustal extension and rifting. The third phase reflects thermal subsidence of Cretaceous and Tertiary age, and coincides with seafloor spreading in the North Atlantic. The basins developed in response to the general east-west extension. Simple extensional structures, accompanied by crustal thinning, dominated in the north-south-trending Porcupine Basin. According to *Jones et al.* (2001), the Porcupine Basin, offshore Ireland, was affected by a Jurassic rifting, followed by Cretaceous and Cenozoic postrift subsidence. However, on sedimentological bases, these authors identified 300−600 m uplift at the Paleocene-Eocene boundary. *Ware and Turner* (2002) analyzing sediment porosities in the east Irish Sea basin suggested that exhumation was mostly <1500 m and laterally highly variable. They interpreted such exhumation variations as the effects of Neogene basin inversion.

## 2.2. Geophysical background

### 2.2.1. Seismic results

In the last decades, in addition to the geological studies described above, the geological setting of Ireland has been studied by the seismic refraction experiments on- and offshore Ireland. The experiments (Fig. 2.5) are reviewed by *Landes et al.* (2005). In the VARNET experiment *Landes et al.* (2005) derived a 3-D velocity model from 2-D crustal velocity models. The derived 3-D crustal model from 2-D seismic refraction velocity models which indicated the

Moho underneath Ireland has a smooth topography. Thereafter, receiver functions (*Landes et al.*, 2006; *Landes et al.*, 2007) confirmed this observation. Overall the results show that the Moho is located at a depth of ~30 km in central Ireland and reaches ~32.5 km depth in southeastern Ireland and under the Shannon Estuary in western Ireland.

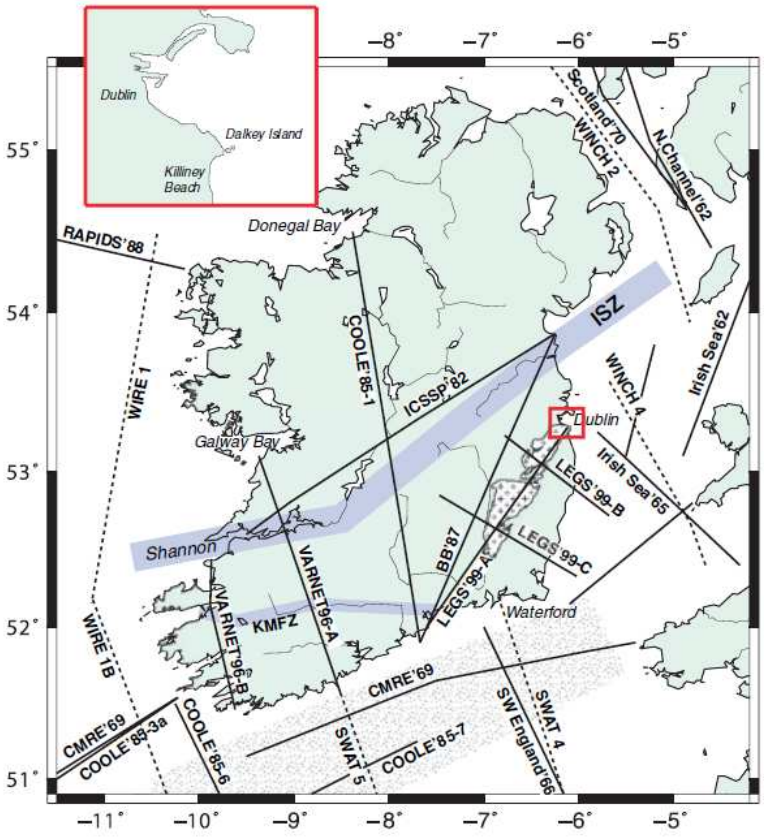



Figure 2.5.: Seismic refraction and reflection profiles onshore and offshore Ireland recorded in the period of 1969-1999. Shown are the CMRE 1969 profiles (*Bamford*, 1971), the ICSSP 1982 profile (*Jacob et al.*, 1985), the COOLE 1985 profiles (*Makris et al.*, 1988; *Lowe and Jacob*, 1989; *O'Reilly et al.*, 1991), the RAPIDS 1988 profile (*O'Reilly et al.*, 1995), the VARNET 1996 Lines A and B (*Masson et al.*, 1998; *Landes et al.*, 2000), and the LEGS 1999 Lines A, B and C (*Hodgson*, 2001). The BIRPS group normal incidence offshore reflection data (dashed lines WIRE, WINCH, SWAT; *Klemperer et al.* (1991) are also shown. The proposed location of the Iapetus Suture Zone (ISZ) and the Killarney Mallow Fault Zone (KMFZ; blue bands) are indicated. Dotted area offshore southern Ireland represents outlines of the North Celtic Sea Basin.

Additionally, the data from 11 seismic refraction profiles shown in Fig. 2.5 reveal that onshore Ireland mean crustal velocities range between 6.25 and 6.5 km/s with crustal thickness

of 28.5-32 km. Superimposed on a three-layer crust, the sedimentary layer has a thickness of approximately 6-8 km at the southern coastline, but only 3-4 km in the vicinity of the Shannon Estuary. The COOLE (Caledonian Onshore-Offshore Lithospheric Experiment) seismic refraction study (*Lowe and Jacob*, 1989) indicated a distinct layer in the mid-crust comprising two laterally continuous velocity discontinuities. In addition, they observed that the depth variations occur across a zone of 60 km and wide-angle reflectors shallow significantly to 45 km. They suggested that this broad zone of crustal change across the Irish Midlands which has complex deformation associated with the ISZ. Offshore seismic studies in the west of Ireland (WIRE lines, *Klemperer et al.* (1991); Fig. 2.5) resolved strong north-dipping reflectors in a 50-km wide zone, between 5 and 30 km depth, in the vicinity of the putative ISZ.

The Irish seismological lithospheric experiment (ISLE) followed the VARNET experiment in southern Ireland. For this project, 15 broad-band instruments from the Dublin Institute for Advanced Studies (DIAS) and eight short period instruments (GFZ Potsdam) recorded continuously in the period from November 2002 to July 2003 (*Landes et al.*, 2004). In one part of the experiment, *Landes et al.* (2006) used P-receiver functions to construct a crustal model for Ireland and found that the results were consistent with findings obtained from seismic refraction modelling (e.g., *Lowe and Jacob*, 1989).

*Landes et al.* (2005) concluded from the experiments shown in Fig. 2.5 that throughout Ireland the overall continental crustal thickness is about 30 km with a 2-3 km thick Moho transition zone. The experiments demostrate that the seismic velocity structure of the crust beneath Ireland is less than the global average of 41 km, reported by *Christensen and Mooney* (1995), but more typical of extended crust in their classification. This point is then debated by *Hauser et al.* (2008) in detail. The similarity with "extended crust" breaks down as the average crustal velocity of the Irish crust (Figs. 2.6 and 2.7) is similar to the global average value of ~6.45 km/s. But, the mean value of Poisson's ratio ($\sigma$) for the entire crust (0.24-0.25) is below the global average (0.265) (Poisson's ratio ($\sigma$) for seismically isotropic materials as a function of $Vp$ and $Vs$ velocities is defined as: $\sigma = 1/2[1-(1/(Vp/Vs)^2-1)]$ (*Christensen*, 1996).) Its value

for the lower 10 km of crust (0.258) is particularly anomalous, representing an unusually silica rich composition (Fig. 2.8) compared to that indicated elsewhere from seismic observations and studies of lower crustal xenoliths (*Holbrook et al.*, 1988; *Rudnick and Fountain*, 1995).

*Van den Berg et al.* (2005) experimentally measured Vp and Vs values and calculated them for granulite-facies lower crustal xenoliths from central Ireland close to the Caledonian Iapetus suture zone. They indicated that the measured seismic velocities of granulite-facies metapelitic xenoliths from central Ireland (mean Vp=7.09±0.4 km $s^{-1}$; mean Vs=4.1±0.15 km $s^{-1}$) correlate strongly with mineralogy, especially the modal abundance of garnet and sillimanite. Also, this study shows that with the exception of strongly heterogeneous samples, the velocities calculated from modal mineralogy also agree with experimentally determined values. Moreover, the results obtained from the geochemical and petrophysical measurements on lower crustal xenoliths from the Irish Midlands xenolith suite (*Van den Berg et al.*, 2005) robustly provided support for the accumulation of new crust by tectonic accretion of largely juvenile volcanic lastic sediments, mainly of Lower Palaeozoic age, close to the ISZ, followed by partial melting and emplacement of granitic plutons during and following the Caledonian Orogeny (*Klemperer et al.*, 1991; *Daly and van den Berg*, 2004).

Additionally, the geochemical and geochronological measurements from lower crustal xenoliths date this melting event to the Late Silurian/Early-Mid Devonian, towards the end of Caledonian deformation. As a consequence, this study provides robust evidence which is in broad agreement with results derived from the VARNET controlled source seismic experiment (*Hauser et al.*, 2008).

By means of analysis of the P-wave energy recorded along the wide-angle seismic lines of the VARNET project, the structures of the crust and mantle beneath Ireland, particularly the Iapetus Suture Zone have been investigated (*Masson et al.*, 1998; *Landes et al.*, 2000). In June 1996, *Masson et al.* (1999) obtained teleseismic data from the active source Variscan network experiment (VARNET) in southwestern Ireland (Fig. 2.5).

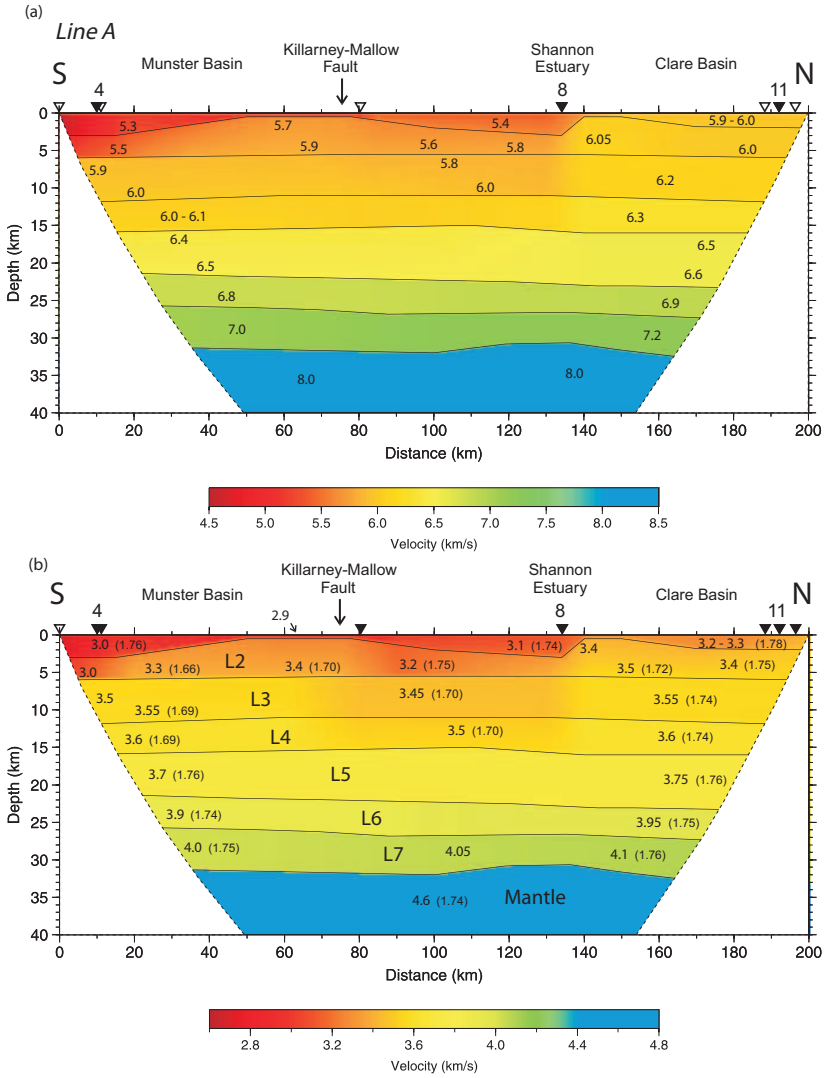



Figure 2.6.: a) P-wave velocity model for VARNET line A (for location, see Fig. 2.5). Numbers indicate the P-wave velocities in km/s. Open triangles mark the shot points, while filled triangles show location of seismic sections. (b) S-wave velocity model for line A. Numbers are S-wave velocities in km/s. Numbers in brackets are the Vp/Vs ratios. Dashed lines indicate the area resolved by reflected and/or refracted rays (from *Hauser et al.*, 2008).

The relative residual times that *Masson et al.* (1999) had calculated for the P-wave arrivals from the two teleseismic events recorded by receivers of the VARNET experiment, vary by 0.5 s along Line A, but only 0.2 s along Line B. The significant anomalies in travel time residuals for line A seems to coincide well with the postulated surface trace of the Caledonian ISZ (Fig. 2.1). *Masson et al.* (1999) suggested deeper velocity perturbations within the lithosphere since the

crustal model from the VARNET experiment cannot account for 0.2 s of variations in residual time. From an analysis of the residual time curves of the two teleseismic events, the possible trace of the Iapetus Suture at depth was inferred in the upper mantle, between 30 and 110 km. The suture is described by a velocity contrast of about 3% and it is located just in the south of the Shannon River Estuary (*Masson et al.*, 1999).

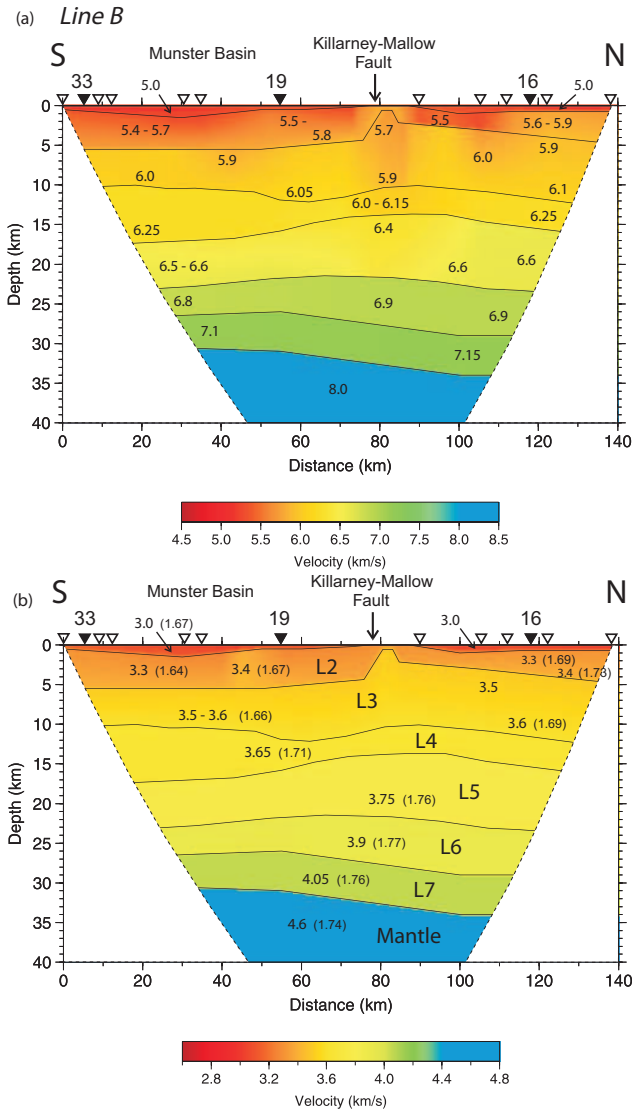



Figure 2.7.: (a) P-wave velocity model for VARNET line B (for location, see Fig. 2.5). Numbers indicate the P-wave velocities in km/s. Triangles mark the shot points, with filled triangles showing locations of seismic sections. (b) S-wave velocity model for line B. Numbers are S-wave velocities in km/s. Numbers in brackets are the Vp/Vs ratios. Dashed lines indicate the area resolved by reflected and/or refracted rays (from *Hauser et al.*, 2008).

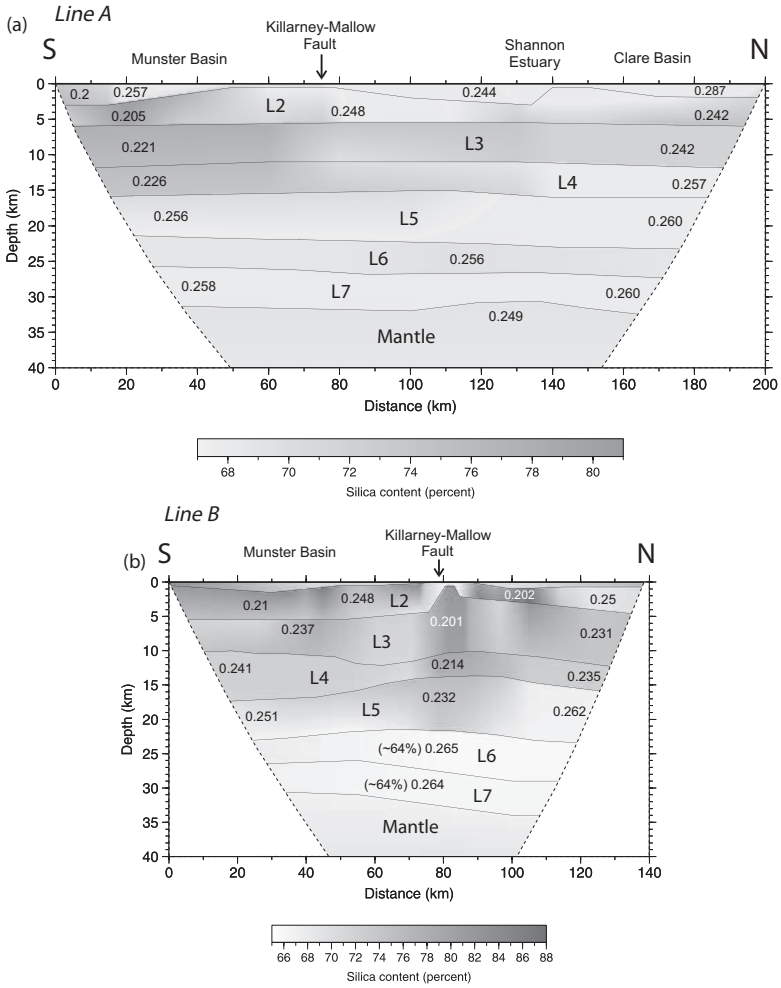



Figure 2.8.: (a) Silica content (%$SiO_2$) determined from the empirical relationship %$SiO_2$ = 100.9-496$\sigma^2$ for Poisson's ratio values ($\sigma$) less than 0.27 across (a) line A, and (b) line B (for more details see *Hauser et al.*, 2008).

Another significant study is S-receiver function study of *Landes et al.* (2007). By means of S-receiver function analysis, the depth of the lithosphere asthenosphere boundary (LAB) was suggested to be systematically deeper in southern (85 ± 5 km) than in northern (55 ± 5 km) Ireland (Fig. 2.9). This lithospheric thinning was explained by thermal erosion related to the Tertiary magmatic processes in the northern part of the country, namely the spreading head of the proto-Iceland plume. Then, *Wawerzinek et al.* (2008) supported it with results derived from a non-linear teleseismic P-wave traveltime tomography study. A low Vp anomaly (30-120 km depth) in the tomography model was explained by ancient and even recent upwelling of hot mantle material related to the spreading of the Iceland plume head.

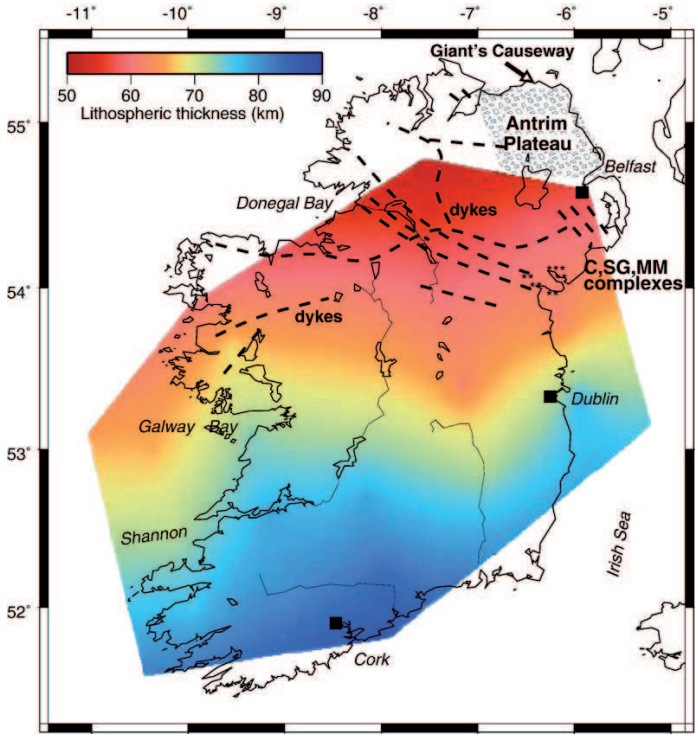



Figure 2.9.: Map of Ireland with smoothed LAB topography. An overall uncertainty in depth of ±5 km is estimated. Superimposed are locations of known BTVP (British Tertiary Volcanic Province) intrusions found in northern Ireland (e.g., *Gamble et al.*, 1999). Dashed lines reflect distribution of Tertiary dykes. Tertiary central complexes consist of Carlingford (C), Slieve Gullion (SG) and Mourne Mountains (MM) complexes (from *Landes et al.*, 2007).

We close this section by giving a brief review of shear-wave splitting analysis of SKS and SKKS phases conducted by *Do et al.* (2006). During the Irish Seismological Lithospheric Experiment (ISLE), shear-wave splitting analysis of SKS and SKKS phases, for the first time in Ireland were carried out on teleseismic data recorded by a temporary network of 23 broadband and short-period stations and two permanent broadband seismic stations. Shear wave splitting analysis constitutes a powerful and popular technique for characterizing particularly azimuthal anisotropy in the upper mantle. Possible anisotropy within the mantle is likely related to present or past deformation because the deformation mechanism influences the preferred orientation and tectonic process so that it controls anisotropy in the mantle (for further explanation see chapter 3). The splitting results from this study indicated an average delay time of 1.2 s. This was attributed to mantle anisotropy since the delay time caused by crustal anisotropy is usually a

maximum of 0.1-0.3 s due to the limited thickness of the crust (*Silver and Chan*, 1991; *Savage*, 1999). A delay time of 1.2 s suggests an anisotropic layer thicknes of 80-100 km, or more, assuming a shear wave velocity of 4.3 km/s and an anistropy of 4%.

*Do et al.* (2006) found a large change in fast polarisation direction between results using events from South America and East Asia (Fig. 2.10). This study indicated that south American events give more consistent fast-polarisation directions of within $\pm 15^0$ (clockwise from north) around the pole (NS direction), but events from East Asia show more variation in fast-polarisation directions, with an average of $\pm 30^0$ from the EW direction. Strong back-azimuththal variations are usually explained considering different factors which affect and complicate the measurement of anisotropy. Often, two (or more) anisotropic layers (*Silver and Savage*, 1994) are suggested to explain azimuthal variations, but dipping symmetry axes or deep origins of anisotropy can also be the cause.

*Do et al.* (2006) suggested that there is no correlation between the deformation related to the tectonic processes and the measured shear wave splitting parameters derived from the South American events. This may indicate that a shallow anisotropy is overprinted by a stronger anisotropy with an origin at a greater depth in the oceanic mantle. However, for the East Asian events the anisotropy agrees reasonably with the Caledonian/Variscan trend with a slight variation across Ireland suggesting lateral heterogeneity at shallow depth. Additionally, they found that there is no correlation between the fast polarisation directions and the present-day absolute plate motion.

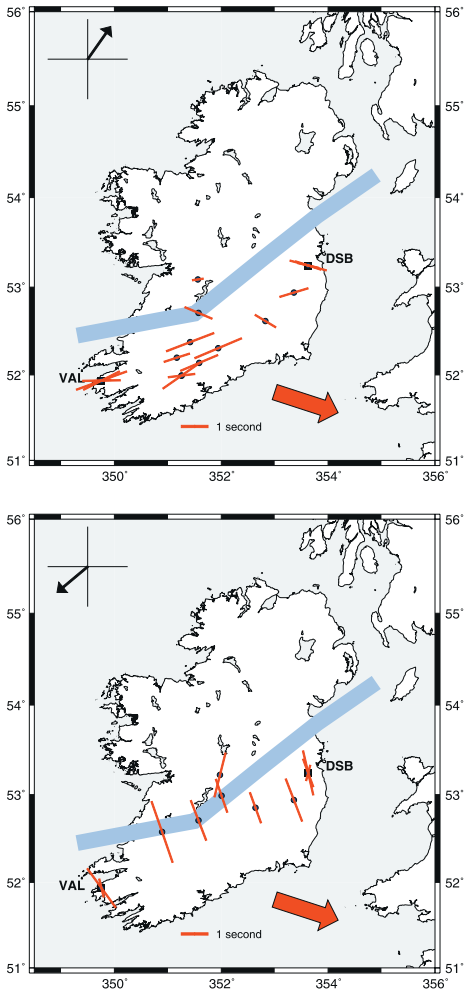



Figure 2.10.: Shear-wave splitting results from temporary and permanent stations (DSB and VAL). Thick lines indicate fast-polarisation directions with length proportional to delay time. Each bar represents a single measurement. (Bottom) Results obtained from events in South America (back-azimuth ~210-240$^0$). Fast-polarisation directions are predominantly NNW-SSE. (Top) Results obtained from events in East Asia (back-azimuth ~ 20 – 80$^0$). Fast directions are predominately E-W (to within ~ 20$^0$). Large arrow shows the absolute plate motion direction based on the NUVEL1A plate model (*Gripp and Gordon*, 1990). The grey band indicates the approximate position of the postulated trace of the Iapetus Suture Zone (ISZ) (After *Phillips et al.*, 1976). There are few measurements in the northwest of the suture due to the poorer data quality from stations in that region (taken from *Do et al.*, 2006).

### 2.2.2. Gravity results

Gravity maps (e.g., *Readman et al.*, 1997) clearly indicate the major structural features that are related to the tectonic development of Ireland. On Fig. 2.11, the four prominent trends (or lineaments) are observed: i) the predominance of NE-SW lineaments in the north and central Ireland, which is related to the Caledonian basement, ii) the NNE-SSW gravity trend in the Irish Midlands, which is parallel to some Caledonian faults in lower Palaeozoic (Ordovician/Silurian) inliers of central and northern Ireland, iii) weak NW-SE trending gravity lineaments, which may be generated by small near surface changes in density, related to fracture systems in the top few km of the crust, and iv) a dominant E-W Variscan gravity fabric in the south of Ireland which overprints the Caledonian fabric.

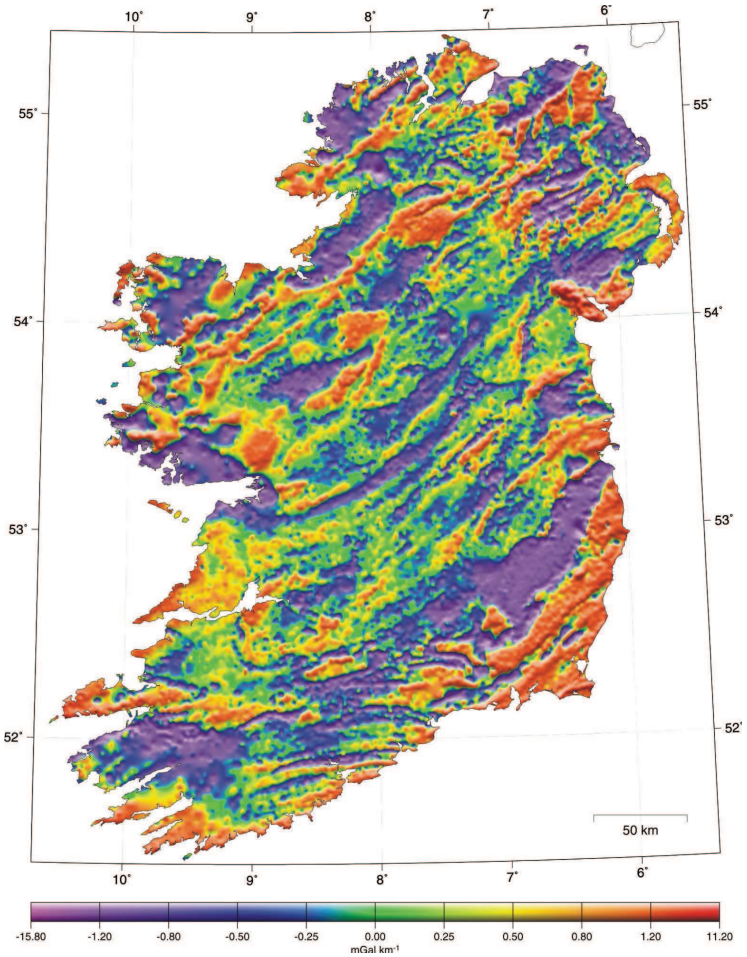



Figure 2.11.: Map of the first vertical derivative of the Bouguer anomaly for Ireland, with simulated illumination from the north (taken from *O'Reilly et al.*, 1996).

In addition, *Readman et al.* (1997) argued that the pattern of gravity anomalies and lineaments suggest that Variscan deformation in the south of Ireland did not involve the entire crust, supporting the idea of a "thin-skinned" tectonic model for the Irish Variscides (*Cooper et al.*, 1986), rather than a "thick-skinned" model (*Sanderson*, 1984). The results obtained from the gravity measurements are also in broad agreement with the results of the VARNET controlled source wide-angle seismic experiment (*Masson et al.*, 1998; *Landes et al.*, 2000).

### 2.2.3. Magnetotelluric (MT) results

Magnetotelluric (MT) study of *Brown and Whelan* (1995) revealed the structure to mid-crustal levels (c. 15 km) which broadly relates to Caledonian structure on the surface. In addition, in order to image particularly the geometry of the ISZ, more recently magnetotelluric (MT) data were collected at 17 sites along the NNW-SSE profile (for details see *Rao et al.*, 2007). The crustal geometry of the ISZ in central Ireland was inferred from an electrical resistivity model derived from broadband and long period magnetotelluric measurements along this profile. *Rao et al.* (2007) observed high conductivity at the middle and lower crustal depths within the ISZ interpreted to be most likely due to metamorphosed graphitic sediments (rich in sulphur) that spatially correlate with a region of deformation interpreted from the seismic refraction studies.

## 2.3. Summary of geophysical results

Finally, it may be said that nearly all previous studies well resolved the crust and the uppermost mantle beneath Ireland. However, the evolution of mantle and especially lithosphere-asthenosphere system is not yet fully understood. *Landes et al.* (2007) used the dataset from the ISLE to investigate the tectonic evolution of lithosphere-asthenosphere beneath Ireland using the S-receiver function method. This study indicated a thinning of the lithosphere towards the north of Ireland, in the region of the Irish part of the BTVP (Fig. 2.9). The lithosphere thins from ~85±5 km thickness in the south to ~55±5 km in the north of Ireland (Fig. 2.9). *Landes*

*et al.* (2007) explained this thinning lithosphere with the spreading of the Proto-Iceland plume and opening of the North Atlantic. *Wawerzinek et al.* (2008) used teleseismic tomography to explain the evolution of Ireland. The delays of teleseismic P-wave travel times (residuals) were inverted into a 3-D seismic velocity model. *Wawerzinek et al.* (2008) indicated faster seismic velocities in the south of Ireland, in contrast to the centre and north of Ireland. This seismic velocity contrast (-1% to -2.5%) in the study area was interpreted as a shallower asthenosphere in the centre to north compared to the south.

In this section, firstly a brief discussion on the thick-skinned model is presented. Although geophysical and geological evidence of the Variscan deformation is derived from different studies (e.g., *Readman et al.*, 1997; *Landes et al.*, 2006), the Variscan deformation is still under debate. To understand and construct a geodynamic model for the Variscan deformation of Ireland, some approaches are suggested: (a) in a thin-skinned model (e.g., *Ford*, 1987), only sediments metasediments and upper crust are involved in the process of deformation. This model seems consistent with the faults which are listric and seem to merge into a subhorizontal master fault (*Meissner*, 1996); (b) in a thick-skinned model (*Sanderson*, 1984), the deformation penetrates deep into the crust as far as to the Mohorovicic discontinuity. According to this model, the whole crust might be deformed during the Variscan Orogeny. The vital difference between both the thin−skinned and the thick−skinned tectonism lies in the depth to which deformation is considered to extend. *Readman et al.* (1997) exhibited, in contrast to the thick-skinned model, Variscan deformation in onshore and offshore southern Ireland can be explained with thin-skinned tectonic model. Pervasive Variscan deformation appears to be confined to the sedimentary and upper crustal structure and has not deformed the entire crust. Nevertheless, this deformation was found to be mostly confined to the hangingwall of the KMF (see Fig. 2.1). Therefore, this supports a thin-skinned interpretation for the subsequent Variscan deformation.

*Rider* (1974) indicated that the surface geology in the northern lowland region is comprised of upper Carboniferous sediments of Clare Basin. The lower to upper Carboniferous clare basin is oriented E-W and extends offshore to the west of Ireland. On the other hand, the region

between the Shannon Estuary and the KMF is dominated by Dinantian carbonates (e.g., *Sevastopulo*, 1981) and Namurain shales and sandstones (e.g., *Rider*, 1974). Due to the gravity data, *Readman et al.* (1997) also suggested that the influence of the Variscan deformation probably extends to at least 30 km north of the KMF. Moreover, *Do et al.* (2006) used shear wave splitting method to investigate possible anisotropy within the crust and mantle beneath southern Ireland. All studies mentioned are very strong but not sufficient to understand the tectonic evolution of Ireland. Therefore, in this study it is aimed to investigate seismic anisotropy within the crust and mantle beneath the whole Ireland using shear wave splitting and surface wave methods for the first time. In the next chapters, the obtained results will be presented that were derived from the methods.

## 2.4. Instrumentation

Here we describe the instrumentation used during 2002-2011 for the ISLE, ISUME and IA projects. Earth Data Limited (EDL) data loggers with Guralp CMG-40T broadband 3-component seismometers at the ISLE and ISUME stations have been used. Nanometrics Trillium 120PA broadband seismometers with Taurus data logger have been used in the IA project stations. A STS-2 seismometer with a Quanterra Q380 data logger has been installed at the permanent station DSB.

### 2.4.1. Seismometers

All stations were installed and serviced by DIAS personnel, except DSB which is a permanent GEOFON broadband station serviced by DIAS near Dublin (see Fig. 4.1). This GEOFON station has a wide spectral response and is only equipped with a special shielding. The recorded data from DSB station is transferred to the IRIS data (The Incorporated Research Institutions for Seismology) DMS (Data Management Center) in real time with the SeedLink protocol. Also, VAL is one of permanent stations, on the west coast, was also used in the ISUME. VAL is

operated by the Irish Meteorological office. DIAS helps to maintain both these stations.

Seismometers were generally installed in sites with low to moderate noise. For the ISLE project, 14 Guralp CMG-40T seismometers were deployed and recorded data from 2002 to 2006. For the ISUME project, 10 Guralp CMG-40T sensors (Fig. 2.12a) were deployed to extend the ISLE coverage and have recorded data from 2006 to present.



(a)



(b)



(c)

Figure 2.12.: Broadband seismometers that have been used in the project, (a) Guralp CMG-40T (eigen period 30 s), (b) Streckeisen STS-2 (eigen period 120 s) and (c) Nanometrics Trillium 120PA (band width from 175 Hz to 120 s).

Additional information about the recording times of each station is given in Appendix B. The CMG-40T seismometer (Fig. 2.12a) is a true broadband force-feedback instrument with measured linearity exceeding 90 dB and direct velocity outputs. It is self-contained in a waterproof stainless steel case with fully-adjustable levelling feet. No mass clamping is required. It has high sensitivity and dynamic range.

In addition to the ISLE and the ISUM projects, initial data from the IA project which is using Trillium 120PA seismometers (Fig. 2.12c) with Nanometrics Taurus recorders have also been used (Fig. 2.13). Twenty stations have now been installed for the IA project and will be deployed for 5 years. For the present study two years of broadband data from eight stations has been used (Fig. 4.1).




Figure 2.13.: (1) Trillum 120PA seismometer, (2) insulating seismometer base, (3) insulated seismometer cover, (4) GPS antenna, (5) Nanometrics Taurus data logger and (6) 12 volt battery.

### 2.4.2. Instrument responses

Seismometers are usually designed to record signals over a specified range of frequencies (or periods) so it is convenient to discuss instruments based on the range of vibration frequencies that they can detect. Thus one way to characterize seismometers is to describe the range of vibration frequencies that they can detect. A plot of the amplification as a versus frequency is called an instrument response. In other words, the response is a function of both the seismometer free period and the period of the galvanometer that picks up a current induced in a coil by the movement of the sensor. The instrument response of a WWSSN (World-Wide Standard Seismic Network) seismograph is given by:

$$V(\omega) = \frac{(-iA\omega^3)}{((-\omega^2 - 2i\epsilon_g\omega + \omega_g^2)(-\omega^2 - 2i\epsilon_s\omega + \omega_s^2) + 4\epsilon_s\epsilon_g\sigma^2\omega^2)}, \tag{2.1}$$

where $V(\omega)$ represents the factor that multiplies a single-frequency signal ($\sin \omega$t) ground displacement to obtain the actual deplection on the photographic record and where A is constant amplication factor. $\omega_s = 2\pi/T_s$ and $\omega_g = 2\pi/T_g$ are the resonance frequencies of the seismometer and galvanometer, respectively, $\sigma$ is a small coupling constant and $\epsilon_s = h_s\omega_s$ and $\epsilon_g = h_g\omega_g$ with $h_s$ and $h_g$ damping constants of the order 1.

An instrument is sensitive to vibrations at frequencies for which the "response" curve is relatively large. Five sample instrument response curves are shown in Fig. 2.14. The frequency is shown along the horizontal axis, and the equivalent period (period = 1/frequency) is shown along the top horizontal axis. The vertical axis shows the ground-motion amplification factor (Fig. 2.14).

To characterize an instrument, what is really important is the range of amplitudes, not the specific amplification, which is usually adjusted depending on the location of the seismometer. We have presented some examples to understand the differences between the response curves for different instruments (Fig. 2.15). In general, instrument response correction is done by transforming the seismogram $u(t)$ to the spectral domain. Dividing $u(\omega)$ by $V(\omega)$ leads in principle to a corrected seismogram (true ground displacement) when this is transformed back to the time

domain. In practice, one should be careful with such procedures, as $|\ V\ | \rightarrow 0$ for very low and higher frequencies. Therefore, instrument correction is generally limited to a finite bandwidth of frequencies. The instrument response of a digital seismometer is much more complicated than that of an electromagnetic seismometer. Very generally, the instrument response is described by an amplification factor $A_i$, and a number of "*poles*" $p_j$ and "*zeros*" $z_j$:

$$V(\omega) = A_i \frac{\prod_{j=1}^{k}(i\omega - z_j)}{\prod_{j=1}^{m}(i\omega - p_j)}. \tag{2.2}$$

$A_i$ splits up in two parts: $A_i = S_d A_0$, where $S_d$ is specified as the stage gain at some frequency $\omega_s$, and where $A_0$ normalizes the ratio of the polynomials to 1 at some normalizing frequency $\omega_n$, usually equal to the angular resonance frequency $\omega_s$ of the seismometer.

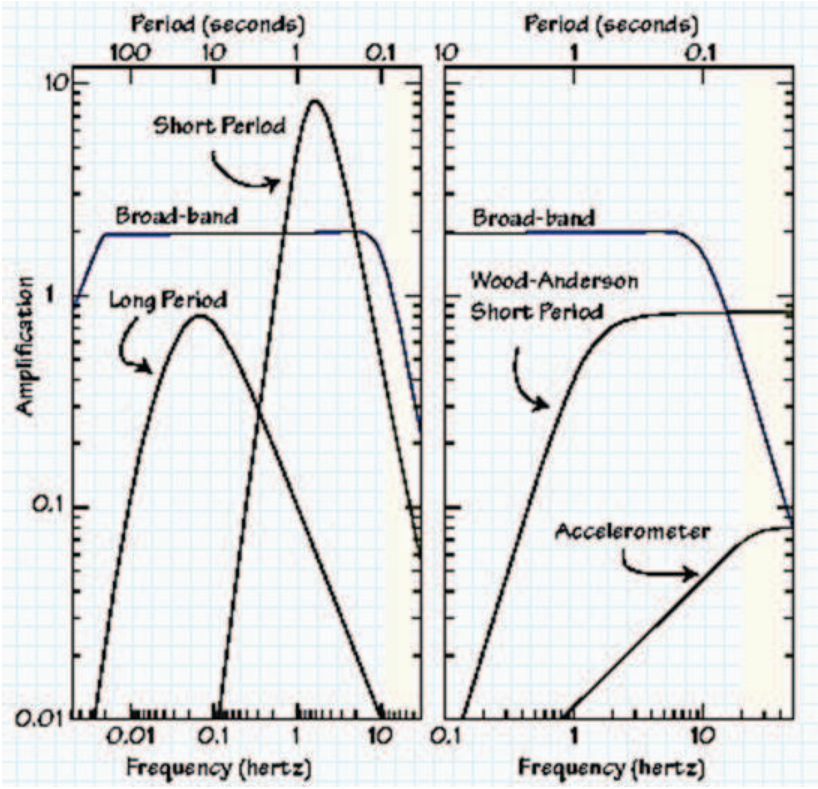
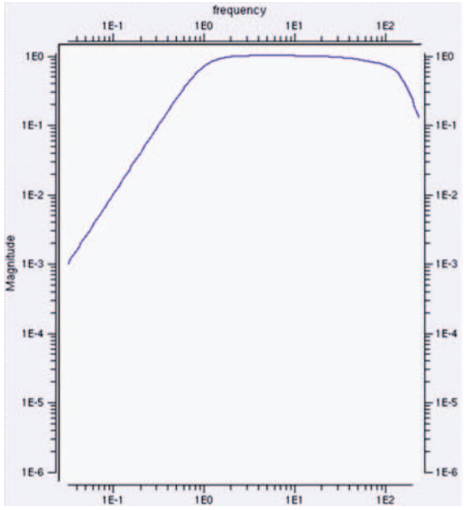
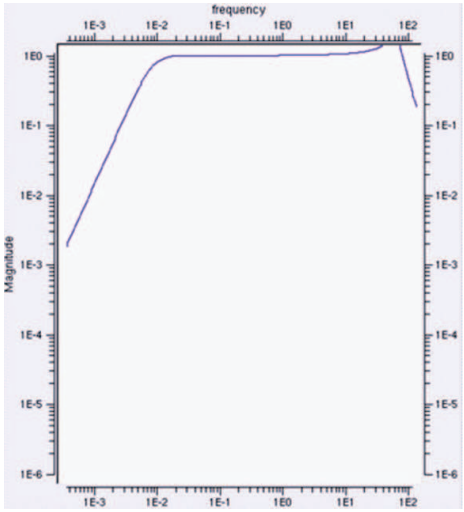


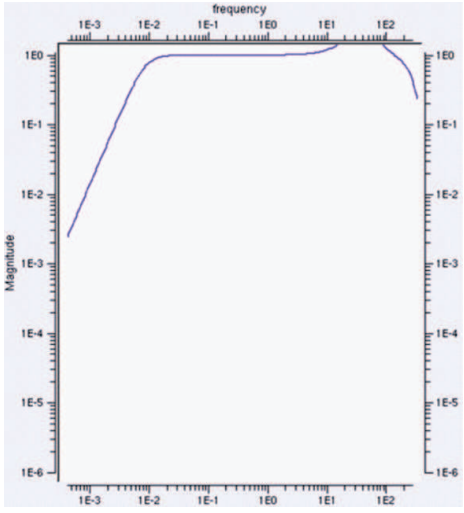

Figure 2.14.: The broad band instrument senses most frequencies equally well; the long-period and short period instruments are called "narrow" band, because they preferentially sense frequencies near 1/(15 s) and 1 hertz respectively. The yellow region is the low end of the frequency range audible to most humans (we can hear waves around 20 hertz to 20,000 hertz).




(a)




(b)




(c)

Figure 2.15.: Instrument response information for (a) Guralp CMG-40T, (b) Streckeisen STS-2 and (c) Nanometrics Trillium 120PA seismometers used in this study, respectively.

Additionally, seismograms distributed in SEED format by the IRIS Data Management Centre is usually used to correct the instrument response. One of the easiest ways to perform the correction of a variety of common instrument type is through the TRANSFER command in the Seismic Analysis Code (SAC). Therefore, the instrument responses are removed using SAC to eliminate the distortion and scaling of the data caused by the instrumentation (see this link[1] for the detailed information about removing the instrument response).

The left panel of this figure is a comparison of a modern broadband seismometer response and the classic (WWSSN) long- and short-period instruments. The same broad-band response is shown in the right panel of the figure, to compare the response with a special short-period instrument, the Wood-Anderson, and an accelerometer. The Wood-Anderson short-period instrument was the one that Charles Richter used to develop his magnitude scale for southern California. The accelerometer is an instrument designed to record large amplitude and high-frequency shaking near large earthquakes.

### 2.4.3. Data recorders

Most broadband stations were deployed with Earth Data Limited (EDL) PR-2400, PR-242 Portable Seismic Data Recorders (Fig. 2.16). These use 386Sx-40 PC unit processors with 2.1 GB removable hard disks. EDL recording boxes have built-in Analogue-to-Digital converters. PR-2400 and PR-242 recording boxes are the first generation instruments made by Earth Data Ltd with specifications requested by DIAS. For the PR-2400 (“Grey” boxes), data is recorded in EDL minute-file format and is downloaded from the built-in computer memory to a removable disk approximately every 14 minutes. For the PR-242 (“Green” boxes), data is recorded in a 10 minute-file format and downloaded from the built-in computer memory to a removable disk approximately every 10 minutes. The sampling rate for the PR-2400 and the PR-242 recorders are 75 and 25 sps, respectively. Recording durations for these instruments are about 3 and 9 weeks, respectively.

[1] the http://seismolab.gso.uri.edu/ savage/sac/commands/transfer.html



Figure 2.16.: EDL (Earth Data Limited) PR-2400 data logger. The removable disk can be seen on the right. The PR-242 is similar in design.

Newer Earth Data loggers, (EDL PR6-24; “blue” boxes, Fig. 2.17) have been used at several stations (see Appendix C). Disk capacity is 40 or 60 GB and the sampling rate is variable between 1 and 3000 sps. The sampling rate for our stations was set at 100 sps. Recording time for these instruments is large, up to about one year. Data conversion to miniseed format is directly done in the blue box.

Nanometrics Taurus data recorders are being used for the IA project stations (Fig. 2.13). The sampling rate for these recorders can be varied from 20 to 500 sps. Data storage for the recorders is presently on 16 Gb flash memory cards which provide recording times of about 9 months at 100 sps. Data is stored in Nanometrics Store format and converted to miniseed after download using Nanometrics Apollo software.

The GEOFON station (DSB) is equipped with a Quanterra Q380 data logger (Fig. 2.18). The data stream from DSB includes various channels, e.g. BH, HH, LH, VH.



Figure 2.17.: EDL (Newer Earth Data Limited) PR6-24 data logger.

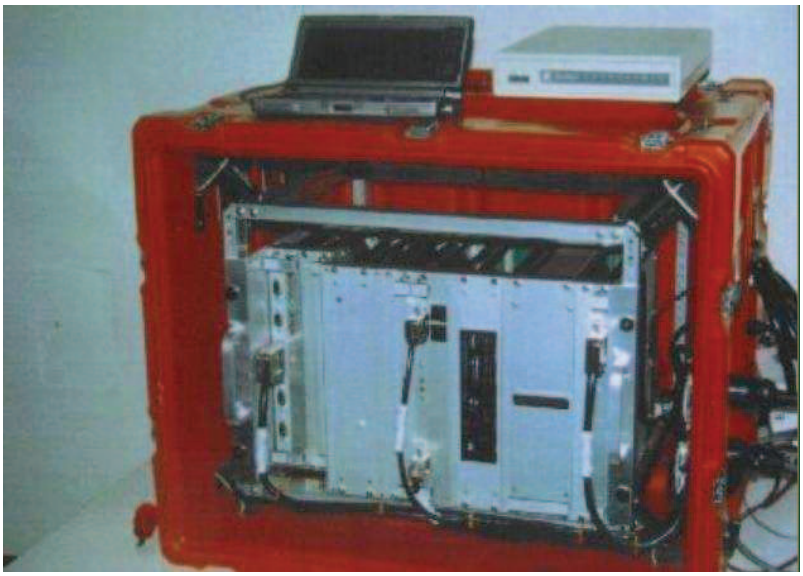


Figure 2.18.: Quanterra Q380 data logger for station DSB.

# 3. Seismic anisotropy, shear wave splitting and surface wave tomography

This chapter concentrates on the theory and mathematical background of anisotropy. First, the origins of anisotropy are described in terms of (small-scale) crystalline anisotropy and (large-scale) structural anisotropy. This section is then followed by a discussion on the possible depths where anisotropy can occur as well as the effects of different tectonic settings. At the end of the chapter, shear-wave splitting and surface wave tomography are described, respectively.

## 3.1. Hooke's Law

In this section, Hooke's law is introduced before presenting a simple definition of isotropic media and the theory of seismic anisotropy. The mechanical behavior of a continuous material is defined by the relation between the stress and strain. This relation is given by Hooke's law which states that the strain is proportional to the stress. Cauchy's formulation in tensor form of this law is

$$\sigma_{ij} = C_{ijkl}\epsilon_{kl} \tag{3.1}$$

where $\sigma$, C and $\epsilon$ denote the stress, a fourth-order tensor and the strain, respectively. This expression (eq. 3.1) contains nine equations for the stress components and each equation contains nine strain components. This is a generalization of Hooke's law. In very early studies of mechanical deformation under applied stress Hooke found that the deformation was linearly proportional to the stress for small deformations. It means that stress and strain depend linearly on each other so that such a medium is called linear elastic. This equation is also the foundation of the theory of linear elasticity.

The $C_{ijkl}$ form a fourth-order tensor since the stress and strain are second-order tensors. This is referred to as the elastic parameter tensor or the stiffness tensor. Hooke's law can lead to complicated relations. In general, a fourth order tensor would have $3^4$ (i.e. 81) independent parameters, but symmetry considerations remarkably simplify the equations and reduce this number for the stiffness tensor because the stress tensor is symmetric so we can have

$$C_{ijkl} = C_{jikl} = C_{ijlk} = C_{jilk}. \tag{3.2}$$

## 3.2. Isotropic media

The simplest case for the elasticity coefficients corresponds to an isotropic medium, that is, a medium with the same properities in all directions. If in the case of isotropy, $C_{ijkl}$ is invariant with respect to rotation, the number of independent parameters reduce to two:

$$C_{ijkl} = \lambda\delta_{ij}\delta_{kl} + \mu(\delta_{ik}\delta_{jl} + \delta_{il}\delta_{jk} \tag{3.3}$$

where $\lambda$ and $\mu$ are called the Lamé parameters, and also $\epsilon$, $\delta$ and $\mu$ denote the strain, the Kronecker delta and the shear modulus, respectively. The shear modulus describes the resistance to the shearing of the medium according to $\sigma_{ij}$=$2\mu\epsilon_{ij}$ with i≠j. The important point here for isotropic material is that the stiffness matrix can be represented by only these Lamé parameters, and is

$$C_{m,n} = \begin{bmatrix} \lambda+2\mu & \lambda & \lambda & 0 & 0 & 0 \\ \lambda & \lambda+2\mu & \lambda & 0 & 0 & 0 \\ \lambda & \lambda & \lambda+2\mu & 0 & 0 & 0 \\ 0 & 0 & 0 & \mu & 0 & 0 \\ 0 & 0 & 0 & 0 & \mu & 0 \\ 0 & 0 & 0 & 0 & 0 & \mu \end{bmatrix}$$

where $ij \rightarrow$ m and $kl \rightarrow$ n according to the Voigt notation.

## 3.3. Seismic anisotropy

Elastic anisotropy manifests itself in the seismic wavefield in many ways, and anisotropy affects the propagation of body and surface waves as well as the free oscillations of the Earth (*Maupin and Park*, 2007; *Long and Silver*, 2009). The basic definition of anisotropy is that seismic anisotropy is commonly defined as the dependence of seismic wave velocities on the propagation direction or polarization of the waves. This is because seismic waves are very sensitive to the varying elastic properties along their travel paths. This can be caused by a variety of factors, from the large-scale (e.g. aligned faults, layering) to the small-scale (e.g. aligned cracks and crystals).

In recent years, seismic anisotropy has been one of the most efficient geological and geodynamical tools for understanding the dynamics of the Earth because seismic anisotropy is a ubiquitous feature of most geological materials. It was recognized early on by seismologists that regions of the Earth's interior are anisotropic (e.g., *Hess*, 1964), and it is now clearly established that seismic anisotropy is present at several depth ranges in the Earth. For example, seismic anisotropy in many regions of the Earth's interior, including the crust, the mantle (particularly the upper mantle), the transition zone, the D" layer, and the inner core, is detected by many researchers (e.g., *Long and Silver*, 2009).

In the following subsections, the origin and the types of anisotropy are described and seismic

anisotropy studies that have been carried out in different regions are reviewed.

### 3.3.1. Origin of anisotropy

In general, due to theoretical and computational convenience, the Earth can be modelled as an isotropic medium for wave propagation. It is assumed that the speed of seismic waves is not affected by the direction of propagation. There is, however, considerable evidence of seismic anisotropy at different depths and different scales throughout the Earth, which may provide insight into Earth's dynamic processes. In particular, thanks to the computational power, measurement of seismic anisotropy represents perhaps the best tool available to geophysicists to directly probe patterns of the deformation at depth. Since the detection of seismic anisotropy is of great importance for the understanding of mineralogy and deformation processes that take place inside the Earth, it is important to find the origin of the anisotropy.

In this section, different possible origins of anisotropy are firstly described (Fig. 3.1) because they are strongly associated with the strain field of the medium and geodynamics.

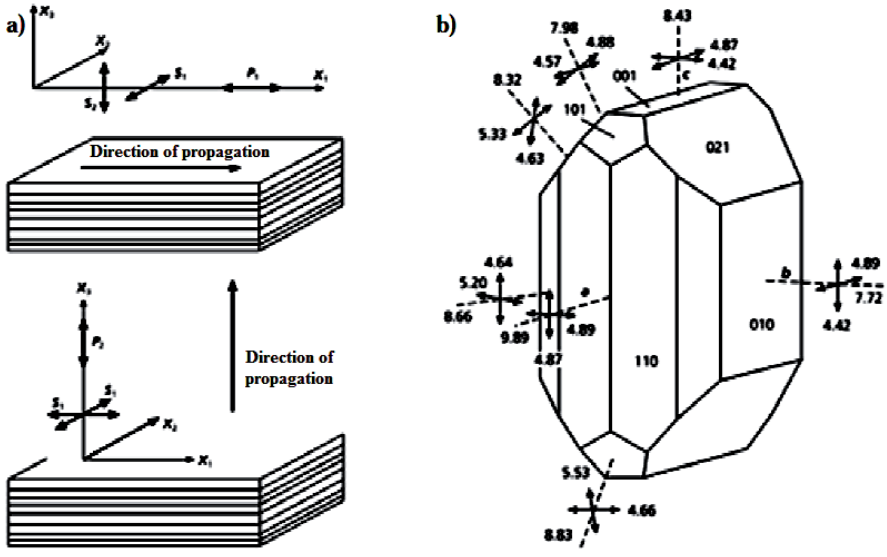



Figure 3.1.: Possible origins of anisotropy (after *Shearer*, 1999): (left) thin layered material results in hexagonal symmetry anisotropy. (right) Minerals like olivine have an intrinsic anisotropy.

Recent studies (e.g., *Crampin*, 1989; *Karato et al.*, 1995; *Long and Silver*, 2008) show that there are many causes of seismic anisotropy in the Earth. However, they are still under debate. Anisotropy in seismic velocities can be caused by alignment of elastically anisotropic crystals (rock fabric or lattice preferred orientation, LPO), alignment of fluid-filled pockets, or parallel layers of rocks with different physical (isotropic or anisotropic) properties. Researchers are seeking ways to distinguish uniquely these various causes by looking at the relationships between different measurable seismic properties for diagnostic signatures.

It is assumed that the speed and the polarization direction of a seismic wave are sensitive to elastic deformation and thus allow us to measure elastic anisotropy. In other words, the speed at which the wave travels is directly linked to the elastic tensor and the directional variation of seismic wave speed (i.e. elastic anisotropy) is hence a measure of strength and direction of anisotropy. Seismic anisotropy is generally reported as the percentage difference between the velocities corresponding to the fastest and slowest orientations:

$$A = (V_{max} - V_{min})/V_{average} \tag{3.4}$$

where $V$ is the P- or S-wave velocity. In general, Hooke's law is used to best define the relation between stress and strain. This law assumes the strains to be sufficiently small and that stress and strain depend linearly on each other. Such a medium is called linear elastic. In its general form, it can be written as:

$$\sigma_{ij} = C_{ijkl}\epsilon_{kl} \tag{3.5}$$

with $i, j, k, l = 1, 2, 3, 4$. The fourth-order tensor $C_{ijkl}$ is called the stiffness tensor or elastic tensor, which consists of 81 entries and describes the elastic properties of a medium. This tensor actually links the applied stress to the resulting deformation of the medium. In eq. 3.5, a stress $\sigma_{ij}$ is defined as acting on the i-plane and being oriented in j-direction (see Appendix A for more details). Consequently, the components with repeating indices are normal stresses, while different indices indicate shear stresses (Fig. 3.2).

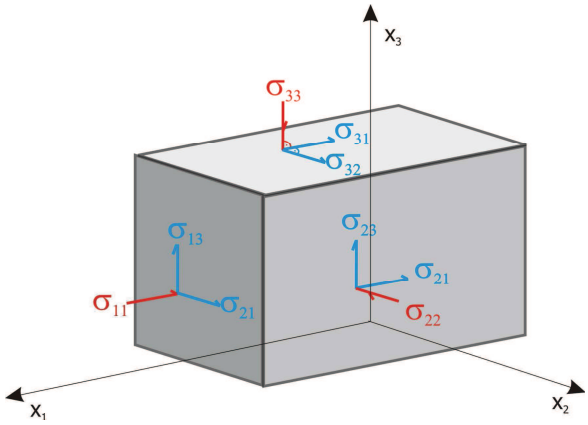



Figure 3.2.: Complete representation of stresses acting on a block. Normal stresses are identified with repeating indices, whereas tangential stresses have different indices.

In general form, Hooke's law makes a complex relation between strain and stress, but symmetry considerations greatly simplify the equations by reducing the number of independent parameters from 81 to 36 (eq. 3.2).

Moreover, general thermodynamics (*Nye*, 1972) requires the existence of a unique strain energy potential, and therefore:

$C_{ijkl} = C_{klij}$ which reduces the number of independent entries in the stiffness tensor to 21. Therefore, $C_{ijkl} = C_{klij}$ also results in 6 independent pairs $(k, l)$. Such symmetries can be used to introduce a 6 x 6 matrix $C_{mn}$ describing the elasticity of the medium $C_{mn}$ derived by assigning the pairs of indices $(i, j)$ and $(k, l)$ to the indices $m$ and $n$ varying from 1 to 6 by taking values of (1,1), (2,2), (3,3), (2,3), (1,3), and (1,2), respectively (*Voigt*, 1928):

$$C_{m,n} = \begin{bmatrix} C_{11} & C_{12} & C_{13} & C_{14} & C_{15} & C_{16} \\ C_{21} & C_{22} & C_{23} & C_{24} & C_{25} & C_{26} \\ C_{31} & C_{32} & C_{33} & C_{34} & C_{35} & C_{36} \\ C_{41} & C_{42} & C_{43} & C_{44} & C_{45} & C_{46} \\ C_{51} & C_{52} & C_{53} & C_{54} & C_{55} & C_{56} \\ C_{61} & C_{62} & C_{63} & C_{64} & C_{65} & C_{66} \end{bmatrix}$$

A further symmetry relation follows from consideration of a strain energy density function,

leaving 21 elastic moduli in the most general elastic material, which has general anisotropy, meaning the stress-strain behavior depends on the orientation of the sample. Before closing this section on the origin of anisotropy, see below some examples of the more common symmetry systems:

**a) Hexagonal symmetry**

Hexagonal symmetry (also called transverse isotropy) has many planes of symmetry along a common axis (the symmetry axis). This symmetry is described by five independent elastic constants. This class is the simplest anisotropic system and is used extensively because it can describe aligned cracks, aligned minerals, and lithologic anisotropy. Hexagonal symmetry with a vertical symmetry axis is called azimuthal isotropy because, with respect to a vertical axis, the elastic properties are invariant in the horizontal plane (Fig. 3.3a). All other orientations of the symmetry axis result in azimuthal anisotropy (Fig. 3.3b), as do all other symmetry systems.

**b) Orthorhombic symmetry**

Orthorhombic systems have three mutually planes of symmetry, defined by nine independent elastic constants. This could be caused by the combination of thin-layer or lithologic anisotropy with vertical aligned cracks, as observed in sedimentary basins (e.g., *Wild and Crampin*, 1991) (Fig. 3.3c).

**c) Monoclinic symmetry**

Fig. 3.3d shows that there is one plane of symmetry in the monoclinic case: monoclinic crystals are symmetric with respect to the plane (010) which is parallel to the two crystallographic axes [100] and [001] (or a-and c-axes). Monoclinic symmetry has 13 elastic constants. An example is the combination of two non-orthogonal sets of parallel cracks with a plane of symmetry perpendicular to the line of intersection of cracks (*Crampin*, 1993a). The ability to distinguish different causes and symmetries of anisotropy is dependent on the orientation and distribution of raypaths measured, the wave types used, and the quality of the data (Fig. 3.3d).

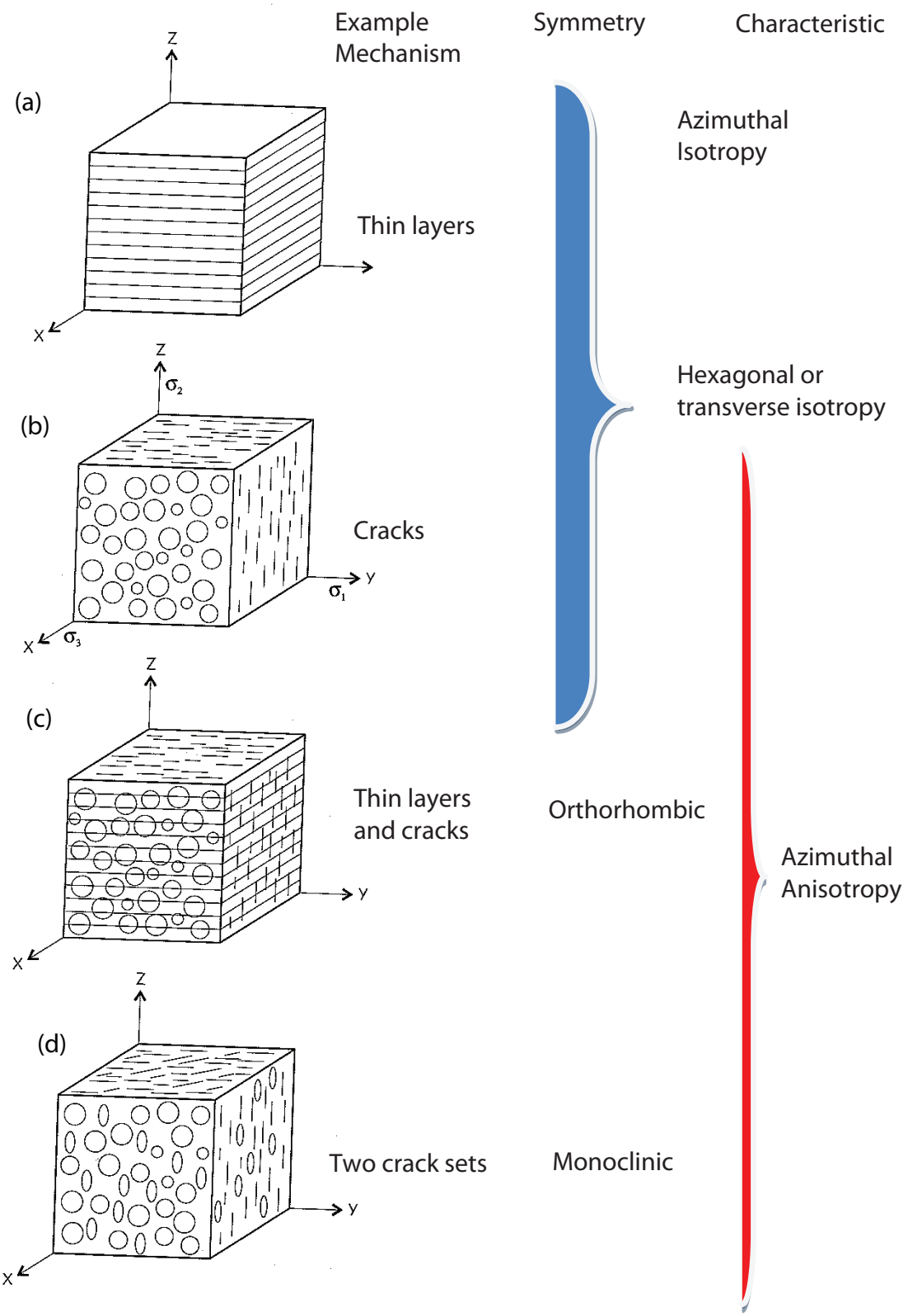



Figure 3.3.: Four mechanisms of seismic anisotropy indicating the three most common symmetry systems and their azimuthal characteristics. The principal stress orientations are indicated for vertically aligned cracks.

### 3.3.2. Structural origins of anisotropy

Here, (large-scale) structural origins and the mineralogical aspects of anisotropy are described. Also, the possible depths where anisotropy can occur are presented.

**A) Crustal anisotropy**

It is well known that various kinds of anisotropy generally occur in the continental crust (e.g., *Savage*, 1999). *Crampin et al.* (1984) indicated evidence from shear wave splitting observations that upper-crustal anisotropy is mainly caused by oriented cracks and micro-fractures. These crack systems are filled with other materials, in general fluids. Therefore, *Crampin et al.* (1984) suggested that the magnitude of anisotropy changes as a function of crack size and amount of cracks. This is the dominant source of anisotropy for the upper (~10 km) part of the crust (*Barruol and Kern*, 1996), since below all cracks are closed. Additionally, due to the characteristics of many shales, clays and mudstones in the upper crust, the anisotropy is caused by horizontal inter-granular platelets of mica and other minerals (e.g, *Crampin and S. Chastin*, 2003). Oriented openings tend to close perpendicular to the maximum principal stress direction $\sigma_1$ (*Crampin*, 1999a) (Fig. 3.3).

On the other hand, at about 10-15 km depth much of the anisotropy disappears because the cracks are closed under pressures of 200 to 300 MPa. Therefore, any crustal anisotropy below these depths is probably developed by other phenomena, for example, by minerals aligned during ductile flow (Fig. 3.4). *Backus* (1962) first suggested that anisotropy in the lower crust is dominated by fine horizontal layers like mylonite zones due to the interactions of reflections and transmissions through thin layers (Fig. 3.4). Fig. 3.4 illustrates the LPO (Lattice Preferred Orientation)-based 3D-velocity distributions of relevant lower crustal and upper mantle rocks (mica gneiss, amphibolite, peridotite) and the directional dependence of P-and S-wave propagation and S-wave polarization. The direction of wave propagation in relation to the preferred orientation of the major minerals and the symmetry of their lattice fabric is of great significance.

As mentioned above, in some cases multiple physical factors could be contributing to the measured anisotropy. The possible causes of crustal anisotropy (e.g., *Crampin et al.*, 1984) are

listed as:

**a) Direct stress-induced anisotropy**

Isotropic materials can become anisotropic when large deviatoric stresses act upon them (*Dahlen*, 1972). However, the stresses required for this are probably too large for regions other than the immediate vicinity of earthquake nucleation zones (*Evans*, 1984).

**b) Aligned minerals**

The major rock forming minerals are anisotropic, thus a bulk alignment of the symmetry axes (possible by a variety of mechanisms) can have an anisotropic effect. Olivine is one of the abundant minerals in the lower crust and is believed to be the main constituent of observed anisotropy in the upper mantle (e.g., *Hess*, 1964).

**c) Lithologic anisotropy**

This refers to sedimentary and low grade metamorphic rocks where flattened or elongated grains (not necessarily anisotropic themselves) are aligned, thereby producing an anisotropic rock mass. The anisotropy of clays (*Slater et al.*, 1993) and shales (*Robertson and Corrigan*, 1983) is probably this type.

**d) Thin-layer anisotropy**

At long wavelengths, thin layers of isotropic material can be anisotropic (*Postma*, 1955). Sedimentary sequences with layers of contrasting lithologies are well documented in geological literature and some observations of anisotropy have been attributed to this source (*Bush and Crampin*, 1991).

**e) Cracks**

Cracks (or fractures) and pore spaces are common in many types of rock. In general, aligned cracks produce effective seismic anisotropy (*Hudson*, 1982). Two characteristics are important to describe the distributions of cracks (fractures) as the origin of the azimuthal splitting: (1) the horizontal projections of the polarizations of the leading split shear waves are usually parallel or subparallel for all ray paths within the shear-wave window (*Crampin and Lovell*, 1991), and (2) this direction is subparallel to the local direction of maximum horizontal compressional stress in

rock volumes where orientations of both polarizations and stress have been reliably determined (e.g., *Crampin and Lovell*, 1991).

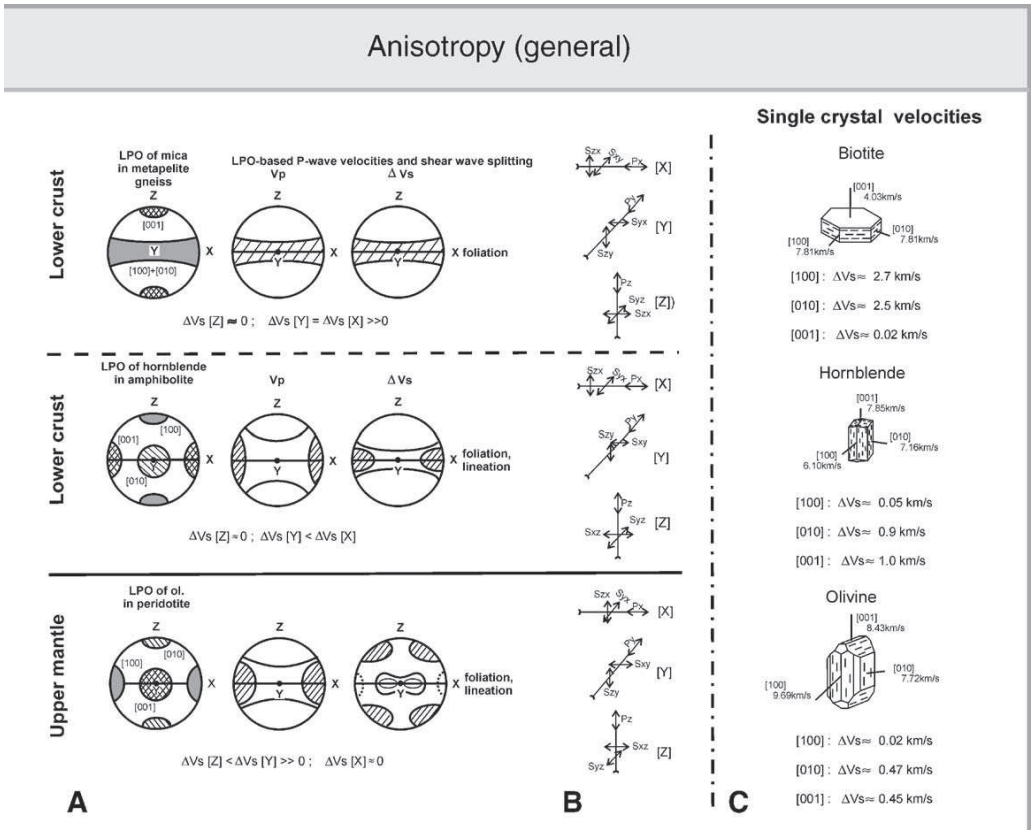



Figure 3.4.: Conceptual model for P- and S-wave propagation in foliated lower crust and upper mantle rocks, dominated by crystallographic preferred orientation (LPO) of biotite, hornblende and olivine, respectively. A) LPO and models of velocity surfaces (Vp and Vs) in foliated lower-crustal and upper mantle rocks. B) Propagation and polarization of P- and S-waves with respect to the structural reference frame X, Y, Z. C) Vp and Vs of dominating single crystals (taken from *Meissner et al.*, 2006).

**B) Mantle anisotropy**

In contrast to highly fractured rocks in the Earth's crust, the Earth's mantle does not contain many cracks or fractures. Therefore, the source of mantle anisotropy has to be different from the source of crustal anisotropy. Recent seismological methods have provided much of the information on the internal structure of the Earth, especially on the mantle, as well as progress towards robust resolution of the superimposed lateral variability of seismic speeds (e.g., *Nolet et al.*, 1994) (Fig. 3.5).

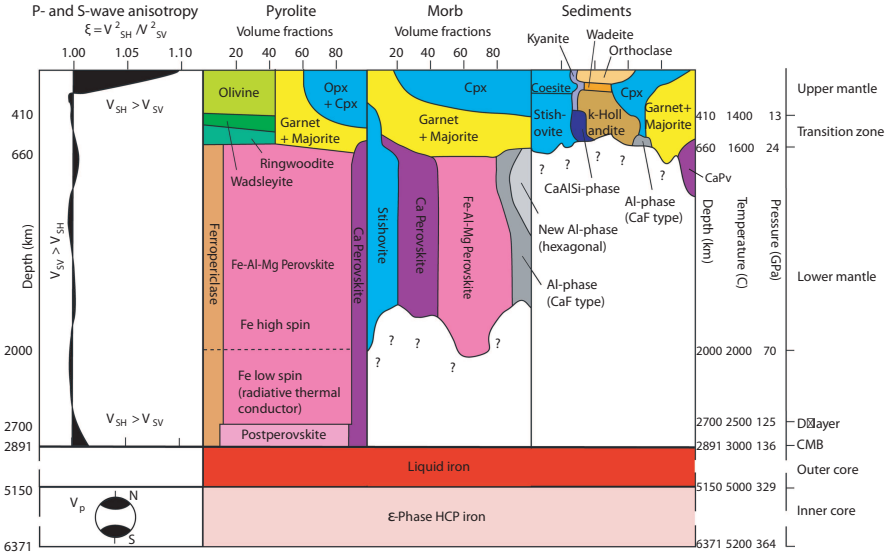



Figure 3.5.: Simplified petrology and seismic anisotropy of the Earth's mantle and core (taken from *Mainprice*, 2007).

The mantle is almost 2900 km thick and comprises the largest part of the Earth's volume, approximately 83%. The mantle is defined commonly with several different layers. One of these layers is the upper mantle which exists from the base of the crust to a depth of about 670 km and is composed of predominantly peridotite, an ultramafic rock made up of the minerals olivine and pyroxene. The upper mantle is commonly divided into two parts: (a) the lithosphere which includes the crust and the uppermost mantle, and which is composed of the hard and rigid outer layer of the Earth, and (b) the asthenosphere, below ~100 to 200 km. The asthenosphere is the weaker, hotter and deeper part of the upper mantle. The boundary between the lithosphere and the asthenosphere is defined by a difference in response to stress: the lithosphere remains rigid for very long periods of geologic time in which it deforms elastically and through brittle failure while the asthenosphere deforms viscously and accommodates strain through plastic deformation.

The lower mantle extends from 670 to 2900 km below the Earth's surface. Its physical properties are different from the upper mantle. Due to cooler temperatures and lower pressures, the rocks in the upper mantle are more rigid and brittle. However, the lower mantle is hot and plastic. The higher pressure causes the formation of minerals that are different from those of

the upper mantle.

Anisotropy is an inherent feature of most minerals and mineral assemblages found in the upper mantle (e.g., *Kern and Tubia*, 1993; *Nicolas and Christensen*, 1987). These anisotropies tend to average out over the large scale if individual crystals are oriented randomly. However, if some force tends to align them, the medium as a whole can become anisotropic. When rocks are progressively deformed over geologic timescales, the alignment of mineral grains (lattice preferred orientation, LPO) results in bulk anisotropy of the rock. Bulk anisotropy can additionally be generated by an ordered assembly of individually isotropic materials of different wave speeds (shape preferred orientation, SPO). Seismic anisotropy especially in the upper mantle are caused by crystallographic or lattice preferred orientation (CPO or LPO), which refers to non-random distributions of the orientations of individually anisotropic mineral grains in mantle rock and is also referred to as fabric or texture (e.g., *Karato et al.*, 1995) (Fig. 3.6). Additionally, the basic physics of LPO development and SPO is briefly reviewed below.

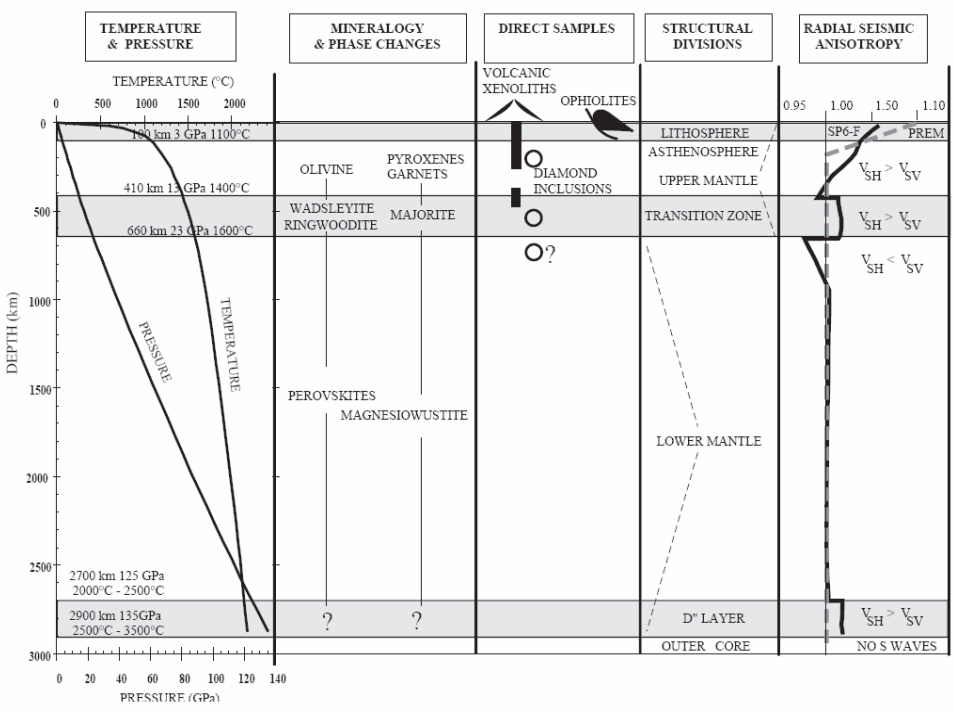



Figure 3.6.: The major physical and chemical variations in the Earth's mantle which control seismic anisotropy partly inspired after *Gillet* (1995). The seismic model SP6-F comes from *Montagner and Kennett* (1996).

**1) Lattice preferred orientation (LPO)**

In recent years, many researchers (e.g., *Wenk*, 1985; *Karato*, 2008) have studied the mechanisms of the development of lattice-preferred orientation (LPO) because the LPO of elastically anisotropic minerals is one of the most important anisotropic structures. In particular, non-random distribution of crystallographic orientation, LPO (or crystallographic preferred orientation; CPO), is one of the significant microstructural characteristics of rocks. In addition, several crustal rocks exhibit LPO anisotropy; particularly phyllosilicates (micas) in the upper-middle crust, and amphibole minerals in lower crust (e.g., *Christensen and Mooney*, 1995) (Fig. 3.4).

As known, LPO in naturally deformed rocks can be measured in laboratory or LPO in rocks deformed in the Earth's interior can be revealed from seismic anisotropy. Therefore, LPO is controlled by both the microscopic physics of deformation or the nucleation -growth of crystals and the macroscopic geometry of field where LPO develops (finite-strain ellipsoid, stress, magnetic field, heat flow etc.) (see Fig. 3.6). This suggests that the relation between LPO and deformation geometry can change with physical (or chemical) conditions of deformation. A question is addressed whether seismic anisotropy due to LPO is related to the kinematic framework (shear direction and shear plane) or to the dynamics of flow (orientation of stress). LPO in minerals can be produced by several physically distinct processes: for example plastic flow with or without recrystallization, viscous flow and anisotropic crystal growth. This implies that its mechanisms in large-scale depend on ductile plastic and viscous deformation as well as the growth process. *Nicolas and Poirier* (1976) indicated that plastic flow induces preferred orientations in minerals. Based on experimental studies, a simple micro-structural model of dynamically recrystallized materials has been proposed. It has been shown that the dominant mechanism of LPO is determined by the relative rates of plastic when both nucleation and growth are easy compared to plastic deformation.

The symmetry and strength of the upper mantle anisotropy reflect a portion of the mantle minerals whose crystallographic axes have been oriented by some deformation process (*Mainprice et al.*, 2005), acting in the past (fossil anisotropy) or at present. Generally, symmetry consider-

ations greatly simplify the equations by reducing the number of independent parameters from 81 to 36:

$C_{ijkl} = C_{jikl} = C_{ijlk} = C_{jilk}$.

Also, general thermodynamics (*Nye*, 1972) requires the existence of a unique strain energy potential, and therefore:

$C_{ijkl} = C_{klij}$

which reduces the number of independent entries in the stiffness tensor to 21. As a result, the most general stiffness tensor for an elastic medium contains 21 independent parameters. In other words, the elastic properties of any material are described by a 4th-order tensor, $C_{ijkl}$, with 21 independent components defined by Hooke's law.

All possible crystals belong to one of nine possible symmetry systems. In the more complicated the symmetry, the independent elastic constants are described by the elastic tensor. Olivine is orthorhombic with nine non-zero elastic constants: C11, C22, C33, C12, C13, C23, C44, C55 and C66. Therefore, for particularly the upper mantle anisotropy, mostly orthorhombic (olivine) is commonly considered because olivine, the primary upper mantle mineral constituent, has an intrinsic single-crystal shear wave anisotropy of ~18%. Consequently, LPO of olivine makes the largest contribution to upper mantle anisotropy even though orthopyroxene makes a smaller contribution. The upper mantle (down to 410 km) is composed of three anisotropic and volumetrically important phases (Fig. 3.7); olivine, enstatite (orthopyroxene) and diopside (clinopyroxene). The figure illustrates the seismic properties of these single crystal in the mantle. Here only LPO olivine was reviewed since the primary cause of the upper mantle anisotropy is olivine. Furthermore, the symmetry of LPO is controlled by the symmetry of the "field" (strain etc.) and the symmetry of crystals. Only one can thus infer the symmetry of deformation from the LPO.

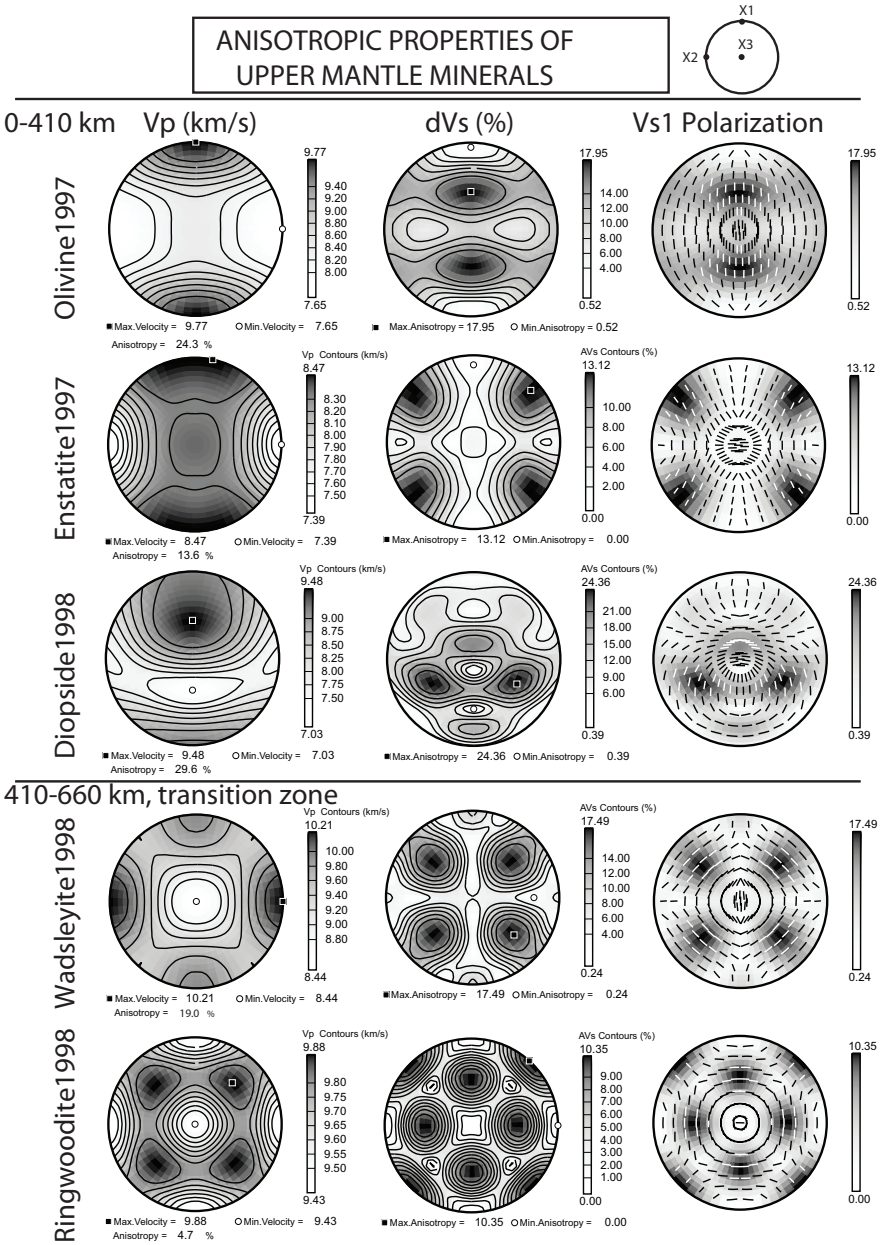



Figure 3.7.: The seismic anisotropy of single crystals of upper mantle minerals. Projections are upper hemisphere. All properties calculated at room pressure and temperature. X1, X2, X3 are the reference axes for the elastic constants, X1=[100], X2=[010] and X3=[001] for cubic, tetragonal and orthorhombic crystals.X1=(100) X2=[010] and X3=[001] for monoclinic. Contours in km/s for Vp (left) and in % anisotropy for dVs (middle). Right: trace of the Vs1 polarization plane (from *Mainprice et al.*, 2000).

**2) Olivine**

Until recently, both experimental studies and examinations of mantle-derived rocks have shown that LPO olivine is quite complex and a variety of olivine fabric types have been identified both in the laboratory and in nature, including A-, B-, C-, D-, and E- type fabrics (e.g., *Mainprice*, 2007; *Karato*, 2008) (Fig. 3.8). At modest stress and temperature, simple shear experiments on dry olivine aggregates done revealed A-type fabric, which is related to dominant slip in the [100] direction on the (010) plane. If in this case, generally the fast axes of individual olivine crystals tend to align in the direction of shear; for horizontal mantle flow, this would imply that the measured fast direction of azimuthal anisotropy should correspond to the horizontal flow direction because the A-axis of the olivine crystals represents the propagation direction of P and S waves with the highest velocities.

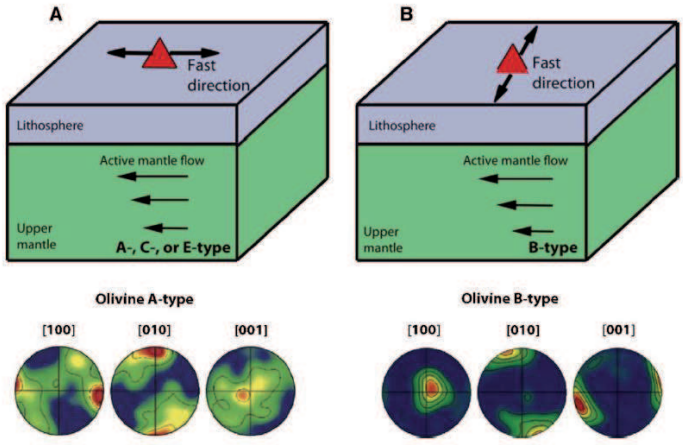



Figure 3.8.: Schematic diagram of the relationship between horizontal mantle flow and the resulting azimuthal anisotropy for different olivine fabric types. (A) In most regions of the asthenosphere, olivine fabric is expected to be A-, C-, or E-type, which would result in a fast axis of anisotropy that is parallel to the (horizontal) flow direction beneath a seismic station. Typical examples of pole figures for experimentally deformed olivine aggregates for A-type fabric are shown; the statistical distribution of the [100], [010], and [001] crystallographic axes are shown with respect to the deformation geometry (the horizontal line represents the shear plane). (B) If B-type olivine fabric, rather than A-, C-, or E-type,dominates, then the same flow direction would result in an observed fast direction that is different by $90^0$. Typical pole figures for B-type olivine are shown. All pole figures are from *Karato* (2008), after *Jung et al.* (2006).

For example, if the A-axis of olivine mineral is close to the horizontal plane, this corresponds to the polarization direction of the fast SKS/SKKS waves that is used in this study. Hence, the A-axis is usually called "the fast axis". Most olivine LPO observed in nature and in the laboratory is associated with a seismically fast direction that aligns parallel to the flow direction (*Ismaïl and Mainprice,* 1998). However, experiments show that at relatively high-stress and wet conditions the seismically fast direction aligns perpendicular to the flow direction, giving rise to B-type olivine fabric (*Jung and Karato,* 2001; *Katayama and Karato,* 2006). *Katayama and Karato* (2006) developed a theoretical fabric-transition model for B- and C-type fabrics which is related to slip in the [001] direction on the (100) plane. This model is constrained by both experimental and natural observations (e.g., *Katayama et al.,* 2005; *Skemer et al.,* 2006) and shows that transition shear stress increases linearly with temperature. B-type fabric is associated with slip in the [001] direction on the (010) plane. This type is usually favoured by high stresses, low temperatures, and some amount of water since recent deformation experiments show that olivine LPO is a function of water content, stress, and temperature (*Karato et al.,* 1995). However, we do not have sufficient information about the possible effect of pressure on olivine fabric.

It is clearly observed that for the B- and C- type fabrics, seismic velocities do not show clear differences compared to the A-axis because it is more difficult to detect their directions from the seismological data (*Maupin and Park,* 2007). At high temperatures and low stresses, the dominant fabric type is expected to change from A-type to E-type ([100](001) slip dominates) to C-type ([001](100) slip dominates) with increasing water content (*Long and Becker,* 2010). A linear extrapolation of the fabric transition from high-stress experimental conditions to the low-stress conditions more suitable for the mantle suggests that the transition temperature for B-type fabric is around 650-900$^0$ C. This range of temperature is consistent with inferred temperatures for natural B-type fabric (*Skemer et al.,* 2006). Geodynamic subduction zone models with experimentally based wet olivine rheology and fabric transitions show that B-type fabric conditions are localized in the fore-arc mantle of subduction zones (*Kneller et al.,* 2007).

### 3) Shape preferred orientation (SPO)

Anisotropic structure can also be produced by shape preferred orientation (SPO), which is associated with the alignment of material with distinct isotropic elastic properties (contrasting with the surrounding matrix), such as melt pockets or cracks in the crust. Such shape preferred orientations (SPO) result in an effective fast and slow orientation of seismic wave propagation with the fast S-wave polarised along the strike of the cracks. In addition, in the lower crust, SPO anisotropy is mainly due to fluid-filled cracks (e.g., *Crampin and Lovell*, 1991). SPO of melt or other materials may contribute to anisotropy in parts of the mantle (e.g., *Greve and Savage*, 2009) or in the D" region (e.g., *Moore et al.*, 2004). D" anisotropy may well be controlled by the SPO of melt or slab graveyard materials (*Kendall and Silver*, 1998) rather than LPO (Fig. 3.9).

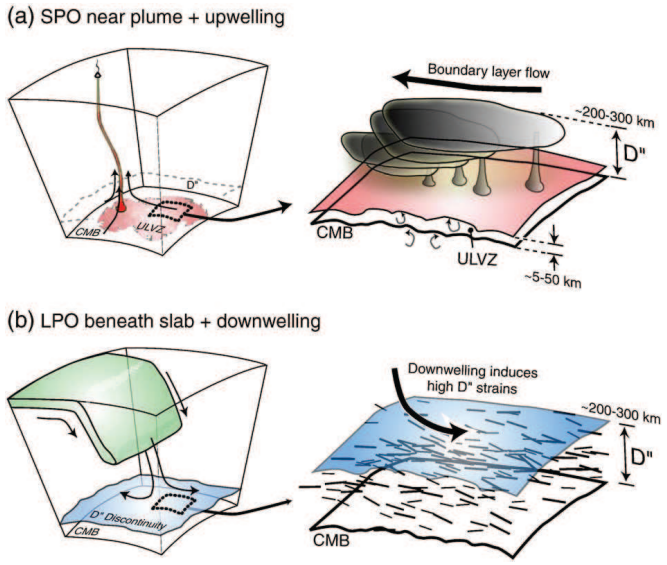



Figure 3.9.: Cartoon of possible mechanisms for D" anisotropy, after *Moore et al.* (2004). In the first scenario (top), partial melt associated with ultra-low velocity zones may occur throughout the D" volume if the melt is close to neutral buoyancy or if advection is fast compared to percolation velocities (*Moore et al.*, 2004). The melt is aligned to produce SPO by horizontal shear flow above the CMB in the vicinity of a narrow upwelling. In the second scenario (bottom), a downgoing slab impinging upon the CMB induces high-stress, highstrain deformation in the dislocation creep regime, which induces the LPO of lowermost mantle minerals (from *Long and Becker*, 2010).

Particularly, beneath mid-ocean ridges and perhaps some portions of subduction systems,

SPO may be thought to be a primary cause of seismic anisotropy. Also, SPO related to decompression melting plays an important role in the development of seismic anisotropy within continental rift zones.

**C) Anisotropy in the lower mantle**

In contrast to the upper mantle, the lower mantle of the Earth is elastically nearly isotropic, with the exception of the D" layer just above the core-mantle-boundary since the dominant constituent mineral in the D" is perovskite [$(Mg,Fe)SiO_3$] which is highly anisotropic (*Karato et al.*, 1995) (Fig. 3.7).

**D) Anisotropy in D"**

Recently, seismological observations and geodynamic models have shown that the lowermost 250-300 km of the mantle, termed D", is a complex region and is significantly seismic anisotropy. The D" layer was originally defined by *Bullen* (1949). The mantle-side portion of this layer (D") is the site of dynamic processes because it may involve both thermal and chemical heterogeneity at various scales. Large amplitude seismic heterogeneity over a wide spectrum of scales (*Lay et al.*, 1998) was observed in the D" region. It is likely related to a multitude of overlapping dynamic processes. The large thermal gradients associated with a thermal boundary layer (TBL), where the heat from the core is mainly transferred across the CMB by thermal conduction is a vital component of the energy budget for mantle and core convection (*Lay et al.*, 2008).

In particular, recent experimental (*Oganov et al.*, 2005) and theoretical (*Wentzcovitch et al.*, 2006) studies show that magnesium silicate perovskite is likely to undergo a phase change at pressures associated with the lowermost mantle and the presence of the postperovskite phase has been invoked to explain some seismological properties of the D" layer (e.g., *Lay and Garnero*, 2007). Although both experimental and theoretical studies indicate that the lower mantle mineral phases exhibit strong single crystal anisotropy at both ambient and high pressure and temperature conditions (*Mainprice et al.*, 2000), the orthorhombic-structured $MgSiO_3$ perovskite minerals do not show any significant preferred orientation at high pressure and low tempera-

ture condition (e.g., *Meade et al.*, 1995). If it is possible to justify the presence of ultra low velocity zones (ULVZs) due to the discontinuity likely to be associated with the post-perovskite phase change, D" can be distinguished from the overlying mantle by the presence of seismic anisotropy (e.g., *Lay et al.*, 1998; *Moore et al.*, 2004).

Dislocation creep occurs in $MgSiO_3$ perovskite at pressure-temperature conditions equivalent to the lower mantle (*Wookey et al.*, 2002). Therefore, deformation-induced alignment of $MgSiO_3$-post-perovskite (ppv) causes seismic anisotropy in the D".

To detect seismic anisotropy in the Earth's mantle and D" layer, phases such as SKS/SKKS, S and ScS are usually used. SKS describes the path of a seismic wave through layers of the Earth, with S indicating a shear wave or S-wave traveling through the mantle, and K indicating a compressional wave or P-wave traveling though the Earth's outer core (see Fig. 3.14). SKKS is similar to SKS, but with two passages through the outer core and one reflection at the CMB (for detail information about SKS and SKKS phases see *Stein and Wysession*, 2003). The phases have some advantages. One of these is that they can enable an integrated view of anisotropy directly beneath a station. Another is that as they are converted from a compressional wave to a shear wave at the core-mantle boundary (CMB) the polarization of the wave before it undergoes splitting is known.

Other shear phases, such as direct S and ScS (a shear wave that reflects off the CMB) are also used in splitting studies (see Fig. 3.14). A single spherical S wave front is quickly broken into various wave fronts by reflections off the surface, mantle discontinuties, and the core. As the wave fronts arrive the surface, they cause arrivals that we call S, ScS and sS, etc. For S waves that travel down to the core, reflected S (ScS) and reflected P (ScP) arrivals can be observed at the same distance. *Nowacki et al.* (2010) used differential splitting in S and ScS (respectively direct and reflected from the core-mantle boundary) to measure anisotropy in D" beneath North and Central America (Fig. 3.10). Although S and ScS splitting are often used for investigating anisotropy in the D", discrepancies in shear wave splitting for SKS and SKKS phases (see chapter 7) for the same event-station pair are used to measure anisotropy in the D" layer (*Long*,

2009). However, the results from these two methods may not be completely comparable because ScS splitting could be affected by source-side anisotropy even though intermediate-depth or deep earthquakes are used.

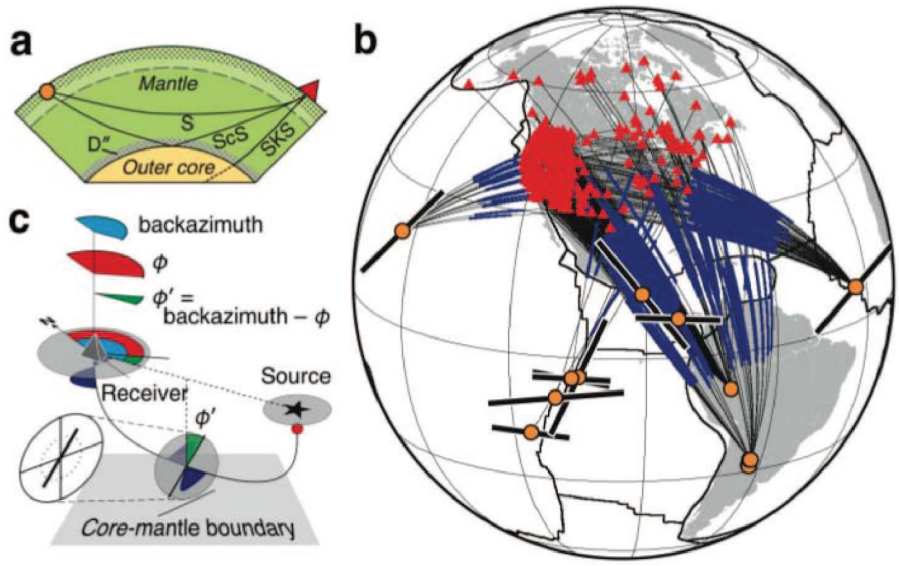



Figure 3.10.: Source-receiver geometry, and explanation of $\acute{\varphi}$. a) Earth section with ray paths for the S, ScS and SKS phases. The stippled upper mantle and grey D" are anisotropic. S turns above D"; ScS samples it. b) Shown are seismic stations (triangles), earthquake epicentres (yellow circles), ray paths (thin blacklines) and ray paths in a 250-km-thick D" (blue lines). c) Relationship of the measured fast directions in the geographic $\varphi$ and ray ($\acute{\varphi}$) reference frames (for more details see *Nowacki et al.*, 2010).

**E) Anisotropy in the outer core**

From a seismological point of view, lateral heterogeneous structure in the fluid outer core of the Earth is a controversial issue. However, *Stevenson* (1987) indicated that if the surfaces of constant density in the Earth's outer core can coincide with the surfaces of constant potential, the outer core could be laterally homogeneous. Then *Wahr and de Vries* (1989) showed that lateral variations, within the core, of the Earth's gravity field result in deformations of equipotential (and equidensity) surfaces with respect to spherical symmetry.

**F) Anisotropy in the inner core**

It is well known from seismological studies that Earth's solid-iron inner core is elastically anisotropic (*Belonoshko et al.*, 2008). In general, seismic studies using compressional body

waves suggest hemispherical variation in the anisotropic structure of the inner core, but are poorly constrained because of a lack of suitable earthquakes and poor receiver distribution. When a preferred orientation of the iron alloy hexagonal crystals is thought to be a primary cause for this anisotropy, then it is rejected due to the fact that hexagonal iron becomes increasingly isotropic on increasing temperature at pressures of the inner core. An alternative explanation is based on iron adopts a body-centered cubic form in the inner core and is also supported by diamond anvil cell experiments.

### 3.3.3. Seismic anisotropy and plate tectonics

The investigation of anisotropy in the Earth has become increasingly important because it allows us to examine the past and present deformation of the Earth's interior. Seismic anisotropy is a significant result of deformation processes. While this deformation in the asthenosphere is associated with relative motion between mantle and overlying plate, the main deformation for the lithosphere occurs at plate boundaries due to continental collisions. Some examples from anisotropic studies are also presented below.

**i) Subduction zones**

Subduction zones exhibit a complex 3D pattern of mantle flow, especially at the corners of the slab. Complexity is possibly added by slab rollback, which may cause torroidal mantle flow beneath the back-arc region (*Hall et al.*, 2000). In subduction systems, possible sources including the overriding plate, the mantle wedge, the slab, and the sub-slab mantle contribute to the development of the anisotropic fabric. For example, trench−parallel splitting directions are found for the Andean Subduction (e.g., *Russo and Silver*, 1994; *Anderson et al.*, 2004), the Aleutian Islands (*Yang et al.*, 1995), and in New Zealand (e.g., *Duclos et al.*, 2005). Beneath the wedge, fast directions are generally trench parallel due to trench−parallel sub-slab mantle flow induced by trench migration (e.g., *Long and Silver*, 2008). In contrast, trench−normal splitting directions are found in the Philippines Subduction zone (*Fouch and Fischer*, 1998) and in Japan (e.g., *Nakajima and Hasegawa*, 2004). However, there are convergent boundaries,

like the Cascadia subduction zone, where trench−perpendicular anisotropy was attributed to a similar sub-slab flow (*Currie et al.*, 2004). In the mantle wedge, fast directions are usually complex, but often show a characteristic change in orientation from trench−perpendicular in the backarc region due to the corner flow induced by the subducting slab, to trench−parallel close to the trench. This change in orientation close to the trench has been mainly interpreted as being due to the presence of B- type olivine or serpentinite fabric in the cold corner of the mantle wedge (e.g., *Karato and Wu*, 1993; *Nakajima and Hasegawa*, 2004), the trench−parallel mantle wedge flow (*Smith et al.*, 2001), and complex 3D flow due to lower crustal foundering (*Behn et al.*, 2007). According to *Jung and Karato* (2001), the relation between flow geometry and seismic anisotropy undergoes marked changes if the olivine includes the water. Under high stress and high water content conditions, the anisotropic b-axes are usually oriented parallel to strain orientation.

Recent observations (e.g., *Hatzfeld et al.*, 2001; *Evangelidis et al.*, 2011) indicated that Aegean region is an ideal place to study seismic anisotropy (Fig. 3.11) in a subduction zone.

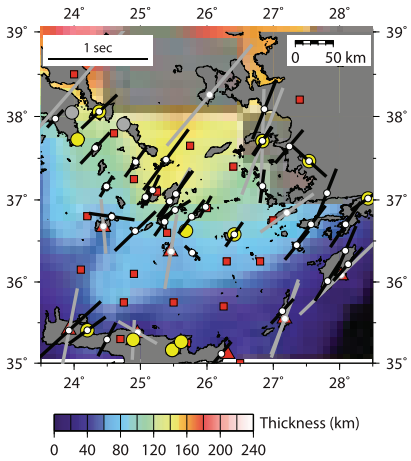



Figure 3.11.: Map of average SKS splitting results ($\phi$, $\delta$t) at each station (this study, black bars; previous study, gray bars) superimposed on a smoothed map of the separation between the Aegean Moho and the subducted African Moho calculated from the receiver function analysis of *Sodoudi et al.* (2006). Orange triangles mark stations where the receiver function analysis estimated the African Moho depth, and orange squares mark centers of boxes where depths of African Moho were estimated from delay times of Sp conversions. Large yellow and gray circles indicate good null measurements by this and previous studies, respectively (taken from *Evangelidis et al.*, 2011).

*Evangelidis et al.* (2011) indicated that fast anisotropy directions are trench perpendicular in the backarc area and trench parallel near the trench. Anisotropy measurements near the volcanic arc mark the transition between these two regions. In the back arc, a gradual increase is observed in delay times from south to north, with a prevailing NE-SW direction.

**ii) Rifting**

A rift is an elongated topographic depression overlying a lithosphere which has been significantly modified by extension. The mechanism of continental rifts can be separated into active and passive rifting. Although the rifting of continents is a component of plate tectonics, the mechanism for break-up is poorly understood. Seismological investigations is often used to construct geodynamic models for rifting systems. For instance, the East Africa Rift system (EARs) is an ideal place to study seismic anisotropy (Fig. 3.12). A range of mechanisms is responsible for anisotropy, including periodic thin layering of contrasting materials, oriented pockets of melt, and the lattice-preferred orientation (LPO) of olivine crystals.

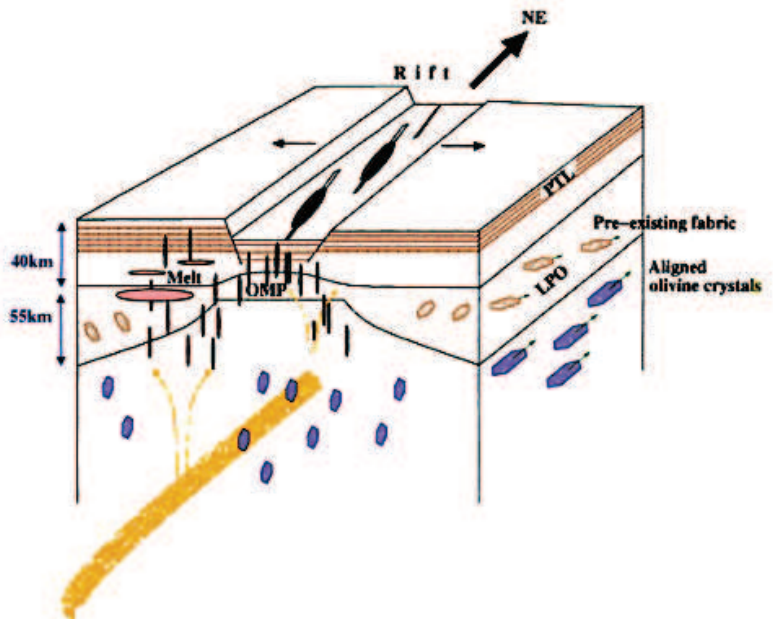



Figure 3.12.: Model of seismic anisotropy beneath the East African Rift System (after *Kendall et al.*, 2006). A range of mechanisms including periodic thin layering of contrasting materials, oriented pockets of melt, and the lattice-preferred orientation (LPO) of olivine crystalsis is responsible for the observed anisotropy in the rift (for more details see *Kendall et al.*, 2006).

**iii) Orogens**

For orogens, mantle deformation from past and present activity is generally responsible for seismic anisotropy. In general, the majority of orogenies are the primary result of the Wilson cycle of continental breakup and collision due to plate interactions, plate internal deformation, and plate coupling to the convecting mantle below. In fact, mountain chains on the surface are the fundamental consequences of the collision of tectonic units. The deformation in orogens strongly depend on the rheology. A commonly accepted model for the strength of the lithosphere assumes a brittle upper crust, followed by a ductile lower crust and a strong upper mantle (*Molnar and Lyon-Caen*, 1988). The observed coherence within crustal deformation implies that the mantle plays a major role in orogeny because kinematic coupling between crust and upper mantle is probably developed. Therefore, surface features with anisotropy orientations can be comparable. In contrast, a minimum in the strength of the lower crust may be related to a decoupling between upper mantle and crust. However, a strong coupling between crust and mantle is potentially responsible for vertically coherent deformation (*Silver*, 1996). For example, *Flesch et al.* (2005) compared the Central Asian surface deformation field inferred from GPS and fault slip rate data with mantle deformation inferred from SKS splitting. The study indicated a fundamental change in deformation regime throughout the study area. *Barruol et al.* (1997) measured anisotropy in the Appalachians and observed that the splitting directions follow the geologic trend. Moreover, *Barruol et al.* (1997) suggested two possible causes: (1) the local dominance of asthenospheric flow, motivated by the proximity of a pervasive low-velocity anomaly, and (2) lithospheric deformation in a transcontinental strike-slip fault zone active during the Appalachian collision, to explain this observation. This suggestion implies that lithospheric anisotropy is mixed with small asthenospheric contributions.

**iv) Oceans**

Firstly, *Hess* (1964) investigated seismic anisotropy in the uppermost mantle beneath the oceans and suggested that the observed anisotropy is a result of a preferential orientation of its constituent olivine crystals. Note that investigating anisotropy beneath oceanic plates allows

to constrain mantle flow. The fact that oceanic plates are relatively young (<200 Ma) means that they are generally undisturbed. Therefore, it is possible to compare anisotropy with plate motion directions.

## 3.4. Shear wave splitting and surface wave tomography

In this study, to detect anisotropy within the Irish crust and upper mantle, two methods which are surface wave tomograpy and shear wave splitting have been used. Therefore, in this section the fundamental characteristics of these methods are described in detail.

### 3.4.1. Shear wave splitting

Recently shear-wave splitting has become a widely used method to investigate seismic anisotropy at depth. In particular, it provides an exceptional possibility to probe the fabric of crust and mantle rocks (*Silver*, 1996; *Savage*, 1999). When a shear wave propagates through an anisotropic medium, energy is partitioned into orthogonally polarized fast and slow shear waves (Fig. 3.13). This property is called “shear-wave splitting” or sometimes “birefringence”.

Shear wave splitting can be described in terms of two parameters: the fast polarization direction ($\phi$) and the lag time between fast and slow shear waves ($\delta$t). They are evaluated in the ZRT (Z-vertical, R-radial, T-transverse) coordinate system only from the horizontal components (NS and EW) of the shear waves. The simplest forms of splitting analysis implicitly assume a vertical angle of incidence for a SKS/SKKS wave. However, in reality the angle of incidence is not exactly zero and can be up to several degrees (e.g. up to 7-15$^0$ found in this study).

Additionally, splitting parameters provide information on the layer thickness and nature of the rocks that the wave propagated through because the splitting time is a function of the thickness of the anisotropic layer and the magnitude of the anisotropy and the fast polarization direction can provide information about the orientation of the anisotropy. Therefore, the measurements of anisotropy provide constraints on rock fabric and geological or geodynamical processes.

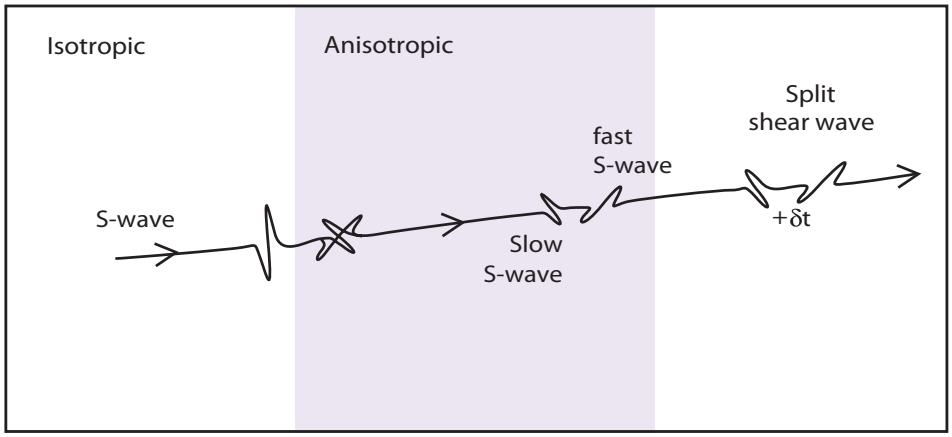



Figure 3.13.: Shear wave splitting occurs for a shear wave traveling through an anisotropic medium (shaded). When the incident shear wave arrives at an anisotropic medium, it splits into two shear waves of perpendicular polarization, along the seismic fast and slow direction, respectively. Traveling through the anisotropic medium, the two waves accumulate a delay time $\delta$t. The shear-wave splitting techniques invert for $\delta$t and the fast polarization direction $\phi$.

In an isotropic medium, a P wave has linear particle motion which is parallel to the propagation direction. An S wave in an isotropic medium has the particle motion perpendicular to the propagation direction with two components polarised on the horizontal plane (SH) and vertical plane (SV). Propagation in an anisotropic medium has a quasi-P wave with linear particle motion that is not strictly aligned with the propagation direction and two quasi-S waves (qS1 and qS2 which are polarised parallel and perpendicular to the fast direction, see Fig. 1 in the study of *Savage* (1999)). The quasi-S waves are separated by a time $\delta$t.

As previously mentioned, the time delay $\delta$t between the two quasi-S waves depends on both the path length in the anisotropic material and the difference in speed between the two quasi-S waves (*Savage*, 1999). This delay time is given by:

$$\delta t = L(1/V_{S1} - 1/V_{S2}) \tag{3.6}$$

where $V_{S1}$ and $V_{S2}$ represent the speeds of the two quasi-shear waves and the medium properties, respectively and $L$ is the length of the anisotropic path traversed. The differences between $V_{S1}$ and $V_{S2}$ are also reported as a percent anisotropy $k_s$, calculated as

$$k_s = 200(V_{S1} - V_{S2})/(V_{S1} + V_{S2}). \tag{3.7}$$

It is important to note that this type of anisotropy is different from the intrinsic anisotropy of the material, which is defined as the percent difference between the maximum and minimum velocities (*Birch*, 1961). In general, the intrinsic anisotropy is higher than $k_s$ because these values vary depending on propagation direction (*Savage*, 1999).

**A) Seismic phases for shear wave splitting**

A clear manifestation of shear wave splitting depends on a range of frequencies and also is sensitive to the path length in different parts of the Earth. Figs. 3.14 and 3.15 show seismic phases that are used for splitting analysis.

Seismic phases for shear wave splitting are chosen according to the purpose of the study. Distance between sources and receivers, incidence angle, and source parameters of events should also be taken into account. Particularly core-refracted phases SKS and SKKS are popular with studying mantle anisotropy, as well as direct S waves at local and teleseismic distances and also ScS phases since these phases are very useful to detect the geometry and the strength of seismic anisotropy in the Earth.

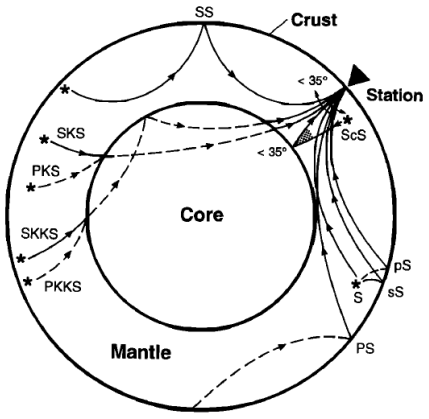



Figure 3.14.: Phases that have been used for shear wave splitting studies. Solid lines are S path segments, dashed lines are P path segments, and stars are earthquake sources. The shear wave window of $35^0$ at the surface and at the core-mantle boundary ensures phases with smaller incidence angles will yield linear S wave particle motion for isotropic propagation (from *Savage*, 1999).

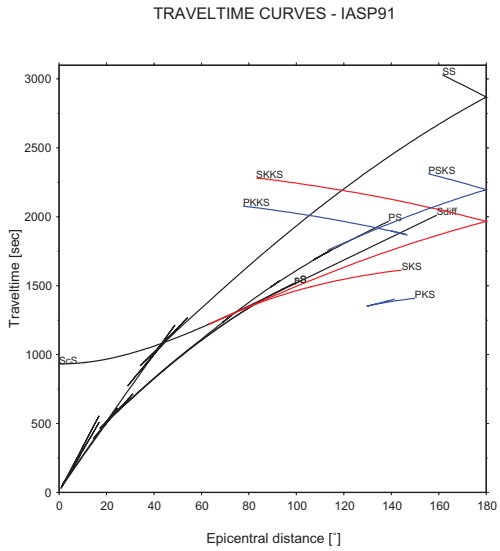



Figure 3.15.: Travel time curve for seismic wave phases computed for an earthquake at the surface according to the standard IASP91 Earth velocity model (from *Kennett and Engdahl*, 1991), SKS and SKKS are particularly marked red. In general core refracted shear-phases used for shear-wave splitting occur at distances between 85 and $150^0$. Mostly these are well separated from other phases, which could otherwise contaminate the signal of the phase of interest.

**i) Direct S wave**

Deep earthquakes are very useful for detecting local splitting from direct S waves at local distances since such earthquakes can provide clear and visible direct S waves. Therefore, they are used to characterize anisotropy in the mantle wedge and to detect local splitting above subducting slabs where such deep earthquakes occur. The approach is to remove the effects of the receiver-side shear wave splitting to isolate and obtain the source-side splitting parameters. This can be accomplished by applying the inverse of the receiver-side shear wave splitting operator (e.g., *Kaneshima and Silver*, 1992; *Silver and Savage*, 1994). Once the receiver-side splitting is removed, only the source-side splitting operator should remain (e.g., *Sandvol and Ni*, 1997). Teleseismic S phases from distances of greater than about $60^0$ with near-vertical incidence angles can also be used. However, in this case it is usually hard to interpret the results because of the lack of information about where anisotropy occurs along the travel-time path of shear-waves, at the source side or the receiver side, or indeed both. Direct S wave can also be used to detect upper mantle anisotropy underneath the receiver. But, it is not easy because the

initial polarization of direct S is not fixed by the backazimuth. As a result, the focal mechanism from the seismogram is used to predict the initial polarizations of direct S waves.

**ii) Converted core phases**

In general, teleseismic shear-wave splitting of core-refracted phases (SKS, SKKS) is usually used to get information about the anisotropy located on the station-side of the epicenter-station path. A significant part of the anisotropy originates in the upper mantle region where olivine is the most abundant mineral and is highly anisotropic (e.g., *Silver*, 1996; *Savage*, 1999; *Long and Silver*, 2009). Therefore, these phases are commonly used to investigate anisotropic structure in the upper mantle.

As mentioned before, these phases begin as a S wave at the source-side and then convert to a P wave at the liquid outer core (Fig. 3.14). Therefore, they travel through the fluid outer core as P waves and then converts back to S waves at the CMB nearer to the point beneath the receiver. The initial polarization of the shear wave (before it has passed through an anisotropic medium) is therefore known because its unperturbed polarization is controlled by the P-to-S conversion at the core mantle boundary (CMB). This point is significant to determine unambiguous splitting parameters. This conversion at CMB also means that the observed anisotropy must be localized between the CMB and surface. Moreover, the nearly vertical propagation of these core-refracted phases through the upper mantle means that the incidence angle will be well within the so-called "shear wave window" (shear phases that have incidence angles larger than $35^0$ at the surface may be affected by nonlinear shear particle motion in the absence of anisotropy (e.g., *Savage*, 1999) (Fig. 3.14).

**iii) Other phases**

In addition to S, ScS phase is also used to investigate seismic anisotropy in the lowermost mantle (D") (e.g., *Wookey et al.*, 2005b). To remove the effect of near-source and near-receiver anisotropy and to determine elastic anisotropy in the D", differential S-ScS splitting has been used recently. The applicable events of epicentral distance ranges between 60 and $85^0$ for the differential S-ScS splitting (e.g., *Wookey et al.*, 2005a) (Fig. 3.14).

**B) Methods for shear-wave splitting measurements**

There are a variety of methods that have been developed to determine splitting parameters from broadband seismic data. The methods are based on the visual and statistical examination of splitting analysis. Visual inspection of individual waveforms is more reliable and preferable than partially or fully automated processes (e.g., *Teanby et al.*, 2004; *Evans et al.*, 2006) in spite of taking spending much more researcher time. The most common methods are:

**i) The transverse component minimization method**

*Ando et al.* (1980) introduced this method with rotated horizontal seismograms and selected preferential polarisations. This method is based on determining travel time delays between two split and orthogonally polarized shear waves. As described above, when shear waves propagate through anisotropic media, they split into two quasi shear waves: fast and slow. Note that the splitting parameters, $\phi$, $\delta$t, correspond to the orientation of the fast quasi-S phase and the time delay between the fast and slow components, respectively. Therefore, the interference between the fast and slow phases is responsible for elliptical particle motion. The separation of the different shear-wave arrival times was clearly seen so that shear-wave splitting parameters ($\phi$ and $\delta$t) were estimated for the upper mantle (*Ando et al.*, 1980). Afterwards, the combination of preferred polarisations for seismogram rotation became standard, both above small earthquakes in the crust (e.g., *Buchbinder*, 1985; *Gao et al.*, 1998) and in upper mantle studies (*Silver and Chan*, 1988; *Silver and Chan*, 1991).

Subsequently, *Silver and Chan* (1991) further developed the transverse component minimization method. The method is based upon the principle that a shear wave is linearly polarized in the absence of anisotropy and that passage through an anisotropic medium might result in significant energy on the transverse component and an elliptical particle motion, which is indicative of shear wave splitting. The method performs a grid search over all possible values of $\phi$ and $\delta$t (up to a reasonable maximum delay time value, usually ~4 s), rotates and time-shifts the horizontal components appropriately, and measures the amount of energy on the corrected transverse component, producing a contour plot of transverse component energy for all possi-

ble pairs of splitting parameters. The best-fitting parameters correspond to the minimum on this contour plot; formal errors on the measurements are calculated using the inverse F test (*Silver and Chan*, 1991) and represent the 95% confidence level (and are thus approximately 2 standard deviations). The test is thus performed for each set of possible parameters to determine whether or not the shear wave splitting parameters are within the bounds of the confidence region.

In addition, this method also makes visual inspection of individual waveforms significant because "manual check" is usually required to verify the quality of individual waveforms and particle motions.

The method is usually applied to individual seismograms and then individual measurements of ($\phi$, $\delta$t) are averaged. To obtain best-fitting splitting parameters for a given station, generally splitting parameters are weighted by the individual errors on each measurement. This procedure implicitly assumes that the anisotropy consists of a single homogeneous layer beneath the station since it assumes that all seismograms share the same set of splitting parameters. If this assumption is violated due to variations in splitting parameters with back-azimuth and incidence angle, the resulting measurement will be difficult to interpret and potentially valuable information about vertically heterogeneous anisotropy is lost (*Long and Silver*, 2009).

**ii) The cross-correlation method**

The automated analysis of shear-wave splitting on teleseismic shear-waves was first used by *Fukao* (1984) and then *Bowman and Ando* (1987). The method shares the same theoretical approach as the transverse component minimization method. A grid-search approach in the method is used to estimate the best-fitting splitting parameters by rotating and time-shifting the horizontal components. Shear-wave splitting time-delays are estimated from the lags of cross correlations of the preferentially rotated wave trains (*Fukao*, 1984). Also, linearity tests in the method were developed to check the quality of the measurements.

**iii) The multichannel (splitting intensity) method**

The original idea for the multichannel method was firstly introduced by *Vinnik et al.* (1989). Then *Chevrot* (2000) modified the method as an alternative to single-record methods such as

the transverse component minimization and cross correlation methods. When the delay time ($\delta$t) between the split shear waves is small compared to the dominant period of the waveform, radial and transverse components for an incident SKS pulse $w(t)$ are given by *Silver and Chan* (1988) and *Chevrot* (2000):

$$R(t) = wt \tag{3.8}$$

$$T(t) = -1/2(\delta t sin(2\beta)R'(t)) \tag{3.9}$$

where $R'(t)$ is the time derivative of the radial component and $\beta$ is the angle between the fast direction $\phi$ and the incoming polarization direction. The splitting intensity ($S$) is defined as the amplitude of the transverse component. The transverse component is thus simply the time derivative of the radial component multiplied by a sinusoidal factor whose amplitude depends on the splitting delay $\delta$t and whose phase depends on the fast axis orientation $\phi$. In other words, the transverse component can be calculated by

$$T(t) = 0.5S\,R'(t) \tag{3.10}$$

where $S$ is the splitting intensity. The main advantage of the method is that the possible variation in the amount of energy on the uncorrected transverse component can be predicted with incoming polarization angle (equivalent to the backazimuth for SKS-type phases) for a single, horizontal layer of anisotropy.

**iv) The cross-convolution method**

The above methods are all based on the assumption that the shear wave under consideration has undergone splitting due to a single laterally homogeneous layer of anisotropy with a horizontal axis of symmetry. However, in the real Earth, shear waves may pass through multiple regions of anisotropy and have dipping axes of anisotropic symmetry. To overcome this problem *Menke and Levin* (2003) proposed a cross-convolution method. The method comprises convolving the observed radial and tangential component seismograms with the impulse responses predicted by a hypothetical Earth model, and then varying the model to minimize the

misfit between observed and predicted seismograms.

First, *Menke and Levin* (2003) presumed that a seismic station detects several teleseismic phases, such as SKS phases, from a variety of sources with different angles of incidence and azimuths. Let the radial-horizontal and transverse-horizontal components be denoted, $V_i^{obs}$(t), and, $H_i^{obs}$(t), respectively. Here the subscript and indexes denote i and the N phases such as SKS, SKKS and PKS, respectively. They assumed that these seismograms have been windowed to isolate the phase of interest. Here each seismogram is also represented as the convolution of a "source" wavelet, $s_i$(t), with the radial and transverse impulse response functions, $v_i$(t) and $h_i$(t), respectively. These response functions quantify the effect of near-receiver structure on the phase:

$$V_i^{obs}(t) = s_i^{true}(t) * v_i^{true}(t) \tag{3.11}$$

$$H_i^{obs}(t) = s_i^{true}(t) * h_i^{true}(t) \tag{3.12}$$

where the superscript "true" is used to indicate that in the absence of noise the observed seismograms are related to the actual source wavelet and impulse responses. The term, $s(t)$, is a "source" wavelet in the sense that it characterizes the waveform of the phase before it interacts with the near-receiver structure. It describes both the effects of the earthquake source itself and subsequent modification by structure far from the receiver. A significant aspect of these equations is that the same source wavelet appears in both equations

In this method, a model, *m*, for the near-receiver earth structure is assumed. Here the vector, m, denotes whatever parameters might be needed to define that model. For example, in the simple case of one-layer anisotropy, m=$[\tau,\Theta]^T$ (transpose denotes $T$), would represent the splitting delay, $\tau$, and azimuth, $\Theta$, of the fast anisotropic axis. In more complicated cases it might include additional parameters that describe additional anisotropic layers, crustal thickness, interface dip, etc. In addition, they assumed that a method of predicting the impulse responses $v_i^{pre}(m,t)$ and $h_i^{pre}(m,t)$ of the earth model, *m*, is available. Then the predicted seismograms are:

$$V_i^{pre}(t) = s_i^{true}(t) * v_i^{pre}(m,t) \tag{3.13}$$

$$H_i^{pre}(t) = s_i^{true}(t) * h_i^{pre}(m,t) \tag{3.14}$$

Here the superscript, "pre", stands for "predicted". Therefore, a model, $m$, is selected. This model should best match the predicted seismograms to the observed ones. The presence of the source wavelet term in these equations is an impediment to this goal, since it is, in general, unknown.

After that, the source wavelet from these equations are removed by convolving eq. 3.11 by $h_i^{pre}(m,t)$ and eq. 3.12 by $v_i^{pre}(m,t)$:

$$h_i^{pre}(m,t) * V_i^{obs}(t) = s_i^{true}(t) * v_i^{true}(t) * h_i^{pre}(m,t) \tag{3.15}$$

$$v_i^{pre}(m,t) * H_i^{obs}(t) = s_i^{true}(t) * h_i^{true}(t) * v_i^{pre}(m,t). \tag{3.16}$$

If the model, $m$, is a good one, $v_i^{pre}(m,t) \approx v_i^{true}(t)$ and $h_i^{pre}(m,t) \approx h_i^{true}(t)$.

As seen, the right hand sides of eqns. 3.15 and 3.16 are approximately equal. By equating the left hand sides it can be found that:

$$h_i^{pre}(m,t) * V_i^{obs}(t) \approx v_i^{pre}(m,t) * H_i^{obs}(t) \tag{3.17}$$

Least-squares minimization of the error in eq 3.17 is used to find an estimate of the model: find the $m^{est}$ that minimizes

$$E(m) = (1/N) \sum_i \| \, h_i^{pre}(m,t) * V_i^{obs}(t) - v_i^{pre}(m,t) * H_i^{obs}(t) \, \|^2 \tag{3.18}$$

with respect to $m$. Here the superscript "est" denotes "estimated" and $\| \ . \ \|^2$ denotes some measure of the difference between the two timeseries. Note that the misfit, $E(m)$, is zero if all the seismograms are exactly matched and is of order unity if all the fits are poor.

This method was applied to one and two layer anisotropy by *Menke and Levin* (2003). An exhaustive grid search is also used to solve both the one-layer and two-layer problems. This approach is computationally intensive, but avoids the problems associated with linearized inversions (e.g. mistaking local minima in $E(m)$ for the global minimum).

The waveform fitting technique developed by *Menke and Levin* (2003) allows the testing of shear waves (e.g., SKS and similar phases) for splitting, as predicted by anisotropic earth models. In addition, the synthetic tests show that the technique can successfully recover orientation and magnitude parameters for one or more layers of anisotropy, either from individual seismograms or from suites of observations that include a broad range of backazimuths. The tests on synthetic and real data (*Menke and Levin*, 2003) indicate that the cross-convolution method yields similar results to traditional methods in the presence of a single horizontal layer of anisotropy. Also, this method shows that it may do a better job of distinguishing whether complex anisotropic models are required by a given data set.

**v) Comparison of splitting methods**

As described above, recently a variety of shear wave splitting measurement methods have been developed to measure splitting parameters from broadband seismic data. For these methods, generally processing steps such as filtering, rotating the seismogram components, identifying records with high signal-to-noise ratio, choosing a time window for the analysis, and the visual and/or statistical examination of the resulting diagnostic plots and error estimates are required. Although there have been several efforts to partially or fully automate the process of making shear wave splitting measurements (e.g., *Teanby et al.*, 2004), most shear wave splitting analysts continue to rely on visual inspection of individual waveforms as a final check of the data. As seen, each method has advantages and disadvantages with their own assumptions, biases, preprocessing steps, and error estimation procedures. Therefore, comparisons among different measurement methods are instructive.

*Vecsey et al.* (2008) tested various splitting analysis methods and found that the transverse component minimization method usually gave the most reliable and robust results. They also

found that this was particularly the case for noisy data. In particular, the method is more reliable for SKS-type phases than other methods because the initial polarizations of the phases correspond to the backazimuth (assuming that the polarization has been unaffected by other factors, such as extreme lateral heterogeneity). Therefore, the transverse component minimization method for our study is preferred to measure SKS and SKKS splitting parameters. However, for direct S-phases it is not feasible since the initial polarization must either be modelled from the (imperfectly known) source mechanism or estimated from the seismogram along with the splitting parameters.

### 3.4.2. Surface wave tomography

As previously mentioned, seismic anisotropy is an efficient tool for investigating the dynamics of the Earth's interior. In this section, surface waves and azimuthal and radial anisotropy are described in detail. Then, a commonly used two-station method is briefly described.

**A) Surface waves**

Generally, after the P and S waves, large amplitude longer wavelength waves arrive. These waves are surface waves whose energy is concentrated near the Earth's surface. As a consequence of geometric spreading, their energy spreads two-dimensionally and decays with distance r from the source approximately as $r^{-1}$. Hence, at large distances from the source, surface waves are prominent on the seismograms. Two distinct types of surface waves, known as Love and Rayleigh waves (Fig. 3.16), always propagate near the Earth's surface.

Love waves are made up of $S_H$ waves. Rayleigh waves are made up of interfering P and $S_V$ waves reflected from the free surface. Furthermore, Love-wave displacement is parallel to the free surface and perpendicular to the direction of propagation (toroidal) while Rayleigh-wave displacement on a plane is perpendicular to Love-wave displacement (spheroidal). Surface waves propagate parallel to the surface of the earth. Thus, the penetration depth is proportional to their wavelength. For this reason, different modes of a surface wave travel at different velocities (reflecting the velocity structure of the Earth), leading to a dispersion of the signal. This can

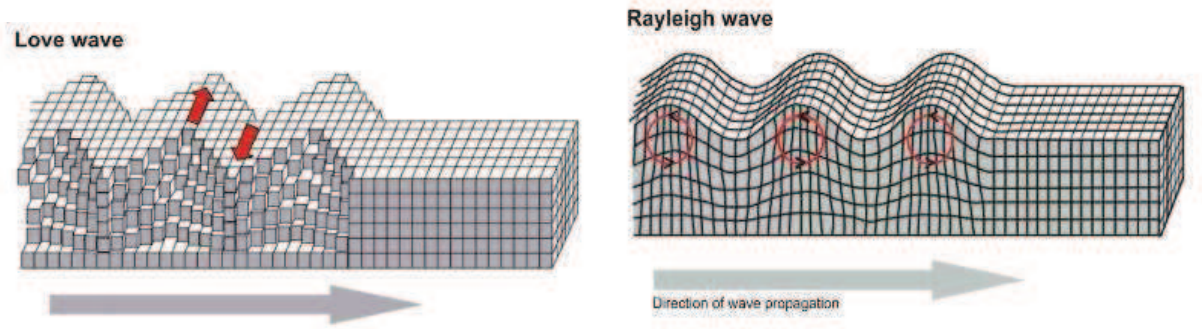



Figure 3.16.: Sketch of the particle motion of Love and Rayleigh waves (after *Lay and Wallace*, 1995).

in turn be used to study the depth structure of the Earth. However, the long wave lengths limit the lateral resolution (~400 km; *Debayle et al.*, 2005) because they are sensitive to the elastic properties of the deeper layers. On the other hand, short wavelengths are sensitive to superficial layers. Due to this cause, a given mode of surface waves has different velocities at different wavelengths, leading to the dispersion of the seismic signal.

In general, crustal surface waves have periods which are typically in the range of 10-30s. Their wavelengths reach 30 to 100 km. Mantle surface waves have longer periods and exhibit wavelengths of several hundred kilometers. Particularly at very long periods, the Love and Rayleigh waves can be represented by a superposition of toroidol and spheroidal vibrations of the whole Earth (e.g., *Aki and Richards*, 1980). If $R$ denotes the Earth's radius, the relationship between the eigenperiod $T_n$ of a given spherical normal mode of the angular order "$n$" and the phase velocity $C_n$ of the associated surface wave is:

$$C_n = 2\pi R/(n + 1/2)T_n. \tag{3.19}$$

**i) Dispersion**

Surface waves are dispersive (if Rayleigh waves are not in a homogeneous half-space with constant Vp and Vs) because waves with longer wavelengths (lower frequency) travel deeper than short wavelengths (higher frequency). Since in general seismic speed increases with depth, longer wavelengths travel faster than shorter wavelengths. In other words, their speed of prop-

agation is a function of their frequency. Due to this reason, individual harmonic components of the surface wave seismogram (individual modes) propagate over the globe at different speeds. Almost any seismic source excites waves that comprise a continuous spectrum of frequencies, each harmonic component having velocity, c($\omega$), which is called the phase velocity c($\omega$). However, the velocity with which surface wave energy associated with a particular frequency travels is called the group velocity U($\omega$). The group and the phase velocities are both functions of frequency. The group velocity of surface waves is the velocity at which surface energy of a given frequency travels. The discrimination between the group velocity U(t), with which the energy of the wave group moves and the phase velocity c(T), with which the wave peaks and troughs at a given frequency travel along the surface, is generally used if dispersive waves are analyzed.

Therefore, in Fig. 3.17 (a), straight lines passing through the origin mark the surface wave signal of any particular frequency on each successive record. Fig. 3.17 (b) shows dispersion curves appropriate for the records of the Fig. 3.17.

In this example, notice that the group velocity is less than the phase velocity. They differ from Love and Rayleigh waves and also depend on the velocity-depth structure of the Earth along the considered segment of the travel path (Fig. 3.18).

As observed in Fig. 3.18, c(T) is always increasing with period and is larger than U(T). An important point here is that dispersion curves are generally used to get information about the velocity structure of mainly the crust and upper mantle. Therefore, from the inversion of surface wave dispersion data, information on the shear-wave velocity structure of the crust, and, when using periods up to about 500 s (mantle surface waves), even of the upper mantle and the transition zone can be derived. In the section, the derivation of dispersive curves will be briefly reviewed.

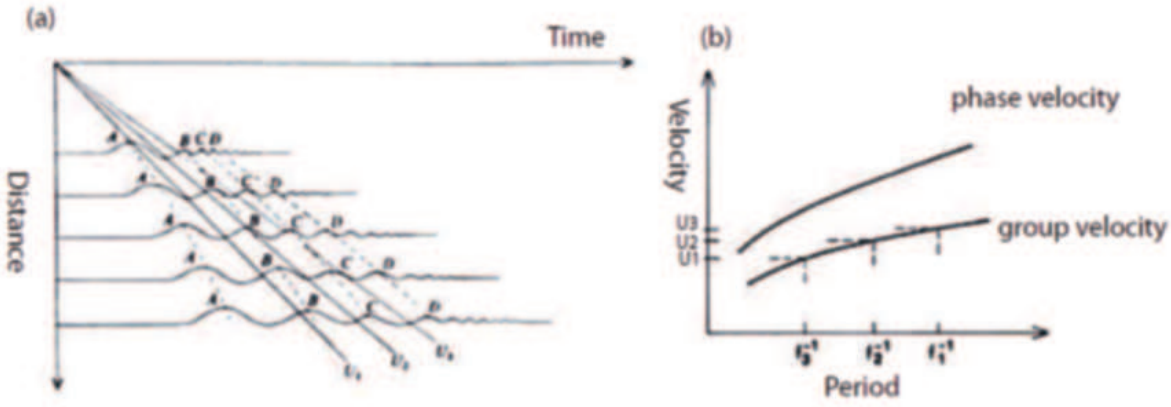



Figure 3.17.: Example of increasing waveform dispersion with increasing distance. Dispersion of a surface-wave packet: five idealized low-frequency seismograms, increasingly far from the epicenter. The letters A, B, C, D (and associated dashed lines) denote different surface-wave phases. The derivatives of the curves marked U1, U2, U3 coincide with group velocities at different frequencies. Taken from *Officer* (1974).

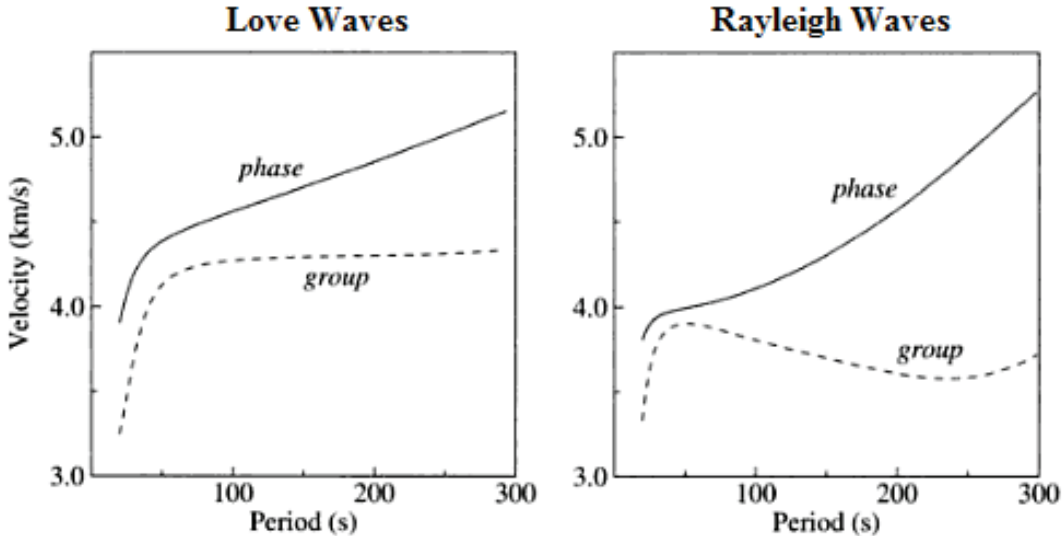



Figure 3.18.: Fundamental Love and Rayleigh dispersion curves from the isotropic PREM model (taken from *Laske and Masters*, 1996).

**ii) Measurement of group and phase velocity**

As the wave spreads outward, dispersion modifies it, spreading the energy out over a wave-train, as indicated in Fig. 3.17. Thus, one can visualize the surface wave having started from the source essentially as undispersed pulse, with each frequency component having an amplitude A($\omega$) and initial phase, $\theta_0(\omega)$, determined by the excitation of the source and medium. The fact that the surface wave velocities vary depending on the depth range sampled by each period makes surface wave dispersion valuable for studying the structure of the Earth. These studies are conducted both with Love waves, whose dispersion depends on the shear velocity, and Rayleigh waves, whose dispersion depends on both compressional and the shear velocities. Group velocities are easier to measure because they are the velocities at which a wave group visible on a seismogram travels. The group velocity is found by dividing the distance between the source and the receiver by the travel time of the wave group.

The phase velocity can be found through observations in two ways. One method uses seismograms recorded at two stations at distances $x_1$ and $x_2$ from an earthquake. If the waves arrive at times $t_1$ and $t_2$, taking the Fourier transform at each station gives the phase as a function of angular frequency:

$$\theta_1(\omega) = \omega * t_1 - \omega * x_1/c(\omega) + \Phi_i(\omega) + 2n\pi \tag{3.20}$$

$$\theta_2(\omega) = \omega * t_2 - \omega * x_2/c(\omega) + \Phi_i(\omega) + 2m\pi \tag{3.21}$$

and then the difference between these equations are found:

$$\theta_{21} = \theta_2 - \theta_1 \tag{3.22}$$

where $\theta_{21}$ denotes this difference. Thus, it is used to solve for the phase velocity:

$$c(\omega) = \omega * (x_2 - x_1)/[\omega(t_2 - t_1) + 2(m - n)\pi - \theta_{21}(\omega)]. \tag{3.23}$$

The initial phase is common to both stations, so that the $\Phi_i(\omega)$ term drops out if the seismometers have the same response, and so contribute to the same phase shifts. If the seismometers have different responses, a correction term is added. The $2(m\text{-}n)\pi$ term is found emprically by ensuring that the phase velocity at long periods is usually reasonable.

Note that to estimate phase-velocity for each frequency, each harmonic term at a given point in its cycle is associated with a peak or trough of a particular period of oscilliation, and the differential time and propagation distance between corresponding cycles are used.

Another method is a single-station method. The single-station measurement of phase velocity can be made by predicting the phase at the earthquake from its focal mechanism. If $\phi_i(\omega)$ is assumed to be known, the phase velocity is

$$c(\omega) = \omega * x/[\omega * t + \phi_i(\omega) + 2n\pi - \Phi(\omega)]. \tag{3.24}$$

In this study we used the two-station method modified by *Meier et al.* (2004) combining cross-correlation with an efficient scheme of filtering and windowing of the signal in the frequency and time domains. This method is basically based on the assumption that the seismic wave propagates along a great circle through epicentre and station and the phase is assumed to represent the integral over the local wave-number along the path. Furthermore, this two-station method is used to measure group velocity dispersion between the stations measuring the difference in arrival times of filtered wave packets if the two stations are located on the same great-circle path. Additionally, this approximation is valid for smooth and long-wavelength lateral heterogeneity. Recent studies have indicated (e.g., *Lebedev et al.*, 2009) that this method is very useful, especially for providing accurate measurements in broad period ranges (for detailed information on this method see *Meier et al.*, 2004).

**B) Radial and azimuthal anisotropy**

Firstly, a brief definition of radial and azimuthal anisotropy is presented before describing some methods such as surface wave tomography applied to dispersion data to measure radial and azimuthal anisotropy in the Earth's interior.

One of the most significant forms of anisotropy, known as radial anisotropy (also known as transverse isotropy), occurs for a stack of layered materials. Although each layer is isotropic in its properties, these properties are different from each other. Hence, the elastic properties, and the seismic velocities, of the stack as a whole are identical regardless of the amount of rotation about the axis of symmetry, that is perpendicular to the layers. A transversely isotropic material can be characterized by five independent elastic coefficients, $A$, $C$, $F$, $L$, $N$, that represent its aggregate properties. If the axis of symmetry is $x_3$ (see Fig. 3.19), the elastic constant matrix becomes

$$C_{m,n} = \begin{bmatrix} A & A-2N & F & 0 & 0 & 0 \\ A-2N & F & F & 0 & 0 & 0 \\ F & F & C & 0 & 0 & 0 \\ 0 & 0 & 0 & L & 0 & 0 \\ 0 & 0 & 0 & 0 & L & 0 \\ 0 & 0 & 0 & 0 & 0 & N \end{bmatrix}$$

This matrix gives the velocities of waves propagating in different directions. Namely, first waves propagate in the $x_1$ direction , as shown in Fig. 3.19. For the isotropic case, $A$ corresponds to $\lambda + 2\mu$ for the $x_1$ direction. Moreover, $N$ corresponds to $\mu$ for the $x_2$ direction and $L$ corresponds to $\mu$ for the $x_3$ direction. Then, by using the analogy, the P and orthogonal S velocities can be defined as:

$$P_1 = (A/\rho)^{1/2}, S_1 = (N/\rho)^{1/2}, S_2 = (L/\rho)^{1/2}. \tag{3.25}$$

In general, the horizontally layered earth indicates transverse isotropy about a vertical axis. The $S_H$ wave velocity $S_1$ is generally faster than the $S_V$ wave velocity $S_2$ because the $S_H$ displacement is preferentially in the fast layers while $S_V$ samples both equally. As a result of this, the shear velocity is generally inferred from the dispersion of Love waves.

Transverse isotropy is usually characterized by three parameters:

$$\xi = (N/L) = (S_1/S_2)^2, \phi = (C/A) = (P_1/P_2)^2, \eta = F/(A - 2L). \quad (3.26)$$

If the material is isotropic $\xi = \phi = \eta = 1$. For layered structures, generally $\xi > 1$ and , $\phi < 1$.

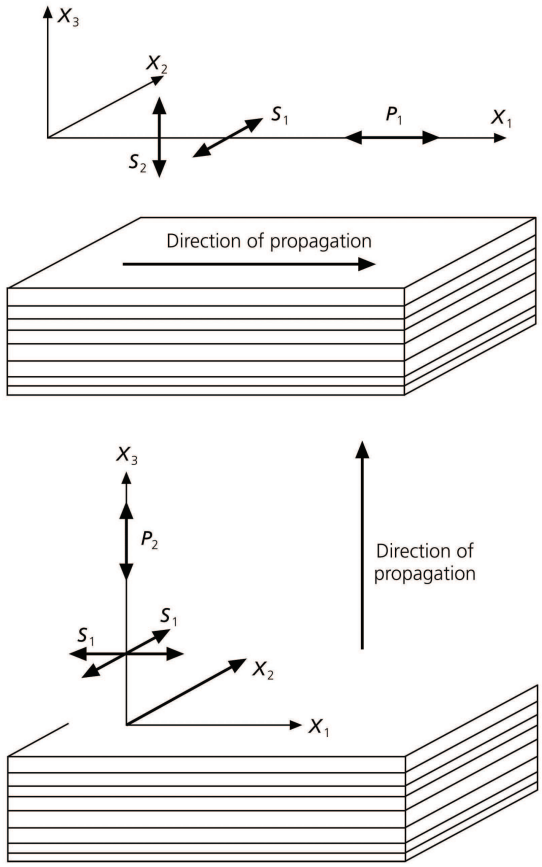



Figure 3.19.: Top: Directions of oscillations for P and S waves propagating in the $x_1$ direction, in the plane of layering. The shear wave oscillating in the plane of the layering has velocity $S_1$, which is generally faster than that for the shear wave oscillating across the layers, $S_2$. Bottom: Directions of oscillations for P and S waves propagating in the $x_3$ direction, perpendicular to the layering. The compressional wave velocity, $P_2$, is generally less than $P_1$. Both shear waves have the same velocity, $S_1$.

Besides radial anisotropy, there is a second common type of anisotropy that is called azimuthal anisotropy. The term is generally used if the seismic wave properties depend on the azimuth of propagation in the horizontal plane. One way to obtain this is to have transverse isotropy with the $x_3$ axis (Fig. 3.19) turned to the horizontal. In general, the P-wave velocity varies with azimuth as:

$$P(\theta) = A_1 + A_2 cos(2\theta) + A_3 sin(2\theta) + A_4 cos(4\theta) + A_5 sin(4\theta) \quad (3.27)$$

where the constants $A_i$ depend on the 21 elastic constants. In other words, the waves at different frequencies will propagate at different speeds due to the fact that they depend on the elastic properties of rocks in the sampled depth-range. As a result, multi-frequency surface wave packets are clearly observed to disperse as they propagate away from their source. From the point of view of tomography, this means that the surface-wave signal filtered at different frequencies will provide information about different regions (depth ranges) of the Earth.

Dispersion data have proven to be well suited for isotropic and anisotropic investigations at the mantle and crustal scale (e.g., *Deschamps et al.*, 2008; *Polat et al.*, 2012). In particular, fundamental mode Rayleigh wave dispersion curves can be inverted for Vs models and azimuthal variations of Rayleigh phase velocities can constrain azimuthal anisotropy with good vertical resolution. For example, *Montagner and Nataf* (1988) presented a method for inverting at the same time the two kinds of observable anisotropy, i.e. the radial anisotropy, obtained from the simultaneous inversion of Rayleigh and Love waves, and the azimuthal anisotropy directly derived from the regionalization of phase or group dispersion curves.

In particular, to constrain the distribution of azimuthal anisotropy in three dimensions, surface wave tomography is more suitable than shear wave splitting techniques which have good lateral resolution but limited depth resolution (e.g., *Fouch and Rondenay*, 2006) because variations in surface wave azimuthal anisotropy as a function of period can constrain the depths of anisotropic layers (e.g., *Montagner et al.*, 2000).

Recent studies (e.g., *Darbyshire and Lebedev*, 2009) have indicated that the interstation Rayleigh and Love wave dispersion curves can be used as input for a tomographic inversion procedure producing azimuthally anisotropic phase-velocity maps. Each measured interstation dispersion curve $C_i(\omega)$ depends on the structure of the Earth in the area of the two stations. The measurements thus constrain the distribution of deviations of phase velocity from a regional average:

$$\int_{\theta}\int_{\phi} K_i(\omega,\theta,\phi)\delta C(\omega,\theta,\phi)d\phi d\theta = \delta C_i(\omega) \pm \Delta C_i(\omega), \tag{3.28}$$

where $\theta$ and $\phi$ are coordinates, $\delta$C$(\omega,\theta,\phi)$ is the phase-velocity deviation at a point ($\theta$, $\phi$) and frequency $\omega$, and $\delta$C$_i(\omega)$ and $\Delta$C$_i(\omega)$ are the measured interstation-average phase-velocity anomaly and the measurement error, respectively, and the kernel $K_i(\omega,\theta,\phi)$ defines the sensitivity area for the $i$th station pair (see *Darbyshire and Lebedev*, 2009; *Lebedev et al.*, 2009).

In summary, seismic surface waves have proved to be a very powerful tool for investigating the small- and large-scale anisotropic properties of the Earth's crust and upper mantle. The pioneering study of *Forsyth* (1975) for the Pasific Ocean had revived interest in this subject after debatable studies about surface-wave anisotropy (e.g., *Boore*, 1969). Although surface waves in more general anisotropic media indicate many peculiar features and are more difficult to analyse, it is well suited to provide information about different regions (depth ranges) of the Earth. Thanks to surface wave observations, the determination of anisotropy can extend to a depth of about 300 km, especially beneath oceans.

**C) The Love/Rayleigh wave incompatibility**

There are observations of Love- and Rayleigh-wave dispersion curves which cannot be accounted for simple isotropic models presenting smooth depth variations of velocity. Such observations are referred to as Rayleigh/Love-wave discrepancies. *Anderson* (1961) first measured radial anisotropy through several observations of Love/Rayleigh-wave discrepancies. After this discovery of seismic anisotropy, *Aki and Kaminuma* (1963) found azimuthal dependence of seismic wave velocities. Unambiguous large-scale anisotropic effects have been obtained both from body waves by S wave splitting (e.g, *Silver and Chan*, 1991)) and from surface waves through azimuthal and radial anisotropy (e.g., *Lebedev et al.*, 2009).

In general, transversely isotropic models are well adapted to fit such observations since they allow one to fit simultaneously both sets of dispersion curves without introducing unrealistic velocity fluctuations of the model along the vertical coordinate. Because these observations of Love/Rayleigh-wave discrepancies are directly connected with the polarization of the

waves, anisotropy of transversely isotropic structures is often referred to as some “polarization anisotropy” in the seismological terminology.

In particular, discrepancies in dispersion curves of Love and Rayleigh waves are well explained by hexagonal anisotropy with a vertical axis of symmetry. *Smith and Dahlen* (1973) indicated that a slight elastic anisotropy gives rise to an azimuthal dependence of the phase velocities of both Love and Rayleigh waves of the form:

$$C_L(\omega, \Phi) = A_1(\omega) + A_2(\omega)cos(2\Phi) + A_3(\omega)sin(2\Phi) + A_4(\omega)cos(4\Phi) + A_5(\omega)sin(4\Phi) \quad (3.29)$$

$$C_L(\omega, \Phi) \approx C_R(\omega, \Phi). \quad (3.30)$$

*Smith and Dahlen* (1973) first wrote a theoretical relation, valid in a half-space medium, between slight perturbations $\delta$c in the phase velocity $C$ of Love and Rayleigh waves, and the azimuth of their direction of propagation.

**D) Resolution tests**

For seismic tomography, some resolution tests such as checkerboard tests and resolution matrices have been developed. Here they are briefly reviewed.

**i) Checkerboard tests**

In most seismic tomography studies, the resolution, or spatial extent of the smallest seismic velocity anomaly that can be imaged and is typically evaluated through synthetic tests. Given the data coverage (geographic distribution of sources and stations for which measurements are available), ray-theoretical travel times in a given velocity model (i.e. a checkerboard function) are calculated for each ray path. A synthetic data set is thus assembled, and inverted with the same algorithm used to invert real seismic data. The similarity of the solution model to the one from which synthetic data were computed is a measure of the completeness of the data set: in the ideal case of perfect coverage, the input and output model should coincide (e.g., *Boschi and*

*Dziewonski*, 1999).

For example, the use of a two-station method in the surface wave analysis presents restrictions on path coverage due to the standard great-circle requirement inherent in the method. Some interstation paths could not be analysed due to a lack of events near the corresponding great-circle paths. Therefore, the choices of optimal smoothing and damping parameters should be given special attention because smoothing and damping are standard means of regularizing a tomographic inversion. The choice of smoothing/damping parameters may be based on examination of trade-offs between model resolution and roughness (e.g., *Menke and Abbott*, 1990). The model roughness is defined as the average difference between the anomaly at a given knot point and the anomalies at its nearest-neighbour grid knots. Oversmoothing results in a lack of resolution that obscures the regional variations of interest, whereas undersmoothing results in good variance reduction but with models dominated by noise due to errors in the given data. As a consequence, initially an appropriate range of smoothing and damping parameters should be determined by examining trade-off curves for model roughness against variance reduction for isotropic and anisotropic regularizations.

Note that surface waves at different periods are sensitive to elastic properties in different depth ranges; measuring Rayleigh- and Love-wave dispersion over broad period ranges (including, in particular, short periods of 10-20 s) enables one to resolve trade-offs between model parameters in the crust and in the upper mantle and, thus, determine isotropic and anisotropic seismic structure of both the crust and the mantle with a substantially higher accuracy.

**ii) Resolution matrices**

As mentioned above, in seismic tomography studies resolution tests (e.g., checkerboard tests) and resolution matrices are usually used to estimate the robustness of the seismic features. In order to prescribe test models $m^{test}$ and calculate their associated test data, this equation is followed:

$$d^{test} = Gm^{test}. \tag{3.31}$$

Then, these test data are inverted for phase velocity maps using the procedure described above. In general, it is expected that the damping and smoothing should be nearly similar to those of a final preferred model. Therefore, resolution tests can give information about changes in the anisotropy pattern measured in a study area.

Resolution matrices are less intuitive, but they provide valuable information about the amount of trade-offs between the inverted parameters, in particular between the isotropic and anisotropic terms.

The least squares solution to the inverse problem is

$$X^{LS} = (A^T A + D)^{-1} A^T d \tag{3.32}$$

where $A$ is a matrix related to the sensitivity kernels and model parameterization, $D$ is a damping matrix containing the sum of selected norm and roughness regularization, and $d$ is the vector containing phase velocity variance from a starting model. Thus, a resolution matrix $R$ (*Trampert and Leveque*, 1990) can be defined:

$$R = (A^T A + D)^{-1} A^T A. \tag{3.33}$$

This matrix directly quantifies the relative contribution of neighbouring parameters in the solution of the inverse problem at adjacent nodes of a proposed model. With ideal resolution, $R = I$, where $I$ is the identity matrix. However, with real data, the off-diagonal elements of the resolution matrix will not equal zero. Each of these off-diagonal elements represents the relative contribution of neighbouring free parameters to the solution at each node.

**E) Basis functions**

Basis functions are now briefly reviewed. They are generally used in the inversions of the dispersion data. In common inversions of phase-velocity data, each basis function is used to define two independent parameters: one for an isotropic Vs perturbation and another for the amount of anisotropy within the depth range spanned by the function. Different parameterisations with

different numbers of parameters in the mantle, as well as different definitions of damping, were used in a series of test inversions for each profile so as to make sure that the obtained results and conclusions are robust with respect to the (arbitrary) choice of the parameterisation.

An example of how to perform basis functions in inversions of surface-wave measurements for the Moho and LAB depth is given by *Lebedev et al.* (2013). For example, for every point along the Moho-depth axis, *Lebedev et al.* (2013) performed a non-linear gradient search inversion in which the Moho depth is fixed and the crustal and mantle structure is varied, so as to minimise the misfit between the synthetic and measured phase-velocity curves. In the study, perturbations to the background shear-speed profiles are parameterised using 15-20 boxcar (crust) and triangle (mantle) basis functions, with the width of the basis functions increasing with depth. It is important to note that the crustal and mantle structure is over-parameterised, i.e. the number of basis functions is large enough so that the choice of a particular number does not affect the minimum misfit achievable with various Moho depths. In such cases, generally compressional-wave speed perturbations are coupled to shear-wave speed ones ($\delta Vp$ (m/s)=$\delta Vs$ (m/s)). This assumption is reasonable for the upper mantle, but not always for the crust, particularly in sedimentary layers (*Lebedev et al.*, 2013).

The non-linear gradient search was performed with the Levenberg-Marquardt algorithm for resolving the lithosphere-asthenosphere boundary with seismic Rayleigh waves (*Bartzsch et al.*, 2011). In the study, synthetic phase velocities were computed directly from one-dimensional (1-D) Earth models at every step during the gradient search, using a last version of the MINEOS modes code of Masters[1]. This code was originally developed by *Nolet* (1990).

In the study conducted by *Bartzsch et al.* (2011), the LAB depth and thickness are fixed in each gradient-search inversion, but the wave speeds in both the crust and upper mantle are free to vary. They parametrized the crust and mantle with boxcar and triangle basis functions. Here, a typical set of basis functions is shown in Fig. 3.20, as an example.

[1] http://igppweb.ucsd.edu/gabi/rem.dir/surface/minos.html

If the mantle lithosphere layer is sufficiently thick, its structure cannot parametrize only with one boxcar basis function (Fig. 3.20). However, with multiple triangular basis functions, the thick mantle lithosphere layer can be parametrized. It is important that the crustal and mantle structure is overparametrized, i.e. the number of basis functions is large enough so that the choice of a particular number does not affect the value of the minimum misfit achievable with various LAB depths and thicknesses (*Bartzsch et al.*, 2011). With reasonably accurate phase-velocity measurements, small damping is sufficient to rule out exotic models with unrealistic shear-speed values.

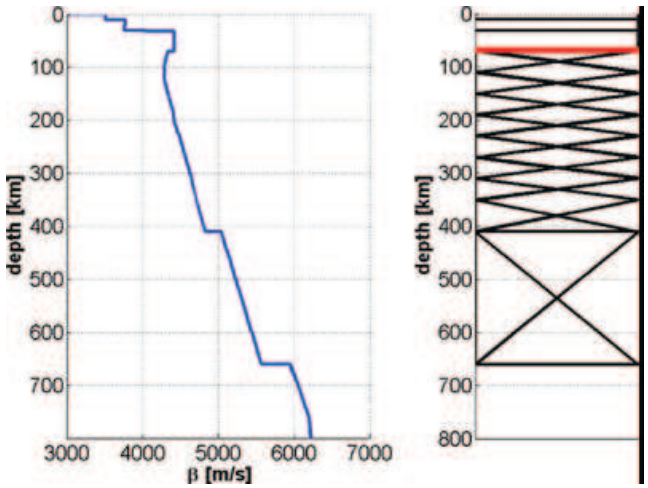



Figure 3.20.: An example S-velocity profile (left-hand panel) and example parametrization (right-hand panel), as used in the tests and inversions. The crust and the thin mantle lithosphere in this example are parametrized with boxcar basis functions; the asthenosphere and deeper upper mantle with triangular basis functions. The depth and width of the LAB are also varied in the tests and inversions (taken from *Bartzsch et al.*, 2011).

## 3.5. Review of anisotropy studies in the North Atlantic region, UK and Ireland

Previous anisotropic studies for the North Atlantic region, UK (the United Kingdom) and Ireland are briefly summarized since Ireland is located in northwestern Europe and inherits a similar geological history and tectonic development to the North Atlantic region and UK.

**A) Anisotropic structure of the North Atlantic region**

Before reviewing anisotropy studies in this region, let us give a brief review on its tectonic and geologic structure. Particularly in the large-scale, the Iceland Plume and Mid-North Atlantic Ridge System have a significant influence on the structure of mantle flow in the North Atlantic region because plume driven flow from the Iceland plume and spreading-driven flow from the Mid-Atlantic Ridge System are superimposed (Fig. 3.21). Recently, *Rickers et al.* (2013) has derived a high-resolution S-velocity model of the North Atlantic region, covering the upper and part of the lower mantle to a depth of 1300 km. They found two distinguishable strong low-velocity regions beneath Iceland and beneath the Kolbeinsey Ridge west of Jan Mayen. A sub-lithospheric low-velocity layer is imaged beneath much of the oceanic lithosphere, consistent with the long-wavelength bathymetric high of the North Atlantic (*Rickers et al.*, 2013). In addition, *Rickers et al.* (2013) claim that it is possible to also observe the low velocity layer locally beneath the continental lithosphere of the southern Scandinavian Mountains,the Danish Basin, part of the British Isles and eastern Greenland. In the North Atlantic the plume arrived under central or southeastern Greenland about 58 Ma ago (*Torsvik*, 2001), presumably caused rifting and plume-related volcanism in western, northern and eastern Greenland (e.g., *Scarrow*, 2000) and finally initiated massive volcanism and continental breakup between the North American and Eurasian Plates. The North American and Eurasian continental margins are drifting apart since the onset of ocean spreading in the North Atlantic about 55 Ma ago. *White* (1989) indicated that the continental breakup went along with the eruption of large amounts of magma within a short geological time. Following the breakup, the magma production rate along the Mid-Atlantic Ridge remained locally unusually high. According to *Jones et al.* (2002), this resulted in the formation of Iceland (Fig. 3.21), which is part of an extensive bathymetric and gravimetric high observed over much of the North Atlantic.

In this region, early studies on seismic anisotropy indicated results different from each other (e.g., *Montagner and Tanimoto*, 1991; *Woodward and Masters*, 1991). For example, the map by *Montagner and Tanimoto* (1991) indicates a weak frequency-(depth)-dependent anisotropy

with a predominantly NW-SE fast seismic direction for the entire region. However, another global study on azimuthal seismic anisotropy using long-period SS-S times (*Woodward and Masters*, 1991) surprisingly did not give an indication of upper mantle anisotropy in the North Atlantic region. Then, *Yang and Fischer* (1994) analyzed SS arrivals for shear-wave splitting and found some indication of upper mantle anisotropy beneath the Atlantic, with the inferred orientation for the central North Atlantic in approximate agreement with the global anisotropy model of *Montagner and Tanimoto* (1991). A recent surface wave study by *Ekstrom* (2001) has indicated a constant WNW-ESE direction for the region around Iceland at 50-150 s periods (max. sensitivity between 80 and 250 km), but their resolution is poor since azimuthal anisotropy studies on a global scale only provide the averaged effect over large areas. Another recent studies by *Debayle et al.* (2005) and *Pilidou et al.* (2005) have indicated an anisotropy field in NW-SE direction over most of the North Atlantic, but rotation to nearly E-W slightly north of the Charlie-Gibbs Fracture Zone (southward of a latitude of $\sim 56^0$N) and north of $82^0$N, and a predominately N-S direction across the Greenland shield at 500 km depth.

Another study by *Silveira and Stutzmann* (2002) indicated that the mid-Atlantic ridge (MAR) is a shallow structure in the North Atlantic corresponding to a negative velocity anomaly down to about 150 km depth. In contrast, the ridge negative signature is visible in the south Atlantic down to the deepest depth inverted, that is 300 km depth. *Silveira and Stutzmann* (2002) also suggested that this difference is probably related to the presence of hot-spots along or close to the ridge axis in the south Atlantic and may indicate a different mechanism for the ridge between the north and south Atlantic. As these negative velocity anomalies caused by hot-spots can extend from the surface down to at least 300 km depth, they are much broader than the supposed size of the hot-spots and seem to be connected along a north-south direction. In addition, anisotropic tomography of the Atlantic Ocean (*Silveira and Stutzmann*, 2002) clearly exhibited that in most parts of the Atlantic, the azimuthal anisotropy directions remain stable with increasing depth (Fig. 3.22).

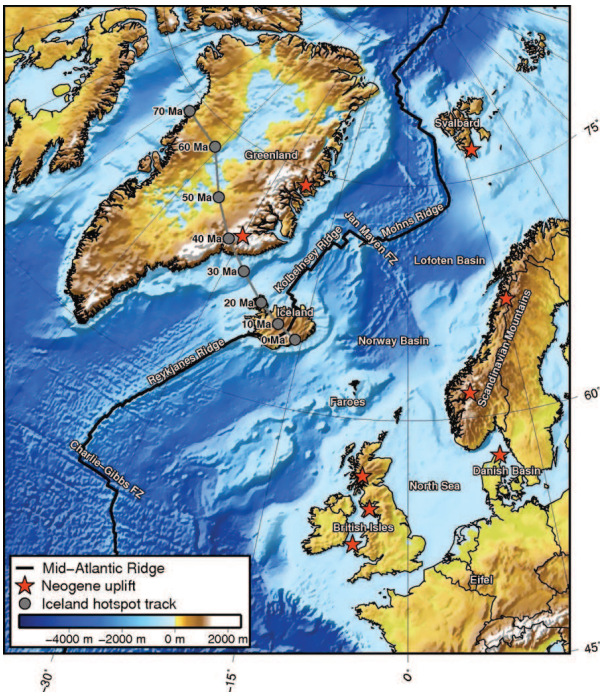



Figure 3.21.: Topography and bathymetry of the North Atlantic region (taken from *Rickers et al.*, 2013).

In addition, their anisotropy directions are consistent with body wave anisotropy measurements determined by *Wolfe and Solomon* (1998) using SS-wave splitting. According to this study, the Atlantic average radial anisotropy is also similar to that of the PREM model, that is positive down to about 220 km, but with slightly smaller amplitude. As previously mentioned, not only the anisotropic structure of the North Atlantic region but also that of Iceland have a significant effect on the anisotropic structure of Ireland. A number of seismic anisotropy measurements have been done in Iceland. Iceland is one of the few locations on the Earth where a mantle plume and a spreading ridge coincide. Iceland is a hotspot located on the North Atlantic Ridge, with the Reykjanes Ridge to the south and the Kolbeinsey Ridge to the north. Anisotropy observations on Iceland at very shallow (crustal) depth (*Menke et al.*, 1994) show ridge parallel anisotropy in the SW. The general appearance of the anisotropy field is characteristic for a large-scale upwelling, with its centre north of Iceland. The area to the north of Iceland and along the northern ridge system, where the flow is essentially vertical, is characterized by weak horizontal anisotropy of varying direction. According to *Marquart et al.* (2007), in the Atlantic

south of Iceland, azimuthal anisotropy significantly changes from NW-SE close to the European continent to NE-SW across the Reykjanes Ridge (Fig. 3.23).

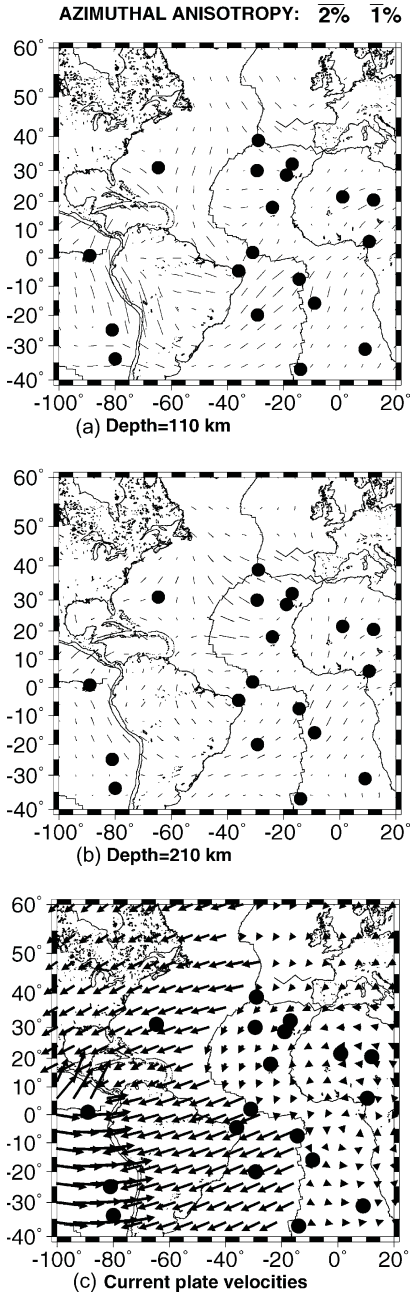



Figure 3.22.: S-wave velocity azimuthal anisotropy for (a) 110 km; (b) 210 km depth. The S-wave velocity fast directions are given by the bars azimuth. The length of the bars are proportional to the intensity with respect to the scale on top of the figure. (c) Current plate velocities calculated from model NUVEL-1 (*Gripp and Gordon*, 1990) (taken from *Silveira and Stutzmann*, 2002).

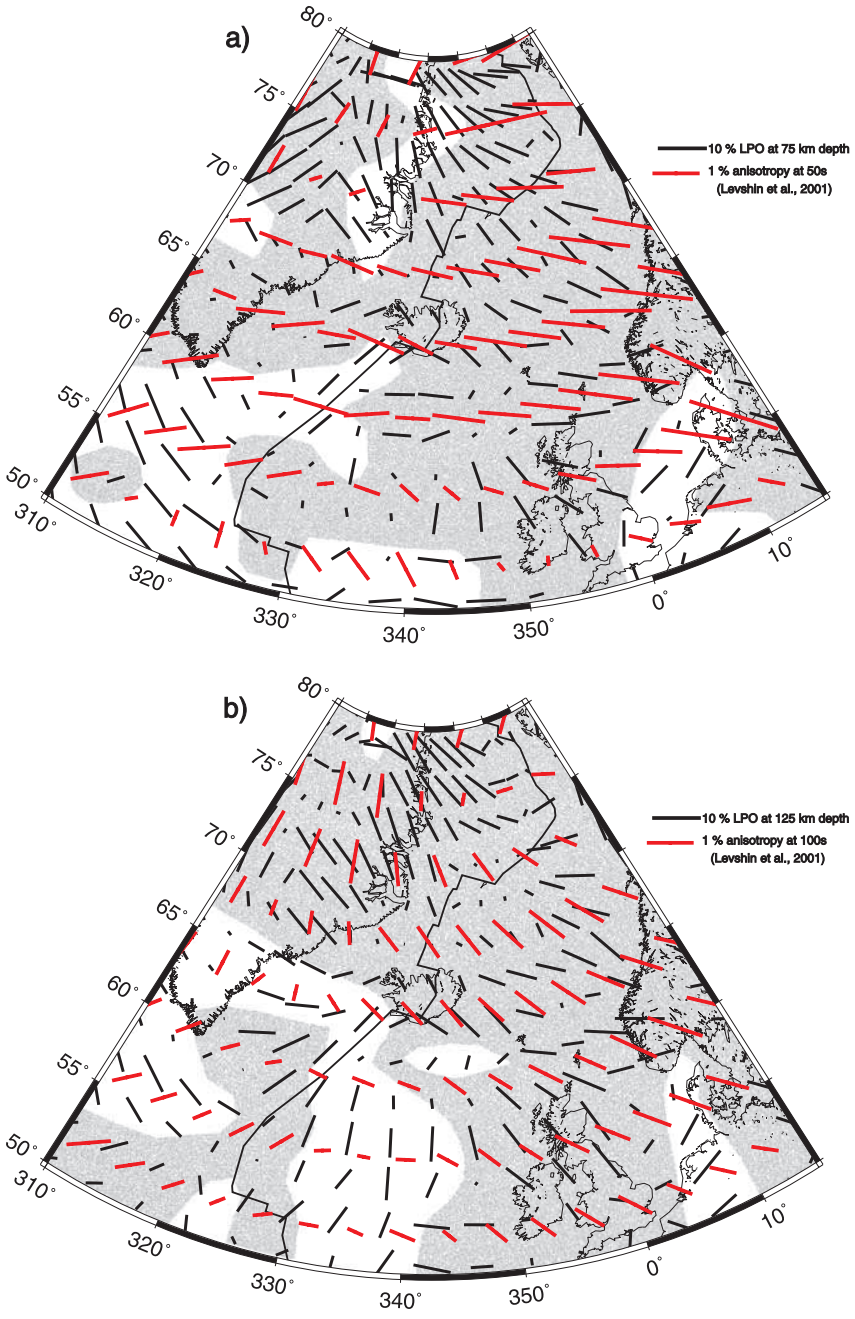



Figure 3.23.: Horizontal component of LPO directions of the regional flow model (black bars) and azimuthal anisotropy (red bars) in the North Atlantic region based on Rayleigh waves after *Levshin et al.* (2001) for periods of (a) 50 s and (b) 100 s, respectively. Regions where the fit is better than $45^0$ are indicated in light gray (taken from *Marquart et al.*, 2007).

Moreover, splitting parameters determined for Iceland by *Xue and Allen* (2005) (Fig. 3.24) are very consistent with regional anisotropic models (e.g., *Pilidou et al.*, 2005). *Xue and Allen* (2005) suggested that the observed anisotropy pattern beneath Iceland is well aligned with ridge-channeled flow: horizontal flow of upwelling material toward and then along the North Atlantic Ridge. Also, the pattern of splitting parameters indicates a single layer of anisotropy located in the upper mantle (Fig. 3.24).

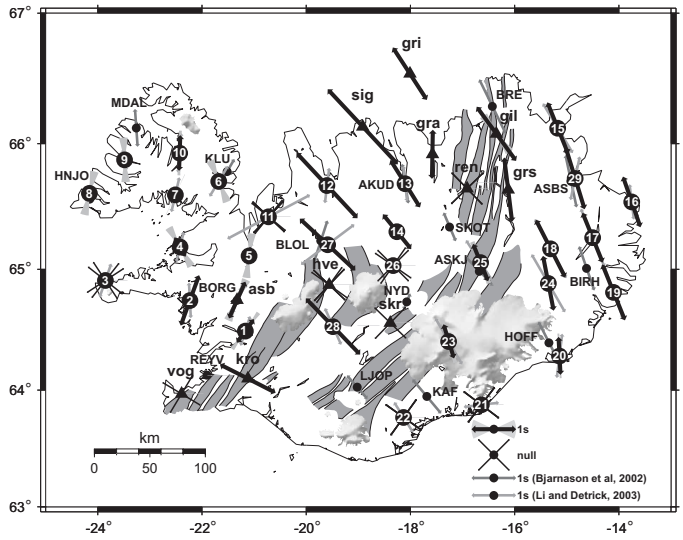



Figure 3.24.: Splitting results across Iceland. At each station the line orientation gives the fast splitting direction Φ, and its length is linearly proportional to $\delta$t. The black thickest lines indicate fast axis orientation and thin crosses indicate null results. The light gray wedges indicate the 95% confidence region in the polarization direction. The thin dark gray lines indicate the results from *Bjarnason et al.* (2002); the thin light gray lines indicate the results from *Li and Detrick* (2003). Also the neovolcanic zones (gray region) and glaciers (light gray shades) are indicated, respectively.

**B) Shear-wave splitting results from previous studies in Ireland and the UK**

Here previous anisotropic studies on teleseismic data from the UK (the United Kingdom) and Ireland conducted by *Helffrich* (1995); *Do et al.* (2006); *Bastow et al.* (2007) are reviewed.

In section 2.2, we briefly reviewed the study of *Do et al.* (2006). *Do et al.* (2006) collected teleseismic data from 1991 to 2006 recorded by 23 temporary and 2 permanent stations deployed in the southwest of Ireland. The purpose of the study was to investigate possible anisotropy within the crust and mantle related to Caledonian deformation. *Do et al.* (2006)

found that the splitting results show an average apparent delay time of 1.2 s, suggesting an anisotropic layer of ~80-100 km, or more, in thickness within the mantle (Fig. 3.25). A large change in fast polarisation direction was found between results from the South American and East Asian event clusters (see Fig. 2.10). For this, one possible explanation suggested by *Do et al.* (2006) is a deep origin for the anisotropy, although dipping symmetry axes could not be excluded. The study also shows that the measured anisotropy from the East Asian event cluster agrees reasonably with the Caledonian/Variscan trend with a slight variation across the ISZ suggesting lateral heterogeneity at shallow depth. However, they found that there is no correlation of the anisotropy with regional tectonic trends for the South American events (see Fig. 2.10). This may mean that a shallow anisotropy is overprinted by a stronger anisotropy with an origin at a greater depth in the oceanic mantle. Additionally, they found that there is no correlation between the fast polarisation directions and the present-day absolute plate motion.

Existing studies of shear wave splitting in the British Isles suggested that the fast shear wave polarization direction $\phi$ of the anisotropy commonly parallels the trend of the dominant surface structures in the area, which are mostly of Caledonian or Variscan age (e.g., *Helffrich*, 1995) (Fig. 3.25). This indicates the presence of lithospheric deformation, which has been preserved over geological time.

Recently, *Bastow et al.* (2007) have also investigated seismic anisotropy beneath a closely spaced seismic network in Scotland using shear wave splitting analysis of teleseismic SKS and PKS phases (Fig. 3.25). The results indicated considerable variations in the strength ($\delta$t= 0.5-1.5 s) and orientation of anisotropy. In addition, *Bastow et al.* (2007) found that there are rapid spatial variations in $\phi$ and $\delta$t which confirm strong contributions by crustal anisotropic layers. Moreover, *Bastow et al.* (2007) also showed that the results significantly track Scotlands tectonic history from the Precambrian emplacement of crustal basement through the activation of large-scale faulting and thrusting during the Caledonian (Fig. 3.25). As a consequence, the shallow lithosphere beneath Scotland has preserved a fossil anisotropic signature, up to hundreds of millions of years after it was formed. They suggested that the anisotropy in Scotland is

most likely a lithospheric fossil anisotropy. Therefore, the results from the study confirmed the hypothesis suggested by *Silver and Chan* (1991) is that splitting under continents monitors the lithosphere's remnant strain from the last previous deformation event.

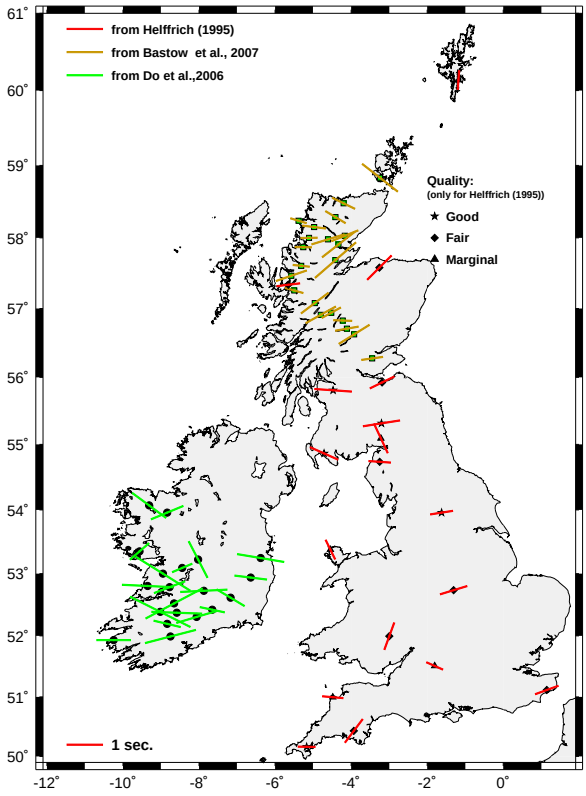



Figure 3.25.: Results and qualities of splitting measurements in the UK stations are obtained from a study of *Helffrich* (1995). Shear wave splitting results in the region of the Scottish Highlands and Ireland are taken from *Bastow et al.* (2007) and *Do et al.* (2006), respectively. The orientation of the bars shows the alignment of faster shear waves and the length of the bar is proportional to the magnitude of the splitting.

In summary, these studies of *Do et al.* (2006) and *Bastow et al.* (2007) suggested that there is no correlation between present-day absolute plate motions and the fast polarization directions measured in Ireland and the UK, respectively. The studies also indicated that the anisotropy in Ireland and the UK is most likely a lithospheric fossil anisotropy. Although *Do et al.* (2006) found that there is a clear variation in fast polarization directions with back-azimuth, *Helffrich* (1995) and *Bastow et al.* (2007) reported no dependence with back azimuth of fast polarization directions.

# 4. Shear-wave splitting analysis

The main target of this chapter is to present a detailed description of teleseismic data acquisition and processing during the Irish Seismological Lithospheric Experiment (ISLE) from 2002 to 2005, the Irish Seismological Upper Mantle Experiment from 2006 to present and the Ireland Array (IA) from 2010 to present. The collected and processed data from the permanent stations in Ireland are also presented in this chapter. Additional technical information related to data acquisition is provided in Appendix B. At the end of the chapter, results from shear wave splitting observations in Ireland are presented and also preliminary interpretation and discussions of the results are given.

## 4.1. Irish Seismological Upper Mantle Experiment

### 4.1.1. Overview

One of the basic purposes of this project is to investigate elastic anisotropy beneath Ireland using the Shear Wave Splitting (SWS) method. In this study, teleseismic data was recorded at 2 permanent stations and more than 40 temporary stations from the Irish Seismic Lithospheric Experiment (ISLE), the Irish Seismological Upper Mantle Experiment (ISUME) and the Ireland Array (IA) projects. The study covered all of Ireland with broadband seismic stations (Fig. 4.1), for the first time. The ISLE and the ISUME stations were equipped with Guralp CMG-40T (eigenperiod 30 s) seismometers. The permanent station VAL was equipped with a Guralp CMG-40T and DSB with a Streckeisen STS-2 seismometer (eigenperiod 120 s). The IA

stations have Trillium 120PA (band width from 175 Hz to 120 s) seismometers (manufactured by Nanometrics Inc.). Data from the ISLE, the ISUME and the IA projects have been recorded from 2002 to 2006, from 2006 to 2011 and from 2010 to present, respectively.

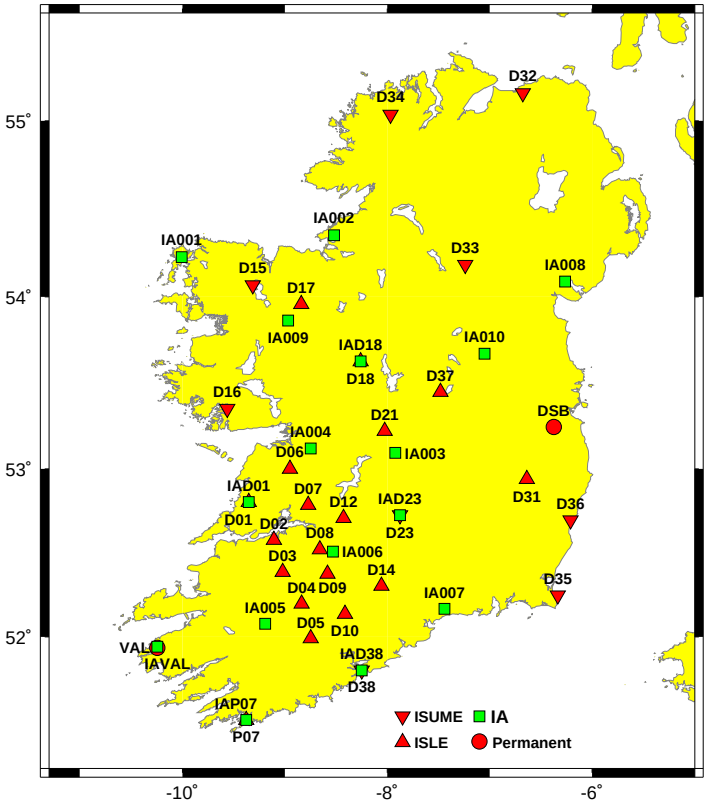



Figure 4.1.: Location map of all seismic stations deployed in Ireland up to 2011. The ISLE, the ISUME, the IA and Permanent stations are depicted by red triangles, inverted red triangles, green squares and red circles, respectively.

### 4.1.2. Site selection and permission

Before the instruments were deployed, station locations were selected according to the following criteria:

**1) Vehicle accessibility**

Ireland has a good and dense road network so that this is not a major consideration for this study.

**2) Site conditions**

Good locations for particularly temporary stations are unused sheds, garages and abandoned houses, as shown by (Fig. 4.2a).

**3) Power supply**

The seismic station is usually powered by a 12 V DC battery which is trickle-charged by a mains battery charger (Fig. 4.2b). Therefore, a nearby mains power sources is required. Distances from the power source to recording instruments should ideally be no more than about 20-30 m.

**4) Security**

In general, we look for sites that offer some degree of security and are not generally visible from public roads or paths.

**5) Infrastructure and environmental noise**

The geological situation and the proximity of the noise sources affect the noise level. Seismometers are, wherever possible installed on solid basement rock or a concrete base, away from sources of noise such as roads, rail lines, etc. Besides ground noise, environmental conditions must be considered. Wind and short-term variations of temperature may induce noise. The effects are minimized by using the insulated covers over the seismometers and by installing inside buildings or by burying the seismometers.

**6) Satellite view**

GPS is used for timing. Therefore, a good sky view is necessary. A high position such as on a shed's roof is preferred in order to enhance signal reception (Fig. 4.2c).

**7) Local contacts and maintenance personnel**

Landowners and farmers in Ireland are generally very helpful. Therefore, it was usually not a problem to obtain permission for our stations. Most sites were found through contact with local Irish Agriculture and Food Development Authority (TEAGASC[1]) officers who were very helpful and have good local knowledge of potentially suitable sites.

[1] http:www.teagasc.ie



(a)



(b)



(c)

Figure 4.2.: Examples of sites selected for temporary station deployments: (a) an unused shed; (b) Seismometer is placed under the white polystyrene box to insulate against rapid temperature variations and draughts. The battery charger and battery can be seen on the right of the recorder; (c) GPS antenna is on the roof (in the red box).

### 4.1.3. Event selection

A data set of suitable teleseismic events was based on the following criteria:

**a) Epicentral distance**

Epicentral distance is a very significant criterion for shear wave splitting analysis. Core phases such as SKS, PKS, and SKKS are easily observed beyond $85^0$ as the phases avoid the contamination by other phases, such as S, sS, and ScS (Figs. 4.3 and 4.4).

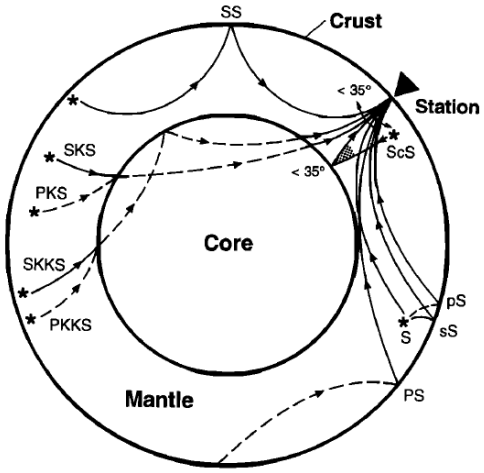



Figure 4.3.: Phases used for shear wave splitting studies. Solid lines are S path segments, dashed lines are P path segments, and stars are earthquake sources.

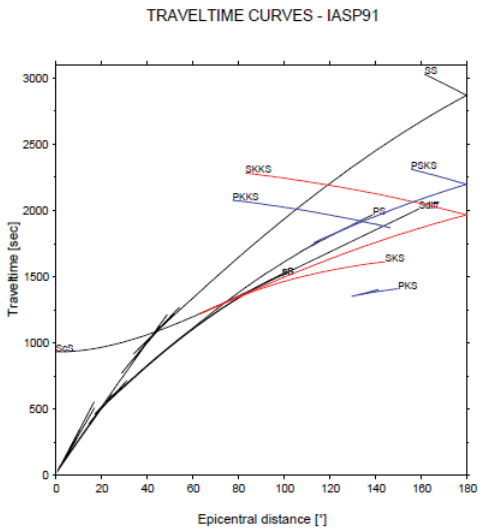



Figure 4.4.: Travel time curve for seismic wave phases computed for an earthquake at the surface according to the standard IASP91 Earth velocity model (*Kennett and Engdahl*, 1991), SKS and SKKS are particularly marked red.

Therefore, data from all the events with the epicentral distance in the range of 85 to $160^0$ are selected.

**b) Event magnitude**

For this study, events of magnitude ≥ 5.8 Mw were selected at these epicentral distances.

**c) Depth**

Hypocentral depth is not an important criterion for teleseismic shear wave splitting. However, in this study we observed that intermediate earthquakes (70-300 km deep) are more suitable than shallow earthquakes (0-70 km deep) and deep earthquakes (300-700 km deep) to determine splitting parameters accurately. This may be related to the influence of the magnitude and focal mechanisms on the S/N on the transverse component. This point will also be discussed in the section 4.2.1.

### 4.1.4. Data processing

The two main stages of teleseismic data processing are data extraction and format conversion. In DIAS, the main processing is done using the Seismic Handler (SH) package developed by *Stammler* (1993). The steps concerning data preparations and pre-processing are described below:

**a) Data extraction**

Earthquake information for the teleseismic event list was searched via online catalogues from the National Earthquake Information Center (NEIC) and Advanced National Seismic System (ANSS), which are parts of the Earthquake Bulletins of the US Geological Survey (USGS).

The earthquake parameters from the event list are used for obtaining other basic parameters, such as epicentral distance, back-azimuth and theoretical P-onset times. From the calculated parameters, time windows for SKS/SKKS arrivals are then predicted for each station. Time windows were extracted from 30 minutes to 120 minutes in length depending on event magnitude, depth and epicentral distance. Data extraction is done on Linux OS using automated scripts developed by *Do et al.* (2006).

**b) Q-format conversion**

The EDL data from the PR242 and 2400 recorders were first converted to miniseed format. Then, it is converted to Seismic Handler Q format.

**c) Problems and corrections**

Generally, spike and missing minute files are a common problem in seismic data processing. Such problems are difficult to reveal with automated scripts. Therefore, we checked each waveform manually. The spike often appears after a data gap because it is related to missing minute files. For example, if huge spikes are observed on the seismograms, it indicates gaps of data somewhere within the extracted time window. Missing minute files thus result in a gap of data. When minute files are extracted from the raw dataset, this is defined well. However, the appended Q-files do not usually indicate any sign of this gap because SH generally ignores the time gap between the last sample and the first sample of two consecutive minute files when these two files are appended. SH simply obtains the time from the first minute file and then counts the sample numbers and adds on the time. Appending two Q-files can thus produce an inaccurate time axis on the seismic trace if there is a time gap between the two files. The routine way to fix this problem is to get the missing file name from the report generated when data is extracted, then create dummy traces to fill the gap in the time window. Henceforth, continuous time will be preserved throughout the processing. Also, faulty samples appearing in a minute file generates spikes with anomalous amplitude. The routine to deal with this problem is to replace the minute file that includes the spike by a dummy trace of similar length. Another possible way is to replace these faulty samples with interpolated samples within the single Q-file (one minute) using the SH command “MEND”.

**d) Further processing**

Header information is added to each event-station record. Then, filtering techniques are applied to the extracted data to improve the signal noise ratio (SNR). Detailed information on filtering is given in the main processing section. Although the sampling rate of raw data is 25, 75, or 100 sps, the data is resampled with 20 samples per second to make the datasets

compatible.

### 4.1.5. Global earthquake distribution

The global distribution of the teleseismic events selected for shear-wave splitting analysis is shown in Fig. 4.5. As observed in Fig. 4.5, earthquake clusters are distributed along the principal plate boundaries, major ridge systems, collision zones and subduction zones.

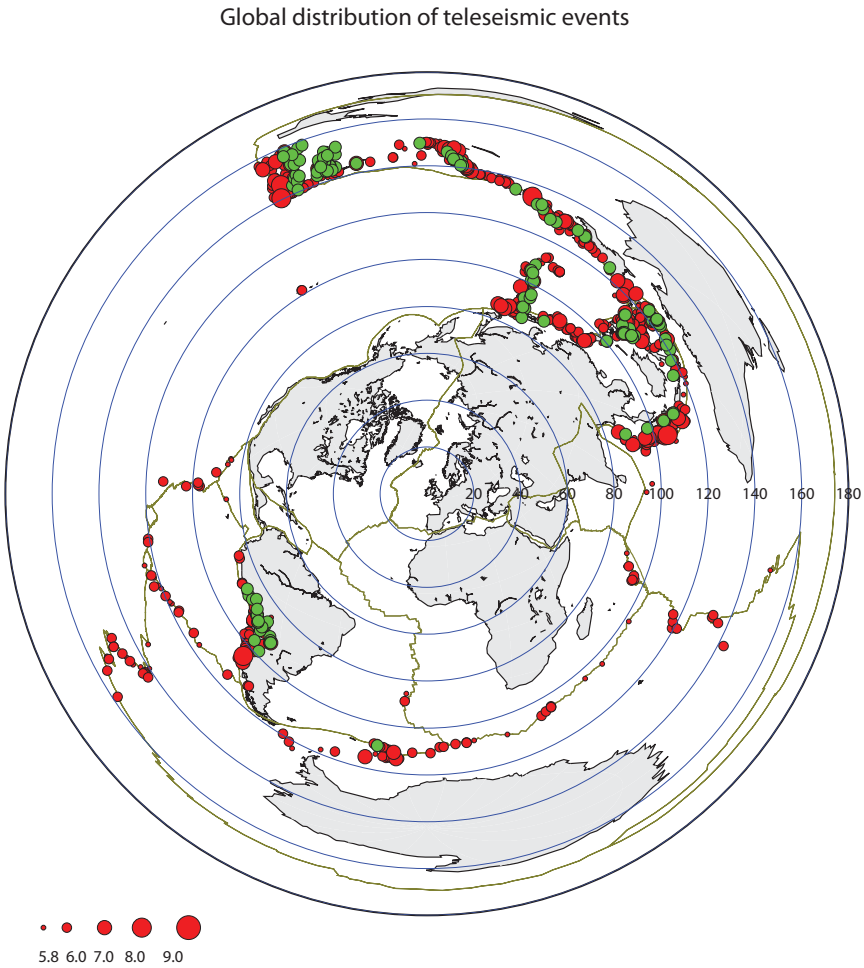



Figure 4.5.: Global distribution of suitable earthquakes ($\Delta \geq 85^0$ and magnitude $\geq 5.8$) selected for splitting analysis from 01/01/2003 to 31/09/2011. Total number of the selected events is 1189. Green circles indicate 205 events with hypocentral depth greater than 100 km. (Azimuthal Equidistant Projection centred on 8W, 53N. Circles are 20 degree radius).

Histograms of the selected event parameters are shown in Fig. 4.6. The data is from 01 January-2006 to 09 September-2011. According to the described selection criteria above, thus a total of 1132 events were initially selected. In addition to the initial dataset, a total of 58 events from 2003 to 2006 was reselected and then added to the final dataset. Therefore, in this study, we finally analyzed a total of 1190 events from 2003 to 2011 (Figs. 4.5 and 4.6).

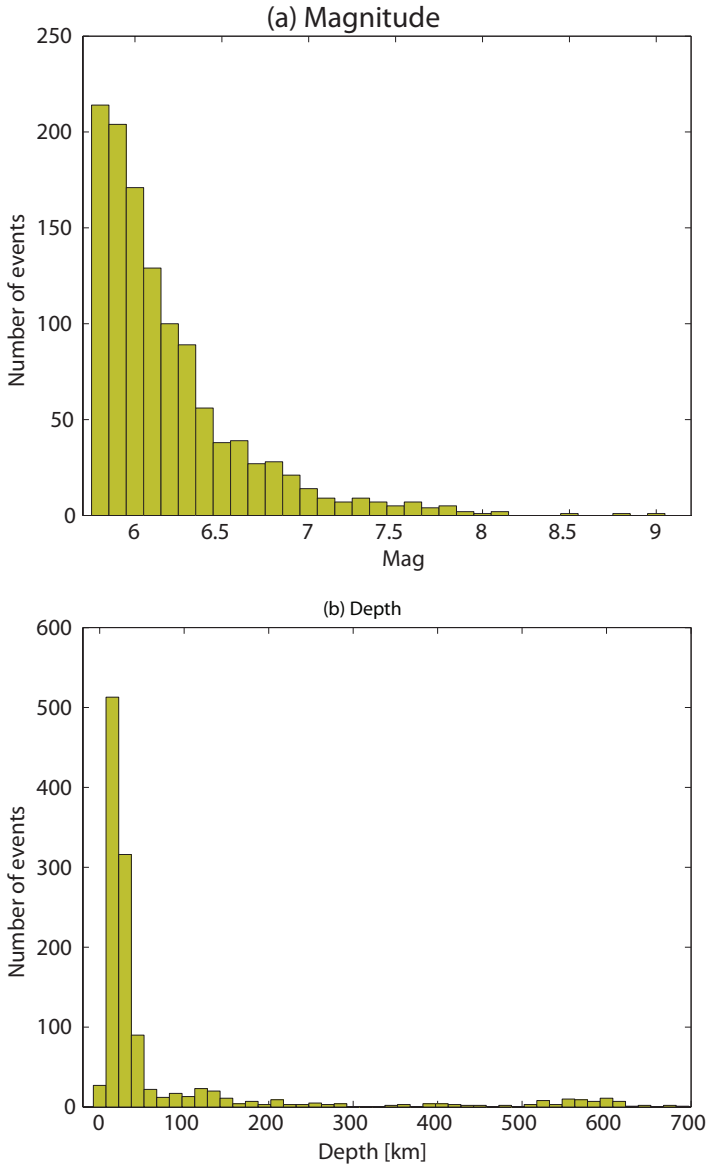


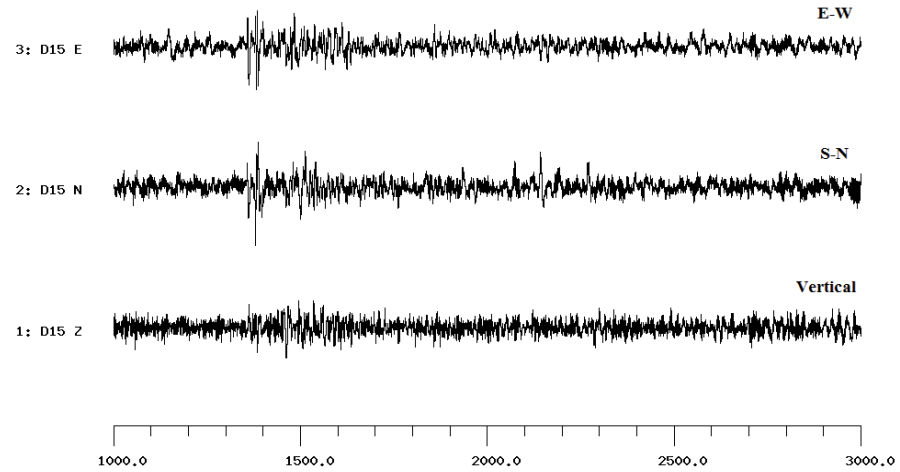

Figure 4.6.: Histograms of earthquake parameters: (a) magnitude and (b) hypocentral depth distribution for the selected events, respectively.

### 4.1.6. Routine shear wave splitting analysis

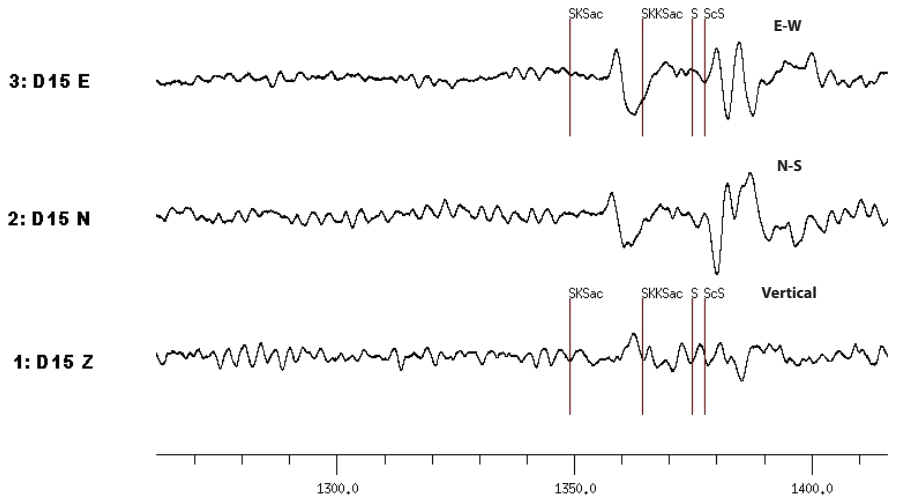
We used a splitting analysis program based on the original inversion method of *Silver and Chan* (1991), modified by Ruempker in 2000. Nowadays, this method is very popular and more reliable than other methods, such as the cross-correlation method (*Fukao*, 1984) to calculate the shear wave splitting parameters, i.e. fast polarization direction ($\phi$) and delay time ($\delta$t) between the fast and slow shear waves. In this method, the calculated $\phi$ and $\delta$t are sensitive to the choice of the manually selected shear wave analysis window. All the measurements went through a time-consuming manual screening process to provide reliable results and ensure that no high-quality SKS/SKKS traces were excluded. Therefore, unreliable or very low quality results are removed. Most importantly, SKS/SKKS phases should be visible on the horizontal seismograms. Fig. 4.7 shows an example of a reliable high quality event that is selected for splitting analysis.

Firstly, a theoretical phase picker is used to identify SKS/SKKS arrivals and then successive splitting measurements are made on a range of window lengths around the SKS/SKKS arrivals with good S/N ratios (i.e. $\geq 3$) (Fig. 4.8). Time windows of different lengths are visually checked to determine an acceptable window length of the analyzed signals because reliable results, in general, are stable over a range of windows lengths. Therefore, the most reliable result is derived from the determined windows over which the splitting parameters remain stable.

In this way, high quality measurements are assured. Furthermore, the measured splitting parameters were checked by analyzing the particle motion of each phase since elliptical particle motions are clearly indicative of shear wave splitting. We have used the following three steps to determine $\phi$ and $\delta$t from SKS and SKKS phases: (1) phase and splitting detection, (2) inversion for splitting parameters, and (3) quality control and error estimation.




(a)




(b)

Figure 4.7.: (a) Raw horizontal and vertical seismograms (E-W, N-S and Vertical components) of an event with $\phi_{baz} \sim 230.603^0$, $\Delta \sim 90.05^0$, depth~289.5 km, and magnitude of 6.4) recorded by station D15. (b) Unfiltered E-W, N-S and Vertical components with theoretical picks marked.

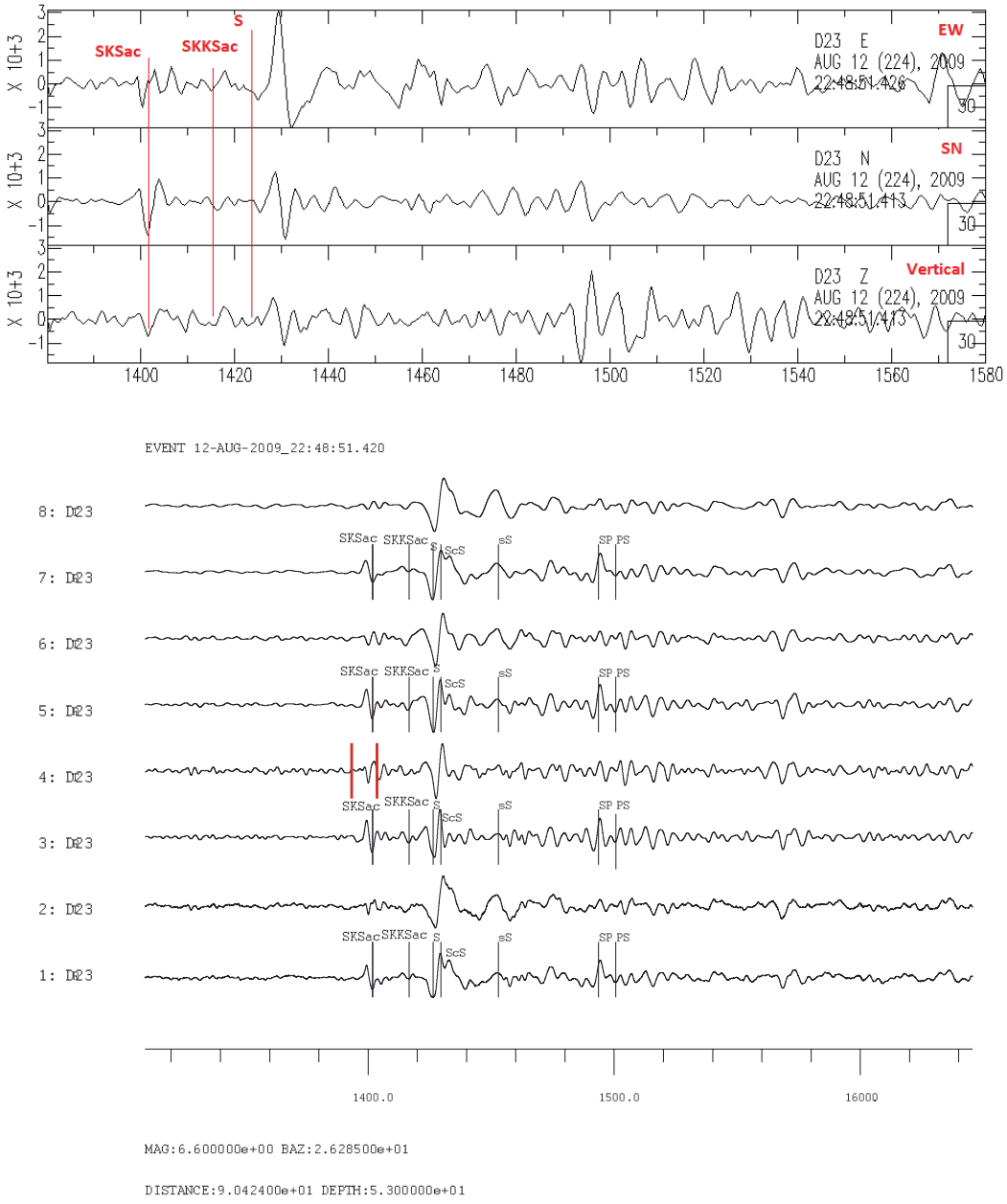



Figure 4.8.: (top) Raw horizontal and vertical seismograms (EW, NS and vertical components) of an event with $\phi_{baz}$ ~26.28$^0$, $\Delta$ ~90.42$^0$ and magnitude of 6.6 recorded by station D23. Time is in seconds. Theoretical picks marked on seismograms. (bottom) Seismic traces show radial and transverse components after rotating the horizontal components to back-azimuth. Traces 1-2 are unfiltered broadband seismograms. Traces 3-4 are band-pass filtered (2-10 s). Traces 5-6 are band-pass filtered (3-15s). Traces 7-8 are band-pass filtered (4-30 s). Then, each trace is picked in terms of the core phases. The red lines show time window on trace 4 for SKS phase. The beginning and end time of the measurement window was manually picked. Amplitudes on all seismograms are traced-normalized within the selected time window.

**1) Phase and splitting detection**

**a) Filtering**

Prior to the shear wave splitting analysis, the data was filtered using a 4-pole Butterworth bandpass filter in different ranges consisting of 2-10s, 3-15s and 4-30s to eliminate very high frequency and low frequency noise. An example of detecting seismic phases on unfiltered and filtered waveforms is shown in Fig. 4.8. Although filtering is an effective way to reduce the high noise level in the data and enhance the visibility of the signal, filtering is largely ineffective when the S/N ratio is very low and splitting is small (*Restivo and Helffrich*, 1999). Although other types of filters are used, in our case it was found that a 4-pole Butterworth bandpass filter in these ranges gives robust measurements on individual seismograms.

**b) Selection of time windows for SKS and SKKS phases**

The theoretical arrival times of the SKS/SKKS phases were calculated from 1-D Earth velocity Model IASP91 (*Kennett and Engdahl*, 1991). Each of the seismograms is visually inspected to adjust the beginning and ending values of the SKS and SKKS window (Fig. 4.8).

Time windows usually varied in length from minimum 6 sec to maximum 20 sec. To increase the reliability of splitting parameters, time windows in different lengths were also checked. In addition, the selected window length of the seismogram's transverse component is routinely checked by analyzing the particle motion of the SKS/SKKS phase because elliptical particle motions are indicative of shear wave splitting. Therefore, suspicious measurements due to improper window lengths of analyzed signals are eliminated. The advantage of picking the window length by visual inspection and particle motions of the phases is that the reliability of the measurements is increased and also the subjectivity in window picking is strongly removed.

**c) Discussion on splitting problems**

Problems, related to noise in the data and the length of the analysed waveform exist. Here these are discussed.

**i) Filtering**

Correctly determining arrival time of the phases depends on the quality of data and the signal

to noise ratio (SNR) because the detectability of the split signal on the tangential component depends on the signal to noise (S/N) levels of seismograms. As known, it is not always easy to collect high quality data for splitting analysis so preparation such as filtering and windowing before the main splitting process are important. In our case, special attention has been given to filtering because our raw data are often noisy, making the records difficult to analyse.

Firstly, all of the seismograms selected were filtered with various band-pass ranges and after many tests, 2-10s, 3-15s and 4-30s were routinely used (Fig. 4.8). Examples of these tests are shown in Figs. 4.9, 4.10 and 4.11. The tests indicated that filters and time windows have a significant influence on the results of the splitting analysis.

Our observations from the tests clearly exhibited that narrower filters seem useful to increase the signal to noise ratio (SNR) even though the measured error bars on the splitting parameters may increase (Fig. 4.9). The tests indicated that such narrow filters occasionally can produce acceptable results having moderate error bars, but they make the waveforms more oscillatory. Therefore, we suggested that such narrow filters are not so reliable for determining splitting parameters. The main point is to clearly observe shear wave energy on the transverse component because shear wave energy is much lower on the transverse component than on the radial component. Finally, we found that S/N ratios smaller than 3 on the horizontal components and 2-10 s bandpass filtered transverse and radial seismograms often produced poor splitting measurements.

In summary, the filtering tests indicated that suitable filtering significantly improves the confidence in phase detection. Although 2-20 s Butterworth bandpass filters are very suitable to remove long period and high frequency noise, such low quality events requiring this degree of filtering were generally not used.

**ii) Window length**

In addition to the influence of filters in splitting analysis, we also checked time windows. A common problem is the choice of shear-wave analysis window because the uncertainties in each splitting measurement are occasionally related to the length of windowing of the phases.

In fact, splitting parameters ($\phi$,$\delta$t) are very sensitive to the choice of shear-wave analysis window. This means that manual selection of the shear-wave analysis window is subjective and can strongly affect the estimated splitting results. To decrease the influence of subjectivity of window selection on the parameters, we need an adequate S/N ratio. Reliable splitting parameters that are stable over a wide range of different window lengths and intervals are obtained from high S/N ratio seismograms. In the context of measuring splitting parameters, a window length should not be shorter than the dominant period of the SKS and SKKS waveforms. Also, the signal/noise ratio on T component and the particle motion should be visually inspected. Here the impact of the length of the time windows was checked by choosing narrow, medium, and wide window lengths (10s (Fig. 4.9), 16s (Fig. 4.10) and 24s (Fig. 4.11)), respectively.

As observed in Fig. 4.11, the wide window selected for splitting analysis usually increases the unwanted signal length so that noise gets into window. It means that the "effective" noise within the window increases. As a result of this, the formal error increases. On the other hand, the narrow window generally decreases the wanted signal length. This results in a lack of all the energy of the phase, and, as a consequence, the determined splitting parameters from the narrow windows become unreliable.

It was found that the determined splitting parameters were very similar as long as the window length was at least as long as the period, but that the size of the error bar varied with window size (see Figs. 4.9, 4.10 and 4.11). We found that the analysis window should begin between ~6 and ~10 seconds before the core phase and end after the phase to check the behaviour of the particle motion to ensure that corrected seismograms had approximately linear particle motion. Generally measurement window lengths of 8-15 s were selected in order to complete the elliptical particle motion of the two split SKS or SKKS phases

In summary, based on the all observations, we suggested that lengths of the measurement windows should be about 8-15 s (they are not absolute) for SKS and SKKS phases because it is hard to complete the elliptical particle motions of SKS and SKKS if their time windows are less than the dominant frequency of SKS and SKKS.

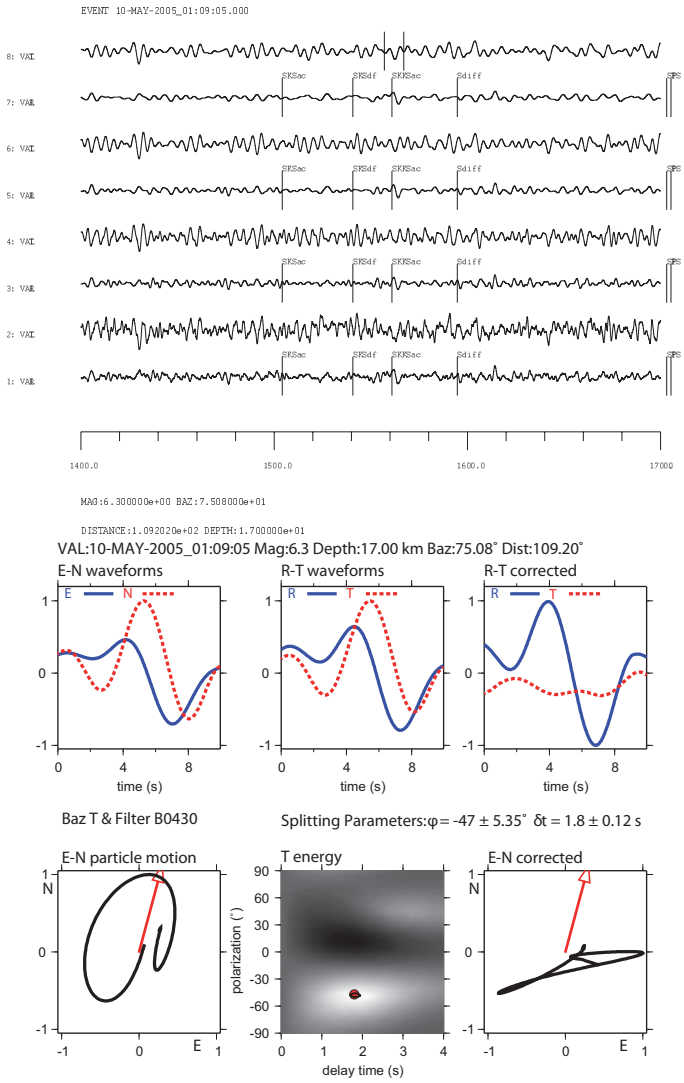



Figure 4.9.: (top) The teleseismic noisy event is tested with a range of window sizes at station VAL. Seismic traces show radial and transverse components after rotating the horizontal components to back-azimuth. Traces 1-2 are unfiltered broadband seismograms. Traces 3-4 are band-pass filtered (2-10 s). Traces 5-6 are band-pass filtered (3-15s). Traces 7-8 are band-pass filtered (4-30 s). The small time window is shown on trace 8 for SKKS phase. The beginning and end time of the measurement window was manually picked. Amplitudes on all seismograms are traced-normalized. (bottom) the result of the small windowing splitting analysis: Upper three figures, are from left to right, (i) the original horizontal components of the SKKS arrivals, (ii) radial and transverse components before splitting correction and (iii) the radial and transverse components after correction. The lower three figures are, from left to right (i) particle motion of the original traces, (ii) contour plot of transverse energy as function of $\phi$, $\delta$t where the red dot shows the minimum, within 95% confidence, indicating the splitting parameters, and (iii) the particle motion diagrams after correction for anisotropy. Red arrows in the particle motion diagram show the direction of event back-azimuth.

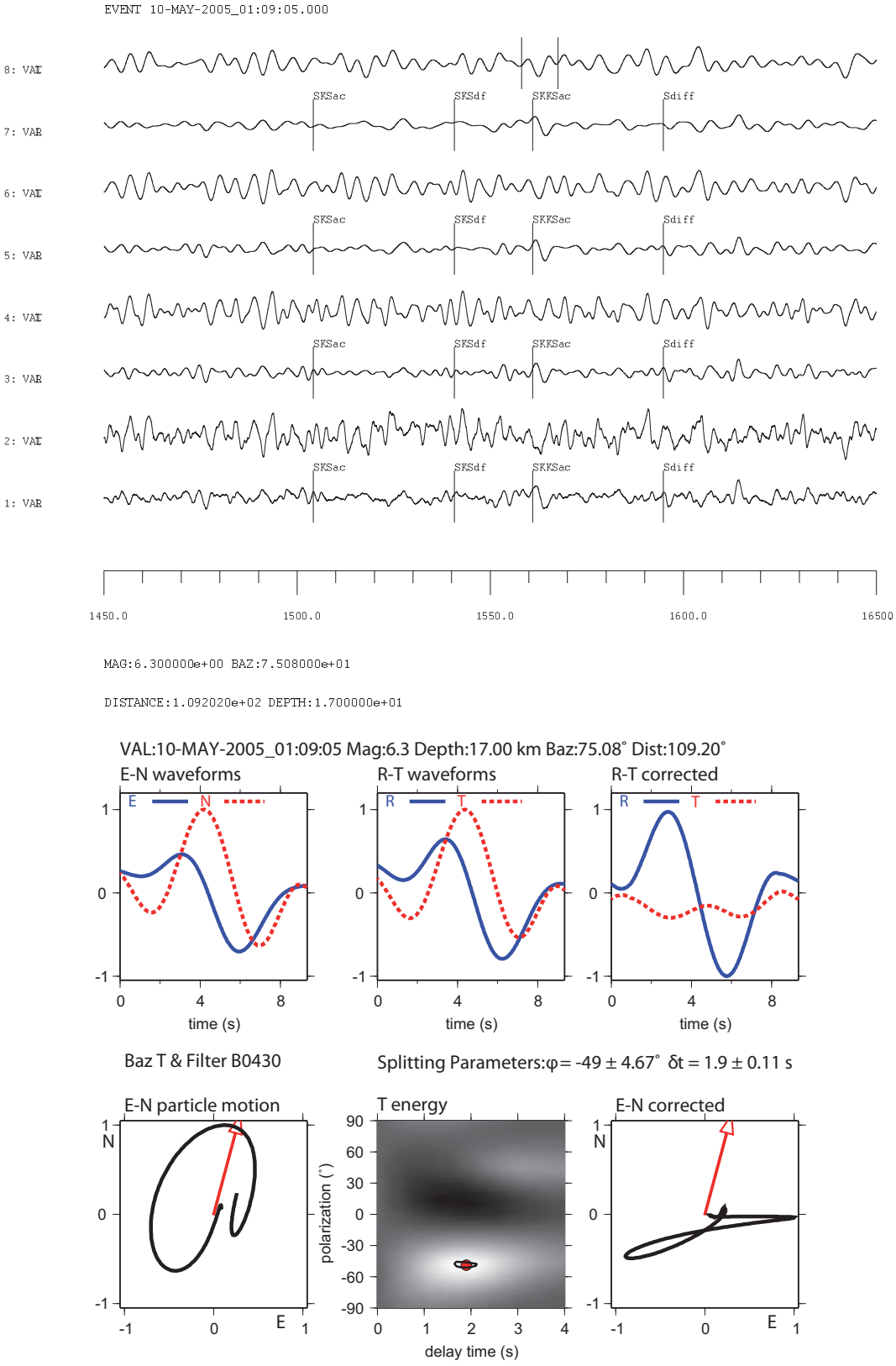



Figure 4.10.: (top) The medium time window is shown on trace 8 for SKKS phase. (bottom) Showing the result of the medium windowing splitting measurement (for further details, see Fig. 4.9).

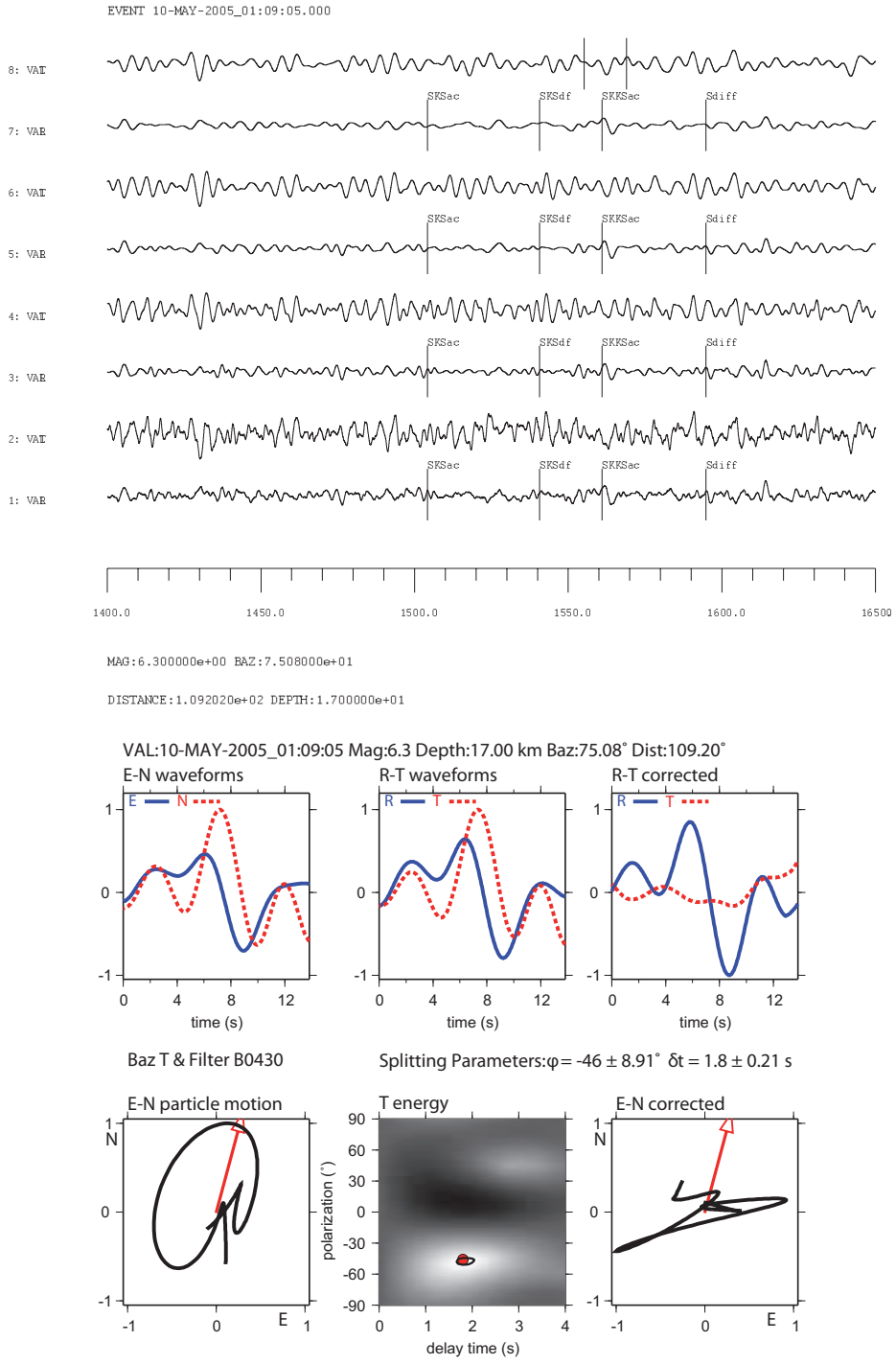



Figure 4.11.: (top) The large time window is shown on trace 8 for SKKS phase. (bottom) Showing the result of the large windowing splitting measurement (for further details, see Fig. 4.9).

**2) Inversion for splitting parameters**

The transverse component minimization method of *Silver and Chan* (1991), described in the subsection 3.4.1 of chapter 3, is the most commonly used to invert SKS/SKKS horizantal seismogram pairs obtained from broadband data and was applied to the dataset of this research. This method utilizes a grid search approach to determine the pair of splitting parameters ($\phi$ and $\delta$t), which best minimizes the amount of energy on the transverse component (equivalently, which best linearizes the corrected particle motion) when the effect of splitting is accounted for. The main principle of this method is that a shear wave is linearly polarized in the absence of anisotropy and that passage through an anisotropic medium will result in significant energy on the transverse component and an elliptical particle motion, which is diagnostic of shear wave splitting.

The method can be applied either to the horizontal components, rotated into a radial (R) and transverse (T) coordinate system (where the so-called radial component corresponds to the backazimuthal direction for core phases or to the initial polarization direction for direct S waves), or to the QT components in a ray-coordinate based LQT coordinate system (*Sileny and Plomerova*, 1996; *Vecsey et al.*, 2008). According to this method, the coordinate systems are equivalent for a perfectly vertical incidence angle.

To determine the splitting parameters, a grid search is performed over all possible values (the parameter space) of $\phi$ and $\delta$t (the interval from $-90^0$ to $90^0$ for $\phi$ and up to a reasonable maximum delay time value, usually ~4 s). The method of *Silver and Chan* (1991) rotates and time-shifts the horizontal components appropriately, and measures the amount of energy on the corrected transverse component, producing a contour plot of transverse component energy for all possible pairs of splitting parameters. The best-fitting parameters thus correspond to the minimum on this contour plot. After correcting the seismogram with the parameters determined by minimizing the energy in the measurement window of the seismogram‘s tangential component, the determined splitting parameters are then checked by analyzing the particle motion since elliptical particle motions are indicative of shear wave splitting. Formal errors on the measurements

are estimated using an F test formulation described by *Silver and Chan* (1991). For each set of possible parameters, the test is performed in order to determine whether or not the splitting parameters are within the bounds of a 95% confidence region.

**3) Quality control and error estimation**

A high S/N ratio is required in both the radial and transverse components to obtain high quality splitting measurements. Seismograms were visually checked in order to discard low-quality SKS/SKKS traces. Another requirement is that SKS energy in the transverse components should be visible before splitting correction and should be sufficiently removed after determining the optimal parameters. This is ensured by analysing the particle motion of the used phase because elliptical particle motions are indicative of shear wave splitting.

The estimated formal error values using the inverse F test (*Silver and Chan*, 1991) are also calculated for each splitting pair because the quality of splitting measurements also depends on these error values. This test is based on an assumption that the root mean square (rms) amplitude for an n-point discrete time series behaves as a $X^2$ with the number of degrees of freedom equal to approximately one degree of freedom per second. Therefore, in this study the error analysis is carefully performed to analyze errors in the inversion by determining a confidence region for fast direction and lag time.

Following the above criteria, the final results were classified into four categories, namely high, medium, poor and null as follows:

**a) High quality**

For a high quality measurement, energy on both radial and transverse original waveforms should be clearly visible. Before and after splitting corrections, particle motions should be strongly elliptical and linear, respectively. In addition, contour plots of the transverse component energy should have a small region of minimum energy and 95% confidence level must be small, i.e. $\leq 2^0$ for $\sigma_\phi$ and 0.1 s for $\sigma_{\delta t}$. Fig. 4.12 shows an example of a high quality measurement.

**b) Medium quality**

Measurements in this category approach those of high quality, but with lower S/N on the radial and transverse components. Formal error in splitting parameter measurements should be small $\leq 7^0$ and $\leq$ 0.1 s. Fig. 4.13 indicates an example of a medium quality measurement.

**c) Low quality**

Low quality measurements are defined by: 1) signal to noise ratio is lower than 5, but should be more than 2 to see anisotropic energy on raw radial and transverse components, 2) original particle motion is weakly elliptical, 3) the particle motion of the corrected waveforms are only partly linear, 4) formal error in $\phi$ is $\pm$ $7^0$-$10^0$ and in $\delta$t is greater than $\pm$0.1 s. For low quality measurements, visual inspection is given more importance than the formal error. For example in Fig. 4.14, the formal errors in the splitting parameters are very low. But elliptical particle motion of the original SKS phase and linear particle motion of the corrected seismograms are very poor, so it is evaluated as a poor quality measurement.

**d) Null measurements**

There are two reasons for null measurements; (i) very weak anisotropy or no anisotropy along the path traversed by the shear wave, or (ii) the initial polarization of the phase is nearly parallel to either the fast or slow direction of symmetry of the anisotropic medium. In these cases the incoming shear wave is not split (*Savage*, 1999). It is therefore significant to identify such so-called Null measurements. Null measurements are usually treated separately (*Silver and Chan*, 1991; *Barruol et al.*, 1997; *Currie et al.*, 2004) or even neglected in shear-wave splitting studies. Nulls do not constrain the delay time and the estimated fast axis corresponds either to the (real) fast or slow axis. In the absence of anisotropy the estimated fast axis simply reflects the initial polarization, which for SKS/SKKS waves usually corresponds to the backazimuth. Fig. 4.15 indicates an example of a high quality null measurement.

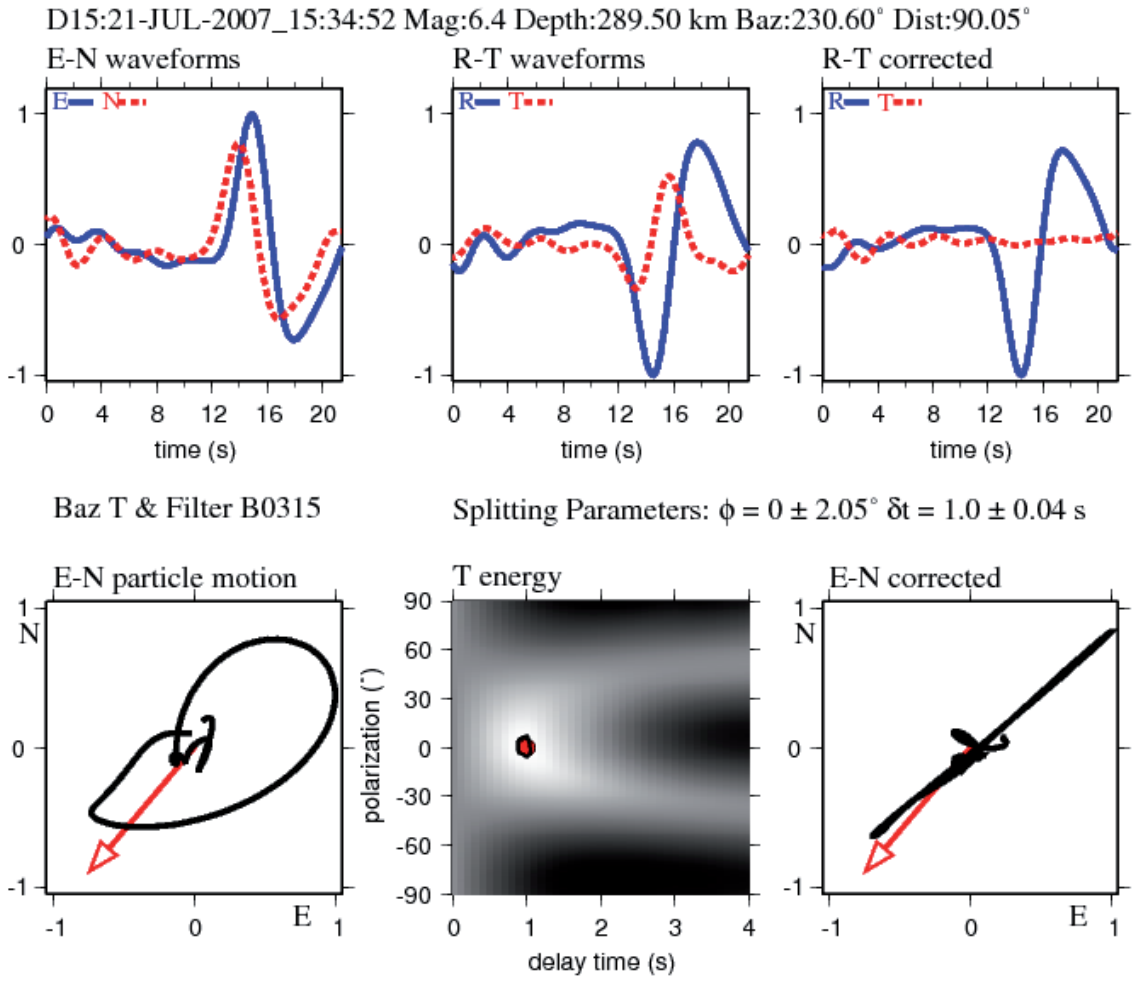



Figure 4.12.: A high quality shear wave splitting measurement. Upper three figures from left to right show (i) the original NS and EW components of the SKKS arrivals, (ii) radial and transverse components (the components are obtained from the horizontal components by rotation to the BAZ direction) before splitting correction and (iii) the radial and transverse components after correction. The lower part of the figure from the left to the right indicates (i) particle motion of the original horizontal components, (ii) contour plot of transverse energy as function of the fast polarization direction $\phi$ and the time delay $\delta$t, where the red dot shows the minimum energy with respect to within 95% confidence, and (iii) the particle motion diagram after the applied correction for seismic anisotropy to the horizontal components. Red arrows in the particle motion diagrams indicate the direction of back-azimuth.

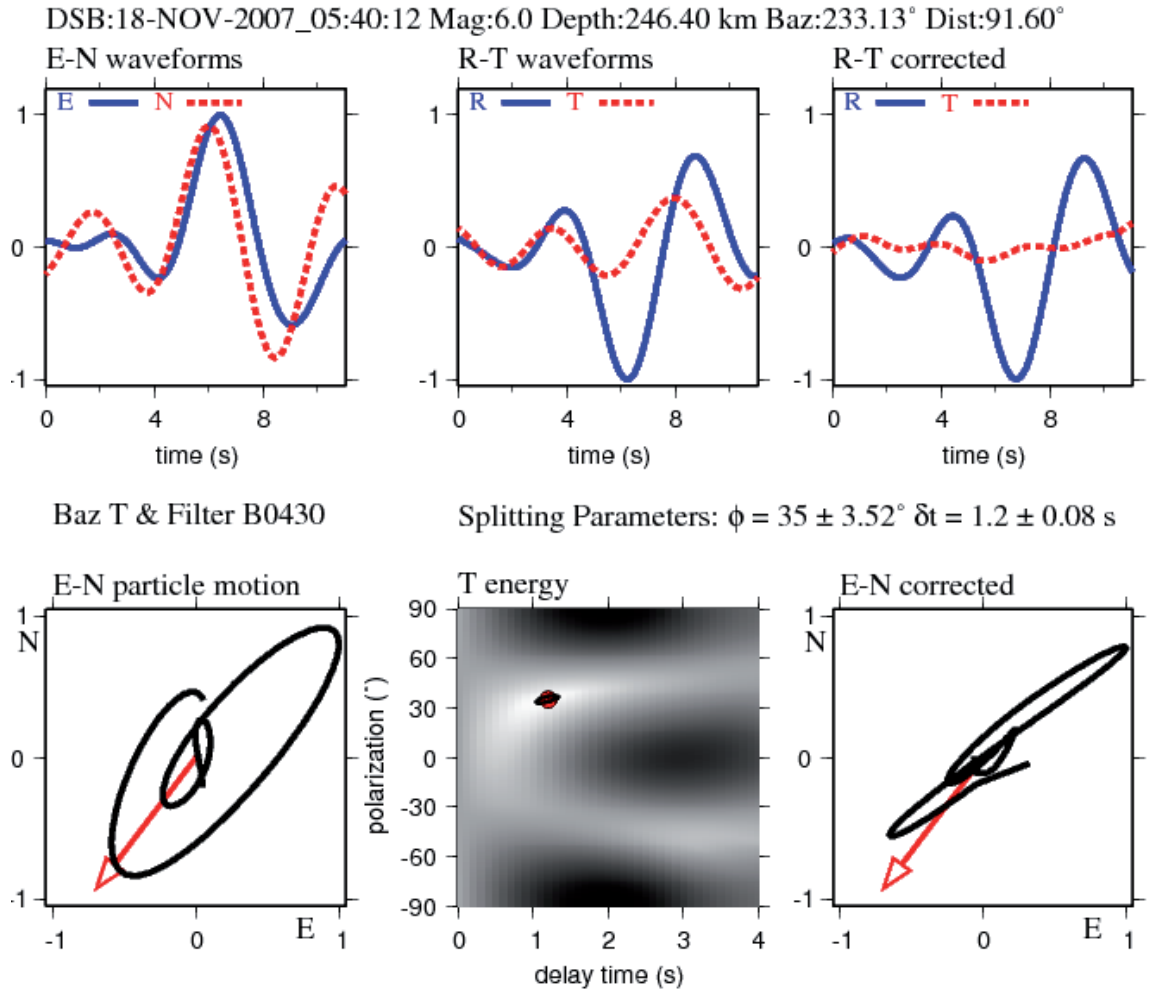



Figure 4.13.: An example of a medium quality shear wave splitting measurement (see Fig. 4.12 for explanations).

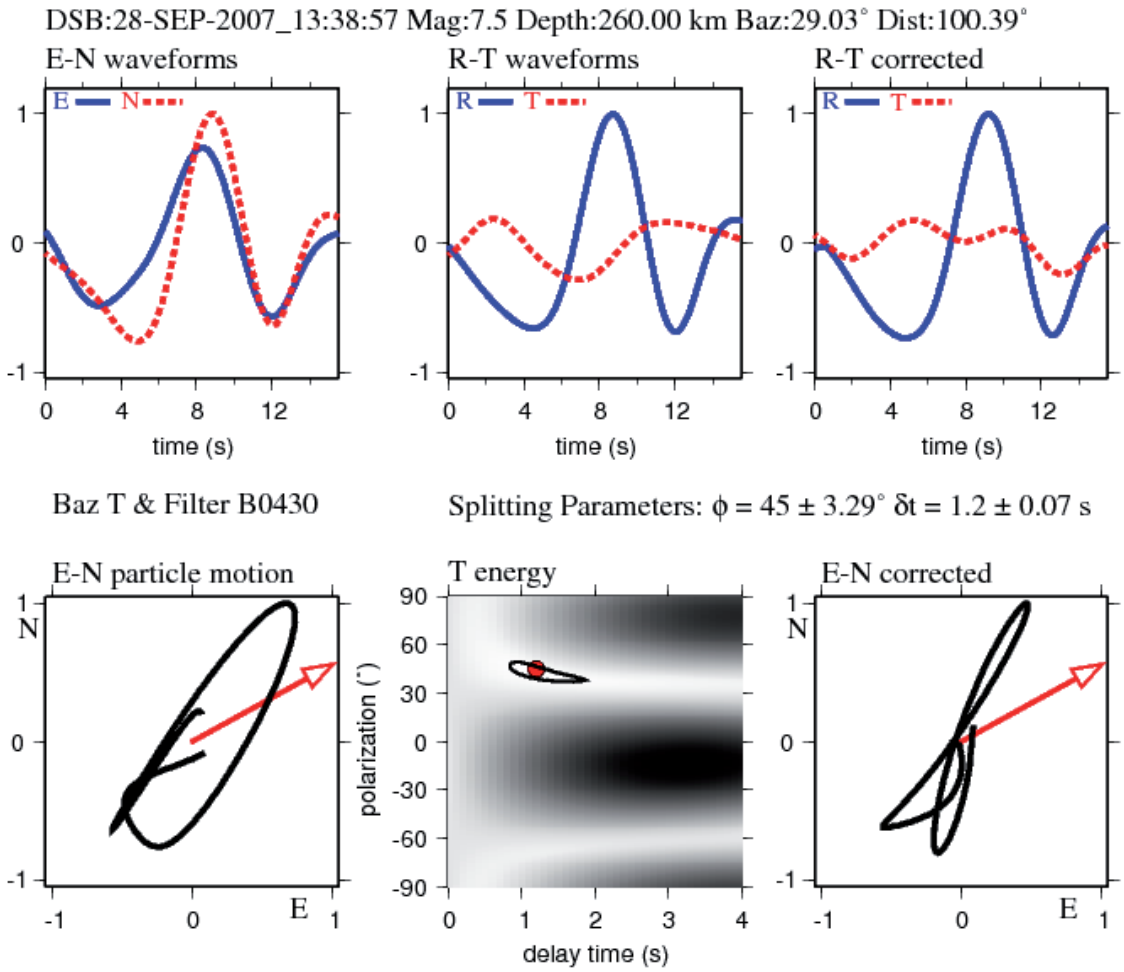



Figure 4.14.: An example of a low quality shear wave splitting measurement (see Fig. 4.12 for explanations).

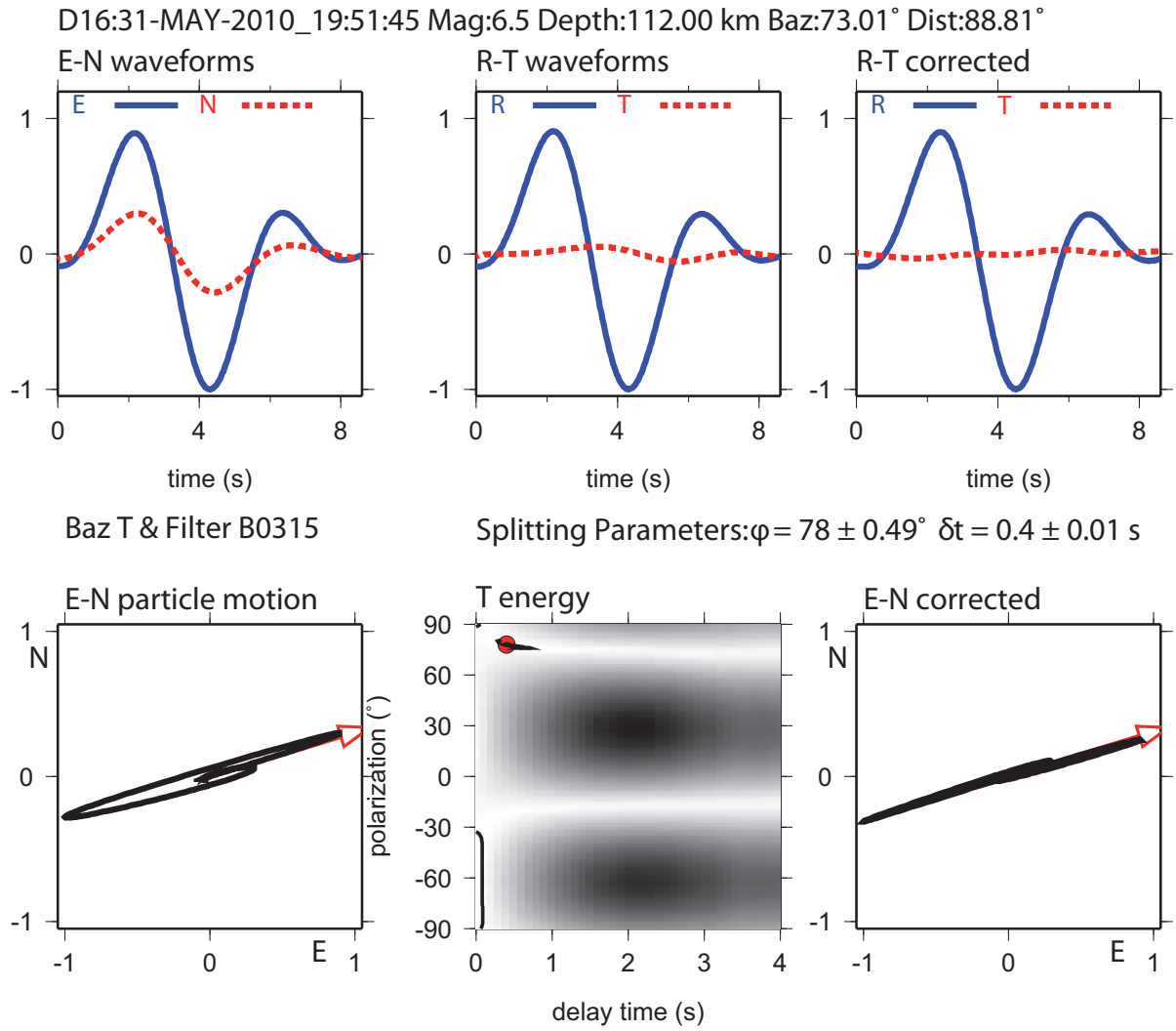



Figure 4.15.: An example of a high quality null shear wave splitting measurement (see Fig. 4.12 for explanations).

## 4.2. Shear-wave splitting results

### 4.2.1. General results

Initially 1132 teleseismic earthquakes were selected from 2006 to 2011 for the shear-wave splitting analysis (Fig. 4.4) of which 20% provided well constrained shear wave splitting parameters (Fig. 4.16). Many events were discarded due to low S/N ratio. Additionally, a total of 58 events from 2003 to 2006 were remeasured from the event catalog of *Do et al.* (2006). In this study, a total of 1190 events was therefore selected for the splitting analysis. The final events used are shown in Fig. 4.16. Also, this figure indicates histograms of back-azimuth (baz), distance, depth and magnitude.

It is found that there were two major event clusters: from East Asia ($\phi_{baz}$~0-90$^0$) and from South America ($\phi_{baz}$~180-270$^0$) (see the top of the Fig. 4.16). The results categorized with respect to quality and phase parameters, respectively are shown in Fig. 4.17.

A total of 98 high, 111 medium, 83 low quality and 144 null measurements have been obtained, among which 287 are SKS and 150 SKKS measurements (Fig. 4.17) (see Appendix D for complete listing of results). The results for the EA and SA event clusters are shown in Fig. 4.18. This figure clearly shows that nearly all the stations produced a considerable number of splitting measurements. Additionally, a minority of the events have a back azimuth in the range of 90-180$^0$ and 270-360$^0$ (Fig. 4.19) (see Appendix D for further details).

For the EA cluster, there were 183 and 105 individual SKS and SKKS splitting measurements (Fig. 4.20) and for the SA cluster, 103 and 39 individual SKS and SKKS splitting measurements (Fig. 4.21).

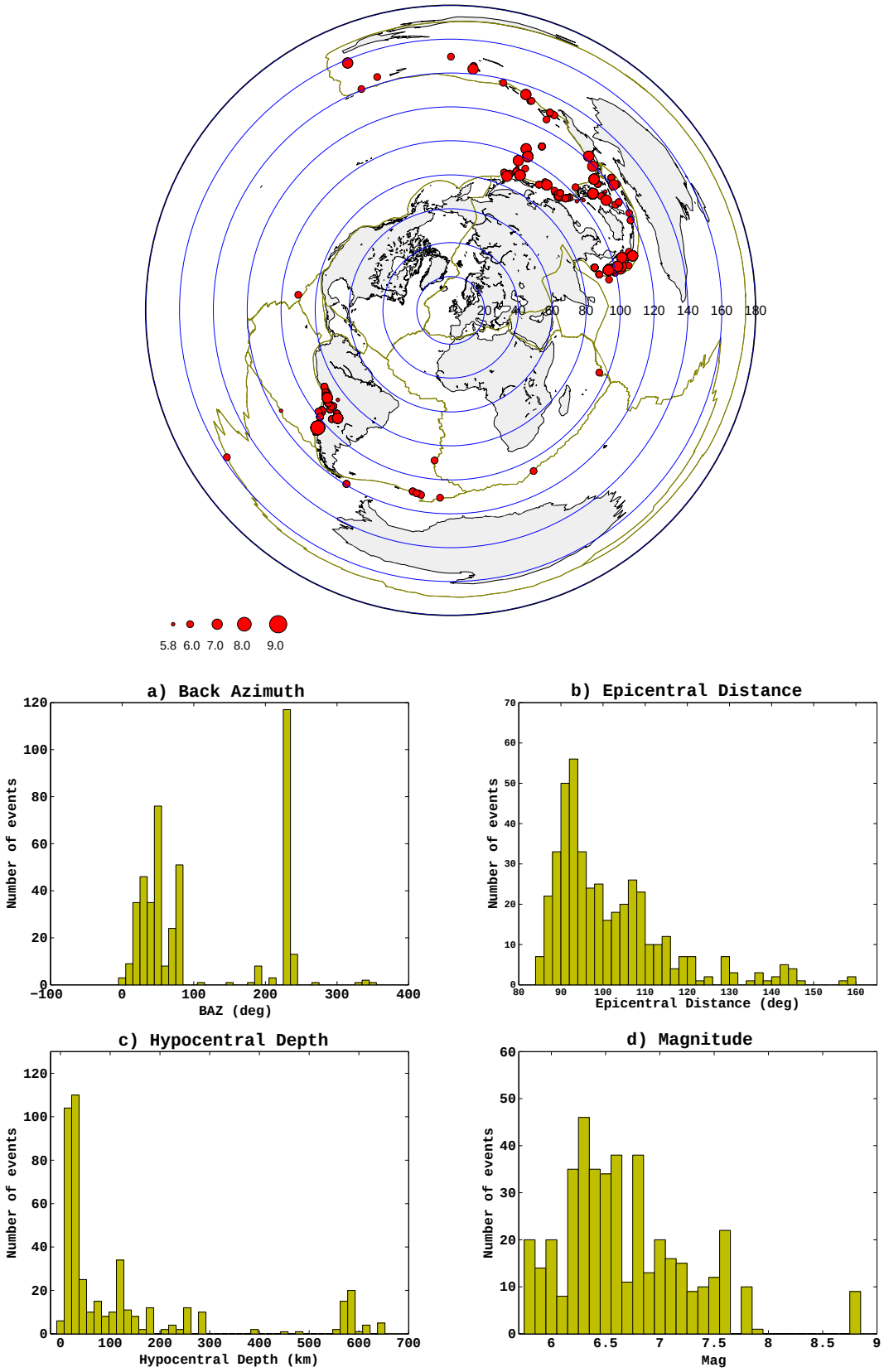



Figure 4.16.: (top) Global distribution and (bottom) histograms of the final selected shear-wave splitting events recorded by permanent and temporary stations deployed in Ireland from 01/01/2003 to 31/09/2011.

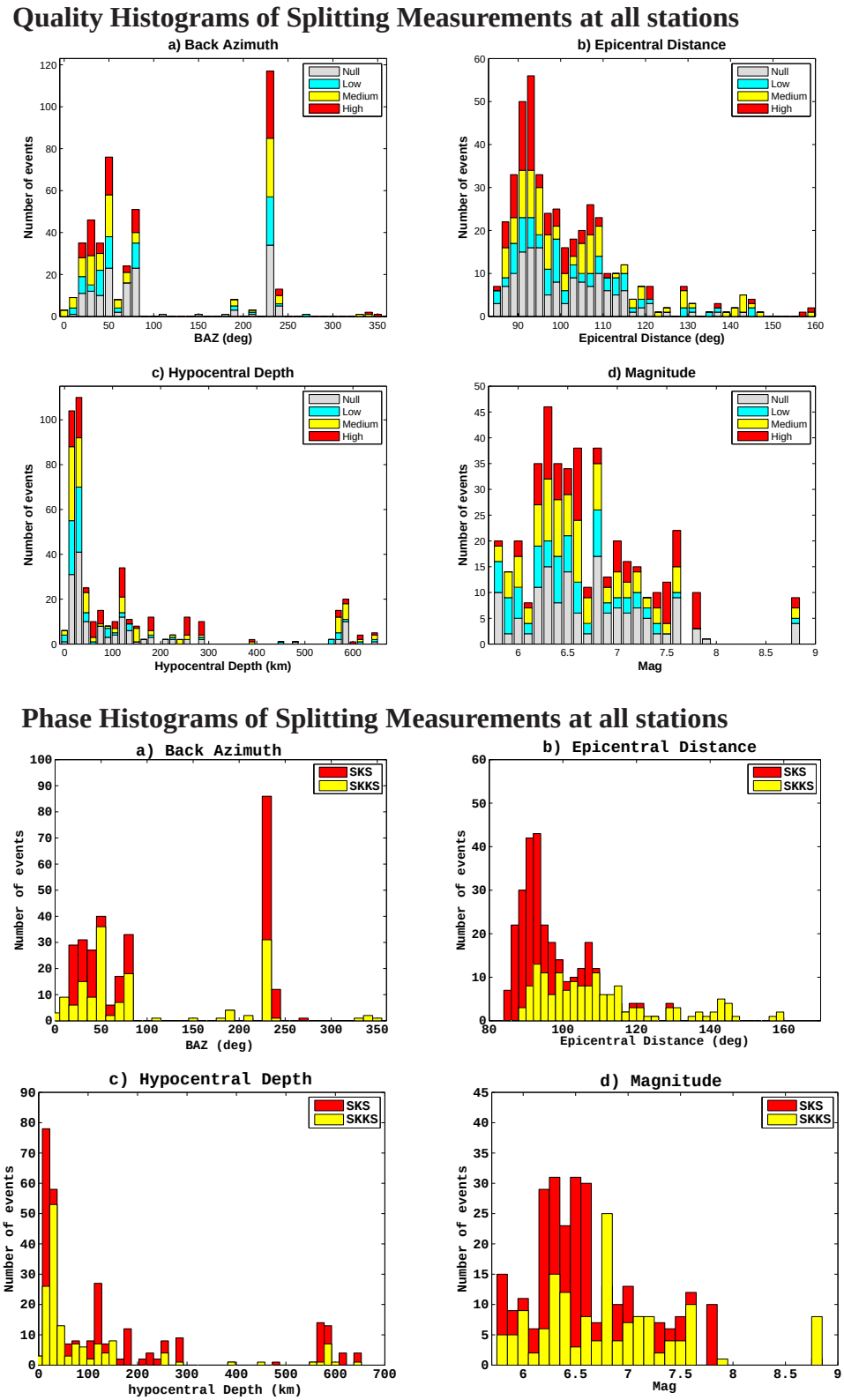



Figure 4.17.: Quality (top) and Phase (bottom) histograms of splitting measurements at all stations: (a) $\phi_{baz}$, bin size = $10^0$; (b) $\Delta$, bin size = $2.0^0$ ; c) event depths, bin size = 15 km; and d) event magnitudes, bin size = 0.1. Null, low, medium, high quality, SKS and SKKS measurements are color-coded, as indicated by the legend at up right.

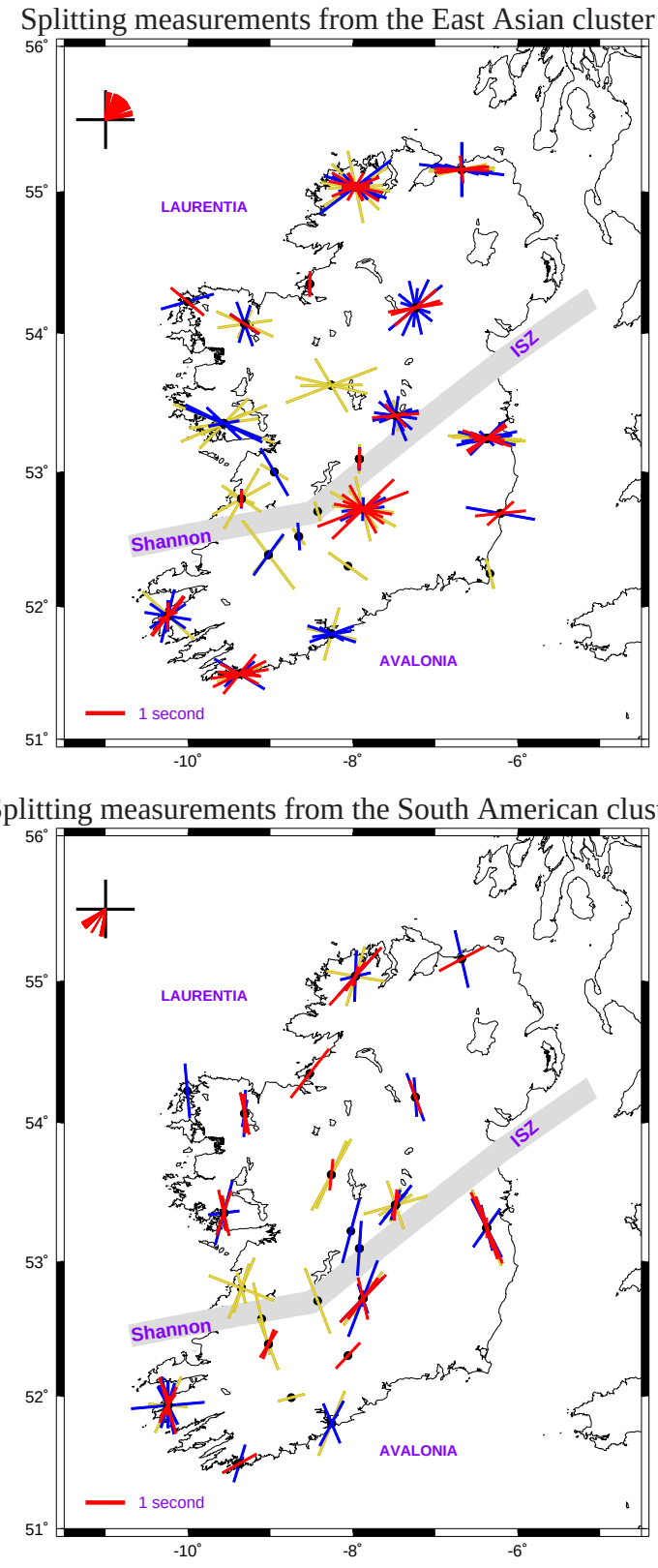



Figure 4.18.: Summary of individual shear-wave splitting measurements from the EA (top) and the SA (bottom) event clusters. Bars indicate fast polarization directions ($\phi$) and delay time ($\delta$t). The length of bars is proportional to $\delta$t. Red, blue and yellow filled bars indicate high, medium and low quality measurements respectively. Arrows in top corners show event back azimuths.

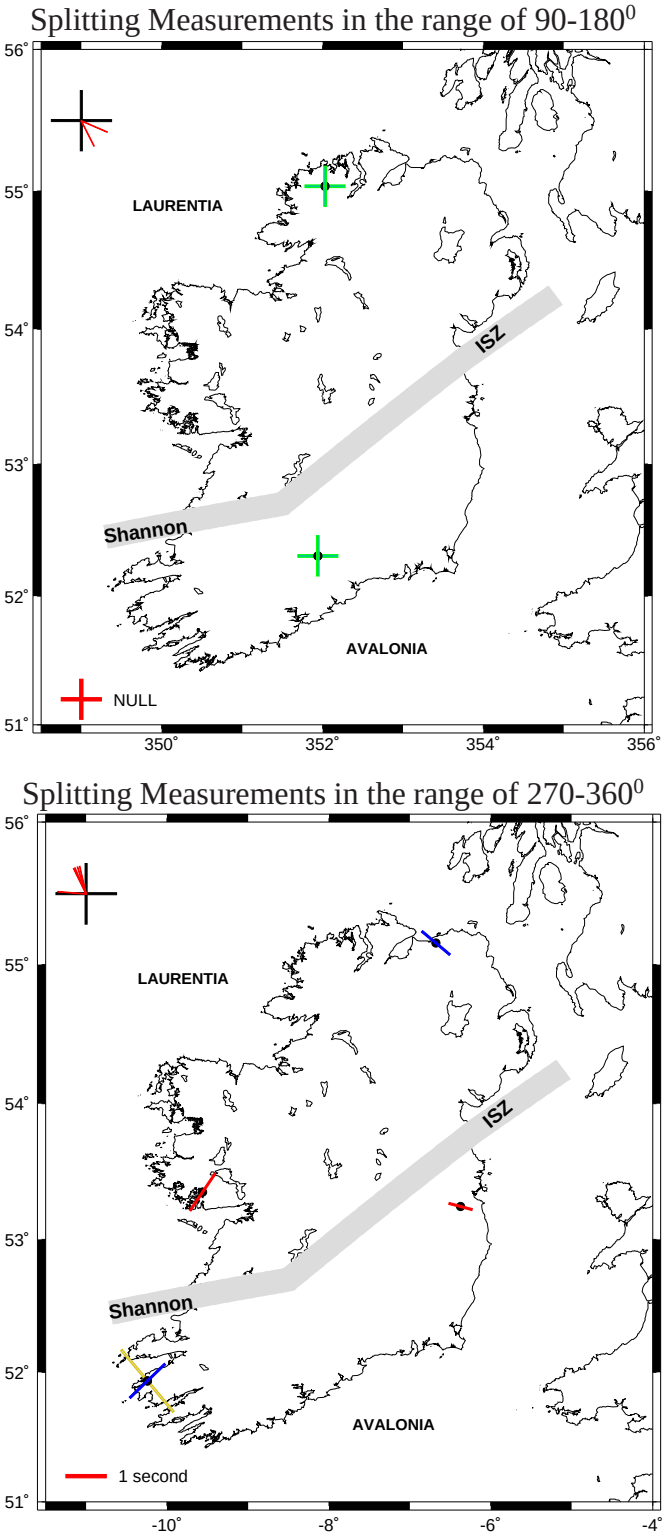



Figure 4.19.: Shear wave splitting measurements from events with back azimuths in the range of 90-180$^0$ (top) and 270-360$^0$ (bottom) respectively. Bars indicate fast polarization directions ($\phi$) and delay time ($\delta$t). (top) Green filled bars show null measurements. (bottom) Red, blue and yellow filled bars indicate high, medium and low quality measurements, respectively. Arrows in top corners show event back azimuths.

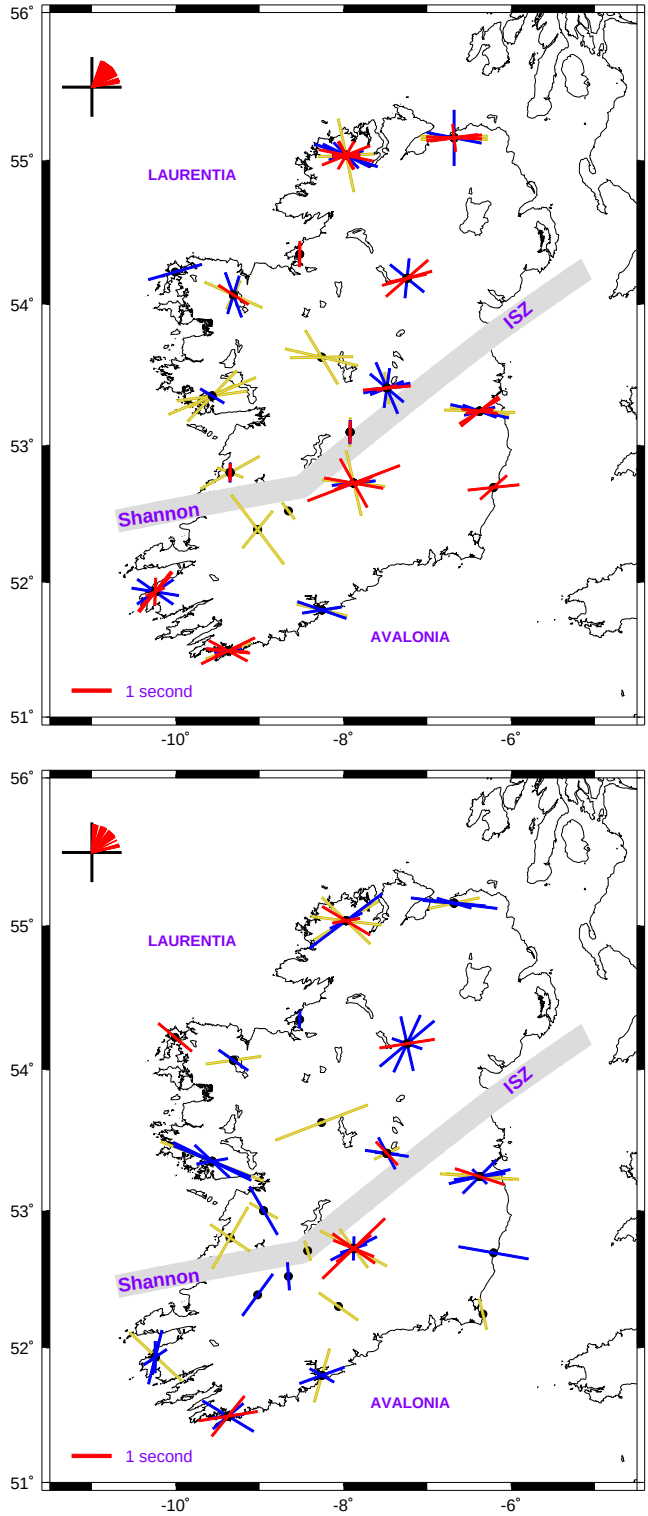



Figure 4.20.: Summary of individual SKS (top) and SKKS (bottom) shear-wave splitting measurements from the EA event cluster. Bars indicate fast polarization directions ($\phi$) and delay time ($\delta$t). The length of bars is proportional to $\delta$t. Red, blue and yellow filled bars indicate high, medium and low quality measurements, respectively. Arrows in top corners show event back azimuths.

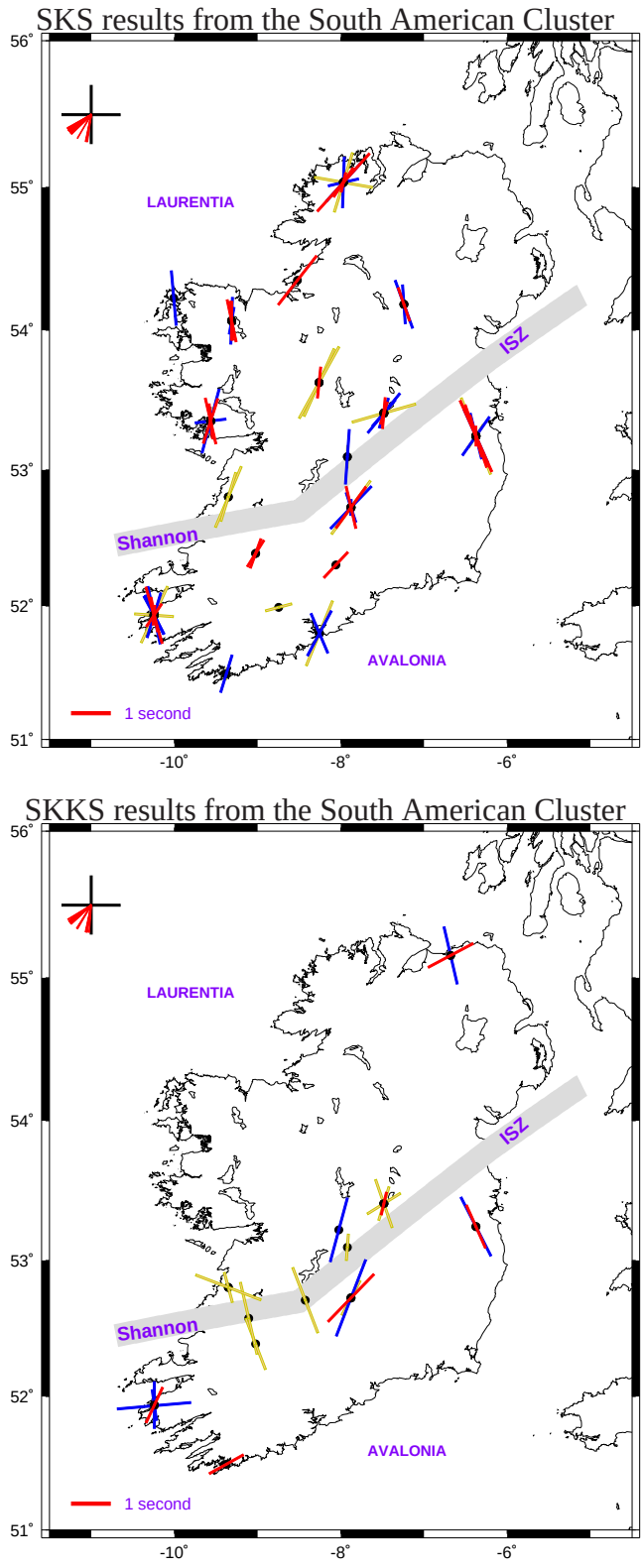



Figure 4.21.: Summary of individual SKS (top) and SKKS (bottom) shear-wave splitting measurements from the SA event cluster. Bars indicate fast polarization directions ($\phi$) and delay time ($\delta$t). The length of bars is proportional to $\delta$t. Red, blue and yellow filled bars indicate high, medium and low quality measurements, respectively. Arrows in top corners show event back azimuths.

In general, it has been observed that there was very strong variation in the fast polarization directions with back-azimuth. The splitting parameters (Appendix D) at each station are averaged in order to find an overall resultant. Under assumption of a single anisotropic layer with a hexagonal symmetry and a horizontally oriented fast axis (i.e. consistent with horizontal flow), theory predicts no azimuthal variations in the measured splitting parameters for near-vertical incidence. However, in our case it is clearly observed that the assumptions may be not valid because the splitting parameters strongly change with back-azimuth. In general such cases are explained with multiple or dipping layers of anisotropy (*Silver and Savage*, 1994; *Mainprice and Silver*, 1993). Here the suggested possible mechanisms are not considered, but they will be presented in chapter 7.

**A) Averaged SKS and SKKS results**

Firstly averaged splitting results calculated from SKS and SKKS splitting measurements from the EA and SA event clusters were calculated (Fig. 4.22) (see Appendix F) (see Appendix G for details on the calculation method).

Uniform fast polarization directions are not observed over all Ireland (Fig. 4.22). In particular, in central Ireland, the fast polarization directions strongly exhibit a scattering pattern. Nevertheless, in southern, eastern and northern Ireland fast polarizatin directions show the E-W pattern (Fig. 4.22). Meanwhile, a consistent N-S trend of $\phi$, similar to splitting results obtained from South American event cluster, is observed at stations IA002, D21, IAVAL and D08 (Fig. 4.22). It may suggest that at these stations, the number of South American events used in the averaging process is less than 50% of the total number events. This probably reflects the weak N-S trend of $\phi$ observed in Fig. 4.22.

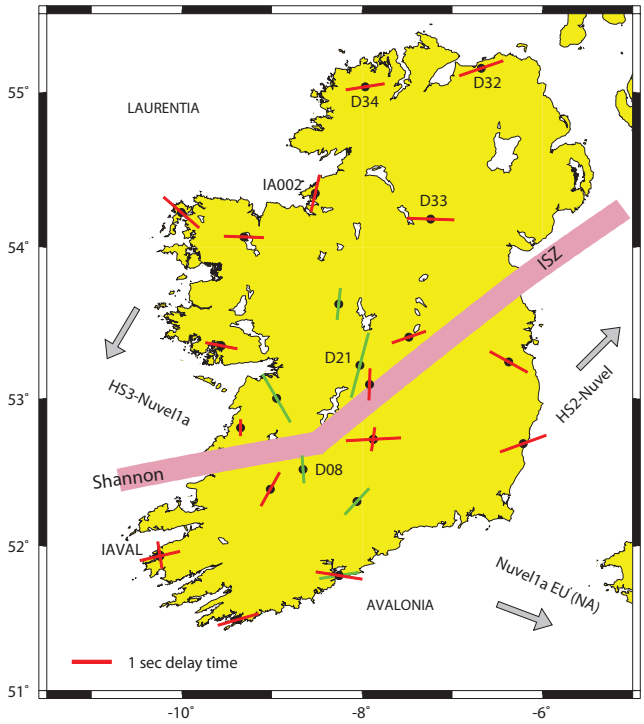



Figure 4.22.: Summary of the averaged splitting parameters from high and medium quality (SKS and SKKS) measurements from the East Asian and South American clusters at all Irish stations used in this study. Bars indicate fast polarisation directions with length proportional to delay times. Each red bar represents an average measurement (if there is more than one measurement). Single measurements (if there is only one measurement per station) are plotted as green bars.

**B) Averaged SKS results from the EA and SA clusters**

Then SKS and SKKS splitting measurements were separately evaluated. Although the calculation of mean values may be misleading, we still think it is useful to calculate these averages in order to get a first-order estimate on anisotropy. To calculate mean values, only high and medium quality splitting measurements are used. The averaged values of the SKS and SKKS splitting parameters are given in Appendix F and displayed in Figs. 4.23 and 4.24. The general pattern of anisotropy determined from SKS and SKKS splitting parameters is relatively homogeneous over all Ireland for each cluster (Figs. 4.23 and 4.24).

**i) The averaged SKS splitting parameters from the EA event cluster**

The averaged SKS splitting parameters from the EA event cluster show that fast polarization directions ($\phi$) are predominantly E-W (within $\pm 35^0$) with average delay times ($\delta$t) of about 1 s

(Fig. 4.23). In central Ireland, however, there is more scatter in the fast polarization directions and a few stations near to the ISZ show primarily N-S orientations with much smaller lag times. This suggests that there are spatial variations in splitting parameters. Variations over short length scales are often interpreted as being due to lateral heterogeneity in shallow anisotropy (*Long and Silver*, 2009). There are particularly striking examples have been documented in studies by *Fouch et al.* (2004) for the Kaapvaal Craton and by *Mattatall and Fouch* (2007) for the San Andreas Fault near Parkfield. *Mattatall and Fouch* (2007) found splitting variations over distances of just a few km and interpreted them as being due to anisotropy in the shallow crust. They further argued that such extreme small-scale variations indicate a larger contribution to broadband splitting measurements from the crust than is usually accounted for.

*Bastow et al.* (2007) suggested that rapid spatial variations in $\phi$ and $\delta$t found in Scotland indicate significant contributions by crustal anisotropic layers. According to these arguments, crustal anisotropy caused by the effect of transpressional deformation during the closure of the Iapetus Ocean (*Dewey and Mange*, 1999; *Helffrich*, 1995) presumably causes the spatial variations in $\delta$t and $\phi$. Additionally, the observed spatial variations are also incoherent within the main tectonic units such as the ISZ.

One of the most significant results of this study is the presence of fault/suture-parallel fast directions. Stations D23, D32, D33, D34, D36, D37, DSB and VAL, located close to the ISZ, display significantly fault/suture-parallel anisotropy. Thus, it can be confirmed that there is an important correspondence between structural trends such as the ISZ and anisotropy in the lithospheric mantle. Additionally, the average fast polarization directions from the EA event cluster are reasonably consistent with those of *Do et al.* (2006) (see the top part of Fig. 2.10) and the earlier work of *Helffrich* (1995) recorded by permanent stations in Ireland and the UK, respectively (Fig. 3.25). If we assume 4% anisotropy and an average shear velocity of 4.7 km/s for the entire lithosphere, then it suggests that the fault/suture-parallel anisotropy may extend from the surface to ~120 km.

In summary, the average SKS fast polarization directions obtained from the EA event clus-

ter are more closely aligned with the ISZ related to the Caledonian deformation, suggesting a stronger correlation with "frozen" deformation in the lithosphere to depths of 120 km. On the other hand, the spatial variations of the fast directions in central Ireland suggest that there are significant lateral anisotropy variations within the crust.

**ii) The averaged SKS splitting parameters from the SA event cluster**

The average SKS fast polarization directions from the SA event cluster exhibit nearly N-S orientations (about 10-20$^0$) and are fairly consistent over the whole country (Fig. 4.23). As shown in Fig. 4.23, the average delay time for this cluster is slightly more than 1.0 s. Surprisingly, no abrupt changes in anisotropy directions are observed across the tectonic units. Results from all stations for this cluster show no fault/suture-parallel anisotropy. The lack of fault/suture-parallel anisotropy at these stations confirmed that a simple one-layer anisotropy with horizontal symmetry axis aligned with the dominant Caledonian deformation trend is insufficient to explain the approximately N-S fast axis orientations. Although there is no correlation between fast polarization directions from this cluster and tectonic units in the study area, it has been observed that the N-S orietations of splitting parameters are consistent with LPO of olivine calculated from the 3-D flow model at a depth of 175 km for the North Atlantic region on the regional scale (*Marquart et al.*, 2007) (see Fig. 7.2).

As a consequence, it is not possible to interpret $\delta$t obtained from the South American cluster based only on the same values of lithospheric thickness and anisotropy as for the East Asian cluster. Thus, we suggest that additional methods are required to explain the N-S anisotropic pattern obtained from the SA event cluster. These will be discussed in the last chapter.

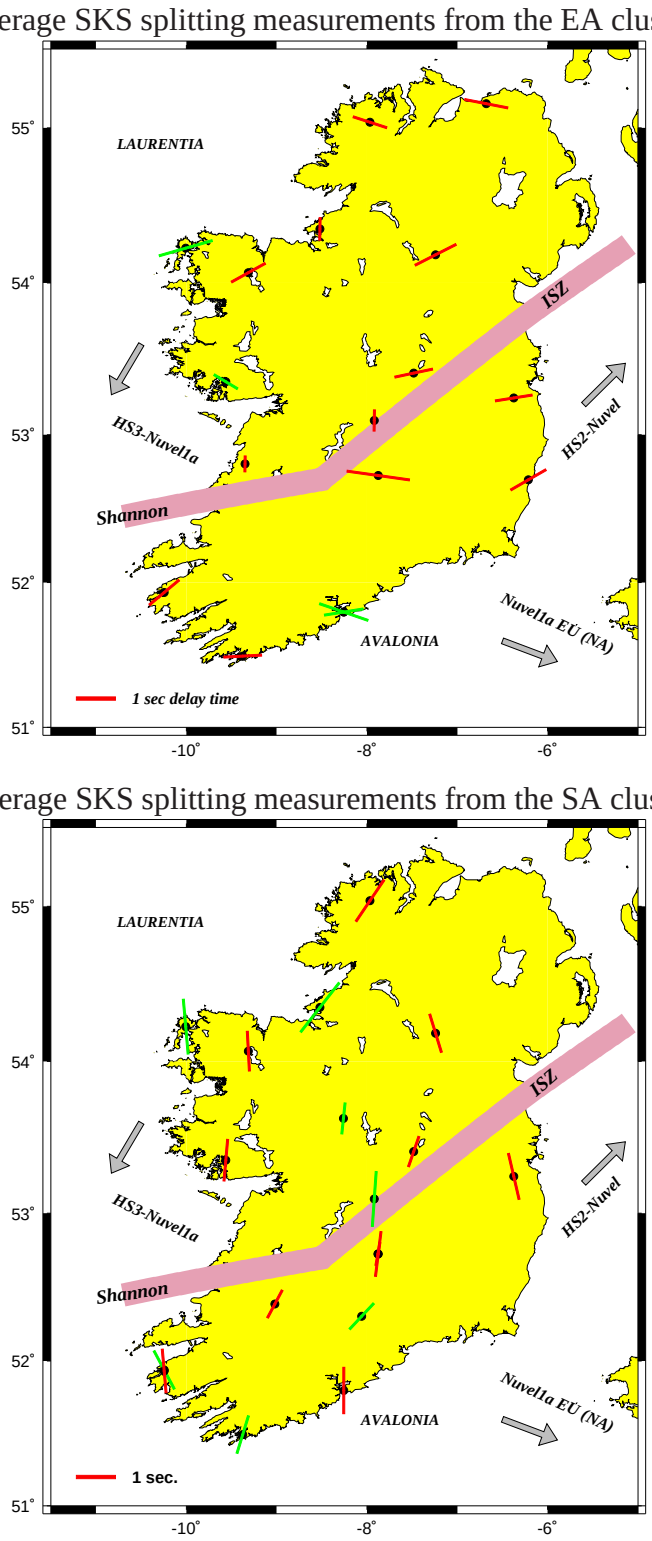
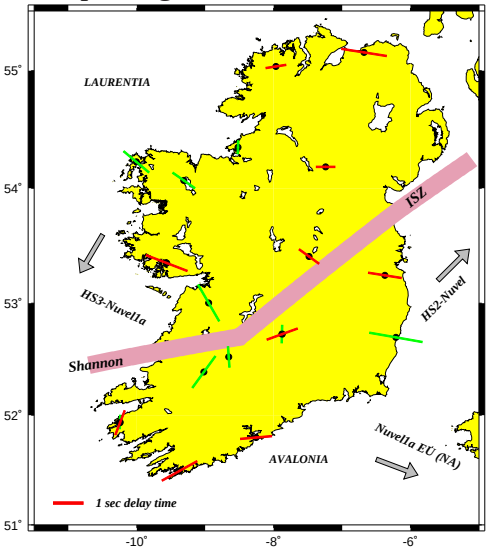



Figure 4.23.: Averaged fast directions and delay times from SKS measurements from the main clusters. The length of bars is proportional to $\delta$t. Each red bar represents a weighted average measurement (if there is more than one measurement). Single measurements (if there is only one measurement per station) are plotted as green bars.

**B) Averaged SKKS results from the EA and SA event clusters**

The average SKKS splitting parameters mapped in Fig. 4.24 suggest that average SKKS parameters from the EA cluster vary over Ireland. However, this may be because there is only one high or medium quality measurement at a few stations located in central Ireland, near to the ISZ (see Fig. 4.20).

Average SKKS splitting measurements from the EA cluster




Average SKKS splitting measurements from the SA cluster

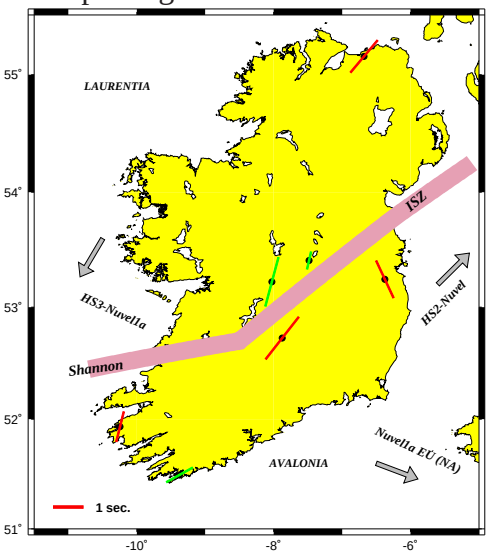



Figure 4.24.: Averaged fast directions and delay times from SKKS measurements from the main clusters. The length of bars is proportional to $\delta$t. Each red bar represents a weighted average measurement (if there is more than one measurement). Single measurements (if there is only one measurement per station) are plotted as green bars.

If single measurements are discarded (green bars in Fig. 4.24), we observe that the average SKKS fast polarization directions become fairly consistent with the average SKS fast-axis orientations (Fig. 4.23). Although the number of average SKKS splitting measurements from the SA event cluster is not large and also some stations have only single measurements, the averaged SKKS fast orientations are consistent with the averaged SKS fast polarization directions (Figs. 4.23 and 4.24).

**C) Summary of results**

The results are briefly summarized as follows:

(1) The majority of measurements are obtained from the EA and SA event clusters (Appendix D).

(2) The number of SKS measurements from the EA and SA clusters is larger than the number of SKKS measurements. Figs. 4.20 and 4.21 also show that the range of BAZ directions from the East Asia event cluster is larger and more scattered than the South America event cluster.

(3) A strong scatter in the SKS and SKKS splitting parameters from the EA cluster is observed and the observed delay times range from 0.4 to 2.5 s (Fig. 4.20). In contrast, it was observed that the fast polarization directions of the SKS phase measurements from the SA cluster are relatively uniform and the observed delay times range from 0.7 to 2.0 s (Fig. 4.21).

(4) The measurement of the fast direction and delay times for the EA and the SA cluster has commonly errors of about $\pm 3^0$ and less than $\pm$ 0.1 seconds, respectively (two standard deviations) (Appendix D). To make the final results robust, fast directions with errors higher than $10^0$ or delay times with errors higher than 0.1 seconds have been discarded. This means that such measurements have not been included in any of the figures.

(5) Fig. 4.17 indicates that a major number of high and medium quality measurements are within the back azimuth range from 200 to $240^0$. The low quality splitting measurements are observed outside this range (Fig. 4.17).

(6) A strong scattering in splitting parameters has been determined from the EA event cluster, in contrast to the SA event cluster (Fig. 4.18). However, there is still a noticeable scatter in the

splitting parameters from the SA event cluster.

In order to explain the scatter in the results these ways have been tried as follows:

(a) Individual SKS and SKKS shear-wave splitting measurements from the EA and SA event clusters were separately plotted (Figs. 4.20 and 4.21).

(b) High quality SKS and SKKS parameters only were plotted (Fig. 4.25). In particular, the high quality measurements from the SA event cluster are less scattered and show that the fast polarization directions are relatively uniform with lag times of ~1.0 s. They exhibit primarily N-S orientations. As shown in Fig. 4.25, all high quality measurements from this cluster are within the back azimuth range 220-250$^0$. This observation potentially provides sufficient evidence to explain uniformity in splitting parameters within the narrow back-azimuthal range. However, splitting parameters from the EA cluster suggest that that splitting parameters are very sensitive to variations in back-azimuth (see Fig. 4.26) possibly caused by complex anisotropy including lower mantle anisotropy.

(7) In Fig. 4.23, averaged splitting parameters calculated from high and medium quality measurements are very consistent with the well defined high quality measurements shown in Fig. 4.25.

(8) The backazimuth variations of the splitting parameters are observed at all the stations used in this study (Fig. 4.1). In general, backazimuthal variations in apparent splitting parameters are caused by more complex geometries such as two layers of anisotropy (*Silver and Savage*, 1994) and dipping layers (*Brechner et al.*, 1998). The characteristics of the backazimuthal plots can thus provide evidence, if any, of the presence of several anisotropic layers beneath each station.

(9) Interestingly, no significant difference in delay time measured from the EA and the SA event clusters is observed. However, the measured fast directions from the two clusters are completely different from each other, suggesting that the anisotropy beneath Ireland is complicated.

As seen above, interpretation of shear wave splitting is not easy. Therefore, in the last chapter possible approaches are suggested for understanding the observed complex splitting patterns found in this study.

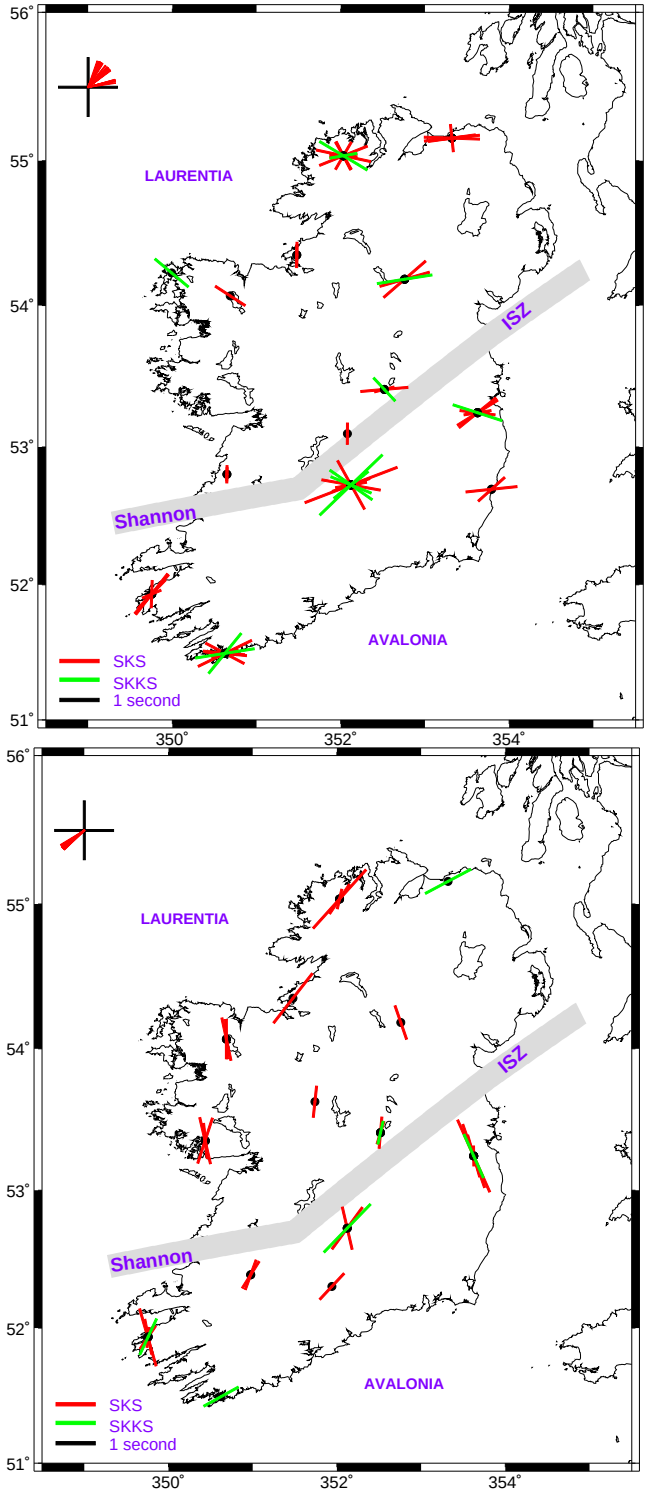



Figure 4.25.: Summary of individual SKS (red bars) and SKKS (green bars) high quality shear-wave splitting measurements from the EA (top) and the SA (bottom) event clusters. Bars indicate fast polarization directions ($\phi$) and delay time ($\delta$t). The length of bars is proportional to $\delta$t. Arrows in top corners show event back azimuths.

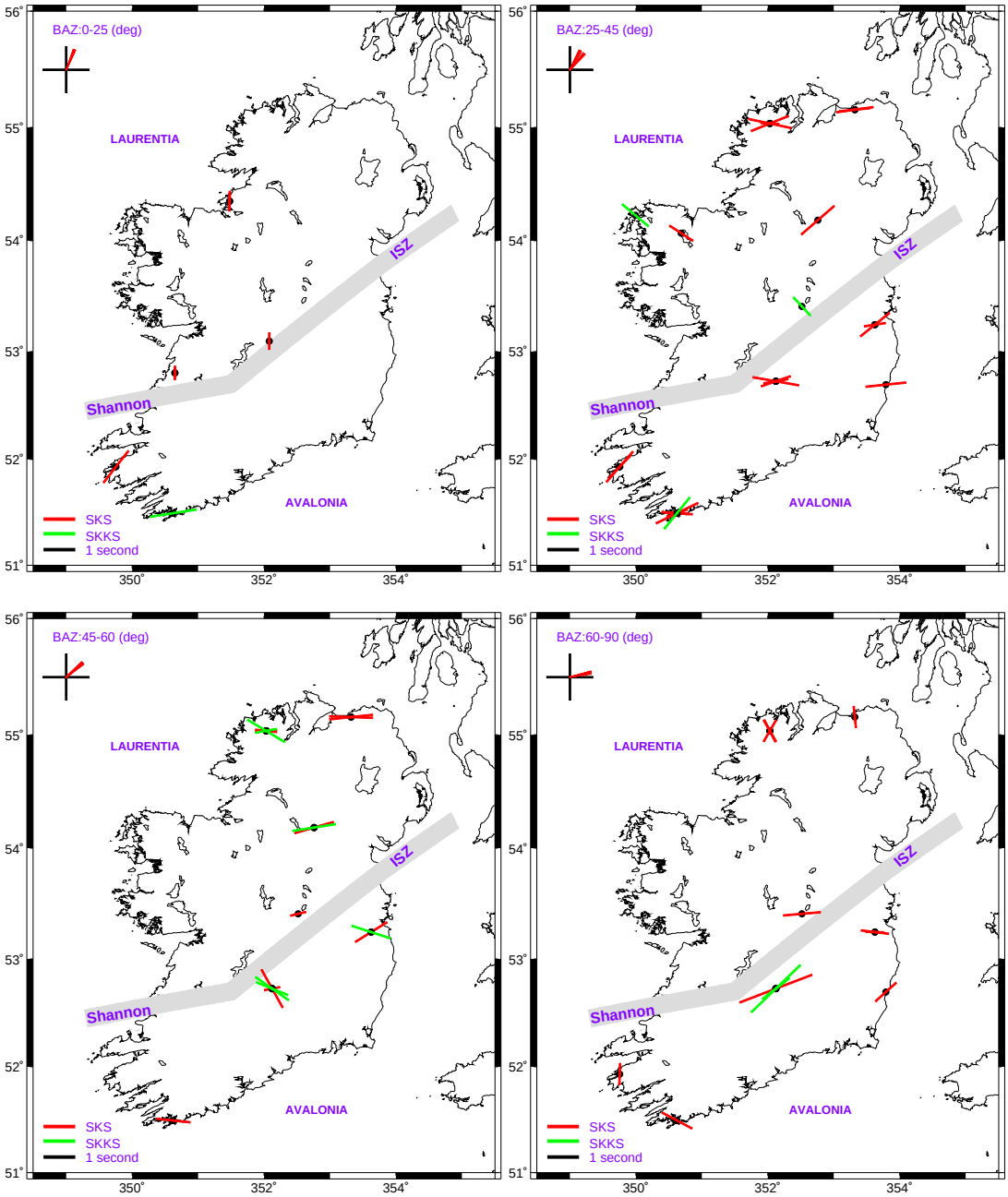



Figure 4.26.: Variations of high quality SKS and SKKS measurements from the EA cluster for different back azimuth ranges. Bars indicate fast polarization directions ($\phi$) and delay time ($\delta$t). The length of bars is proportional to $\delta$t. Arrows in top corners show event back azimuths.

### 4.2.2. Examples from results

**(a) Results from stations D16 and D23**

The distribution of events recorded by two stations D16 and D23 and their splitting measurements in Figs. 4.27, 4.28 and 4.29 has been shown as an example. These figures exhibit:

(1) At station D16, events from East Asia and South America with the back azimuth range $\phi_{baz}$ ~3-76$^0$ and $\phi_{baz}$ ~226-234$^0$ are obtained, respectively, with epicentral distance ranges from 85 to 117$^0$. The events from the main clusters at station D23 with the back azimuth range $\phi_{baz}$ ~20-77$^0$ and $\phi_{baz}$ ~190-235$^0$ are analyzed, respectively, with epicentral distance ranges from 86 to 120$^0$.

(2) The majority of the analysed events have magnitude of 6-7.4 (Fig. 4.27). As a matter of fact, events in the epicentral distance range of 90-110$^0$ with magnitude range of 6.2-7.4 produced high and medium quality measurements (Fig. 4.28).

(3) It has been found in this study that shallow focus earthquakes provide better SKS/SKKS phases than deep focus earthquakes (hypocentral depth more than 500 km) for shear wave splitting analysis (Fig. 4.28). On the other hand, non-null measurements are dominantly obtained from intermediate depth earthquakes (Fig. 4.27).

(4) The number of high quality measurements at D23 station is larger than medium and low quality and null measurements (Fig. 4.27). However, we observed that the number of high quality measurements at D16 station is less than medium and low quality and null measurements (Fig. 4.27). We concluded that it is probably related to station quality.

(5) Phase histograms of splitting parameters shown in Fig. 4.29 indicated that there is no clear correlation between the SKS/SKKS phase distribution of the events and earthquake source parameters such as magnitude and depth. However, the number of the high quality SKS measurements is larger than the number of the high quality of SKKS measurements (Fig. 4.28).

(6) The number of SKS measurements for both stations is larger than the number of SKKS phase measurements (Fig. 4.29). It should be kept in mind that this observation is not unusual because SKKS phase is not as strong as SKS phase on the seismogram.

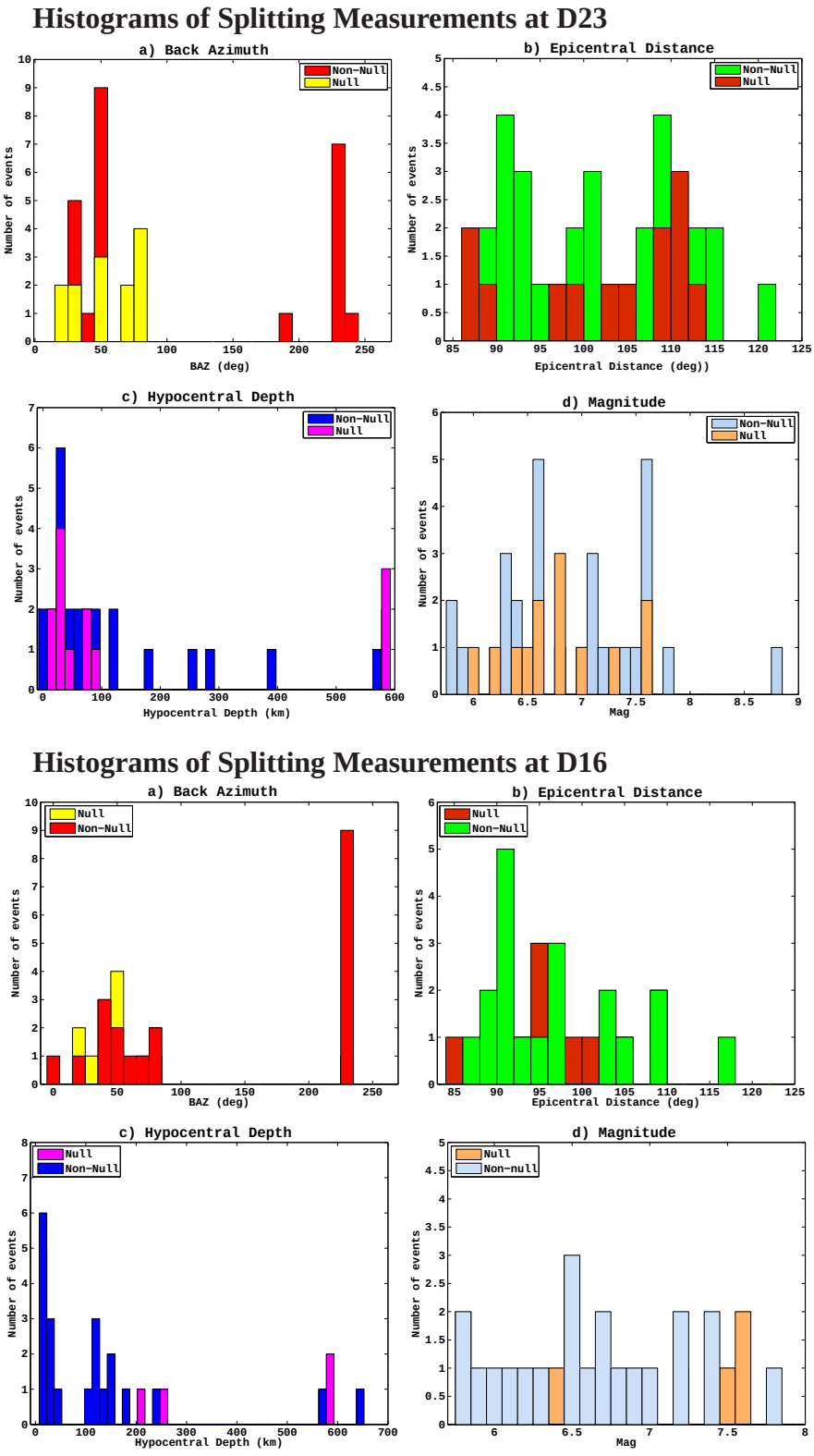



Figure 4.27.: Histograms of splitting measurements at D23 (top) and D16 (bottom): a) $\phi_{baz}$, bin size = $10^0$; b) $\Delta$, bin size = $2.0^0$; c) event magnitudes, bin size = 0:1; and d) event depths, bin size = 15 km. Non null and null measurements are labeled in the figure legend (up right and up left) for D23 and D16 stations.

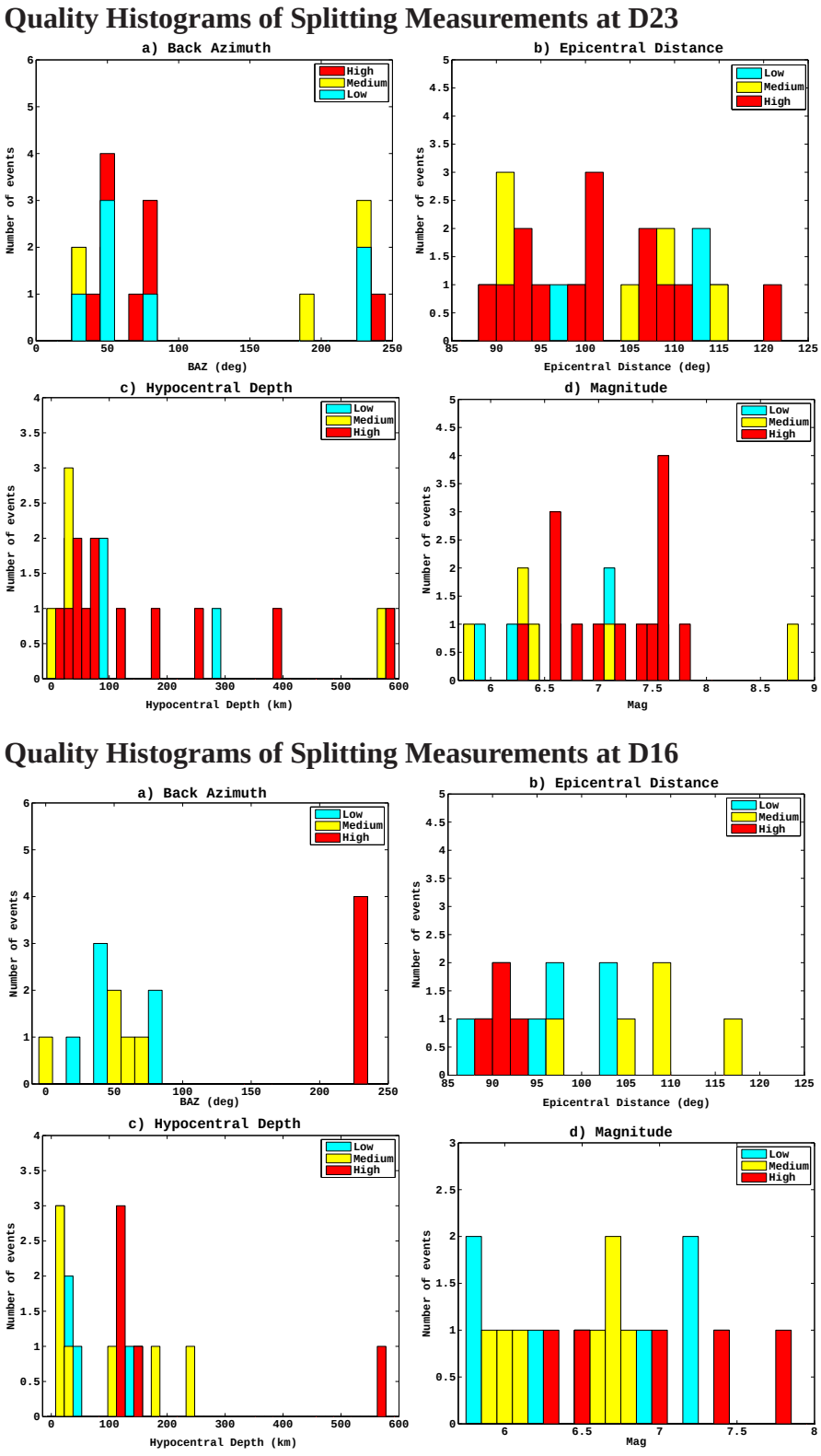



Figure 4.28.: Quality histograms of splitting measurements at D23 (top) and D16 (bottom): a) $\phi_{baz}$, bin size = $10^0$; b) $\Delta$, bin size = $2.0^0$; c) event depths, bin size = 15 km and d) event magnitudes, bin size = 0.1. Red, blue and yellow portions indicate the number of good, medium and low quality measurements, respectively.

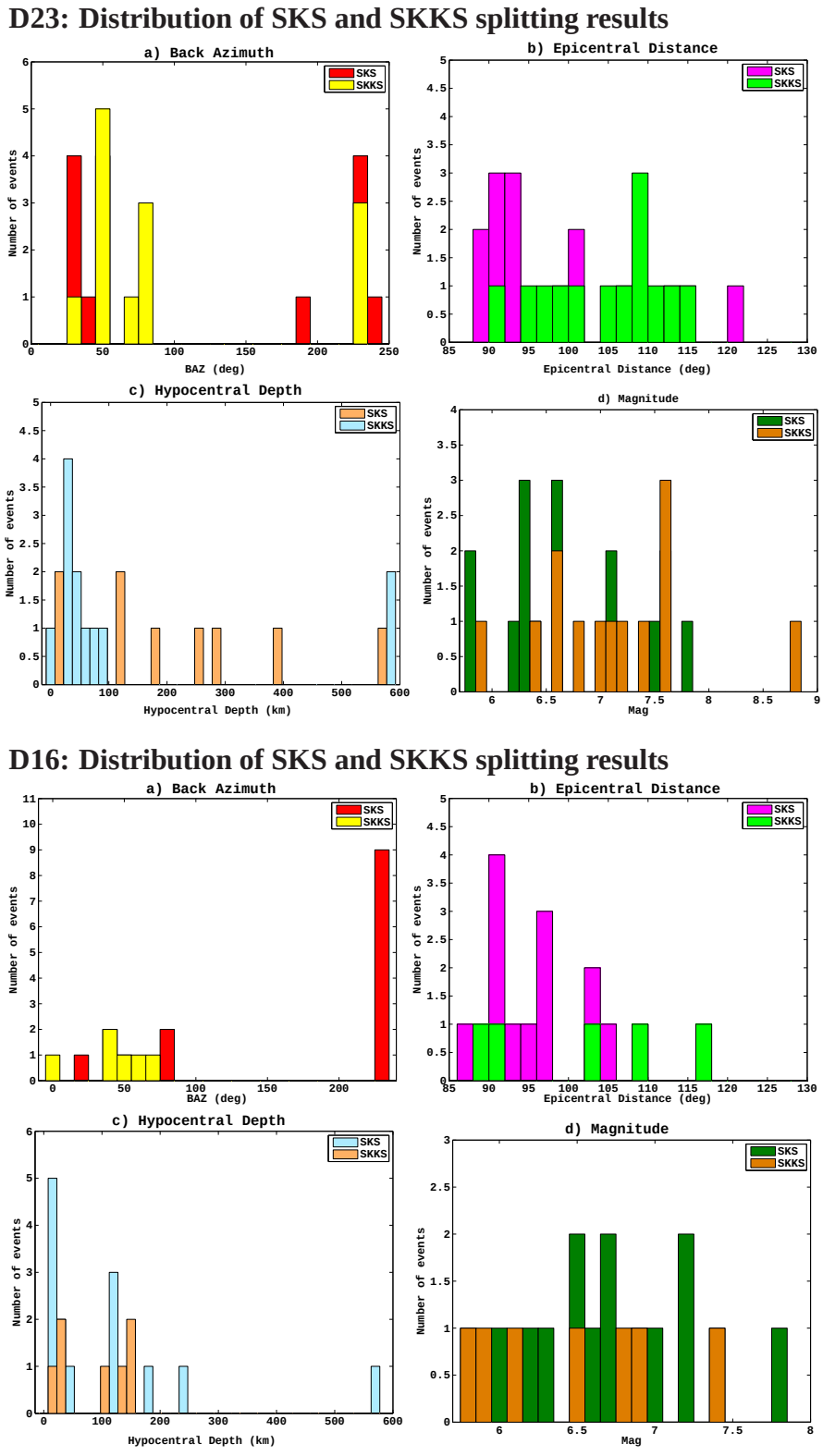



Figure 4.29.: Distribution of SKS and SKKS splitting measurements at D23 (top) and D16 (bottom): a) $\phi_{baz}$, bin size = $10^0$; b) $\Delta$, bin size = $2.0^0$; c) event magnitudes, bin size = 0:1; and d) event depths, bin size = 15 km. SKS and SKKS measurements are color-coded, as indicated by the legend at up right, respectively.

(7) The EA event cluster has a larger azimuthal range than the SA event cluster (see Fig. 4.29).

(8) The performed procedures for measuring and ranking splitting parameters at stations D16 and D23 are also applied to other stations.

**(b) Results from station D34**

In this section, we present the splitting parameters for station D34 (Figs. 4.30 and 4.31) as a representative example of back-azimuthal variation plots. These figures clearly indicate that the results were mainly from two major event clusters.

Here we also compared all results derived from this study with the shear wave splitting results compiled by *Do et al.* (2006). Similar patterns in shear wave splitting parameters from the two studies are clearly observed. As observed in Figs. 4.30 and 4.31, station D34 is a good example to indicate particularly the typical back-azimuthal variation of splitting parameters. In order to reveal the backazimuthal variation of splitting parameters, the individual splitting parameters obtained from station D34 are plotted as a function of backazimuth. The backazimuthal variation plots derived from this analysis are shown in Figs. 4.30 and 4.31.

In addition to the distributions of $\phi$ and $\delta$t versus the back-azimuth on the diagrams (Fig. 4.30), splitting parameters versus angle of incidence (Fig. 4.32) have been plotted to reveal relationship between splitting parameters and incidence angle. Often this type relationship is used to construct a model which is based on inclined or dipping symmetry axes. The splitting parameters from the SA cluster do not show strong variations in splitting parameter, particularly lag times, with the incidence angles that range from 11 to $14^0$ (Fig. 4.32). When the lag times change from 0.5 to 2 s, the incidence angles do not change largely and are dominantly clustered at $13^0$. The interesting conclusion of these plots is that delay times do not correlate well with incidence angle.

However, slight variations in fast-polarization directions obtained from the EA cluster with incidence angle are observed (Fig. 4.32). That may suggest lateral variations of the anisotropy, so that for the station more than one anisotropic layer and/ or the existence of an inclined

axis or dipping axis of symmetry can be considered. Interestingly, similar observations are also observed at other stations used in this study. In the final chapter we will discuss possible models for the origin of these lateral differences and the tectonic consequences.

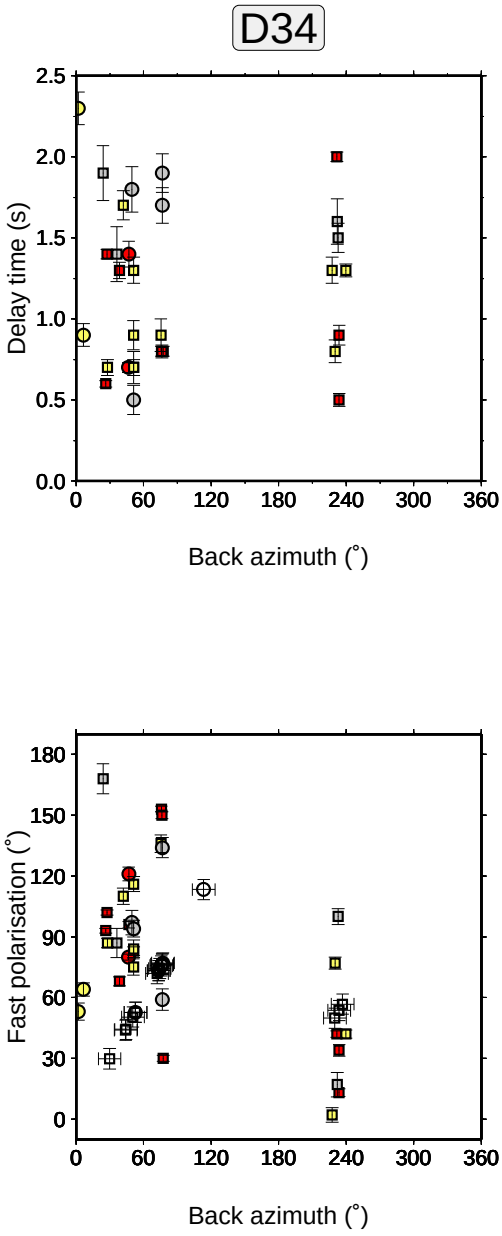



Figure 4.30.: Plots of individual splitting measurements at station D34. Variations of delay time (top) and fast direction (bottom) with back azimuth are shown. Red, yellow and gray filled symbols indicate 12 good, 18 medium and 16 low quality and 20 null splitting measurements, respectively. Circles and squares show results from 47 SKS and 19 SKKS measurements, respectively. Null splitting observations are plotted with two perpendicular error bars.

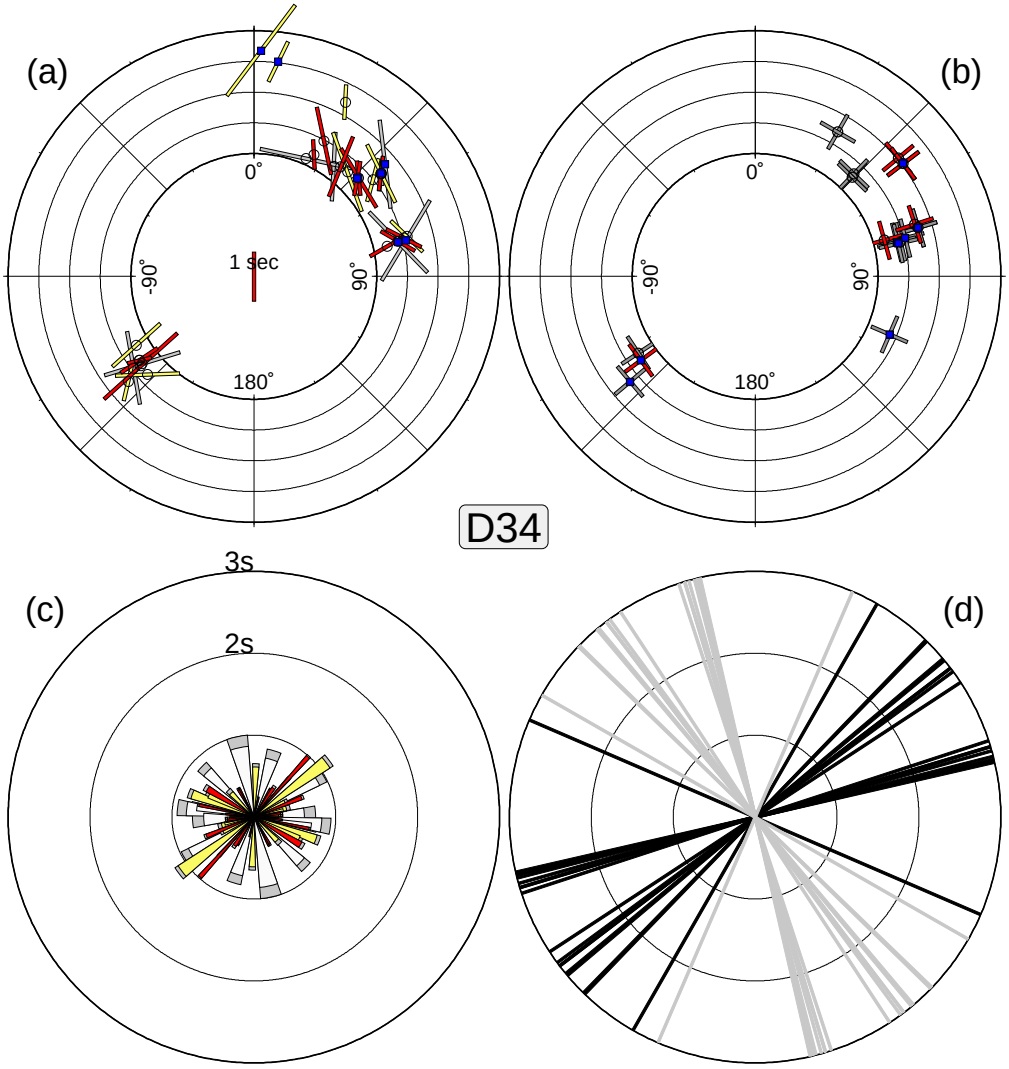



Figure 4.31.: All measurements for D34 plotted at true epicentral distances and back-azimuths. (a) Polar plot of splitting results acquired from individual non-null measurements. Bars show azimuth of $\phi$ with length proportional to $\delta$t. (b) Plot of null measurement. (c) Non-null splitting results are shown as rose diagrams. Wedge length and width exhibit the range of splitting parameters ($\phi$ and $\delta$t). Circles are of 1,2 and 3 s radius. Estimated errors of $\delta$t (gray shaded wedge) and $\phi$ (wedge width) are shown. (d) Rose diagrams of Null-splitting results. Black and gray lines show back-azimuth and its orthogonal direction for each null event. Red, yellow and gray filled symbols show good medium, low quality non-null splitting measurements respectively. Blue squares and open circles exhibit results from SKKS and SKS phases respectively.

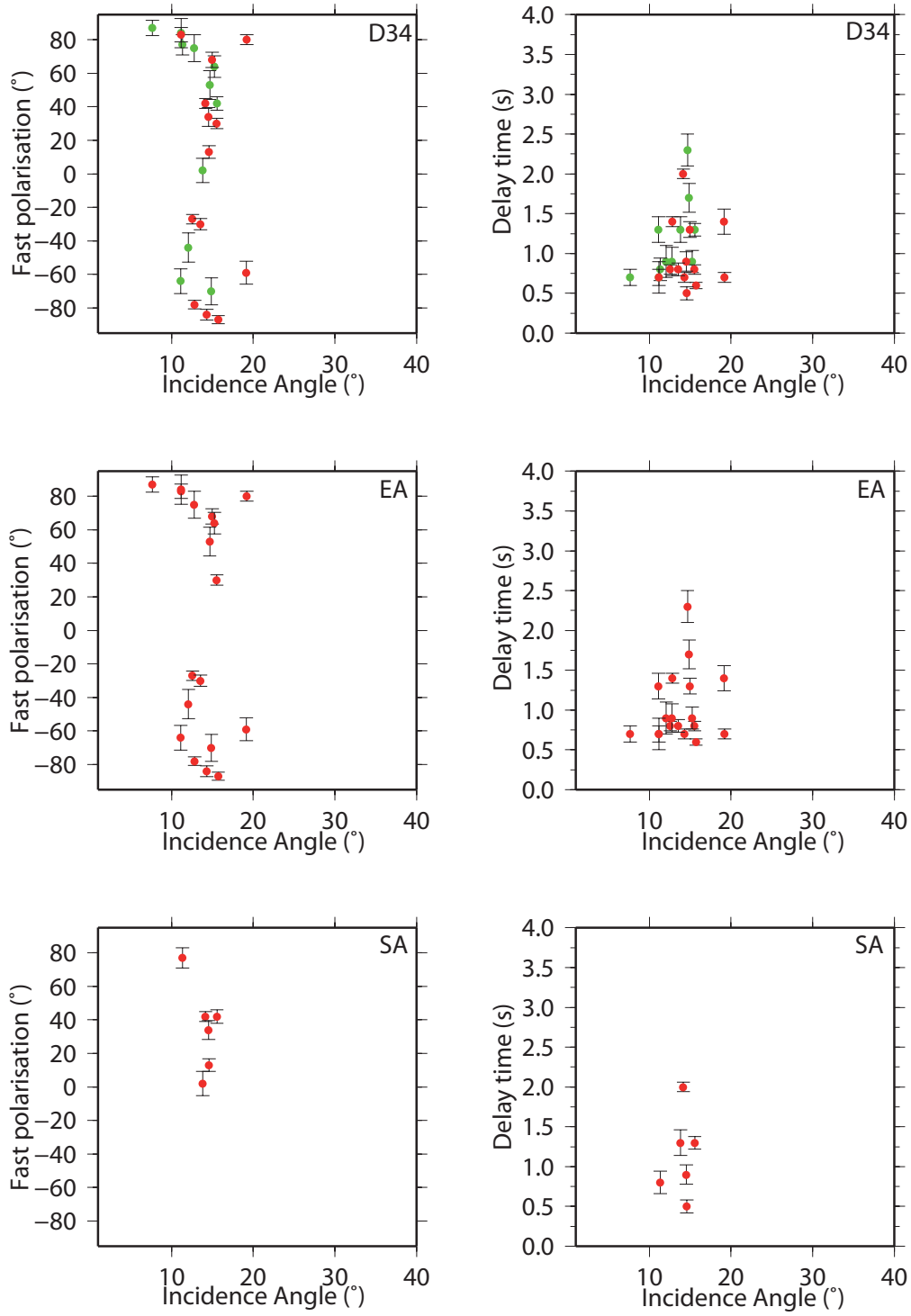



Figure 4.32.: Variations of delay time (right) and fast direction (left) with incidence angle for station D34. Error bars represent 95% confidence intervals for each of the estimated individual parameters. For this analysis, 13 good and 11 medium quality splitting measurements used. First row: red and green filled (bottom) measurements versus angle of incidence are also classified according to the EA and the SA clusters. Second row: for the EA. Third row: for the SA.

## 4.3. Concluding remarks and discussion

As previously presented, in this study shear wave splitting has been examined in teleseismic shear waves obtained from 42 broadband stations located in Ireland. This study is the first extensive investigation of mantle anisotropy along the whole Irish Caledonides. Most of all stations indicated clear evidence for seismic anisotropy beneath the study area.

One of the fundamental results of this study is that the fast polarization directions strongly vary with back-azimuth but there is no clear dependence with back-azimuth of delay times which vary between 0.5 to 2.5 s (Appendices E and F and Figs. 4.23 and 4.24).

A striking change in fast polarisation direction was found between results from South American and East Asian event clusters. For this reason, the results for each event cluster were separately examined. In general, the average results from the clusters show simple and consistent patterns (Figs. 4.23 and 4.24). This allows a comparison of the average fast polarizations with other directions, such as absolute or relative plate motions, stress, or geologic fabric.

Interestingly, we observed that throughout Ireland, fast polarization directions ($\phi$) obtained from the EA event cluster are consistently oriented ~ E-W with ~ 1 s delay times, approximately coincident with the orientation of the tectonic fabric which is dominated by the NE-SW Caledonian trend (Fig. 4.23). Assuming 4% anisotropy and an average shear velocity of 4.7 km/s for the entire lithosphere we can extend suture/fault-parallel anisotropy from the surface to ~120 km. Similar results in the UK were found by *Helffrich* (1995); *Restivo and Helffrich* (1999); *Bastow et al.* (2007) and in Ireland by *Do et al.* (2006) using teleseismic events in East Asia. However, although the average fast polarizations from the East Asian events are generally quite consistent with each other, a few stations located in central Ireland show N-S orientations with a small amount of splitting ($\delta$t $\leq\sim$ 0.5s).

Splitting measurements obtained from the SA event cluster at nearly all stations are, in general, consistent with each other, indicating an average ~N-S fast direction and a delay time of 0.6 to 1.27 s (Fig. 4.23). Spatial variations in the averaged SKS and SKKS splitting parameters from this cluster are not observed (Figs. 4.23 and 4.24). Although there is no correlation

between fast polarization directions from this cluster and tectonic units in the study area or the NE-SW Caledonian or Variscan trend, we observed that the N-S orientations of splitting parameters are consistent with LPO of olivine calculated from the 3-D flow model at a depth of 175 km for the North Atlantic region on the regional scale (*Marquart et al.*, 2007) (see Figs. 7.1 and 7.2).

This result might provide evidence to suggest a deep origin for the anisotropy. It may be expected that the origin of seismic anistropy may be deep in the mantle, even possibly involving the D" layer at the CMB. Although it is not simple to detect seismic anisotropy in the D", one possible way is to compare SKS and SKKS results from a single event as their raypaths in the lower mantle D" are quite separate. This procedure will be described and its results shown in chapter 7.

# 5. Surface wave tomography for azimuthal anisotropy

The aim of this chapter is to describe the surface wave data acquisition, analysis of the fundamental mode Rayleigh wave phase velocities and henceforth determination of azimuthal anisotropy beneath Ireland. The crustal structure features inferred from this study provide crustal anisotropy relating to tectonic evolution of the region.

## 5.1. Data

Recently, the Irish Seismic Lithospheric Experiment (ISLE) (*Do et al.*, 2006; *Landes et al.*, 2006) and the present Irish Seismological Upper Mantle Experiment (ISUME) have covered much of Ireland with intermediate-band seismic stations for the first time. Data recorded at permanent (DSB and VAL) and 22 temporary stations from the ISLE and the ISUME projects (Fig. 5.1) have been used. All stations were equipped with Guralp CMG-40T (eigenperiod 30 s) seismometers, except for DSB (Streckeisen STS-2, eigenperiod 120 s) (see the section 2.4 for details on instrumentation). The ISLE and the ISUME data were recorded from 2002 to 2005 and from 2006 to 2010, respectively.

Earthquake parameters (location, origin time and the scalar moment) have been taken from Centroid Moment Tensor (CMT) catalogues. Then, the obtained information about the earthquakes has been used to prepare the data set for the Rayleigh wave dispersion analysis. Here the data set have been prepared according to the steps that include: (1) insertion of the origin

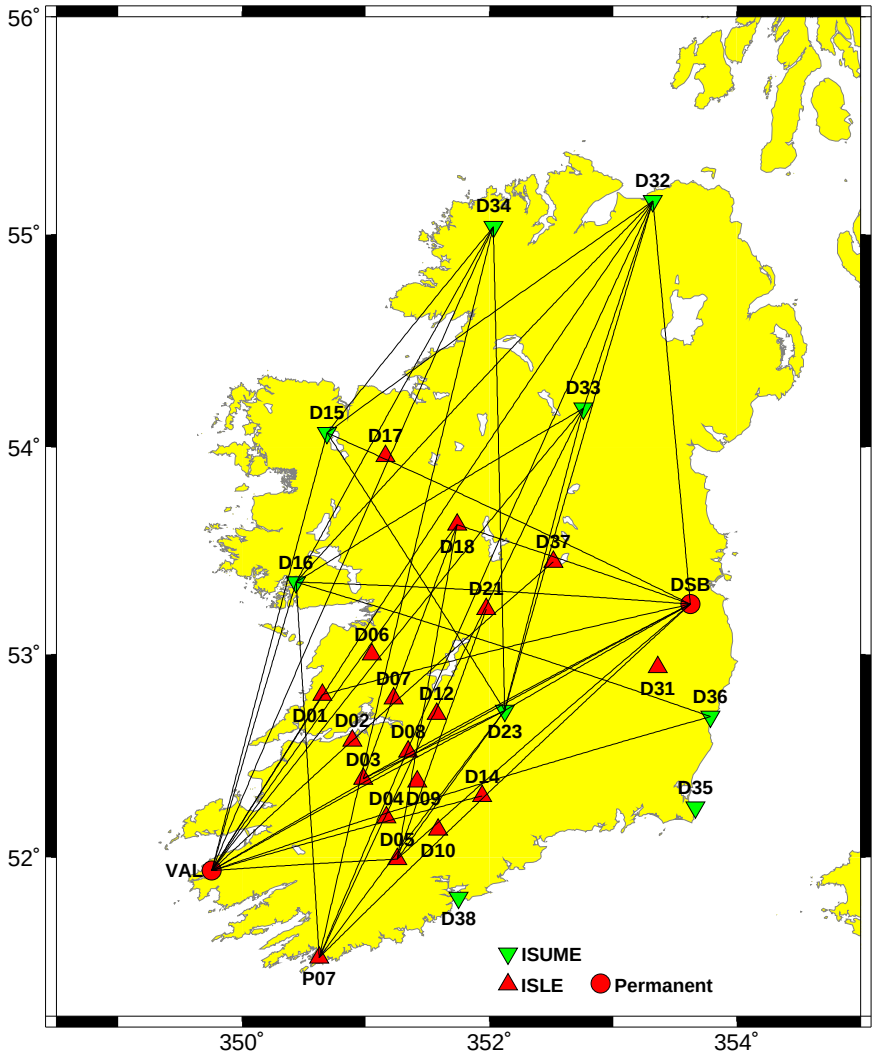



Figure 5.1.: Interstation path coverage used for Rayleigh-wave tomography. ISUME, ISLE, and permanent network stations are depicted by inverted triangles, triangles and circles respectively. Robust Rayleigh-wave phase-velocity curves were measured for the 43 inter-station paths shown.

time and the hypocenter of the earthquake in each seismogram, (2) merge seismograms if they are divided into several pieces, (3) identification of seismograms that are clipped or too short to be used, (4) correction for the instrumental response and calculation of displacement seismograms, (5) rotation of horizontal components. Note that for each station pair, events are only considered if earthquake sources are located approximately on the same great circle path with the stations, the differences between station-event and station-station azimuths being less than 10 degrees.

The complete initial data set included 11490 vertical component seismograms of the events with moment magnitudes ≥ 4.8 that were recorded at the stations depicted in Fig. 5.1. The data set were then used for Rayleigh wave dispersion analysis. As an example, the path between the stations D16 and DSB is shown in Fig. 5.2. Great circles indicating the paths from the sources to the stations are also depicted in the lower part of this figure.

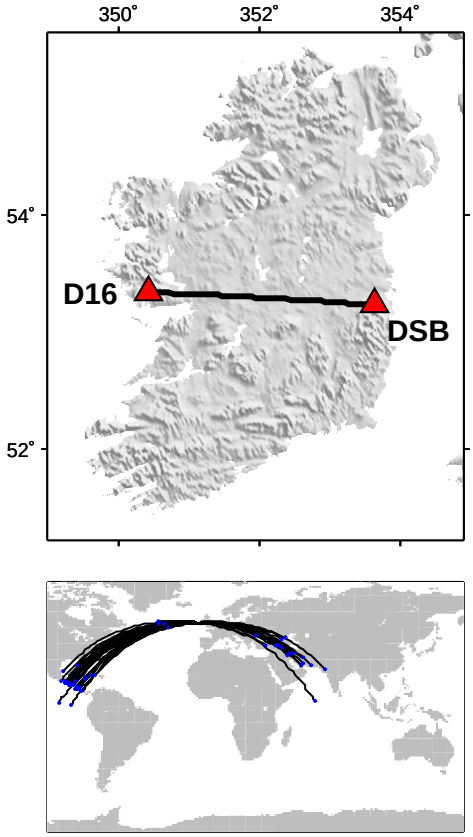



Figure 5.2.: (Top) Inter-station path between the stations D16 and DSB.(Bottom) Great circles between the epicentres and the stations for events used for inter-station, phase-velocity measurements for this station pair.

## 5.2. Interstation phase velocity measurements

In the study, the inter-station technique described by *Meier et al.* (2004) has been used to measure the dispersion curves of fundamental mode Rayleigh waves along 43 interstation paths (Fig. 5.1). Dense crossing of the ray paths provides high resolution for the whole study area,

but the path coverage varies somewhat with period (see later, Fig. 5.6). Although the path density is greater in the west-central part than in the eastern part of the study region (Fig. 5.1), it does not have an enormous influence on the imaging resolution. Additionally, no phase-velocity curves were obtained from stations D38, D35 and D31 due to lack of sufficient data.

This technique (*Meier et al.,* 2004) combines cross-correlation with an efficient scheme of filtering and windowing of the signal in the frequency and time domains, providing accurate measurements in broad period ranges. The interstation phase velocity measurements of the data set used in this study span the period range of 10-30 s and are sensitive to shear velocity structure from the crust down to the uppermost mantle. This period range is broad enough to sample the entire crust of Ireland (~30 km thick in "this part of Europe-see Chapter 2 for details on the geologic and tectonic structure of the study area"), but not to resolve signatures of the whole lithospheric mantle beneath Ireland. The instrumental noise at longer periods (>30 s) negatively influenced the quality of the data. Therefore, the number of measurements for this study was too small for imaging at these periods.

The application of the method is shown in the example in Fig. 5.3. The vertical components of ground velocity at the station pair are indicated with amplitudes as a function of time and frequency. Phase velocities are accepted in a frequency range that is chosen interactively. The reliable part of the phase velocity curve is thus manually selected. The dotted-dashed curve depicts the normalized amplitude spectrum of the cross correlation function, the dashed line the phase velocity curve for an initial model. These curves hence assist the interactive choice of the frequency range in which the estimate of the phase velocity is to be accepted. This process is repeated for all the events and the final dispersion curve is thus obtained as the average of all the phase velocity curves is measured. Rayleigh-wave diffraction and the interference of the fundamental and higher modes can bias inter-station dispersion measurements (e.g., *Friederich et al.*, 2000; *Pedersen,* 2006). These frequency-dependent effects, however, also cause irregularities and roughness of measured curves, and selection of only the smooth portions of the curves (Fig. 5.3) reduces measurement biases. The consistency of measurements made by using waves arriv-

ing from the opposite directions have been routinely verified. A systematic inconsistency was detected for only one pair (D36-P07) and the measurement for this pair was therefore discarded (Fig. 5.4).

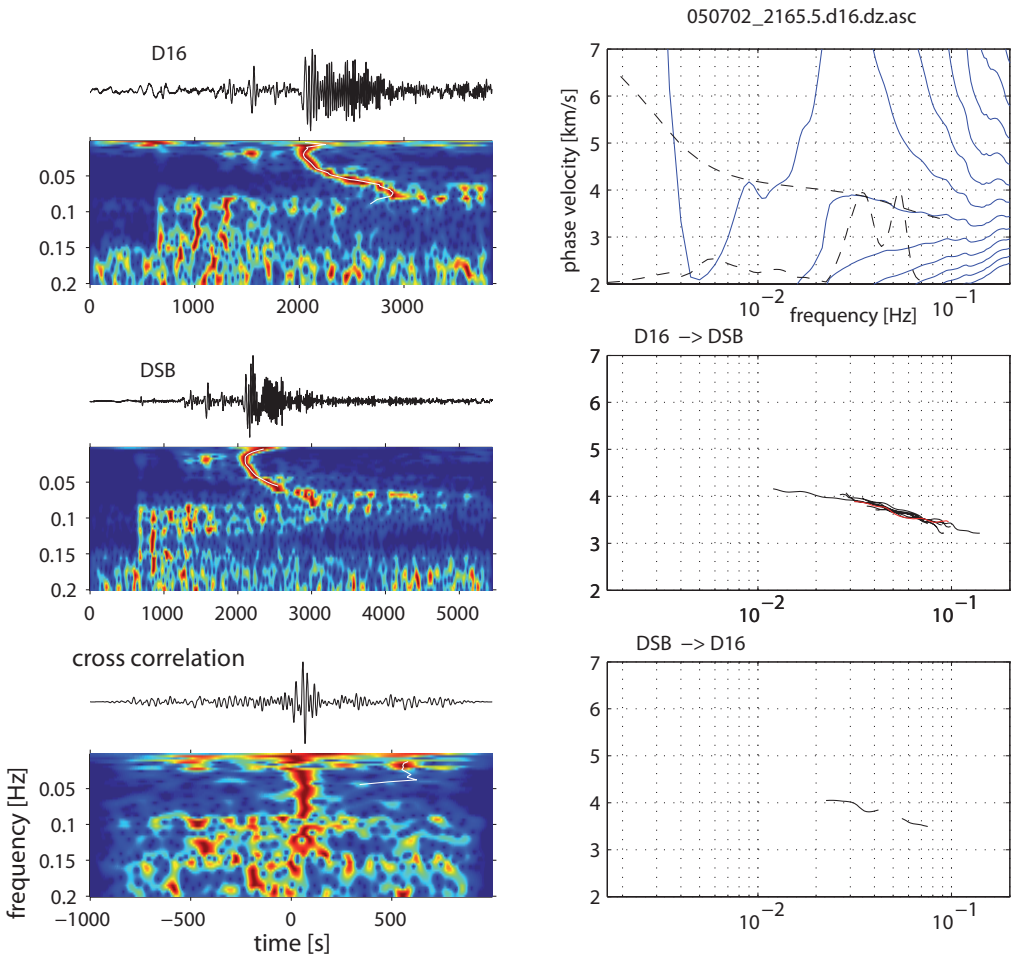



Figure 5.3.: Phase velocity measurements. The example is for the path between the stations D16-DSB and shows the determination of the phase velocity using the two-station method. On the left, the waveforms at the two stations are shown together with amplitudes as a function of time and frequency calculated by the filter techniques. On the left at the bottom, the cross correlation function of the two waveforms is shown. On the right at the upper plot, each blue line indicates the phase velocity of the fundamental Rayleigh mode for an initial model in the frequency domain. The normalized amplitude spectrum of the cross correlation function is depicted by the dashed curve in the upper right plot. The curve is interactively selected. Thus it is comparable to the initial model. The curves in the middle and bottom figures show the phase velocity curves estimated for this example in both directions (i.e. D16-DSB and DSB-D16).

Averaging over many dispersion curves, derived from events in different source regions, is another essential condition for the derivation of robust and accurate measurements. The final phase velocity curves in the data set were averaged from tens of "one-event measurements" at almost all frequencies, with a minimum of 5 one-event measurements at any given frequency (Fig. 5.5). An average over few one-event dispersion curves is unlikely to be robust. Therefore, station pairs with few measurements were not included in the data set. The interstation dispersion measurements of this study have been averaged over 5-~200 individual phase velocity curves.

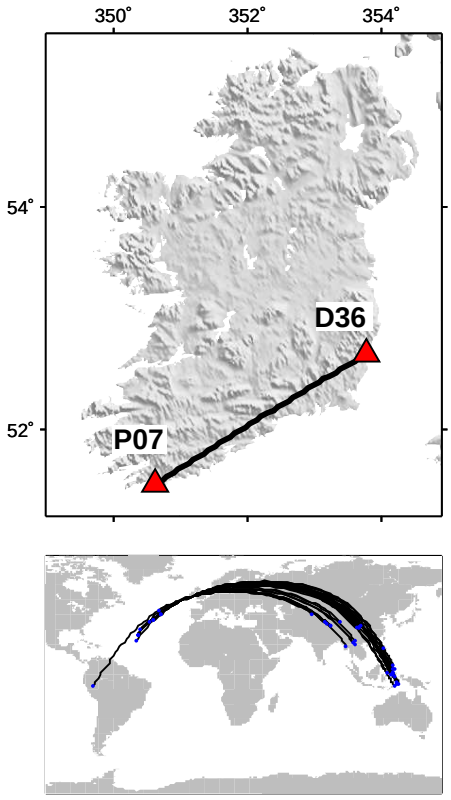



Figure 5.4.: (Top) Inter-station path between the stations D36 and P07 is indicated with the thick black line. (Bottom) Event and source-station path distribution for this pair are also indicated.

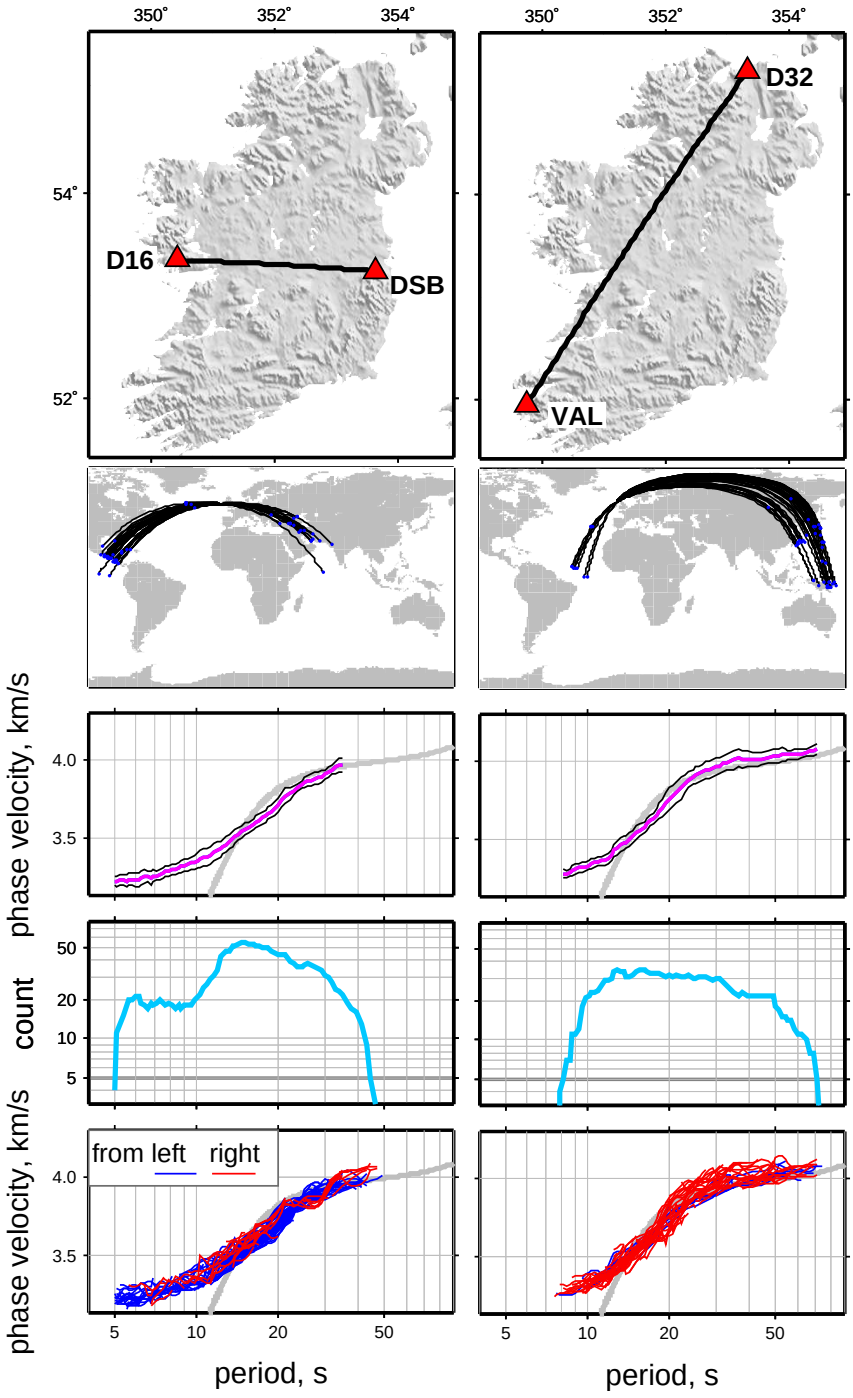



Figure 5.5.: Examples of phase-velocity measurements. First row: Station pairs and interstation paths. Second row: Event and source-station path distributions for each pair. Third row: Measured Rayleigh-wave dispersion curves, averaged from many "one-event" measurements. Grey lines show the PREM (Preliminary Reference Earth Model) (*Dziewonski and Anderson*, 1981) reference curves. Fourth row: Number of one-event measurements at each period. Fifth row: All one-event phase velocity curves measured for each pair. Blue and red indicate different directions of Rayleigh-wave arrival to the pair of stations.

### 5.2.1. Phase velocity maps

Rayleigh wave dispersion curves were obtained from a total of 43 station pairs, although the number for each period varied, as seen in Fig. 5.6. For example, at 10s period, there are no D18-D34 and D32-D33 pairs but they are available at other periods. Nevertheless, variation in the number of pairs does not lead to very significantly different azimuthal coverage at each of the periods. The robust Rayleigh wave dispersion curves were then used to compute isotropic phase velocity maps and anisotropic phase velocity variations (Fig. 5.7). The measurements from the data set provide sufficient azimuthal coverage to map both isotropic and anisotropic phase velocity variations in the period range 10-30 s. At these periods, Rayleigh waves sample primarily the upper crust (about 10 km depth) and uppermost mantle (approximately 45 km depth).

The phase velocity maps (Fig. 5.7) reveal isotropic phase-velocity heterogeneity of around 2%. This reflects the moderate crustal-thickness variability and crustal shear velocity heterogeneity, consistent in amplitude with independent measurements from controlled-source experiments at mid to lower crustal depths in the region (*Hauser et al.*, 2008; *O'Reilly et al.*, 2010). Overall, it can be concluded that Rayleigh-wave phase-velocity maps at periods of 10-30s display changes in the isotropic structure of the Irish crust. Additionally, these maps suggest that the northwest part of the Irish crust is thicker than the other parts at periods of 10 and 20 s. At 25 s period, at which Rayleigh waves sample primarily the lower crust and uppermost mantle, a significant variation in phase velocity between the northern part and the southern part of the Irish crust is observed. This may be related to the effects of Variscan and Caledonian deformation on crustal structure in southern Ireland.

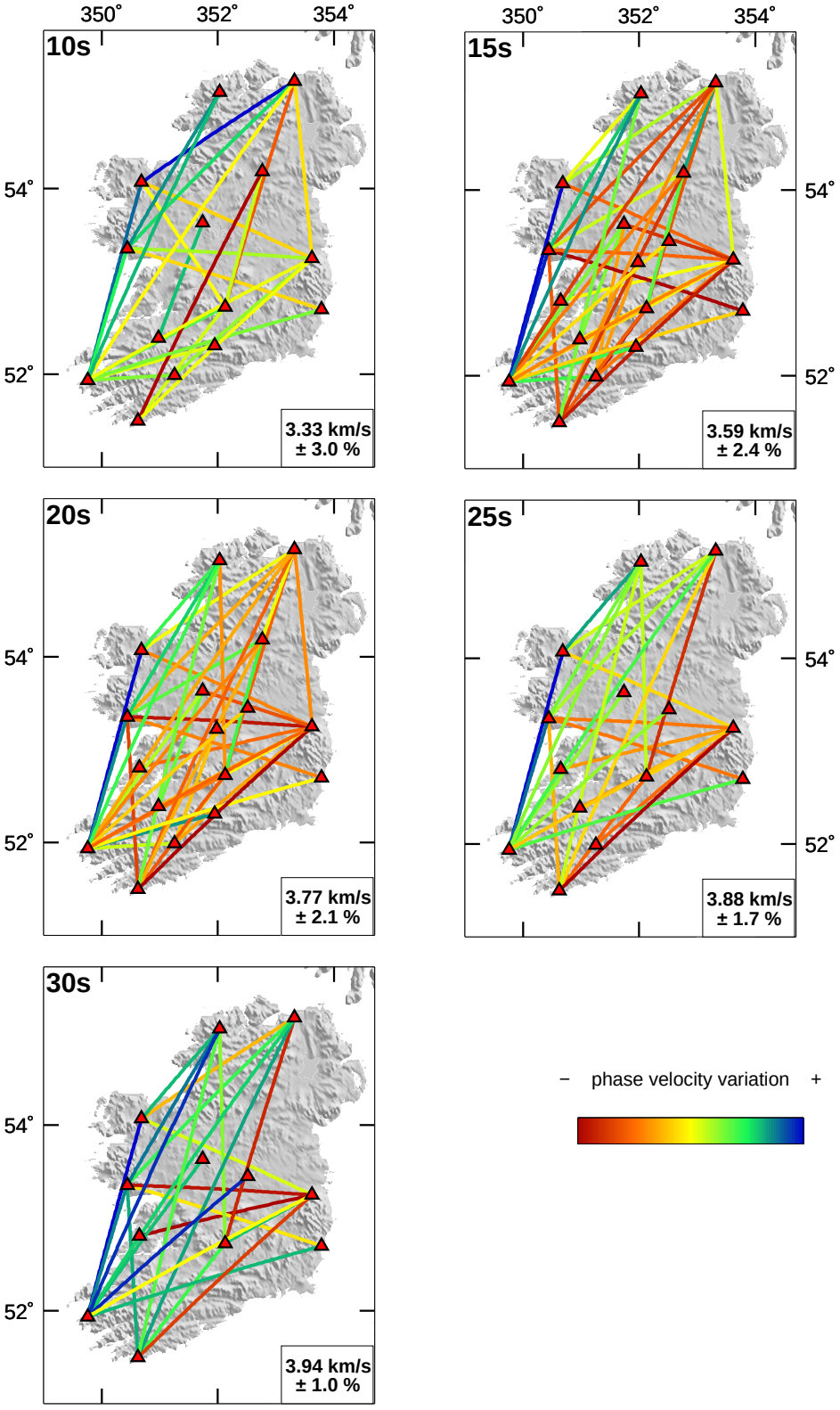



Figure 5.6.: Rayleigh-wave phase-velocity measurements at different periods for different interstation paths. Variations in isotropic phase velocity are given by the colour scale. The period is indicated in the upper left corner and the reference phase velocity and scale limits in the lower right corner of each frame.

## 5.3. Azimuthal anisotropy

The measurements from this study provide sufficient azimuthal coverage to allow the construction of phase velocity maps that include azimuthal anisotropy in the period range of 10-30 s (Fig. 5.7). The theoretical relation between slight perturbations $\delta$C in the phase velocity $C$ of these waves and the azimuth $\Psi$ of their propagation direction is given by *Smith and Dahlen* (1973):

$$\delta C(T,\Psi) = C_0(T) + A_1(T)cos(2\Psi) + A_2(T)sin(2\Psi) + A_3(T)cos(4\Psi) + A_4(T)sin(4\Psi) \quad (5.1)$$

where $T$ is the wave period, $C_0$ is the isotropic phase velocity perturbation, and $A_1$, $A_2$, $A_3$ and $A_4$ are the variables that parameterize azimuthal anisotropy.

The dispersion data have been inverted separately at each wave period for the distributions of the isotropic phase velocity perturbations and the four anisotropy coefficients (eq. 5.1) given in the eq. 5.1, all parameterized at the knots of the same triangular grid with a nearly-uniform spacing of around 100 km. The inversion was performed using the LSQR algorithm of *Paige and Saunders* (1982), with smoothing and slight norm damping (*Lebedev and van der Hilst*, 2008).

Anisotropy patterns reliably resolved only at scale lengths longer than those of the isotropic heterogeneity (*Darbyshire and Lebedev*, 2009); both the $2\Psi$ and $4\Psi$ anisotropy patterns were smoothed more strongly than the isotropic phase-velocity variations. The effect of smoothing is illustrated in Fig. 5.8. A series of test inversions was performed while excluding an increasing portion of the data that were least well fit by the tomographic models (possible "outlier" measurements). The main patterns were robust with the percentage of excluded data varying from 0 to 50% (Fig. 5.9). Our robust models in Fig. 5.7 were computed with 15% of "outlier" measurements excluded. The phase velocity maps (Fig. 5.7) reveal isotropic phase-velocity heterogeneity of around 2%. This reflects the moderate crustal-thickness variability and crustal shear velocity heterogeneity, consistent in amplitude with independent measure-

ments from controlled-source experiments at mid to lower crustal depths in the region (*Hauser et al.*, 2008; *O'Reilly et al.*, 2010).

Azimuthal anisotropy shows a consistently NE-SW fast-propagation direction at periods that sample the crust beneath Ireland (Fig. 5.7). Fig. 5.7 indicates $2\Psi$ pattern with its $\pi$-periodic phase-velocity variations with azimuth. Also, the amplitude of phase-velocity anisotropy indicates a clear maximum at periods near 15 s, indicating that it is due to shear-velocity anisotropy within the middle and lower crust (Fig. 5.7). Somewhat surprisingly, the data require no phase-velocity anisotropy at longer periods (25-30 s) that sample primarily the uppermost mantle (anisotropy in the tomographic solutions at these periods is very small and is not plotted in Fig. 5.7). With its strong smoothness constraints, our inversion was aimed at extracting the dominant, large-scale regional anisotropy pattern, which are reliably determined from the available data. Smaller-scale anisotropy variations may be present in addition to this large-scale pattern. They may be determined in the future when data sampling across Ireland improves further.

Interestingly, we found that the $4\Psi$ terms (see eq. 5.1), often neglected in Rayleigh wave anisotropy imaging (e.g., *Crampin*, 1970), are required by our dataset to be substantially nonzero. It means that Rayleigh wave data requires $2\Psi$ and $4\Psi$ terms. This suggests that earth structures contain oriented olivine crystals (or a similar petrological substance). This approach is probably correct for the mantle, but it is invalid for the crust if a shallow source causes the azimuthal anisotropy (*Trampert and Woodhouse*, 2003). We therefore suggest that the strong existence of $4\Psi$ is probably related to the sources of the observed azimuthal anisotropy that are shallow.

A comparison of variance reductions from a series of the test inversions shows that both the $2\Psi$ and $4\Psi$ terms are needed to fit the data, with the $4\Psi$ terms alone providing a somewhat greater variance reduction than the $2\Psi$ terms alone (Table 5.1). A series of inversions are applied to the data of 15 s period. The results are listed in Table 5.1. Inversions were performed with various proportions of "outliers" (station-station average dispersion curves that are explained the worst by smooth tomographic models) excluded (0-50%), and with isotropic-heterogeneity terms only, isotropic and $2\Psi$ terms, isotropic and $4\Psi$ terms, and isotropic and $2\Psi$ and $4\Psi$ terms

allowed to be non-zero. Values of variance reduction can be compared directly only for inversions of the same data and with the same number of model parameters. In particular, inversions with only isotropic and 4Ψ parameters fit the data better than those with only isotropic and 2Ψ parameters. This is not due to a proportion of highly anomalous measurements even though a progressively smaller percentage of (the most mutually consistent) data is inverted (from 100% to 50% of data).

Table 5.1.: Variance reductions for 15s period

| Percentage of data | Isotropic (Iso) | Iso + 2Ψ | Iso + 4Ψ | Iso + 2Ψ + 4Ψ |
|---|---|---|---|---|
| 100 | 0.1637 | 0.2344 | 0.2734 | 0.3662 |
| 90 | 0.1817 | 0.2788 | 0.3051 | 0.4410 |
| 85 | 0.2420 | 0.3256 | 0.3697 | 0.5422 |
| 80 | 0.2676 | 0.3380 | 0.4058 | 0.5697 |
| 75 | 0.2935 | 0.3694 | 0.4230 | 0.5834 |
| 50 | 0.4599 | 0.4806 | 0.6603 | 0.7386 |

Importantly, the fast-propagation directions given by the 2Ψ terms change if the 4Ψ terms are not included in the solution or forced to be zero (Fig. 5.9). In order to verify that this is not due to a small proportion of highly anomalous measurements, we performed inversions with and without the 4Ψ terms while excluding a progressively larger percentage of "outliers". We observed that the 4Ψ terms are needed to fit our dataset even if only the most mutually consistent 50% of the data are inverted. As a concequence, we concluded that the amount of the 4Ψ signal cannot be neglected in the Irish crust in a large proportion and may be more than 2Ψ anisotropy.

Based on these correlations, the possible sources can be suggested for the observed azimuthal anisotropy. In the case of mantle peridotites, undersaturated in silica and rich in olivine and pyroxene, nearly all of the directional variations in phase velocities can probably be described by the 2Ψ terms (*Smith and Dahlen*, 1973; *Montagner and Nataf*, 1986), although non-zero 4Ψ terms have also been reported (*Trampert and Woodhouse*, 2003). The silica-rich nature of the continental crust, in contrast, as inferred from Poisson's ratios and verified by the geochemistry of the metapelitic xenoliths (*Christensen*, 1996; *Hauser et al.*, 2008) may well cause its basic anisotropic properties to be different from those of the mantle, with both the 2Ψ and 4Ψ terms

being important, at least in some locations.

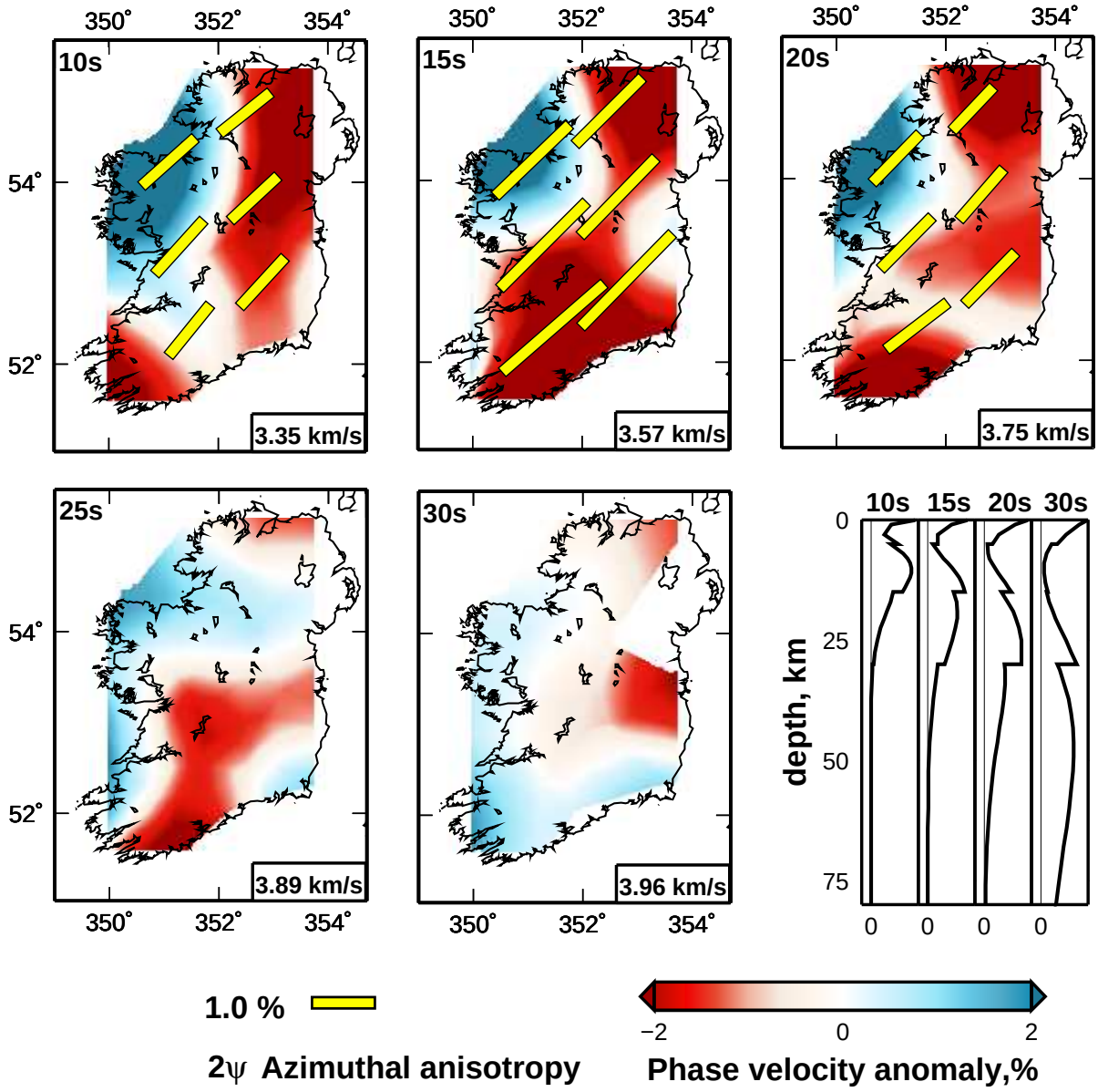



Figure 5.7.: Tomographic maps of Rayleigh-wave phase velocities at different periods. The period and reference phase velocity are indicated in the upper left and lower right corners of the frames, respectively. The isotropic anomalies are shown in the background using the colour scale. Yellow sticks show the fast-propagation directions and strength of azimuthal anisotropy. Fréchet derivatives of Rayleigh-wave phase velocities at 10, 15, 20 and 30 s periods with respect to shear speeds at depth, computed for an (Ireland-like) model with a 30-km thick crust, are shown in the bottom right of the figure.

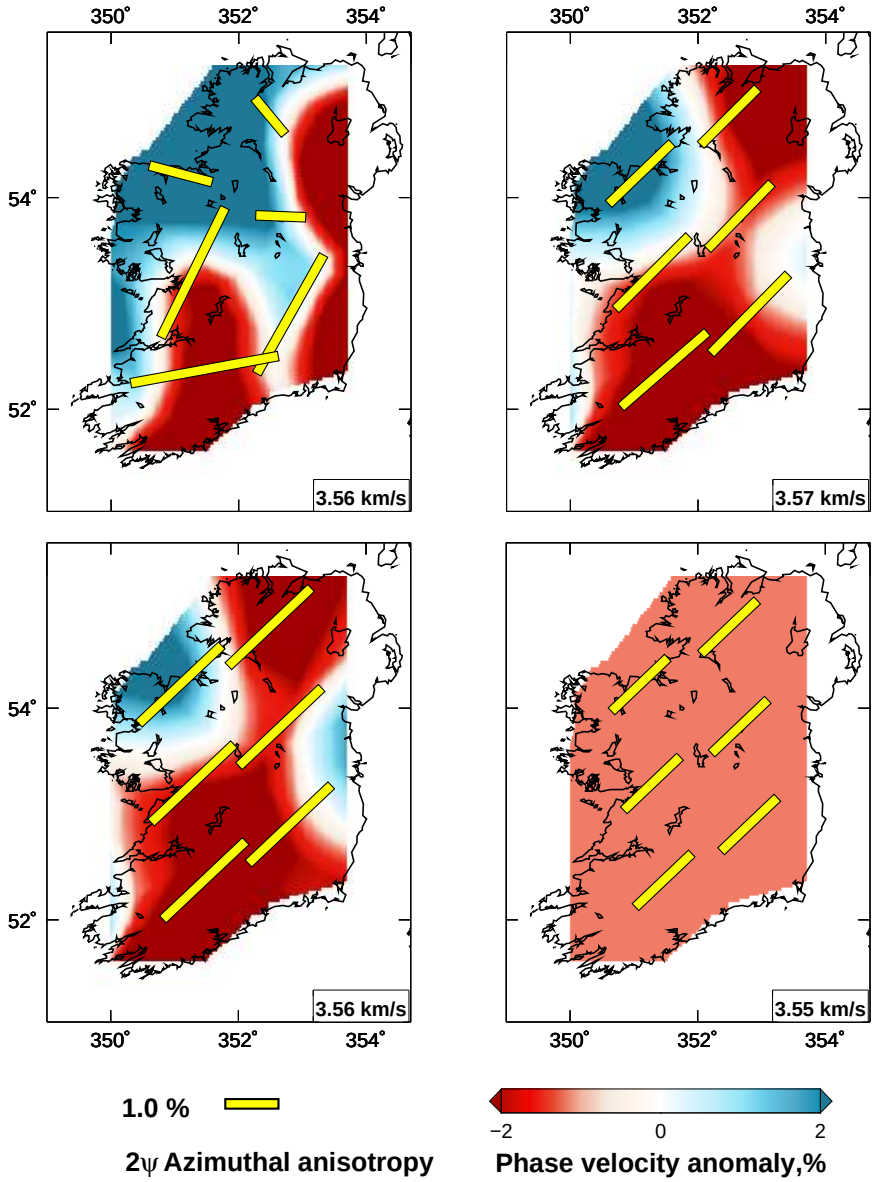



Figure 5.8.: The effect of smoothing: models produced by inversions of the same data at 15-s period, with different lateral smoothing. Top left: no smoothing on isotropic or anisotropic parameters; the model is dominated by noise because the data coverage is insufficient to resolve the small-scale structure. Top right: inversion with our preferred smoothing of isotropic and anisotropic structure; anisotropic structure is smoothed strongly, with only moderate lateral variations in it allowed. Bottom left: inversion with our preferred smoothing of the isotropic structure and with infinitely strong smoothing of the anisotropic structure (no lateral variations in anisotropy). Bottom right: inversion with infinitely strong smoothing of both the isotropic and anisotropic structure (no lateral variations in either). We use the relatively strong smoothing of anisotropy (top right) in order to extract the robust, large-scale dominant pattern of anisotropy. Denser data coverage will be required in the future to resolve variations of anisotropy at smaller scales.

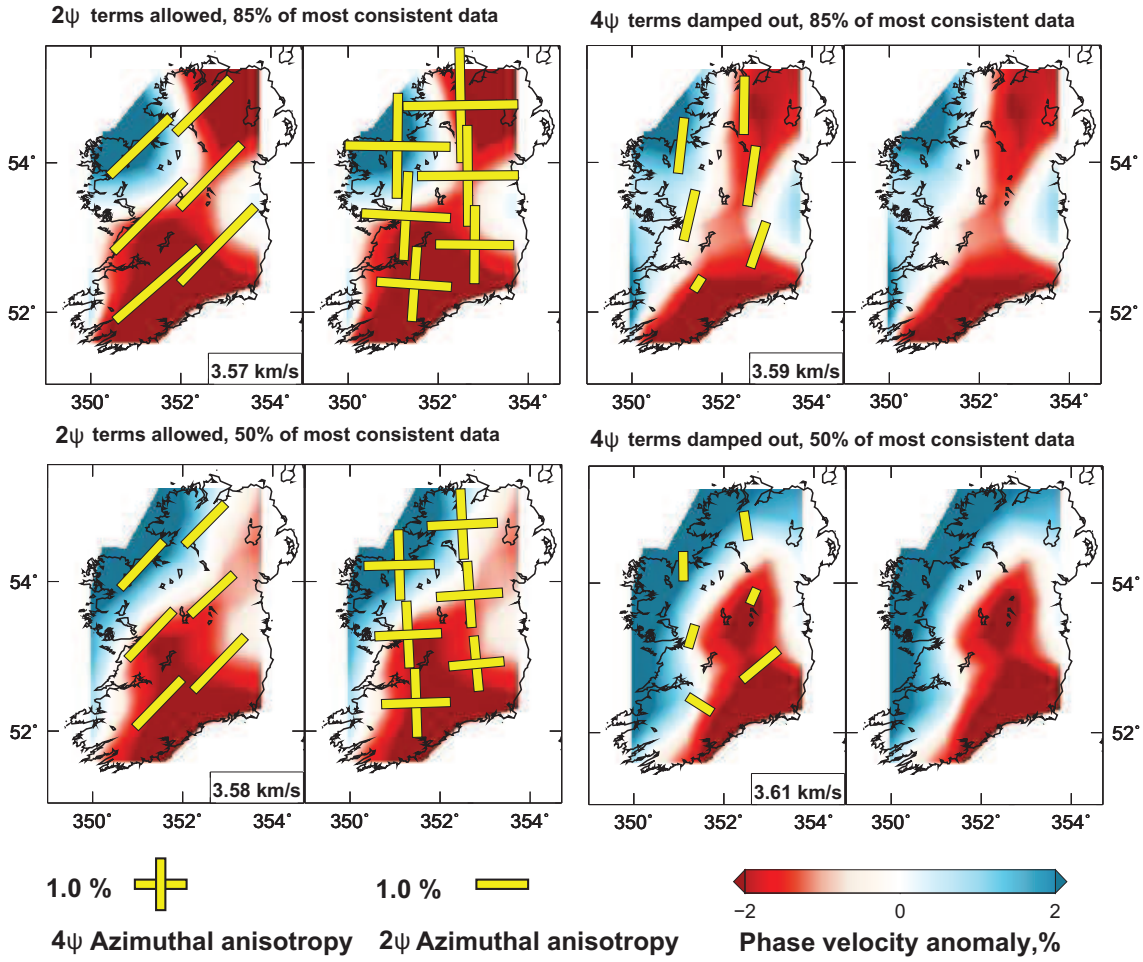



Figure 5.9.: Test inversions at a 15-s period illustrating that the 4Ψ terms (eq. 5.1) are required by the dataset. Top left: the preferred model, as in Fig. 5.7, with the $\pi/2$-periodic ("4Ψ") pattern also shown. The model was computed with 15% "outliers" (data explained the worst by a smooth tomographic model) excluded. The smoothing of the 2Ψ and 4Ψ terms was the same. Bottom left: as top-left but with only 50% of the most mutually consistent data inverted. The fast-propagation directions are robust (i.e. affected little by the data exclusion). Top right: the model computed with 15% outliers excluded and with the "4Ψ" terms damped strongly, so that they equal zero. Bottom right: as top-right, but with only 50% of most-consistent data inverted. The inversions with the 4Ψ terms damped out give different -periodic ("4Ψ") patterns and substantially worse variance reductions (Table 5.1). The average phase velocities are given in the lower right corners of the frames.

## 5.4. Summary and discussion

In this chapter, we have presented a new study of fundamental mode Rayleigh-wave dispersion within the whole of Ireland. We determined average dispersion curves along 43 ray paths. To obtain high-resolution Rayleigh wave phase-velocity maps, Rayleigh-wave fundamental mode dispersion curves along these paths in the study area were inverted to provide new insight into the geodynamic history of Ireland. Additionally, the Rayleigh-wave measurements were used to compute azimuthal anisotropy to provide additional information about past and present deformations within the study areas.

The robust Rayleigh wave dispersion curves from this study were derived from the seismograms recorded by the permanent and temporary intermediate-band stations which covered all of Ireland. These curves along the paths were inverted for Rayleigh wave phase-velocity maps in the period range from 10 to 30 s. Isotropic phase-velocity heterogeneity, also inferred from the phase velocity maps (Fig. 5.6), is approximately 2%. This reflects variations in the moderate crustal-thickness and crustal shear velocity heterogeneity, consistent in amplitude with independent measurements from controlled-source experiments at mid to lower crustal depths in the study area (*Hauser et al.*, 2008; *O'Reilly et al.*, 2010). Additionally, a clear north-west division of the study area, based on isotropic phase velocity anomalies, is apparent in a narrow period range of 10-20 s.

The maps show that it is possible to detect the azimuthal anisotropy beneath the study area. It has been observed that seismic anisotropy exists beneath this area in a form that should cause azimuthal variations in Rayleigh wave phase velocities. Additionally, the observed pattern of the azimuthal anisotropy is very uniform and simple in the period range of 10-20 s. It demostrates that anisotropy of Rayleigh waves resolved at 10-20 s periods shows a NE-SW fast-propagation direction and is largest (up to 2%) at a 15 s period, at which Rayleigh waves sample primarily the middle and lower crust.

In contrast, the observed azimuthal anisotropy at periods sampling the Moho and the uppermost mantle (between 25 and 30 s) is too small to be measurable (Fig. 5.7). A variety of

explanations can be proposed to explain this observation, including an upwelling, toroidal flow around the boundary between the lower crust and the continental lithospheric mantle and large detachment, however no consensus has been reached. For a better understanding of the deformation mechanisms taking place beneath the Irish crust, longer period data ($> 30s$) is required.

The fast-propagation direction resolved at periods of 10-20 s is orientated parallel to the prominent Caledonian NE-SW structural fabrics observed geologically at the surface (*Chew and Stillman*, 2009) and defined by high frequency variation in the gravity field (*Readman et al.*, 1997). While this is not surprising for shorter periods (10 s) that are sensitive to structure in the upper-middle crust, at longer periods (15-20 s) that resolve the middle to lower crustal depths the orientation is identical. This indicates that anisotropic fabrics with a Caledonian orientation persist throughout the entire crust.

A plausible explanation for the presence of the deep-crustal anisotropy is that the fast-propagation directions of anisotropy (defined by the $2\Psi$ terms, Fig. 5.7) probably reflect the orientation of the major axis of the finite strain ellipsoid, due to regional Caledonian (Acadian) pure shear. It may also, at least in part, reflect a paleo-flow direction within a ductile mid to lower crust, driven by Caledonian stresses, and related to the emplacement of the Acadian (~400 Ma) "Newer Granite Suite" (*Chew and Stillman*, 2009; *O'Reilly et al.*, 2012).

The observed anisotropy pattern also indicates that the effects of the Variscan compressional tectonics and the subsequent Mesozoic to Cenozoic lithospheric extension, manifest as large-scale hyper-extended sedimentary basins in the neighbouring North Atlantic, including just offshore Ireland (*O'Reilly et al.*, 2006; *Naylor and Shannon*, 2011), did not overprint the older Caledonian fabrics developed throughout the crust. An orthogonal, NW-SE direction for anisotropy, parallel to the predominant Mesozoic tectonic extension direction, would be anticipated, particularly in the middle and lower, ductile part of the crust, if this were the case.

These overall results are consistent with the available geological and geophysical evidence. The remarkable correlation between the petrophysical and petrological properties of a suite of mid to lower crustal metapelitic xenoliths from central Ireland (*Van den Berg et al.*, 2005) and

the seismic properties, derived from controlled-source imaging, support a Caledonian accretion model for the crustal development (*Hauser et al.*, 2008; *O'Reilly et al.*, 2010). This model implies that continental crustal growth ensued from a subduction related process during the closure of the Iapetus Ocean, which culminated at the Acadian Orogeny. No variation in the amount of deformation between the north and south of Ireland was found suggesting that the effects of the obliquity has created the same anisotropy pattern on each side of the suture. Since early Carboniferous time, the crust has remained relatively stable, with little subsequent modification.

In summary, the apparent preservation of the Caledonian-age fabric indicates that the deep crust of the Eurasian margin in Ireland was neither stretched by the NW-SE extension associated with the opening of the North Atlantic, nor modified significantly by the Cenozoic magmatism in the region. As a consequence, variations in the patterns of both Caledonian-age strain and the Cenozoic magmatism, in this case, may be expected to be observed in the entire Irish crust. This may imply that the Caledonian-age strain relating to continental collision may be mixed with the Variscan compressional tectonics. However, the observed fast-propagation directions and strength of azimuthal anisotropy is not a result of the Cenozoic magmatism. Additionally, the Newer granites produced by the late stage (Late Silurian-Early Devonian) granitic magmatism show differences in age and geochemistry from north to south (*Conliffe et al.*, 2010) of Ireland. This difference in the region straddles the ISZ (*Stone et al.*, 1997). This can explain the crustal anisotropy observed. Therefore, we can detect the crustal anisotropy, in the regional-scale, using the sufficient broadband seismic stations in the study area.

# 6. Surface wave tomography for Radial anisotropy and Shear velocity profile

The major goal of this chapter is to provide a detailed description of Love wave data acquisition and analysis of Love wave dispersion data. In this study, for the first time Love wave dispersion curves are presented to construct phase velocity maps for Ireland. In addition, intermediate-period Rayleigh wave phase velocity measurements obtained from chapter 5 are combined with Love wave measurements to determine radial anisotropy for the whole Irish crust. New constraints on shear wave velocity structure throughout the study area are inferred, including variations in radial anisotropy. Finally, more detailed discussions on the main features of the structure, based on Love-wave tomography and the radially anisotropic shear velocity profile, are presented at the end of the chapter.

## 6.1. Data

For this study, seismograms recorded by 2 permanent (DSB and VAL) and 22 temporary stations from the Irish Seismic Lithospheric Experiment (ISLE) (*Do et al.*, 2006; *Landes et al.*, 2006) and the present Irish Seismological Upper Mantle Experiment (ISUME) projects have been collected. The same stations were used as for the SKS and Rayleigh-wave studies (see section 2.4 for more details on instrumentation).

In chapter 5 only vertical components to measure phase velocity curves for Rayleigh wave were used. In contrast to this, only transverse components are used to compute phase velocity

curves of Love wave in this dispersion analysis. Therefore, first the two horizontal components (E-W and S-N) are rotated to the radial and transverse components. Then, the same preparation steps (see section 5.1) as for Rayleigh waves were used (see the section 5.1 for details on all the stages of data preparation). For example, firstly earthquake information (location, origin time and the scalar moment) has been taken from Centroid Moment Tensor (CMT) catalogues. Then, the dataset for the Love wave dispersion analysis has been prepared according to the obtained information about the earthquakes. All seismograms have undergone careful quality control and instrumental response correction to displacement.

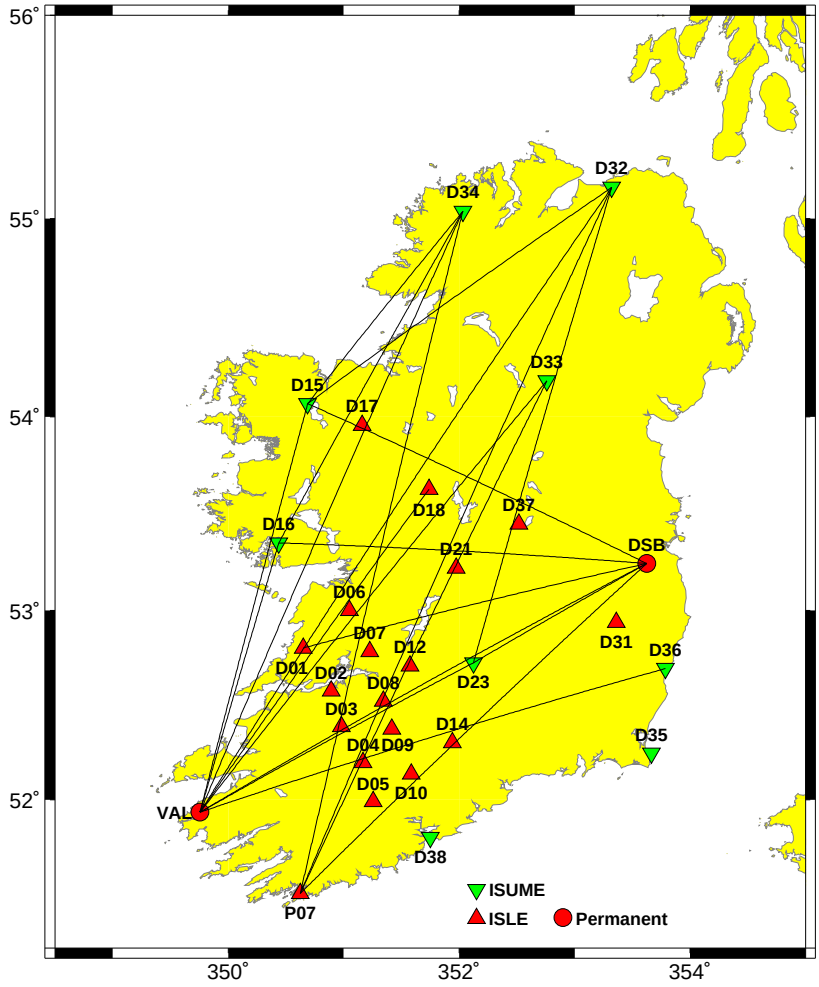



Figure 6.1.: Interstation path coverage used for Love-wave tomography. ISUME, ISLE, and permanent network stations are depicted by inverted triangles, triangles and circles, respectively. Robust Love-wave phase-velocity curves have been measured for the 21 inter-station paths illustrated in the map.

The complete initial dataset comprises 6494 transverse component seismograms obtained from the station-station pairs depicted in Fig. 6.1. As an example, the path between the stations D16 and DSB is shown in Fig. 6.2. In the Fig. 6.2, black lines indicate great circles showing the paths from the sources.

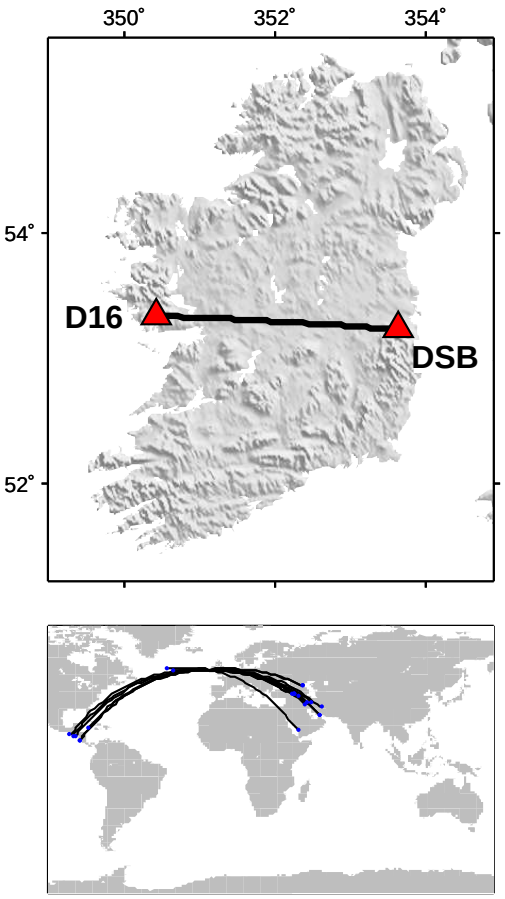



Figure 6.2.: (Top) Example of inter-station path used for Love-wave tomography. (Bottom) Great circles between the epicentres and the stations.

## 6.2. Love-wave phase velocity dispersion measurements

To measure Love-wave dispersion curves the inter-station technique described by *Meier et al.* (2004) is used. With this method, the cross-correlation of the displacement field from a source recorded at two stations is computed. In a detailed scheme of windowing and weighting of the signal in the frequency and time domains, we are able to measure accurate Love wave

dispersion curves with the phase of the cross-correlation function of the transverse recording of an earthquake located on the same great circle arc as the stations.

An example of measurements of Love-wave dispersion curves is shown in Fig. 6.3. Throughout the study, segments of phase-velocity curves are manually selected based on visual inspection of the curves and the time-frequency representation of the waveforms of the analyzed event. The same criteria as used for Rayleigh waves, i.e. the curves are smooth and are not "outliers" (unrealistically far from the average), are used. The average phase velocity and the frequency-dependent confidence intervals were then determined using all curves selected for each interstation path.

A brief explanation of some problems associated with phase-velocity measurement is now presented. Problems such as multipathing, finite-frequency effects and great circle deviations, other than path distribution affect the accuracy of dispersion curves, and can bias phase-velocity measurements. For example, the fundamental modes usually interfere with S and multiple-S waves at long periods. This significantly affects measurement biases and makes cross-correlation measurements difficult. In particular, the effects of higher mode contamination on the measured fundamental mode Love wave phase velocities are significant for some investigated areas. Therefore, such contaminated data, in general, is removed.

Often, these effects are expected to be worse for Love waves than for Rayleigh waves (*Endrun et al.*, 2008). In general, Love wave phase velocities for fundamental and higher modes are difficult to measure because different modes cannot easily be separated. Moreover, Love waves have higher noise level than vertical component Rayleigh wave seismograms. Therefore, Love wave phase measurements are not as robust as Rayleigh wave measurements. Nevertheless, this study has provided sufficient data to measure Love-wave phase velocities.

The effects of the problems relating to Love wave dispersion analysis are reduced by various approaches. The most useful approach is to select only the smooth portions of the curves to reduce biases on the measurements (Fig. 6.3). In addition to this, the consistency of measurements are verified by using waves arriving from the opposite directions. However, in contrast

to the Rayleigh-wave dispersion analysis where an inconsistency was found for one pair (Fig. 5.4), no inconsistencies were found in the Love-wave dispersion analysis.

Another approach is averaging over many dispersion curves for pairs of stations using events in different source regions. For this study, the measured phase-velocity curves are averaged from tens of "one-event measurements" at almost all frequencies, with a minimum of 5 one-event measurements at any given frequency (Fig. 6.4). Therefore, an average curve is computed for each pair used. Averages over fewer than 5 one-event dispersion curves were rejected because such measurements are unlikely to be robust. As a result, nearly half of the pairs were discarded. Therefore, the average uncertainty and systematic bias of the phase-velocity measurements are reduced.

Before constructing phase velocity maps, the period range of each phase-velocity curve is restricted. Phase velocities measured at the periods are close to the reference curves. This suggests that Love-wave phase measurements for the station pairs within Ireland show a similar pattern in a medium broad period range from 10 to 30 s.

In the following section, Love wave phase velocity maps are presented. The maps span the period range of 10-30 s, and have been computed by using only the highest quality dispersion measurements. Then, the phase-velocity measurements have been inverted for isotropic phase velocity maps and the whole-region phase velocity anisotropy.

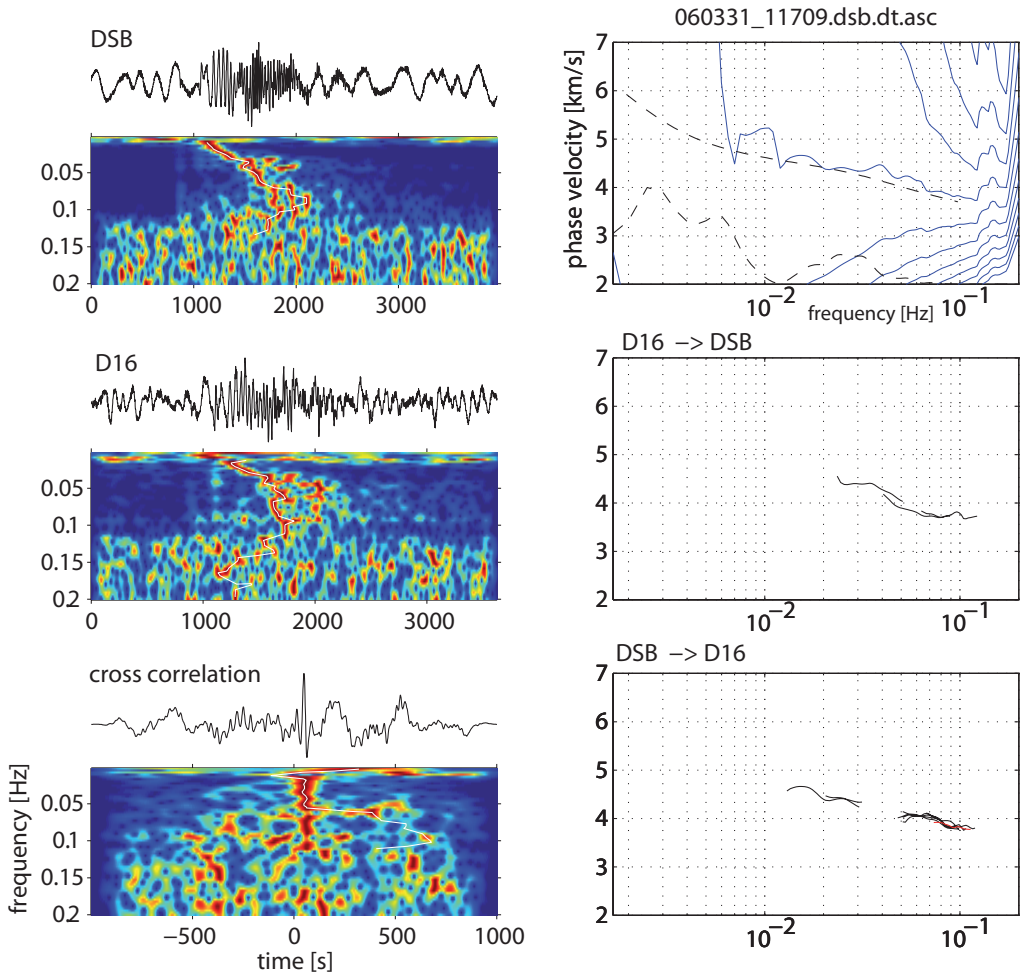



Figure 6.3.: An example (for the path between the stations D16-DSB) showing the determination of the phase velocity of Love wave using the two-station method. On the left, the waveforms at the two stations are shown together with amplitudes as a function of time and frequency calculated by the filter techniques. On the left at the bottom, the cross correlation function of the two waveforms is indicated. On the right at the upper plot, each blue line indicates the phase velocity of Love wave for an initial model in the frequency domain. The normalized amplitude spectrum of the cross correlation function is depicted by the dashed curve in the upper right plot. The curve is interactively selected. It is thus comparable to the initial model. The curves on the middle and the bottom right show the phase velocity curve estimated for this example.

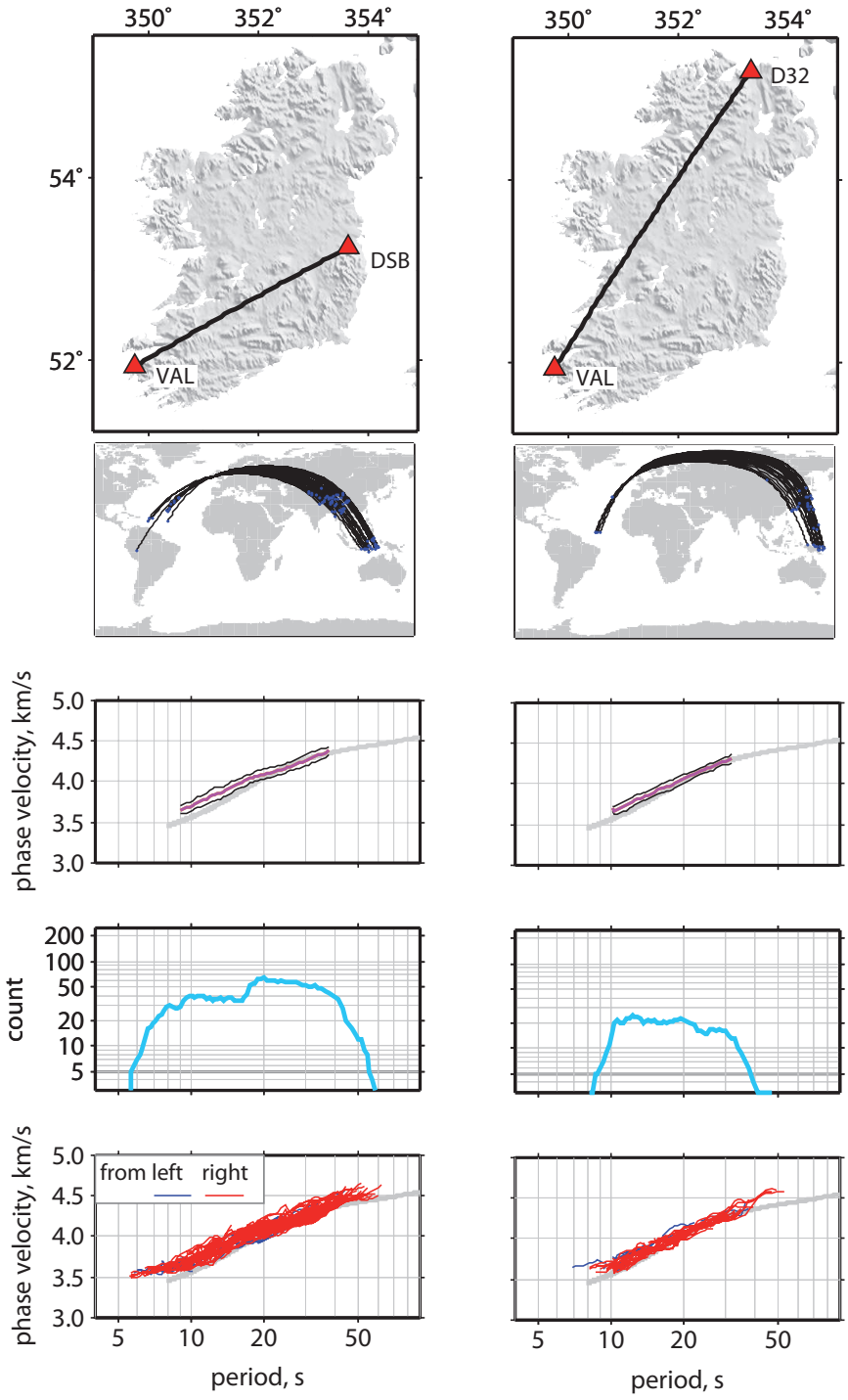



Figure 6.4.: Examples of Love wave-phase-velocity measurements. First row: Station pairs and inter-station paths. Second row: Event and source-station path distributions for each pair. Third row: Measured Love-wave dispersion curves, averaged from many "one-event" measurements. Grey lines show the PREM (Preliminary Reference Earth Model) (*Dziewonski and Anderson*, 1981) reference curves. Fourth row: Number of one-event measurements at each period. Fifth row: All one-event phase velocity curves measured for each pair. Blue and red indicate different directions of Love-wave arrival to the pair of stations.

### 6.2.1. Love wave phase velocity maps

Final dispersion curves were obtained from 21 pairs of stations shown in Fig. 6.1. These were used to compute phase velocity maps in the period range of 10-30 s (Fig. 6.5). However, this figure shows that most of the dispersion curves cover only the 12-30 s period range. It suggests that at 10 s period our data does not have sufficient coverage to map both isotropic and anisotropic phase velocity variations. Therefore, the Love wave phase velocity maps are constructed in the period range of 12-30 s. Love waves at 12-30 s period range sample primarily the middle crust and uppermost mantle (~15-~50 km depths). At these periods, Love waves can thus sample the entire Irish crust which is about 30 km thick (*Lowe and Jacob*, 1989; *Landes et al.*, 2005; *Hauser et al.*, 2008).

At 10-30 s period range (Fig. 6.5), inter-station paths are shown with coloured lines that are determined individually. The results indicate that phase velocities increase from 3.67 to 4.36 km/sec, and the phase velocity distribution of Love wave across Ireland seems consistent with Rayleigh wave phase velocity maps (Fig. 5.6) although Love-wave phase velocities in the 10-30 s period range are greater than Rayleigh wave phase velocities. Moreover, high velocity and low velocity anomalies are detected in the mid-lower crust. It is well known that variations in Love phase velocities are commonly associated with major tectonic units like faults or suture zones in regions because they are dominantly sensitive to the structures (e.g., *Curtis et al.*, 1998; *Cheng et al.*, 2013). In particular, this point is considered for qualitative interpretation of the phase velocity maps.

The phase velocity maps showing in Fig. 6.5 at periods of 12, 15 and 20 s, sampling from the middle crust to the lower crust, show a negative, cone-shaped anomaly between Leinster terrane, which is one of the main tectonic zones in Ireland, and the Killarney-Mallow fault (KMF) (Fig. 2.1). This anomaly roughly corresponds to the thinnest crust in the region (*Landes et al.*, 2005; *Landes et al.*, 2006).

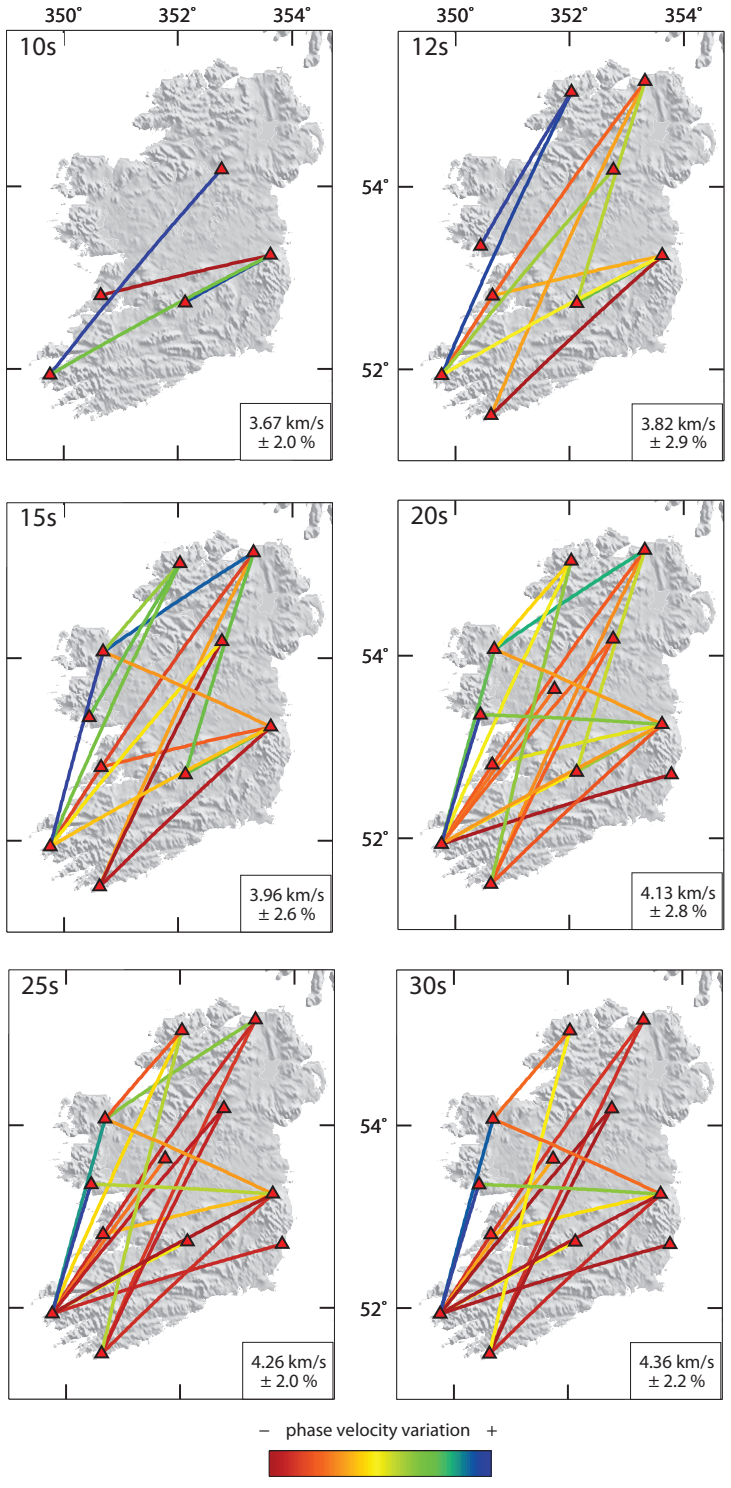



Figure 6.5.: Love-wave phase-velocity measurements at periods of 10-30 s for different inter-station paths. Variations in phase velocity are given by the colour scale. The period is indicated in the upper left corner and the reference phase velocity and scale limits in the lower right corner of each frame.

This is probably related to the mid-crustal flow that might be a result of late-Caledonian igneous orogeny (e.g., *Chew and Stillman,* 2009; *Chew*, 2009). In the rest of Ireland, however, maps (Fig. 6.5) in the given periods indicate a pervasive positive anomaly, which nearly corresponds to the thicker crust (e.g., *Landes et al.*, 2005; *Landes et al.*, 2006).

Additionally, the maps in periods that range from 20 s to 30 s, sampling from the lower crust down to uppermost lithospheric mantle, indicate that phase-speed from west to east significantly decreases (Fig. 6.5) and the phase-speed in Longford terrane and Leinster massif becomes lower (Figs. 2.1 and 6.5). This is probably an indicator of a possible low-velocity zone above a higher-velocity continental lithospheric mantle. This observation is also compatible with the findings of controlled-source experiments at mid to lower crustal depths in the region (*Hauser et al.*, 2008; *O'Reilly et al.*, 2010).

## 6.3. Love-wave anisotropy

The Love-wave measurements in this study were also inverted for Love-wave anisotropy using the same approach as for Rayleigh waves, which was described in chapter 5. Although there are fewer Love-wave measurements than Rayleigh-wave measurements, the Love-wave dispersion measurements from this study yield sufficient azimuthal coverage to map both isotropic and anisotropic phase velocity variations accurately.

If there is anisotropy, Love-wave phase velocities depend on the horizontally polarized shear velocities because velocities vary as a function of horizontal propagation direction (*Smith and Dahlen*, 1973). *Smith and Dahlen* (1973) showed that a plane-layered medium in the presence of a slight general anisotropy gives rise to an azimuthal dependence of the local phase velocity. They also described that a slight elastic anisotropy gives rise to azimuthal dependence of the phase velocities of both Love and Rayleigh waves of the form:

$$\delta C(T,\Psi) = C_0(T) + A_1(T)cos(2\Psi) + A_2(T)sin(2\Psi) + A_3(T)cos(4\Psi) + A_4(T)sin(4\Psi) \quad (6.1)$$

where $C$ is the measured phase velocity, $T$ is the period, $\Psi$ is the azimuth and $C_0$ is the isotropic phase velocity. In eq. 6.1 the coefficients ($A_i$) depend on the elastic properties of the medium and the period. The elastic variables are here used to parameterize elastic anisotropy. Here the dispersion data were inverted separately at a given period for the distributions of the isotropic phase velocity perturbations and the anisotropy coefficients given in the eq. 6.1, all parameterized at the knots of the same triangular grid with a nearly-uniform spacing of around 100 km. The inversion was performed using the LSQR algorithm of *Paige and Saunders* (1982), with smoothing and damping (*Lebedev and van der Hilst*, 2008).

As expected, mode interference, wavefront bending and uncertainties in horizontal component orientations cause some difficulties when describing anisotropic terms ($2\Psi$ and $4\Psi$ terms). Therefore, the $4\Psi$ terms (eq. 6.1) are described with the $90^0$ periodic azimuthal variations. They are more difficult to resolve than the $180^0$ periodic ($2\Psi$) ones. Therefore, for Love-wave anisotropy, only $4\Psi$ term is required.

Recent studies (e.g., *Trampert and Woodhouse*, 2003) have indicated that Rayleigh wave data requires $2\Psi$ and $4\Psi$ terms, but Love wave data needs only $4\Psi$ terms. The physical significance of this is that in earth structure containing oriented olivine crystals (or a similar petrological substance), the Rayleigh-wave azimuthal anisotropy is apparently independent of $4\Psi$ terms, but the Love-wave azimuthal anisotropy is not (*Crampin*, 1970). Thus, the finding of substantial $4\Psi$ terms for Love-wave anisotropy would be compelling evidence for the presence of a petrological cause of the anisotropy. In addition to this, the strong existence of $4\Psi$ would indicate that the sources of the observed azimuthal anisotropy are shallow (*Trampert and Woodhouse*, 2003).

As indicated in Fig. 6.5, the number of station pairs is not sufficient at 10 s period so tomographic maps of Love wave phase velocities including $4\Psi$ terms were computed in the 12-30 s period range (Fig. 6.6). The bar direction indicates the fast direction and the bar length is proportional to the anisotropy amplitude. Also, in this figure the yellow sticks indicate the fast-propagation directions and strength of $4\Psi$ azimuthal anisotropy. The anisotropy amplitude shows a slight gradual decrease at periods of 20-30 s. At 12s, we found that the detected

anisotropy amplitude is not as large as 15s period. In addition, at 12 s, Love-wave anisotropy shows a NE-SW fast-propagation direction. In contrast, at periods of 15-30 s, sampling the middle to lower crust, we detected Love-wave anisotropy with a NW-SE fast-propagation direction. We also observed that anisotropy of Love waves is largest (up to 2%) at a 15 s period.

Additionally, Love-wave phase velocity anomalies are computed as differences of observed curves which are computed according to the reference model PREM (*Dziewonski and Anderson*, 1981). We conclude our results (12-30s periods) are very close to a global continental average. The Love wave phase velocities are increasing from 3.83 to 4.36 km/sec and are larger than Rayleigh wave phase velocities presented in the chapter 5, as expected.

The effects of smoothing and damping on our data are also carefully analyzed in order to examine trade-offs between model resolution and roughness (*Menke and Abbott*, 1990). In tomographic studies, generally smoothing and damping are standard means of regularizing a tomographic inversion. Although choosing the amounts of smoothing and damping parameters is subjective, they are significantly determinative for such studies. The smoothing generally represents lateral averaging over different neighbouring interstation paths. In this study, we observed that the effective smoothing strength was similar for the period range 12-30 s. This may be related to the uniform path coverage at the periods across Ireland. This also suggests that no significant path bias is present in the results of the study.

Both $2\Psi$ and $4\Psi$ anisotropy patterns were smoothed in this study. We observed that the two terms are more strongly smoothed than the isotropic phase-velocity variations, although the isotropic coefficients are better resolved than the anisotropic terms. Additionally, in order to verify the robustness of our results, several resolution tests were performed. The tests suggest that the isotropic component of the model has a higher resolution than the anisotropic component. When a series of test inversions was performed, the portion of the data (including possible "outlier" measurements) did not reduce. We found that the leakage and trade-off between the isotropic and anisotropic terms are not significant (Fig. 6.6), but are not negligible. In particular, the issue of model resolution is considered because the trade-offs between isotropic

and anisotropic phase-velocity heterogeneities are potentially expected in the studies of surface wave tomography that includes a treatment of azimuthal anisotropy. For this reason, detailed tests are then carried out to derive the optimal smoothing and damping values for our inversion (for detailed information about resolution tests see chapter 3 and *Lebedev et al.*, 2013). Also, as a future work, F-tests are recommended to test whether anisotropy is statistically robust (whether 2Ψ or 4Ψ terms are required to explain the data or not).

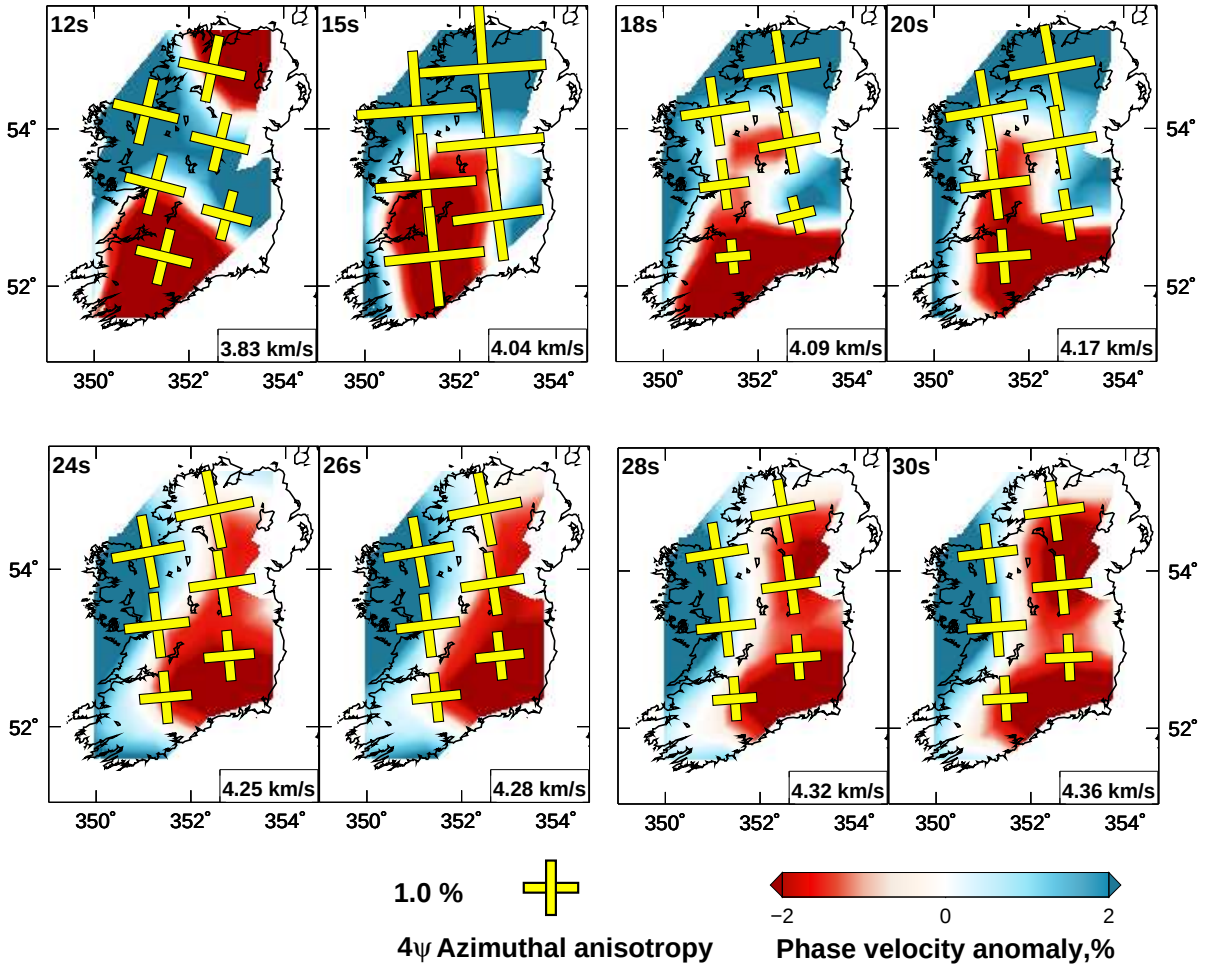



Figure 6.6.: Tomographic maps of Love-wave phase velocities 4Ψ anisotropy at periods of 12-30s. The period and reference phase velocity are indicated in the upper left and lower right corners of the frames, respectively. The isotropic anomalies are shown in the background using the colour scale. Yellow sticks show the fast-propagation directions and strength of 4Ψ azimuthal anisotropy.

### 6.3.1. Radially anisotropic shear velocity profile

One of the main purposes of this study is to constrain variations in radial anisotropy within the crustal and uppermost mantle across Ireland from surface wave dispersion analysis. For this purpose, inter-station broadband dispersion curves of seismic surface waves were measured using the two-station method (*Meier et al.*, 2004). The depth distributions of seismic velocities and their directional dependence (anisotropy) in the crust and uppermost mantle beneath Ireland have been revealed.

In the analysis, the final dispersion curves for Rayleigh and Love waves from 43 and 21 pairs of stations shown in Figs. 5.1 and 6.1 have been used. The one-path average profile including many average dispersion curves from different pairs is usually the preferred way to solve tomographic inverse problems for the distributions of the isotropic and anisotropic heterogeneity (e.g., *Zhang et al.*, 2007; *Endrun et al.*, 2011). Another reason for using this method is that there is not sufficient "one-event" measurements to derive robust averages for the pairs used. Based on this approach, a "one-path" average profile derived from Rayleigh- and Love-wave dispersions curves in the periods of 10-30 s has been obtained. This profile allows one to resolve trade-offs between model parameters in the crust and in the uppermost mantle and, thus, determine isotropic and anisotropic structure of both the crust and the uppermost mantle with a substantially higher accuracy, compared to more conventional, narrower-band measurements. Another advantage of inter-station dispersion analysis is that the local shear-velocity profile (characterizing the average seismic structure beneath the station pair) can be obtained from phase velocity data by solving a small, simple inverse problem (*Lebedev et al.*, 2009).

Model resolution is significantly affected by the density of ray paths, the wavelength of Rayleigh and Love waves, and the smoothing length used in the inversions. Therefore, the issue of model resolution must be addressed carefully in studies of surface wave tomography particularly for resolving the potential trade-offs between isotropic and anisotropic phase-velocity heterogeneities. The models are usually parametrized from the surface to 410 km depth with layers of constant elastic parameters, ranging in thickness from 2 km for the sedimentary cover

to 20 km in the mantle. The inversion parameters are formulated as perturbations to S velocities, with the basis functions (see Chapter 3, section 3.4.2 for further details) being boxcars for the crustal layers and triangles for the mantle layers (e.g., *Nolet*, 1993) (Fig. 6.7).

The inverted Rayleigh- and Love-wave phase velocity curves are used for a profile of vertically and horizontally polarized shear speeds, $Vsv$ and $Vsh$, respectively. Then, a preferred radially anisotropic S-velocity profile is obtained. The inversion is performed by means of non-linear optimisation from the MATLAB toolkit. It is not linearised: synthetic Love- and Rayleigh-wave phase velocities have been recomputed directly from every perturbed $Vsh$ and $Vsv$ profile, respectively, during the gradient search (*Lebedev et al.*, 2006, 2009). Each basis function in our inversions of dispersion data has been used to define two independent parameters. The parameters consist of isotropic $Vs$ perturbation and the amount of anisotropy within the depth range spanned by the basis function. The average shear speed of a profile has been determined using equation 6.2, while the amount of radial anisotropy of a profile has been determined using equation 6.3. Besides them, the Voigt isotropic average (*Voigt*, 1928) has been determined with $Vs(iso)=(2Vsv+Vsh)/3$ (for detailed information about this inversion process, see *Lebedev et al.*, 2009).

$$\delta Vs = Vs(ave) = (Vsh + Vsv)/2 \tag{6.2}$$

$$\delta Vs = Vs(ave) = |Vsh - Vsv|/2 \tag{6.3}$$

For this study triangular basis functions have been preferred instead of boxcar functions, because these allow for various gradients in both isotropic and anisotropic structure but not for sharp discontinuities between the Moho and the 410 km depth (*Lebedev et al.*, 2009). The reference models in the initial inversions are based on the 1-D reference model PREM with shear wave ($Vs$) and compressional wave velocities ($Vp$) from the VARNET project (*Hauser et al.*, 2008) inserted to construct the 1-D initial model.

The basic definition of radial anisotropy is based on the discrepancy between Love and Rayleigh wave phase velocity measurements. The term cannot be defined easily because this discrepancy between them cannot be simultaneously explained by the same isotropic model. However, in the earliest studies (*Aki and Kaminuma*, 1963), the discrepancy between Rayleigh- and Love-wave velocities was generally attributed to radial anisotropy. Recently, some researchers (e.g., *Lebedev et al.*, 2006; *Endrun et al.*, 2008) have used this approach in recent studies and they also indicated that surface wave dispersion measurements are particularly well suited to measure radial anisotropy.

The inversion of phase velocity curves from fundamental Rayleigh- and Love-waves, thus, yields a representative 1-D model of shear wave velocity down to approximately 40 km depths that may be interpreted as estimates of a "one-path" average model for the whole of Ireland. The results of this inversion depend on especially the damping values selected for isotropic and anisotropic parameters and are non-unique. In particular, the damping in the gradient-search inversion forces the $Vsv$ and $Vsh$ profiles to be the same below the depth limit of Love-wave sensitivity (around 45 km) (*Lebedev et al.*, 2009).

In order to interpret radial anisotropy, some possible causes have been suggested (e.g., *Crampin*, 1981; *Montagner*, 1994; *Gaherty*, 2004). One of these is that the measured radial anisotropy can be interpreted as a result of the alignment of anisotropic minerals in the lithosphere and asthenosphere (*Montagner*, 1994). Vertically oriented anisotropic fabric in the upper crust is also another possible cause of radial anisotropy. In addition, *Crampin* (1981) suggested that the effect of cracks is a basic cause particularly for upper crust anisotropy. Recently, some researchers (e.g., *Friederich and Huang*, 1996; *Gaherty*, 2004) have suggested that the simplest model in crystallographic symmetry system to explain radial anisotropy is a transverse isotropic model with a vertical axis of symmetry.

Ultimately, the final results from this analysis are indicated on Fig. 6.7 which summarizes most of our observations and inferences regarding the isotropic and radially anisotropic structures of the Irish crust:

(1) For inversion of Ireland-average Love and Rayleigh phase-velocity curves, a representative VARNET profile is used as a reference model. It is clearly observed that the model derived from the VARNET profile fits the data very well. This means that the resulting average S-crustal velocity model for Ireland is broadly consistent with the velocity models from the wide-angle results (*Hauser et al.*, 2008), showing evidence for crustal layers with laterally varying Moho depths, but these variations are not large. Also, it is apparent that shear velocities $Vs$ in the continental Irish crust, between the upper crust and the Moho, which range from 3.3 to ~4 km/s, are consistent with previous studies (*Van den Berg et al.*, 2005; *Landes et al.*, 2006; *O'Reilly et al.*, 2010). Consequently, based on this observation it can be said that the VARNET profile is representative for the whole Irish crust.

(2) Shear velocity ($Vs$) in the upper crust to Moho increases slightly as a function of depth. Rapid changes in vertical/lateral shear-speed structure are not observed. The observed slight variations in shear velocity explain moderate variations in crustal thickness and radial anisotropy. A possible explanation for no rapid changes of anisotropy with depth is that there is no change in anisotropic symmetry orientation.

(3) The Ireland-average radial anisotropy in the crust and uppermost mantle is slightly higher than the global average; it is slightly greater than 2%. Variations in the amount of the observed radial anisotropy within the upper crust to lower crust are not significantly large and are very smooth.

(4) Radial anisotropy measured from the data which was collected in this study is strongly indicative of horizontal fabric in the crust and uppermost mantle ($Vsh > Vsv$). This is a robust observation and consistently indicates horizontally oriented fabric due to the alignment (lattice preferred orientation (LPO) or shape preferred orientation (SPO)) of intrinsically anisotropic minerals in the crust and uppermost mantle beneath Ireland. The anisotropic fabric of the minerals is probably indicative of the patterns of deformation within the preserved crust that is an important record of its tectonic evolution.

(5) These overall results are consistent with the available geophysical evidence derived from

azimuthal anisotropy (*Polat et al.*, 2012).

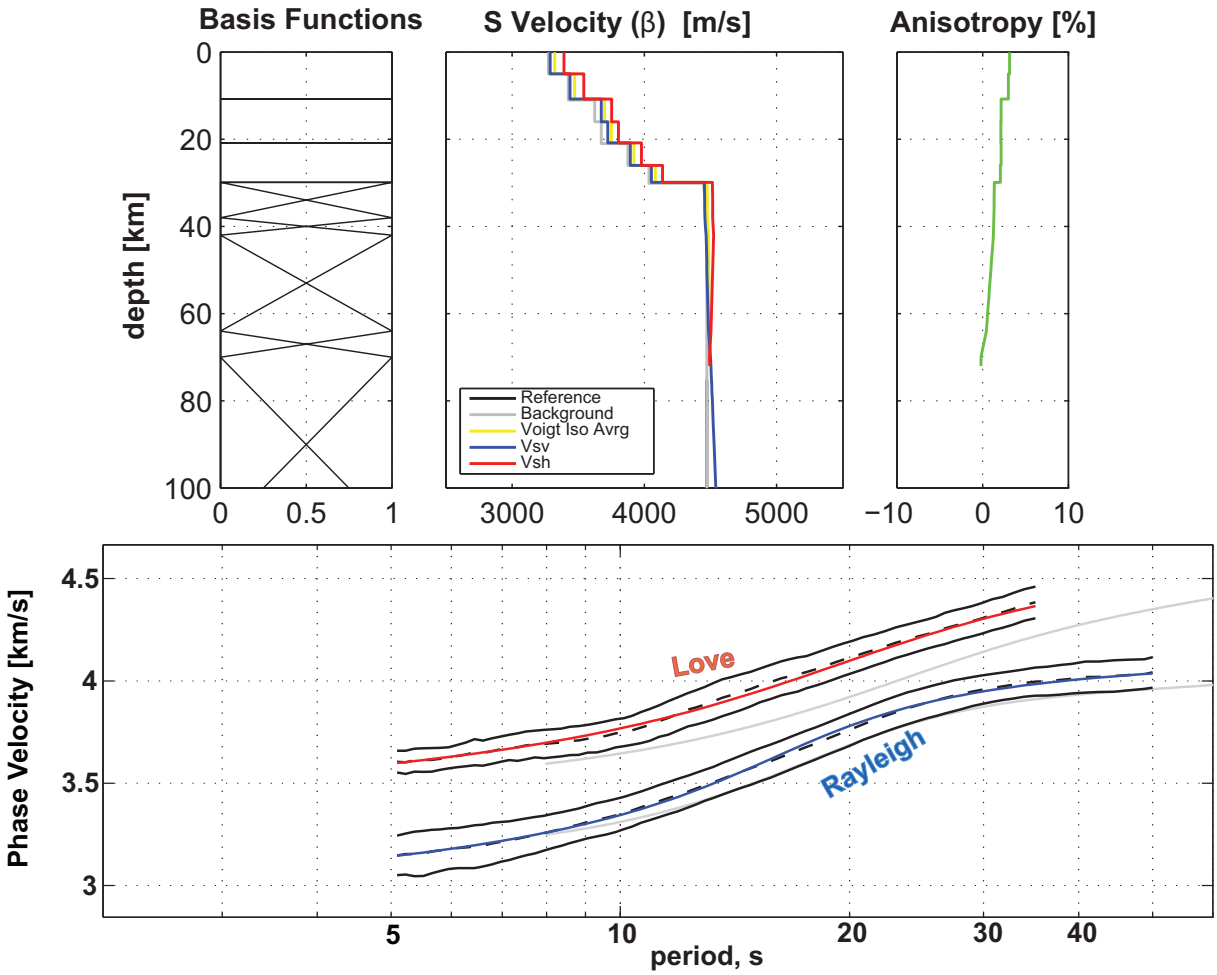



Figure 6.7.: The preferred radially-anisotropic S-velocity profile well fits the data from Ireland. The profiles of *Vsv*, *Vsh*, the isotropic average *Vs*(*iso*), and radial anisotropy are plotted in the depth range in which they are constrained by the data. (bottom) The corresponding synthetic Love and Rayleigh phase-velocity curves computed for the *Vsv* and *Vsh* profiles, respectively, and the measured curves with the errors indicated by the black lines. On the left at the upper plot, the final Basis function ranges from the upper crust to uppermost mantle.

# 7. Discussion on localization of anisotropy in depth

As presented in the previous chapters, during this study the shear wave splitting method and surface wave tomography were used to investigate seismic anisotropy in the mantle, especially the upper mantle, and continental crust beneath Ireland. Both methods were successfully applied to the collected data in this study, for the first time in Ireland. In the first part of this chapter, a variety of possible approaches which are used for localising depths of the detected seismic anisotropy from shear wave splitting analysis is presented. Then the main results from splitting observations and surface wave tomography are discussed.

## 7.1. Possible scenarios for origins of the anisotropy beneath Ireland

In this study, seismic anisotropy has been deduced from SKS and SKKS splitting measurements at 2 permanent and 40 temporary stations (Fig. 4.1) installed in Ireland. The majority of splitting measurements are obtained from earthquakes in South America with back azimuths of 180-270$^0$, and East Asia with back azimuths of 0-90$^0$. The observed splitting parameters ($\phi$ and $\delta$t) are not homogenous over Ireland (Fig. 4.18). Backazimuthal variations of the splitting parameters of teleseismic SKS and SKKS phases have been clearly observed at nearly all stations (Fig. 4.1). It thus makes invalid the assumption that the observed splitting originates

from a simple single anisotropic layer, with horizontal symmetry axis, located in only the upper mantle. Interpretation of such splitting observations requires additional complex models with regard to both geometries and localization of the depth of the anisotropy. Therefore, a variety of explanations is proposed here. Possible origins of anisotropy in the crust, lithosphere, asthenosphere and lower mantle are discussed. Then, the results from this study are interpreted in terms of the tectonic structure of the study area.

Averaging splitting parameters over the entire range of back azimuths leads to erroneous interpretation of the results where there is a significant variation with backazimuth, as observed in the present results. Therefore, the splitting parameters measured from the East Asian and South American event clusters will be separately interpreted and discussed.

### 7.1.1. Lithospheric anisotropy

In recent years, shear wave splitting has become a useful tool especially to measure lithospheric anisotropy because it has the potential to provide insights into the lithospheric structure and the possible mechanical coupling between the crust and the upper mantle. Lattice preferred orientation (LPO) of the most abundant and deformable minerals, particularly olivine, causes the upper mantle to be anisotropic. Therefore, seismic anisotropy in the upper mantle is typically attributed to the alignment of olivine due to tectonic forces (*Silver*, 1996). Note that this is significant because the observed anisotropy can be a consequence of frozen and active deformation within the lithosphere, and/or, in the asthenosphere, respectively. Anisotropy may thus provide a strict constraint on the character of past and present deformation in the lithosphere and sublithospheric mantle. For example, relic deformation in the lithosphere, or especially deep continental lithosphere related to fossil features of past tectonic events causes lithospheric anisotropy, whilst in the asthenosphere it is more likely due to plate-motion controlled flow or localized flow (e.g., *Vinnik et al.*, 1992; *Bormann et al.*, 1996; *Silver and Holt*, 2002).

Until recently, simple approaches have been developed to distinguish between lithospheric and astheonospheric anisotropy. The observed anisotropy in the lithosphere is, in general, as-

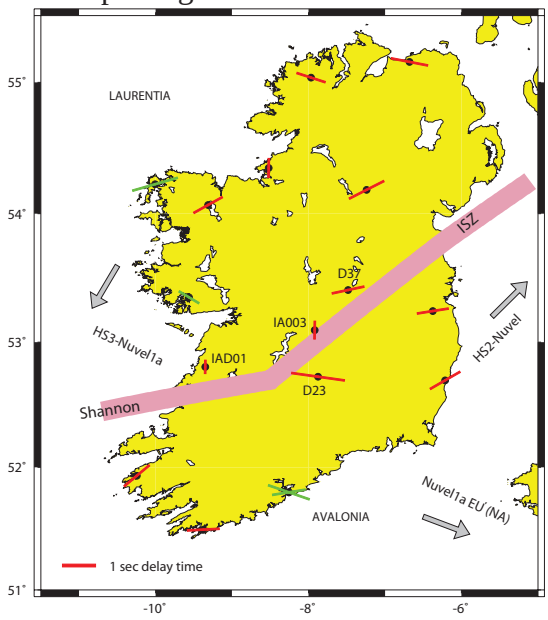
sumed to be associated with ancient geological processes (*Silver and Chan*, 1988), whereas the asthenospheric anisotropy is likely to be related to a result of mantle convection (*Debayle and Kennett*, 2000). However, the relative contributions of lithospheric and asthenospheric anisotropy are difficult to quantify. A recent study by *Conrad et al.* (2007) indicated that especially strong geodynamic modelling is required to help distinguish lithospheric anisotropy from asthenospheric anisotropy. Thus, through geodynamic modeling, the depth of seismic anisotropy may be confined.

Before describing some modelling to explain the results of this study, it is essential to describe one of the hypotheses which has been developed in order to distinguish lithospheric anisotropy from other anisotropic sources such as asthenospheric anisotropy. This hypothesis is based on coherent deformation between crust and subcontinental mantle because elastic deformation generally occurs in the lithospheric mantle. It is generally observed that the fast polarization directions are parallel to finite strain direction in the crust despite the main contribution of the observed anisotropy coming from the mantle (e.g., *Silver*, 1996). This style of deformation is termed vertically-coherent deformation (VCD) (e.g., *Silver and Chan*, 1988; *Silver*, 1996). The determined shear wave splitting parameters from this study are interpreted according to this hypothesis.

**a) East Asian cluster**

For this event cluster, average splitting results show roughly E-W orientations (Fig. 7.1), and also show a relatively moderate uniformity. However, some stations such as D23, IA003 and IAD01 located in the ISZ show rapid spatial variations in $\phi$ and $\delta$t that may be related to crustal anisotropy (Fig. 7.1). As known, the typical delay time value for crustal anisotropy is perhaps 0.1-0.2 s, and that this represents a small contribution to typical delay times determined from teleseismic data and attributed to mantle anisotropy, which are typically ~1 s for most raypath geometries (e.g., *Silver*, 1996; *Long and Silver*, 2009). Therefore, any crustal contribution to broadband data is usually ignored.

Average SKS splitting measurements from the EA cluster




Average SKS splitting measurements from the SA cluster

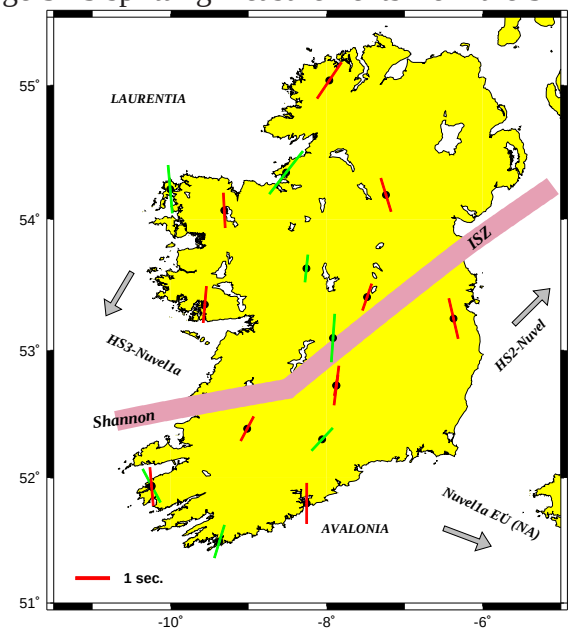



Figure 7.1.: Averaged fast directions and delay times from SKS measurements from the main clusters. The length of bars is proportional to $\delta$t. Each red bar represents a weighted average measurement (if there is more than one measurement). Single measurements (if there is only one measurement per station) are plotted as green bars. Big gray arrows indicate the directions of present-day plate motions which are calculated according to difference refence frames: absolute motion (APM) directions of the Eurasian plate (EU) based on the NUVEL1A plate model (*Gripp and Gordon*, 1990) in the nonet rotation (NNR) and hotspot (HS) reference frames, respectively.

*Bastow et al.* (2007) measured small time delays that are less than 0.4 s in Scotland, but they are perfectly aligned with the tectonic units such as the Great Glen Fault and the Highland Boundary Fault. Additionally, they found rapid spatial variations in $\phi$ and $\delta$t which confirm strong contributions by crustal anisotropic layers. In our case, the measured delay times at the stations IA003 and IAD01 are as small as the delay times measured by *Bastow et al.* (2007) in Scotland. In addition, at some stations D23, IA003 and IAD01 we found some rapid spatial variations in $\phi$ and $\delta$t. Fig. 7.1 shows a $\sim$ 1 s increase in $\delta$t between stations IA003 and D23. The stations are only separated by a distance of $\sim$30 km so Fresnel zone arguments (for more detail, see *Alsina and Snieder*, 1995) suggest that the observed significant difference in $\delta$t is accrued in the crust. Therefore, it is suggested that the crustal contribution to shear wave splitting is quite high. It means that the observed anisotropy beneath central Ireland is probably related to fabrics within deep crustal rocks that preserve a record of deformation during and after the continental collisions. This observation is also confirmed by anisotropic Rayleigh-wave tomography showing that anisotropy of Rayleigh waves at 10-20 s periods indicates a NE-SW fast propagation direction and is largest (up to 2%) at a 15 s period, at which Rayleigh sample primarily the middle and lower crust.

The E-W orientations of fast polarization directions from this cluster are mainly parallel to the Variscan structural fabrics. The Variscan Orogeny (380 Ma) significantly influenced the tectonic and geologic structure of Ireland. Particularly, significant deformation in southern Ireland developed during this orogeny. However, the amount of the measured splitting is not compatible with Variscan units because the extent of the deformation during the Variscan Orogeny is generally considered to be limited to the upper crust (referred to as a “thin-skinned” tectonic model) (e.g., *Landes et al.*, 2000). As a consequence, the contribution of seismic anisotropy caused by Variscan deformation will be small but not negligible. Therefore, we can suggest that the measured anisotropy resides at sub-upper crustal and deeper mantle levels and the significant amount of the observed anisotropy developed during the Caledonian Orogeny.

On the other hand, the accumulative thickness of the anisotropic region ($L$) can be estimated

from the measured delay time ($\delta$t) and the degree of anisotropy ($\delta V_s$) (*Mainprice and Silver*, 1993):

$$\delta t = L\delta V_s/(V_s), \tag{7.1}$$

$$V_s = [V_{smax} + V_{min}]/2 \tag{7.2}$$

and

$$\delta V_s = 100[V_{smax} - V_{min}]/(V_s). \tag{7.3}$$

For example, assuming an average S-wave velocity of about 4.3 km/s and a value of $\delta V_s$ ~ 3.5%, a delay time of ~1.2 s is equivalent to 140 km, which is consistent with the average lithospheric thickness in the study area estimated by *Artemieva* (2006).

In summary, the correlation of $\phi$ with the structural trends seems to support the assumption of the frozen anisotropy hypothesis for the splitting results from the East Asian event cluster. According to this, observed anisotropy generally tracks the strain field developed during the last major pervasive tectonic period (*Silver*, 1996). For our case, presumably the Caledonian Orogeny mainly caused fossil anisotropy in sub-upper crustal strain fields beneath Ireland.

**b) South American cluster**

The fast polarization directions from high quality and averaged measurements obtained from this cluster are relatively uniform and they exhibit approximate N-S orientations (Fig. 7.1). There is not the strong alignment of $\phi$ with either Caledonian and Variscan structural trends as found from the East Asian cluster.

As observed in Fig. 7.1, there is no significant difference in $\delta$t values between measurements from this cluster and the East Asian cluster. However, the observation that the measured $\phi$ from the two clusters are completely different from each other, indicates an anisotropy of a fundamentally different origin is present.

Although there is no correlation between fast polarization directions from this cluster and tectonic units in the study area, it was observed that the N-S orientations of splitting parameters are significantly consistent with long axis of the finite strain ellipsoid at a depth of 175 km for the North Atlantic region on the regional scale (*Marquart et al.*, 2007) (Figs. 7.1 and 7.2).

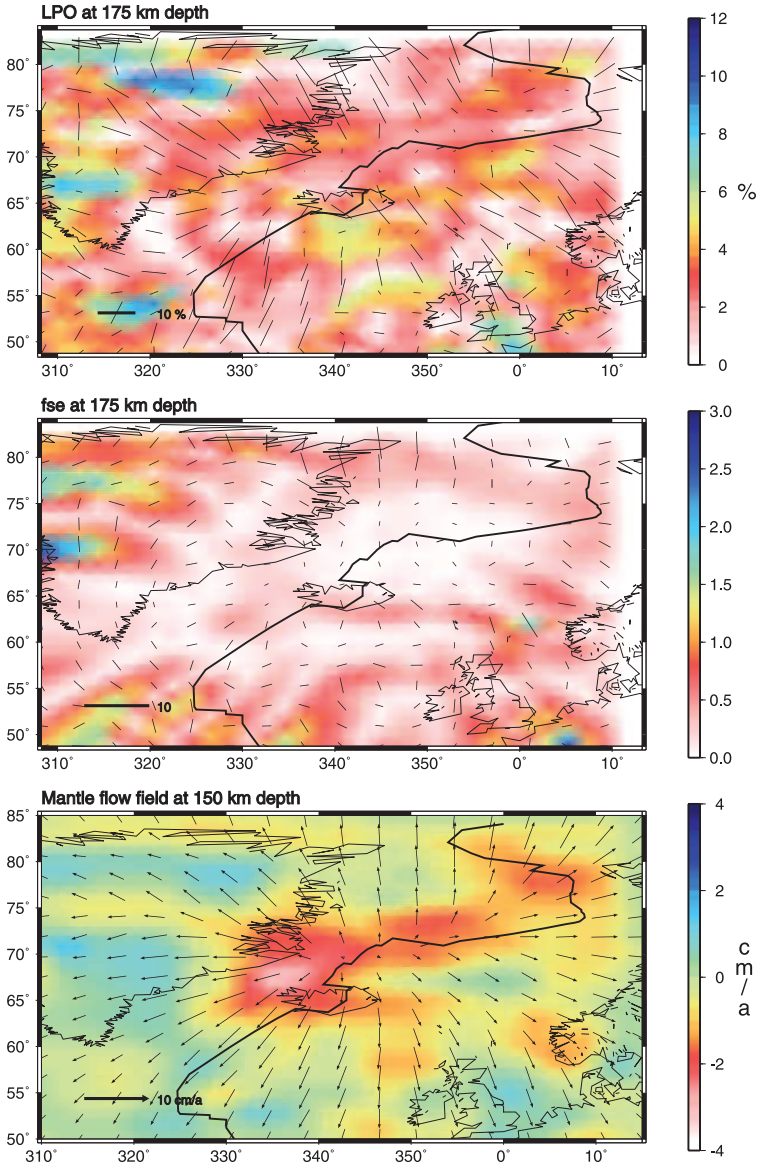



Figure 7.2.: (Bottom) Regional mantle flow model at a depth of 150 km, (middle) long axis of the finite strain ellipsoid, and (top) LPO of olivine at a depth of 175 km based on the 3-D flow model. Vertical components are indicated by color (taken from *Marquart et al.*, 2007).

### 7.1.2. Asthenospheric anisotropy

Simple Asthenospheric Flow (SAF) (*Silver*, 1996) is based on the theory that subcontinental mantle anisotropy is controlled by asthenospheric flow. Generally, asthenospheric flow is used to explain mantle preferred orientation of olivine (e.g., *Russo and Silver*, 1994). In this case, it is also assumed that the a-axis of olivine for vertically propagating shear waves is parallel to the splitting fast polarization direction. Therefore, the flow field and corresponding anisotropic properties are easily predicted. In other words, when flow occurs in simple shear, the a axis of olivine therefore tends to be parallel to the direction of flow (*Savage*, 1999).

When asthenospheric flow causes seismic anisotropy, the mechanism will form the foliation plane and lineation direction in the horizontal plate and thus the lineation direction follows the flow line, which in turn is parallel to the absolute plate motion (APM) direction of the plate (*Silver*, 1996). Thus vertical propagation through the plane will yield less splitting than would vertical propagation through a lithospheric region with transcurrent deformation (e.g., *Mainprice and Silver*, 1993).

It is assumed that the memory of the asthenospheric flow direction is short i.e. a few million years. However, this time duration is enough to completely reorient olivine (e.g., *Mainprice and Silver*, 1993). Therefore, the correlation between anisotropy related to asthenospheric flow and relative plate motion is constructed. Plate motion can be modelled by large convection cells which are produced by thermal convective flow (e.g., *Bunge and Richards*, 1996). One possibility for supporting this idea (e.g., *Leven et al.*, 1981) is that the passive motion of the lithosphere over the relatively stationary asthenosphere orients the fast directions and therefore $\phi$ parallel to the plate motion. In the next section, splitting parameters from this study are examined according to this hypothesis.

According to the plate tectonic theory, the asthenosphere is the region of the Earth between 100-200 km below the surface but perhaps extending as deep as 400 km. Also it is the weak or soft zone in the upper mantle. Hence, the dominant mechanism that controls the deformation of hot, mechanically weak asthenosphere is shear strain related to flow.

Previous studies (e.g., *Tommasi et al.*, 1996) show that in oceanic regions the plate motion is probably related to the mantle flow and therefore to the plate motion whereas in continental areas it is thought to be related to internal deformation (*Silver*, 1996). Here the main question is how much is related to past tectonic activity and how much relates to recent, on-going deformation?

**a) East Asian cluster**

For this cluster, we observed that there is no strong correlation of the fast polarisation directions ($\phi$) with the present-day plate motion directions (Fig. 7.1). This means that large-scale asthenospheric flow cannot make a significant contribution to the observed anisotropy in Ireland. Similarly, *Bastow et al.* (2007) for the Scottish Highlands suggested that asthenospheric fabrics due to the Tertiary rifting and present day plate motions do not strongly influence the splitting parameters observed in the Scottish Highlands. However, *Barruol et al.* (1997) have indicated that the orientation of the fast split shear waves measured in western Europe at a plate-wide scale exhibit a general parallelism with the APM directions and also the Hercynian and Caledonian structures.

**b) South American cluster**

As mentioned before in this chapter, fast polarization directions obtained from this cluster are fairly uniform. There is strong evidence of a fair alignment of the fast polarization directions $\phi$ with the long axis of the finite strain ellipsoid (fse) that often points in the flow directions and mantle flow at a depth of 175 km (Figs. 7.1 and 7.2). This probably suggests that mantle flow in the North Atlantic is likely to cause seismic anisotropy beneath Ireland at a depth of 175 km (Fig. 7.2) (*Marquart et al.*, 2007).

Seismic anisotropy is often used to measure mantle convection because LPO is a function of the finite deformation associated with mantle convection and the long axis of the finite strain ellipsoid (fse) often points into the flow direction. According to this argument, it is possible to accept the long axis of the finite strain ellipsoid (fse) as a possible cause of the anisotropy measured from the SA event cluster.

## 7.2. Seismic anisotropy models

It has been clearly observed that there is a strong dependence on backazimuth for the measured splitting parameters (Fig. 7.1). For a single horizontal layer model, splitting parameters do not vary with initial polarization direction. Such variation can however occur when an anisotropy tensor is inclined to the vertical, or has a more complicated symmetry, or both (Fig. 7.3) (e.g, *Savage*, 1999; *Long and Silver*, 2009).

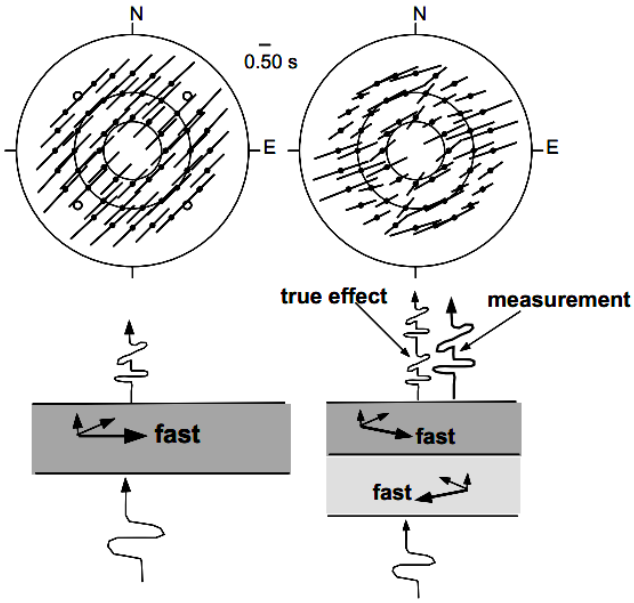



Figure 7.3.: Shear wave splitting in one and two−layer media. Bottom left: A linearly polarized shear wave pulse enters an anisotropic layer and is split into two components that propagate at different velocities. The polarization direction of the faster component is parallel to the fast anisotropic axis of the layer. Top Right: Graphical depiction of the splitting parameters for radially-polarized shear waves of different backazimuths, Φ, and angles of incidence. The orientation of the line segment indicates fast azimuth azimuth, $\phi$, and its length is proportional to delay time,$\delta$t. The position of the line segment on the polar diagram indicates backazimuth and angle of incidence, with the 10, 20 and 40 km/s circles shown (for a detailed description of the anisotropic models see *Levin et al.*, 1999).

Therefore, azimuthal variations in the splitting parameters make interpretation of seismic anisotropy complicated. But, for the case of two or multiple layers of anisotropy, this back azimuthal variation takes the form of a periodic variation in both $\phi$ and $\delta$t measurements with a $\pi/2$ periodicity (*Silver and Savage*, 1994) while a dipping axis of symmetry indicates itself as a $\pi$

periodicity for the case of transversely isotropic (TI) symmetry (e.g., *Chevrot*, 2000). Variations in splitting parameters can also be explained by some possible scenarios that involve an inclined orientation of hexagonal and orthorhombic anisotropic tensors (*Plomerova et al.*, 1996; *Levin et al.*, 1996) and also the combination of two or more layers of anisotropy with hexagonal symmetry and horizontal symmetry axes (*Silver and Savage*, 1994; *Vinnik et al.*, 1995a). Thus, back-azimuth variations in splitting parameters are likely to be related to complex anisotropy in the mantle. We now discuss a two-layer model.

### 7.2.1. Two-layer anisotropy model

**A) Two-layer anisotropy model with a horizontal symmetry axis**

Here the possibility of a two-layer anisotropy model is investigated. The SPLITTING MODELER[1] modelling program, developed by Menke (2001), has been used. This modelling program calculates the predicted fast directions and delay times for a suite of back azimuths from an input model with multiple anisotropic layers.

This method is applied to data from stations DSB and VAL (Figs. 7.4 and 7.5). 44 and 54 reliable shear wave splitting measurements at the these stations (DSB and VAL stations respectively) were used. By using the program the predicted fast directions and delay times for a suite of back azimuths from an input model with multiple anisotropic layers were calculated (for further detail, see *Levin et al.*, 1999).

The two-layer anisotropy model was constructed with a horizontal symmetry axis in both layers. The model included a top layer having a fast polarisation direction oriented parallel to an approximate Caledonian trend (45 clockwise from North), underlain by an anisotropic layer parallel to the plate motion direction NNR $\sim 60^0$ (clockwise from north), calculated from the NUVEL1A plate model (*Gripp and Gordon*, 1990) in the no net rotation frame. According to this approach, we assumed that the top and bottom layer represent the lithospheric and asthenospheric anisotropy media, respectively. We modelled the top layer as 80 km thick, containing

[1] http://www.ldeo.columbia.edu/users/menke/software.html

standard olivine with intrinsic S-wave anisotropy $\delta V_S$ ~3.7%, corresponding to the maximum average of $\delta V_S$ as measured from lithospheric olivine. The bottom layer is 40 km thick, with nearly double magnitude of intrinsic anisotropy. The final observation from the two-layer model with horizontal symmetry axes shows that there is a reasonable correlation between the predicted and the observed splitting parameters from the EA cluster, but not from the SA cluster (Figs. 7.4 and 7.5).

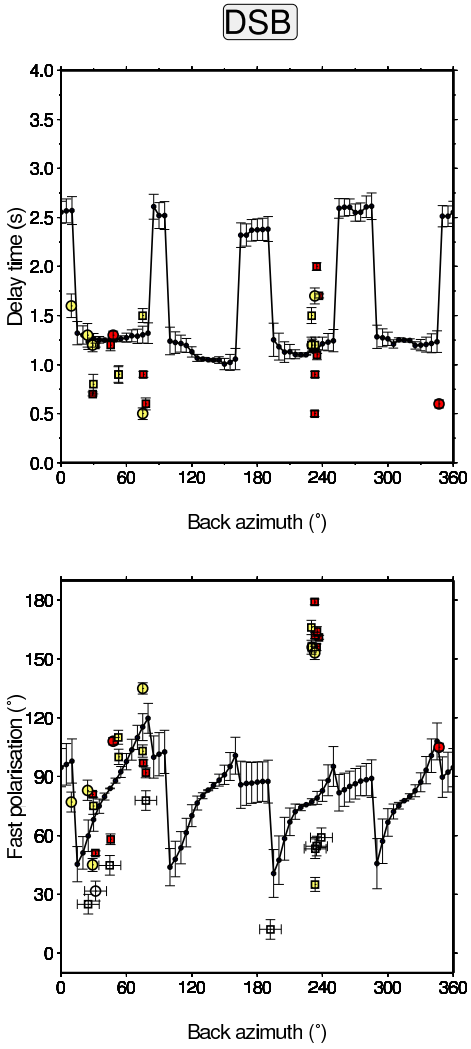



Figure 7.4.: Showing variations of predicted delay times (top) and fast polarisation directions (bottom) calculated from a model of two anisotropic layers with horizontal symmetry axis. Thick solid black lines are predicted curves. Results from medium (yellow symbols) and good (red symbols) splitting measurements carried out at DSB are also plotted. Circles and squares show results from SKS and SKKS measurements, respectively. Null splitting observations are plotted with two perpendicular error bars.

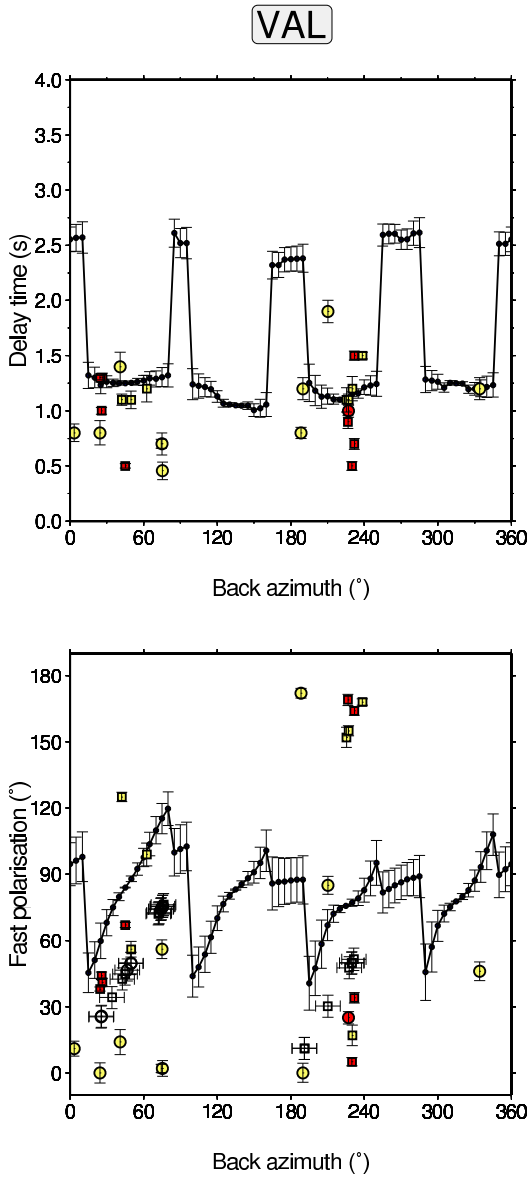



Figure 7.5.: Explanations as in Fig. 7.4.

Another explanation for the variations in splitting parameters is now discussed.

**B) More complex symmetry axis geometry**

As previously mentioned, the SKS and SKKS phases that are commonly used to probe anisotropic structure in the mantle are shown in Fig. 3.15. As known, they provide several advantages over other shear phases, in addition to the fact that its unperturbed polarization is controlled by the P-to-S conversion at the CMB, which is significant from a measurement point of view, this conversion also means that any observed splitting must be due to anisotropic struc-

ture on the receiver side from the CMB to surface. The nearly vertical propagation of SKS through the upper mantle also means that the incidence angle will be well within the so-called shear wave window (shear phases that have incidence angles larger than ~$35^0$ at Fig. 3.14. Nevertheless, due to the properties of the investigated area, sometimes the propagation direction of the phase is not vertical. In other words, if splitting parameters are measured in a complex medium, it is possible that they vary as a function of back azimuth and incidence angle.

In our case, it was clearly observed that there was very strong variation in the fast polarization directions with back-azimuth. In addition to this, the final results have been examined to see if there is a possible relationship between incidence angle and splitting parameters. This type relationship is usually used to construct a model which is based on inclined or dipping symmetry axes, although full symmetry systems have not yet been determined (*Savage*, 1999).

As an example, the splitting parameters of station D34 have been plotted as a function of incidence angle (Fig. 4.32). The conclusion from these plots is that there is no correlation of delay times with incidence angle. However, slight variations in fast-polarization directions obtained from the EA cluster with incidence angle were observed (Fig. 4.32). That may suggest lateral variations of the anisotropy, so for this station we have to consider more than one anisotropic layer and / or the existence of an inclined axis or dipping axis of symmetry. This observation led to further examination using different stations.

The two permanent stations VAL and DSB and one temporary station, D23, were chosen. Medium and high quality splitting measurements from the EA and SA event clusters at these stations have been plotted as a function of incidence angle (Fig. 7.6). The incidence angle varies between 10-20 $^0$. This figure indicates that for DSB and VAL there is no systematic variation of delay time as a function of incidence angle. However, for station D23 a slight increase in delay time with increasing incidence angle is seen. This is important because the variations in shear wave splitting lag times with incidence angle may suggest a purely horizontal symmetry axis for station D23 (*Sandvol et al.*, 2003).

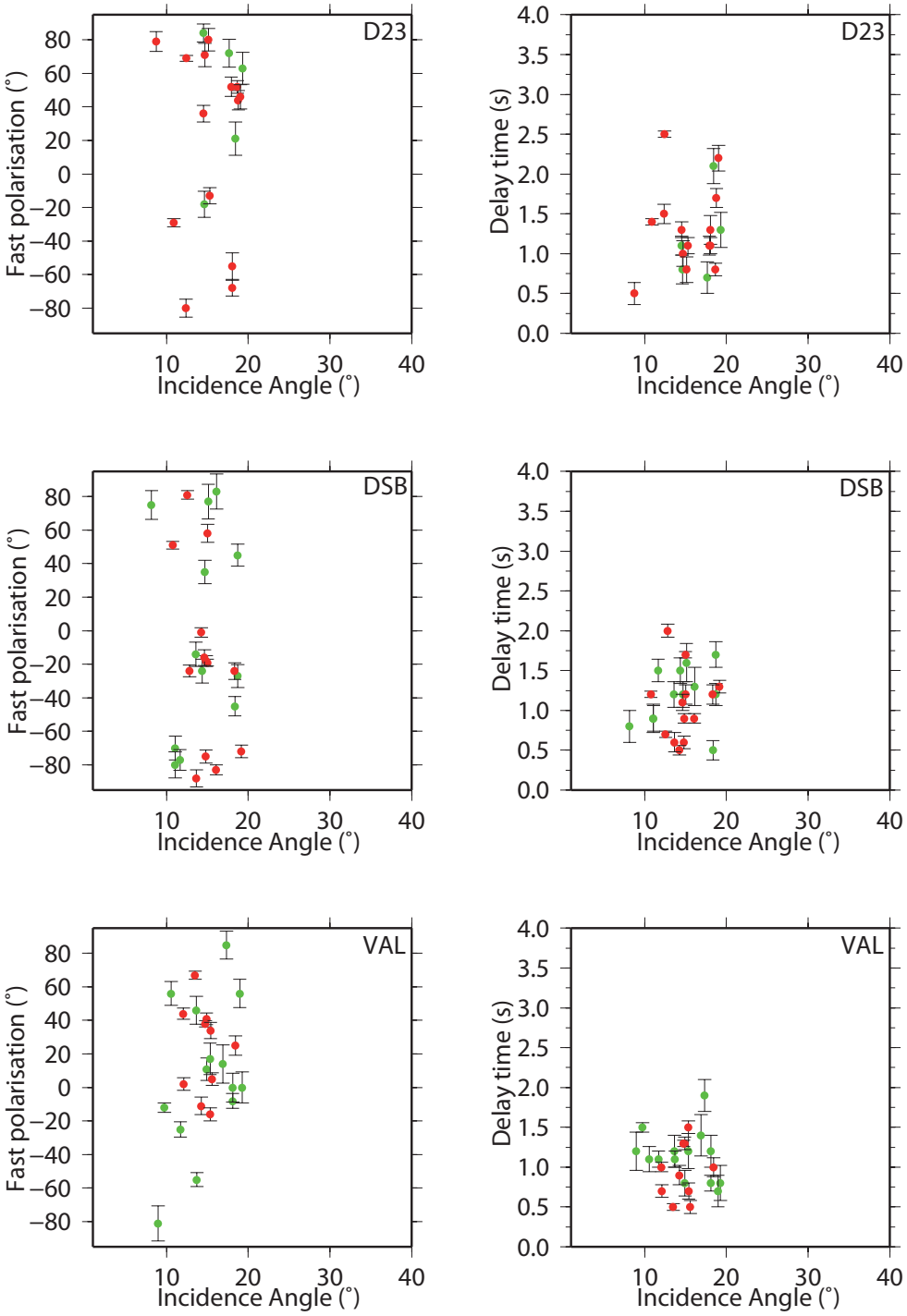



Figure 7.6.: An example of plots of individual splitting measurements versus incidence angle at stations D23, DSB and VAL. Variations of delay time (right) and fast direction (left) with incidence angle are shown respectively. Error bars represent 95% confidence intervals for each of the estimated individual parameters. Red and green filled symbols indicate good and medium quality splitting measurements.

### 7.2.2. Lateral variation and depth of seismic anisotropy from Fresnel zone arguments

So far, this study has indicated that there are several possible causes resulting in seismic anisotropy. We have tried to explain our results from the EA and SA clusters with some arguments previously mentioned. Although they are sufficient to reveal the origins of the observed anisotropy, here we aim to extend further the discussion to help localize the depth of the anisotropy sources.

An approach proposed by *Alsina and Snieder* (1995) based on the calculation of Fresnel zones at different depths for shear-wave arrival has been used in this study. *Alsina and Snieder* (1995) described the concept of Fresnel zones as a function of depth for SKS/SKKS phases arriving nearly vertically at two neighbouring stations (Fig. 7.7). They suggest that differences in splitting results obtained at one station from two events of nearly opposite back azimuths indicate that i) anisotropy occurs at depths larger than $Z_1$ where the Fresnel zones of the two ray paths start to separate (see Fig. 7.7), and/or ii) presence of a lateral variation of anisotropy below $Z_1$. Similarly, differences in splitting results obtained at the two neighbouring stations from events with the same back azimuths indicate lateral variations of anisotropy occurring above depth $Z_2$ where the Fresnel zones of the two ray paths begin to separate. For this approach, stations DSB and VAL were chosen because they are the two most separated stations and have the best constrained splitting results. As previously described in chapter 4, the determined splitting parameters have been mainly obtained from the East Asian (BAZ:0-$90^0$) and the South American (BAZ:180-$270^0$) event clusters coming from nearly opposite back-azimuths. The Fresnel zone radius $Rf$ at a depth $h$ is calculated from the formula $Rf=(Tvh/2)^{1/2}$, where $T$ is the dominant period and $v$ is the wave velocity. The Fresnel zones at 210, 410, 660 and 2890 km depth were calculated assuming velocities of S-waves propagating in the mantle of between 4.3 and 7.2 km/s estimated from the PREM velocity model (*Dziewonski and Anderson*, 1981) with a dominant period of 10 s.

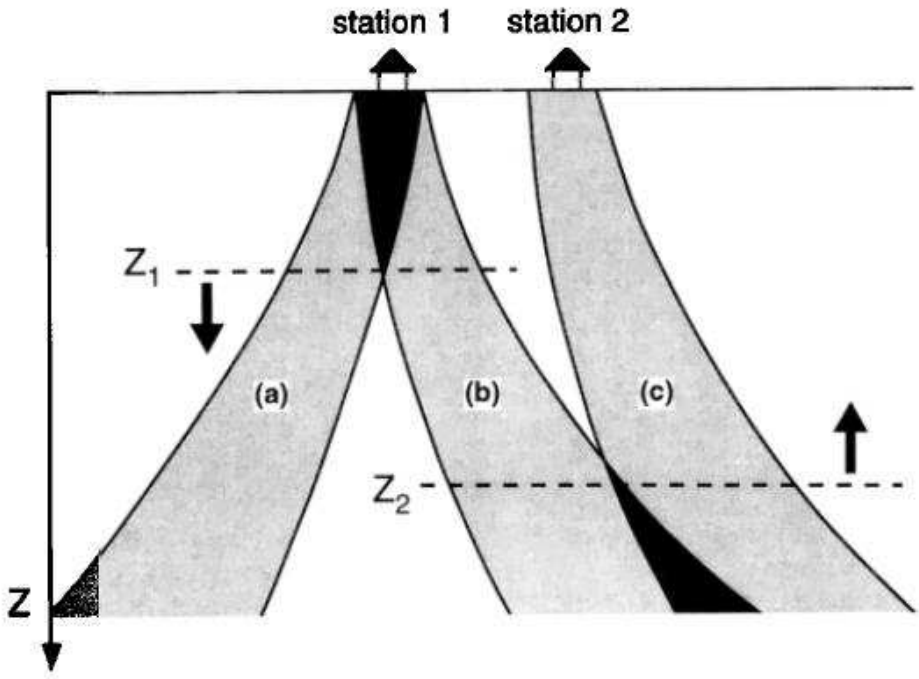



Figure 7.7.: Schematic illustration of the Fresnel zone as a function of depth for SKS phases arriving nearly vertically at two neighboring stations. The two different back azimuths (a and b) at station 1 share a common path above $Z_1$, while similar back azimuths at stations l(a) and 2(c) share a common path below $Z_2$. Thus, assuming a simple symmetry system in which parameters vary little with back azimuth, different results from opposite back azimuths at station 1 suggest that anisotropy occurs below $Z_1$. Similarly, differences in splitting between events from the same back azimuth recorded at stations 1 and 2 would be caused by differences in anisotropy above $Z_2$. Taken from *Alsina and Snieder* (1995).

Figs. 7.8 and 7.9 show local and regional maps, respectively, indicating the piercing points at the different depths for SKS and SKKS phases analysed at DSB and VAL, with the Fresnel zones plotted at central points for each group of exit points at the corresponding depths. Fig. 7.8 indicates that at both DSB and VAL, the Fresnel zones of ray paths from opposite back azimuths, e.g. South America and East Asia, begin to separate below about 410 km depth. Since the fast polarization directions from these two event clusters are distinctly different at both stations (e.g., see Fig. 7.8), this suggests that a possible source of anisotropy below 410 km influences the splitting, at least for data from one of the event clusters.

Fig. 7.8 also shows that the overlap of Fresnel zones for ray paths arriving at DSB and VAL

from similar backazimuths will occur at depths below 660 km. As the results from similar backazimuths at the two stations are similar, this indicates that lateral variations in anisotropy above about 660 km do not significantly affect the splitting results, or that anisotropy outside this depth range dominates the observed anisotropy.

Further information can be obtained by looking at the splitting results from crossing rays. For example, the Fresnel zones of crossing rays from, say, the South American cluster to DSB and from the East Asian cluster to VAL, start to overlap below about 250 km and still overlap at 660 km indicating that they are sampling the same volume of mantle from about 250 km to somewhat below 660 km. The splitting results from these two crossing rays give distinctly different fast polarization directions which therefore suggests that there is a lateral variation in anisotropy originating from either above ~200-300 km, or below 660 km depth (or both).

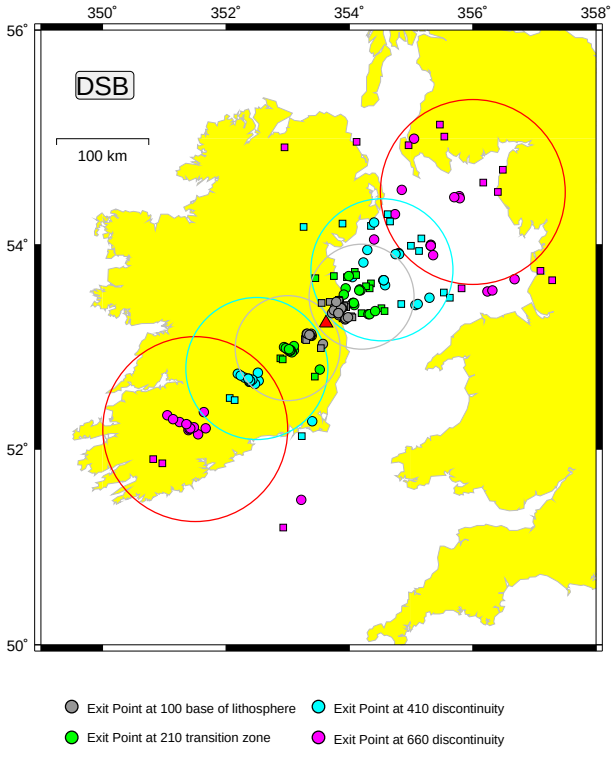
The following is a brief of summary of the results:

(1) A possible presence of anisotropy below ~410 km depth has been revealed by splitting results from two opposite back azimuths from the results at both VAL and DSB.

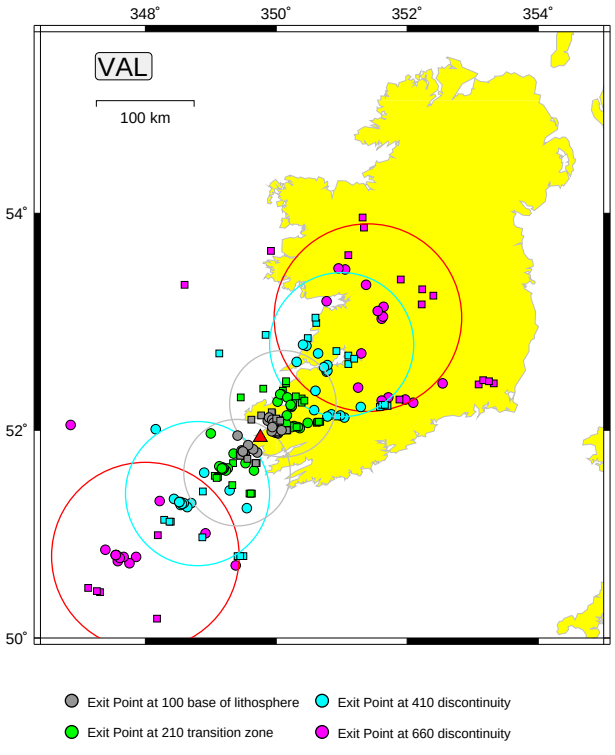
(2) At the stations VAL and DSB, it was observed that above 660 km depth, variations of anisotropy were not clearly observed from the splitting results obtained from similar events.

(3) Splitting results from two crossing rays suggest lateral variation of anisotropy should occur above a depth of about 250 km or below a depth of 660 km (or the D”).

(4) Finally, it can be concluded that a possible existence of anisotropy, or a significant lateral variation in the anisotropy, may be located at depth below a depth of 660 km, or within the D”, or both.




(a)




(b)

Figure 7.8.: Exit points of SKS (circles) and SKKS (squares) phases at different depths for events used at permanent stations DSB and VAL. Red, light blue and grey circles are estimated Fresnel zones at the 660 km, 410 km and 210 km discontinuities for a shear-wave of 0.1 Hz, respectively.

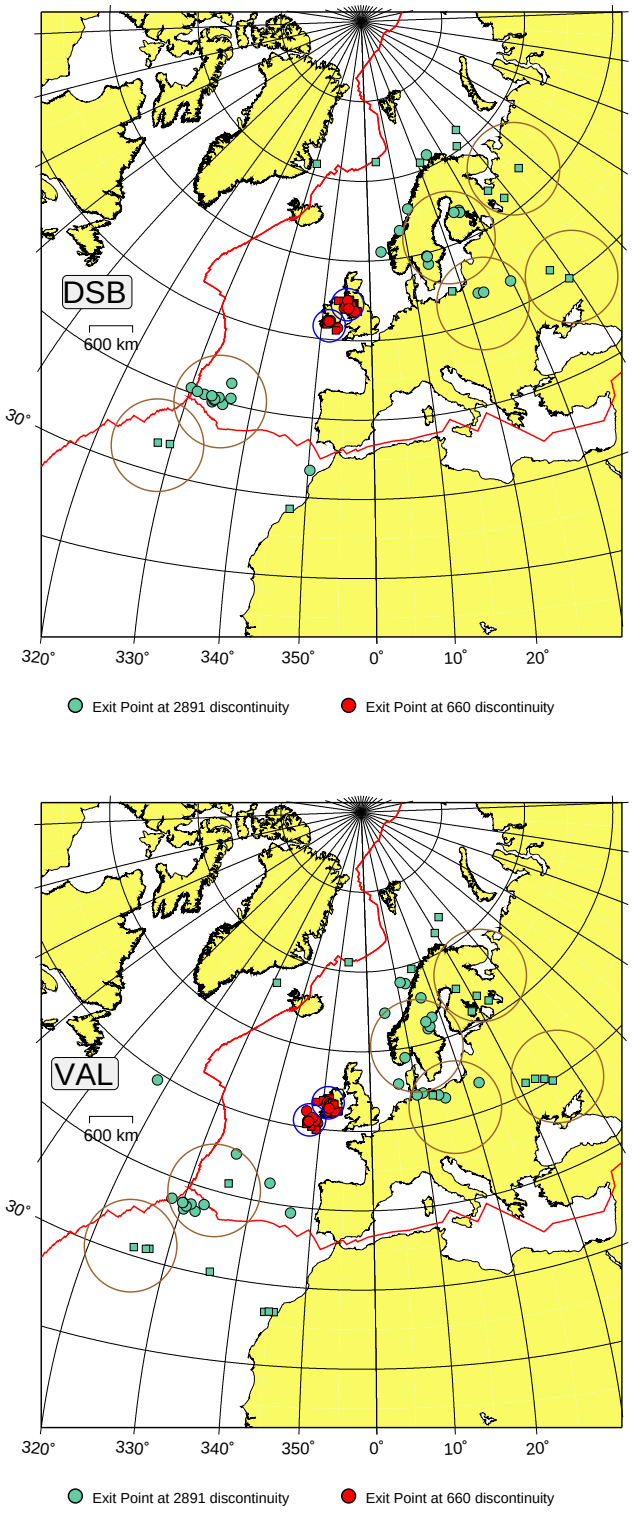



Figure 7.9.: Regional map of exit points of SKS (circles) and SKKS (squares) phases from the Core Mantle Boundary (CMB) and 660 km discontinuity for events used for splitting analysis at permanent seismic stations DSB (a) and VAL (b) (based on the PREM earth velocity model). Plate boundaries are shown as red lines. Orange and blue circles are estimated Fresnel zones at the CMB and 660 km discontinuities for a shear-wave of 0.1 Hz, respectively.

## 7.3. Seismic anisotropy in the lower mantle

Recently, some approaches such as SKS-SKKS splitting discrepancies and a comparison of waveform splitting of SKS and SKKS have been used to detect seismic anisotropy in the lower mantle. In this section, we discuss them and present our results from these approaches.

### 7.3.1. SKS-SKKS splitting discrepancies

It has been found that it is difficult to suggest a unique model in order to reasonably interpret the splitting results from the entire back azimuthal range.

The majority of published shear wave splitting studies (e.g., *Silver*, 1996) assumed the main anisotropy is developed in the upper mantle because the minerals are microscopically anisotropic. However, the transition zones and the lower mantle, and the D" region directly above the CMB can also produce seismic anisotropy since the alignment of anisotropic minerals such as perovskite yields an LPO fabric. The presence of anisotropy in D" has been established in several regions such as the eastern Pacific (e.g., *Long*, 2009) (see chapter 3 for detailed informaton about D").

For detecting anisotropy in the D" layer, some models have been developed, and incorporate transverse isotropy with a vertical symmetry axis (VTI). However, there is some evidence for more complex styles of anisotropy in several regions of D", including tilted transverse isotropy (TTI) and/or azimuthal anisotropy (e.g., *Garnero et al.*, 2004; *Maupin et al.*, 2005). It is significant to note that, as with the isotropic case, VTI anisotropy will not produce any SKS (SKKS, PKS) transverse-component energy as the P-SV-wave system is mathematically decoupled from that for SH-waves (*Aki and Richards*, 1980). It suggests that regardless of epicentral distance, SKS and SKKS cannot produce any shear-wave splitting in a VTI mantle. It is well known that shear-wave splitting in such core phases (SKS/SKKS, PKS) can be produced by a more general form of anisotropy. Sometimes, discrepancies can be observed in shear-wave splitting in SKS and SKKS phases for a given source and station. *James and Assumpçao* (1996) first mentioned discrepancies between SKS and SKKS splitting. Subtle differences in splitting between SKS

and SKKS phases have been attributed to slightly different propagation directions through a dipping layer of upper mantle anisotropy (e.g., *Plomerova et al.*, 2007), but discrepancies are usually attributed to structure in the lower mantle, far away from the receiver (e.g., *Long*, 2009).

It is significant to note that the phases SKS and SKKS travel similar raypaths through the upper mantle but are nearly 1000 km apart at the CMB (Fig. 7.10). Therefore, significant discrepancies can be attributed to lower-mantle effects, such as CMB boundary topography (*Restivo et al.*, 1998), significant lateral velocity gradients, or azimuthal anisotropy.

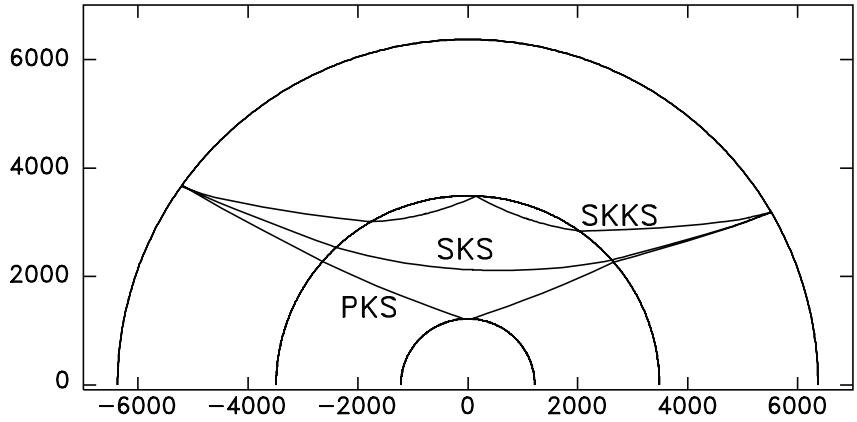



Figure 7.10.: Example raypaths for the core phases SKS, SKKS and PKS. Units are in kilometers (taken from *Hall et al.*, 2004).

Before examining the discrepant SKS/SKKS splitting results, individual SKS (Fig. 7.11) and SKKS (Fig. 7.12) are separately plotted with and without those from the SKS and SKKS discrepant pairs. Therefore, the question is addressed whether the pairs may influence the individual splitting parameters or not.

In order to investigate the lower mantle anisotropy, splitting measurements for SKS and SKKS waves recorded at stations in Ireland (Fig. 7.13) have been used. For discrepancies between SKS and SKKS splitting, only the same event/station pairs are used (Fig. 7.14). Events with magnitude ≥5.8 located in the epicentral distance range from 88 to $136^0$ were used (Fig. 7.15). From this analysis, a total of 46 SKS and SKKS pairs at 16 different stations were obtained. Fig. 7.15 shows an example of the data. High quality records only were used with S/N ratios greater than 3. Some SKS and SKKS waveforms and their particle motion diagrams are

exhibited in Figs. 7.16 and 7.17. Pairs are defined as anomalous when polarization differences between SKS and SKKS directions are greater than $5^0$. The anomalous SKS and SKKS pairs are listed in Table 7.3.1.

For example, at station P07, anomalous pairs are identified (SKS measurements: $\phi$=$39^0$±$1.82^0$; 84±5.71; 50±5.00; 81±2.11 $\delta$t=1.3±0.04s; 0.8±0.13; 1.0±0.12; 1.5±0.05, with corresponding SKKS measurements: $\phi$ =-$86^0$±$1.84^0$; -84±1.79; 86±2.36; NULL, $\delta$t= 1.0±0.04 s; 1.1±0.04; 0.8±0.05, respectively). SKS and SKKS phases at this station show a significant difference in the fast polarization at the backazimuths of 19, 26, 45 and $76^0$. At station D23, it is clearly observed that splitting of SKS differs from SKKS at back azimuths of 50, 74 and $76^0$. Similarly, at other stations such DSB and VAL, we found that SKS splitting is different from SKKS splitting (Table 7.3.1).

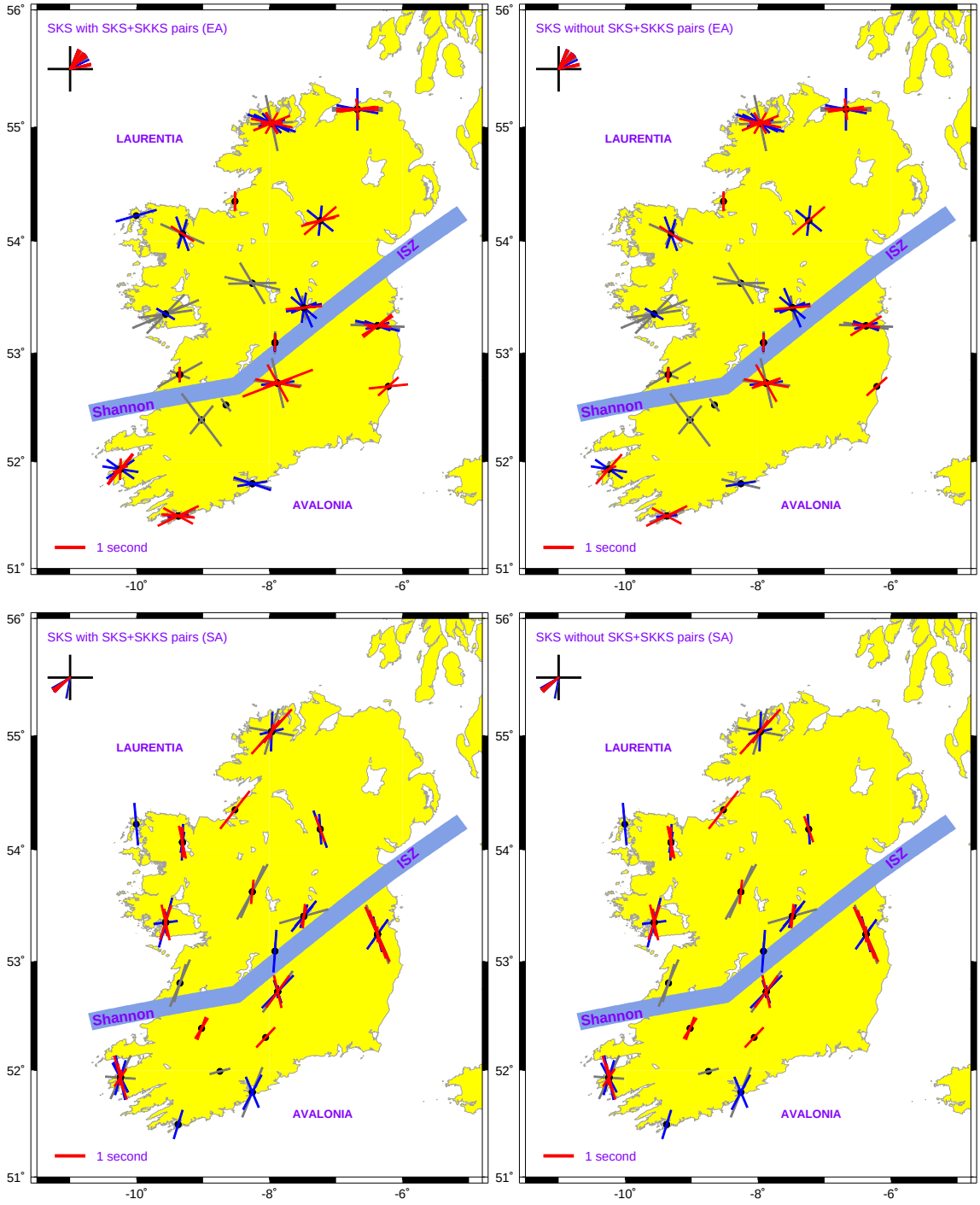



Figure 7.11.: Individual SKS splitting results with SKS/SKKS in the upper left and without SKS/SKKS in the upper right pairs obtained from events in East Asia (BAZ: $0^0$-$90^0$). Individual SKS splitting results with SKS/SKKS in the lower left and without SKS/SKKS in the lower right pairs obtained from events in South America (BAZ:$180^0$-$270^0$). Each individual splitting measurement is represented by a solid segment whose length is proportional to $\delta$t; the direction of the solid segment represents the azimuth of the fast direction $\phi$. Red, blue and gray filled lines show high, medium and low quality measurements respectively. Arrows in top corners show event back azimuths.

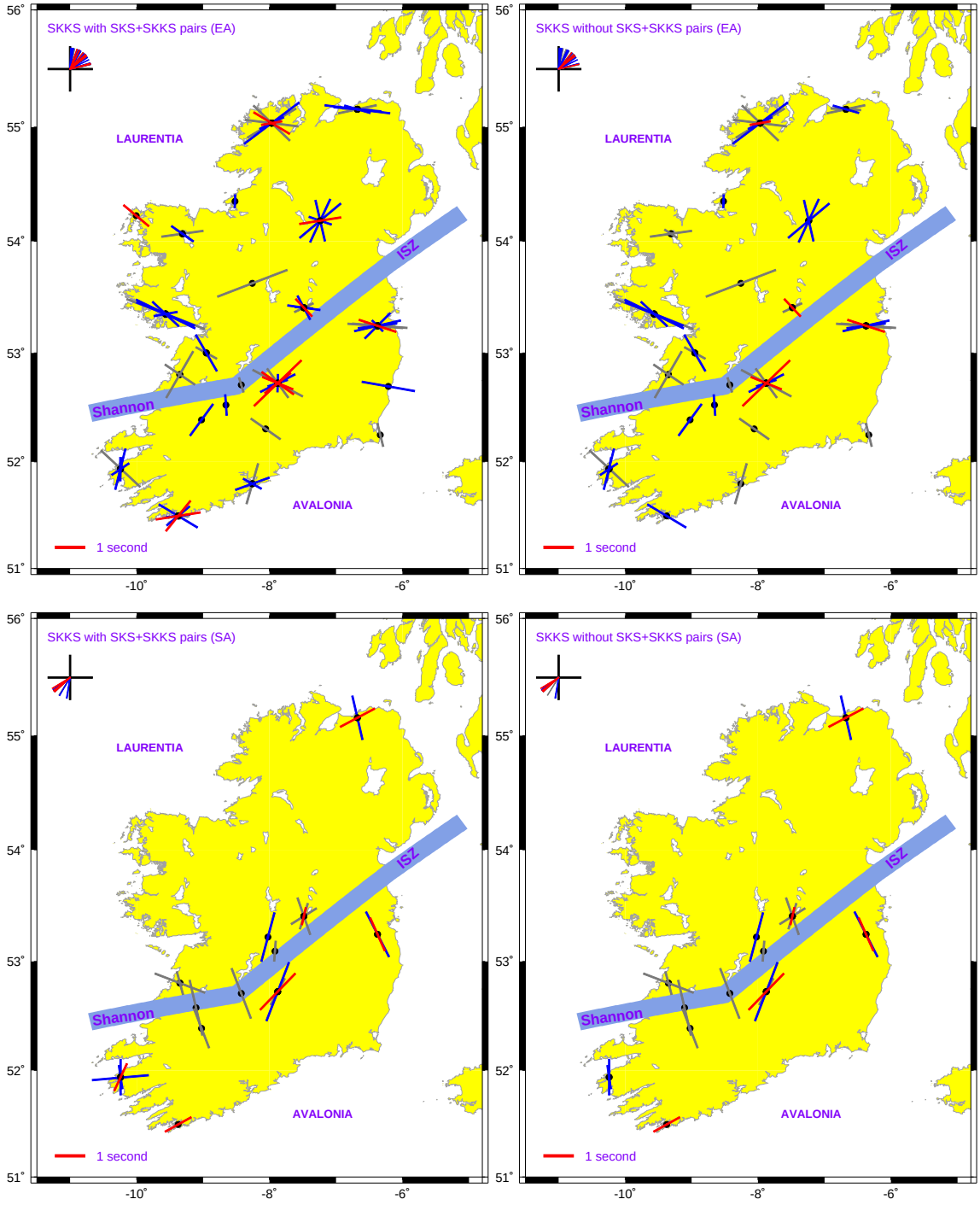



Figure 7.12.: Individual SKKS splitting results with SKS/SKKS in the upper left and without SKS/SKKS in the upper right pairs determined from events in East Asia (BAZ: $0^0$-$90^0$). Individual SKKS splitting results with SKS/SKKS in the lower left and without SKS/SKKS in the lower right pairs determined from events in South America (BAZ:$180^0$-$270^0$). Each individual splitting measurement is represented by a solid segment whose length is proportional to $\delta$t; the direction of the solid segment represents the azimuth of the fast direction $\phi$. Red, blue and gray filled lines show high, medium and low quality measurements respectively. Arrows in top corners show event back azimuths.

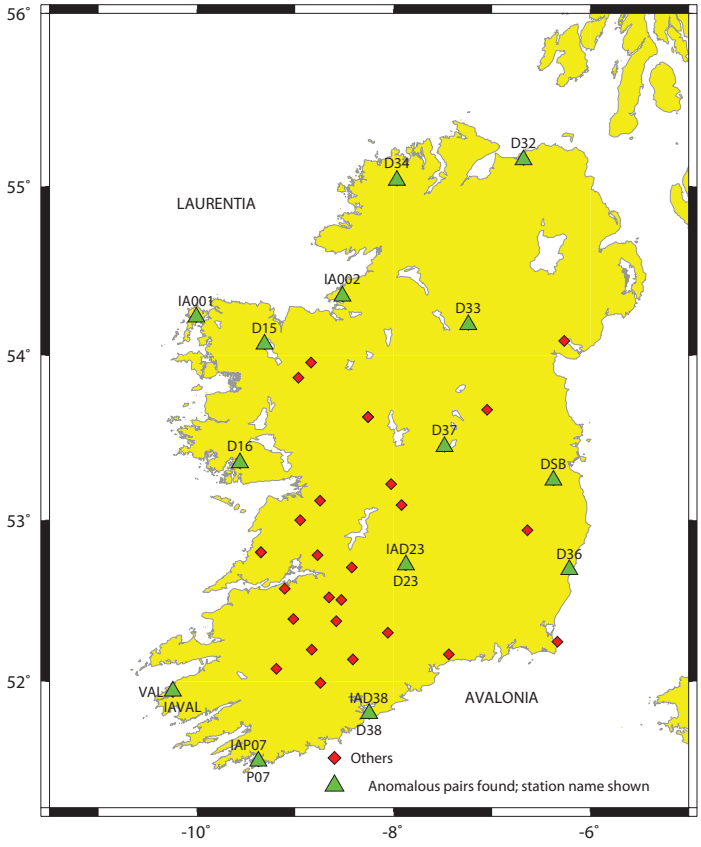



Figure 7.13.: Map showing station locations used in the study. Anomalous SKS/SKKS pairs were observed at stations shown as green triangles.

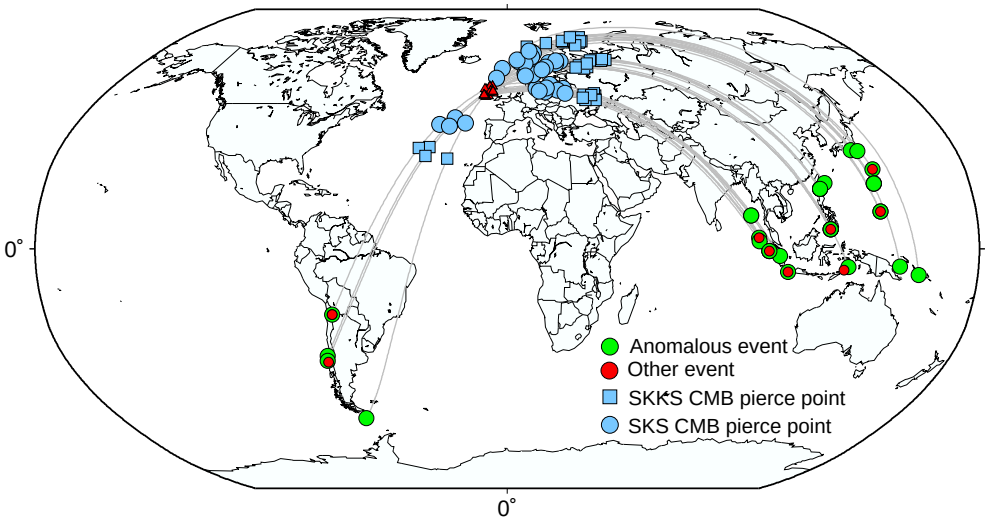



Figure 7.14.: This map shows event locations for all earthquakes that yielded at least one usable SKS-SKKS splitting pair. Grey lines denote great-circle paths for the anomalous pairs, along with the surface projection of the receiver-side core-mantle boundary pierce point for SKS and SKKS.

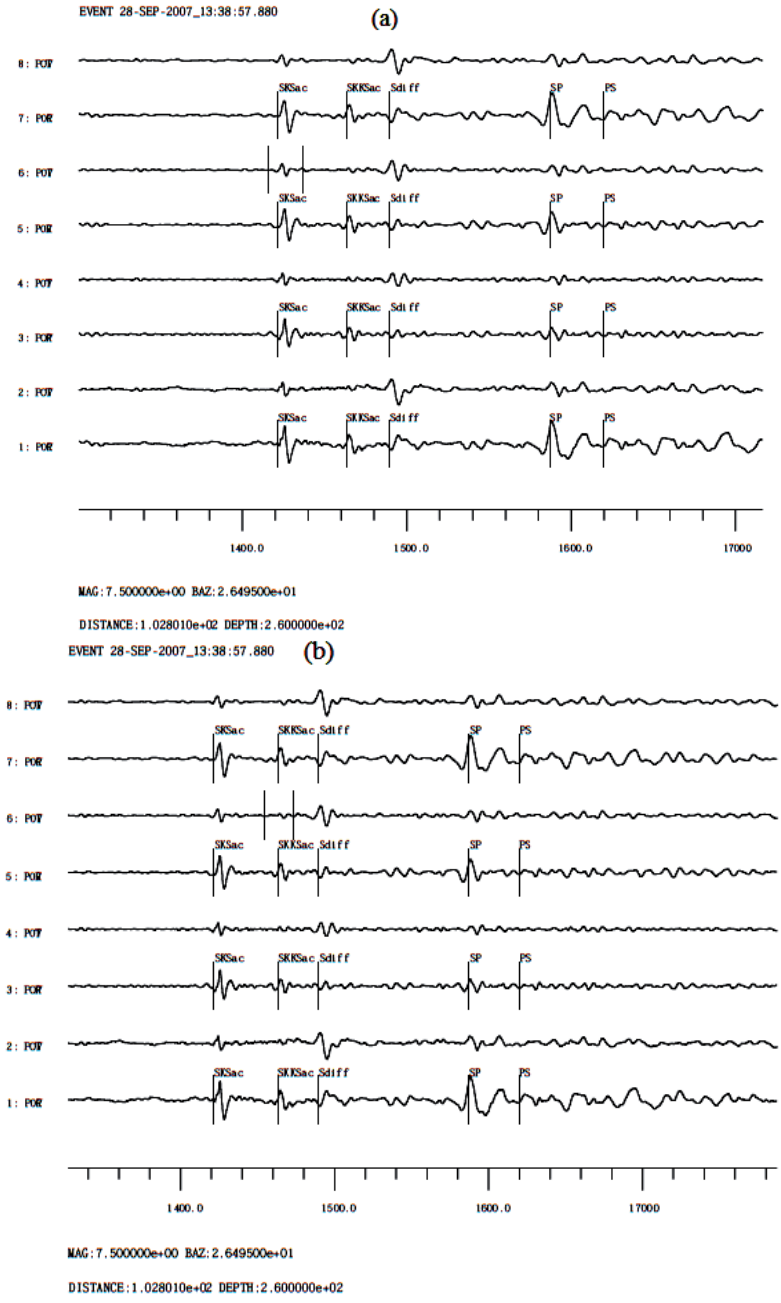



Figure 7.15.: An example of SKS (a) and SKKS (b) pair seismograms from an intermediate earthquake that occurred in the East Asia (BAZ: $26.50^0$, depth: 260 km, magnitude of 7.5) recorded at P07. Original horizontal seismograms (NS and EW) are rotated to backazimuth radial and transverse seismograms. Then, all traces including 3-4, 5-6, 7-8 except 1-2 traces are band-pass filtered in different ranges consisting of 2-10s, 3-15s and 4-30s, respectively. In addition to this, theoretical travel times are picked for each trace. Amplitudes on all seismograms are traced-normalised within the selected time window. Phase windowing is determined according to the beginning and the ending time of the phases.

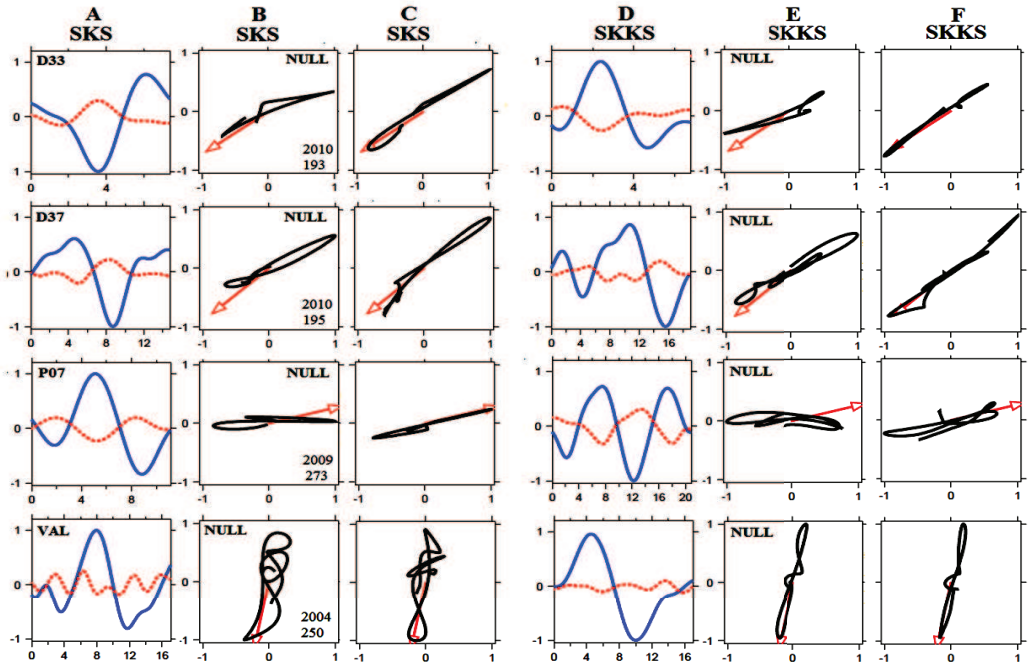



Figure 7.16.: For an indicative of discrepant SKS-SKKS pairs, radial and transverse SKS and SKKS seismograms and particle motion diagrams are shown. In column A, the radial (solid line) and transverse (dashed line) components of the SKS waveform are shown with the station name (upper left). Column B shows the original particle motion with the best-fitting splitting parameters except NULL showing in the lower right corner of the radial and transverse SKS and SKKS seismograms. Column C indicates linear particle motion diagram after correction. The best-fitting splitting parameters (fast direction in degrees, delay time in s) are shown in the lower right corner of the particle motion diagram in column D. Column D, E and F exhibit the corresponding SKKS waveforms and particle motion diagrams, respectively. Null or near-null measurements are indicated by “NULL” in the upper right corner of the particle motion diagram. In the lower right of the column E, the used event date (year and Julian day) is shown.

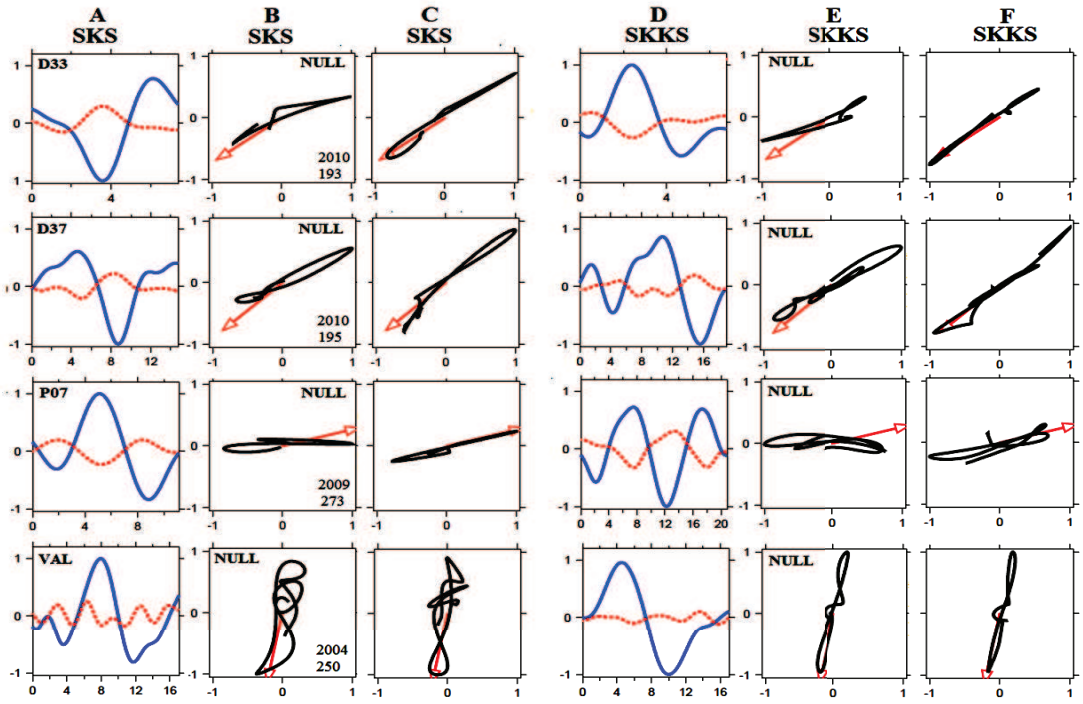



Figure 7.17.: Examples of non-discrepant SKS-SKKS pairs. The symbols and plotting conventions used are the same as in Fig. 7.16.

ANOMALOUS SKS-SKKS pairs (34 total) (S2 denotes SKKS)

| Sta ID | Sta lat. | Sta lon. | Event date | Event lat. | Event lon. | Event depth | BAZ deg. | Dis. deg. | S2 $\phi$ | S2 $\sigma_\phi$ | S2 $\delta$t | S2 $\sigma_{\delta t}$ | SKS $\phi$ | SKS $\sigma_\phi$ | SKS $\delta$t | SKS $\sigma_{\delta t}$ |
|---|---|---|---|---|---|---|---|---|---|---|---|---|---|---|---|---|
| | | | (Y.M.D.) | | | (km) | | | deg. | | s | | deg. | | s | |
| D15 | 54.07 | -9.31 | 080601 | 20.12 | 121.35 | 31.00 | 45.67 | 94.85 | -55 | 3.09 | 0.9 | 0.07 | 81 | 1.77 | Nul | - |
| D16 | 53.35 | -9.56 | 100531 | 11.13 | 93.47 | 112.00 | 73.01 | 88.81 | 80 | 4.14 | 0.8 | 0.10 | Nul | - | Nul | - |
| D23 | 52.73 | -7.88 | 090902 | -7.78 | 107.30 | 46.00 | 74.26 | 111.29 | 52 | 2.86 | 1.1 | 0.06 | Nul | - | Nul | - |
| D23 | 52.73 | -7.88 | 090930 | -0.72 | 99.87 | 81.00 | 76.18 | 101.26 | 52 | 1.90 | 0.8 | 0.04 | 69 | 0.87 | 2.5 | 0.02 |
| D23 | 52.73 | -7.88 | 100723 | 6.49 | 123.47 | 585.80 | 51.69 | 108.07 | -55 | 3.96 | 1.3 | 0.09 | Nul | - | Nul | - |
| D32 | 55.15 | -6.68 | 080509 | 12.52 | 143.18 | 76.00 | 31.03 | 107.96 | -83 | 4.82 | 2.2 | 0.11 | 84 | 1.84 | 1.0 | 0.04 |
| D32 | 55.15 | -6.68 | 080601 | 20.12 | 121.35 | 31.00 | 47.83 | 92.99 | -85 | 3.97 | 1.6 | 0.09 | 84 | 3.60 | 1.4 | 0.08 |
| D33 | 54.18 | -7.24 | 080601 | 20.12 | 121.35 | 31.00 | 47.41 | 93.89 | -71 | 3.10 | 0.8 | 0.07 | 78 | 2.08 | 1.0 | 0.05 |
| D33 | 54.18 | -7.24 | 091024 | -6.13 | 130.38 | 130.00 | 51.56 | 121.17 | 81 | 3.35 | 1.4 | 0.08 | 74 | 2.61 | 1.3 | 0.06 |
| D33 | 54.18 | -7.24 | 100227 | -36.12 | -72.90 | 22.90 | 230.18 | 106.18 | Nul | - | Nul | - | -20 | 3.78 | 1.3 | 0.09 |
| D34 | 55.04 | -7.97 | 080601 | 20.12 | 121.35 | 31.00 | 46.76 | 93.62 | -59 | 3.40 | 1.4 | 0.08 | -84 | 1.62 | 0.7 | 0.03 |
| D34 | 55.04 | -7.97 | 090930 | -0.72 | 99.87 | 81.00 | 75.67 | 100.75 | Nul | - | Nul | - | -27 | 1.36 | 0.8 | 0.03 |
| D34 | 55.04 | -7.97 | 100712 | -22.15 | -68.22 | 115.00 | 233.67 | 92.39 | Nul | - | Nul | - | 13 | 1.89 | 0.5 | 0.04 |

| | | | | | | | | | | | | | | | | |
|---|---|---|---|---|---|---|---|---|---|---|---|---|---|---|---|---|
| D36 | 52.7 | -6.21 | 070928 | 22.01 | 142.67 | 260.00 | 29.23 | 100.83 | -80 | 2.95 | 1.8 | 0.07 | 84 | 2.93 | 1.3 | 0.07 |
| D37 | 53.41 | -7.48 | 100509 | 3.75 | 96.02 | 38.00 | 76.92 | 95.01 | -82 | 3.94 | 1.1 | 0.09 | 85 | 5.55 | 0.8 | 0.13 |
| D37 | 53.41 | -7.48 | 100723 | 6.49 | 123.47 | 585.80 | 51.87 | 107.43 | -85 | 3.40 | 0.6 | 0.08 | 76 | 2.23 | 0.5 | 0.05 |
| D38 | 51.76 | -8.23 | 100426 | 22.18 | 123.63 | 14.70 | 43.86 | 95.17 | 70 | 3.59 | 1.2 | 0.08 | -71 | 2.65 | 1.3 | 0.06 |
| D38 | 51.76 | -8.23 | 100531 | 11.13 | 93.47 | 112.00 | 74.01 | 88.48 | -61 | 5.13 | 0.7 | 0.12 | Nul | - | Nul | - |
| IA001 | 54.23 | -10.01 | 101202 | -6.00 | 149.98 | 33.00 | 26.08 | 129.26 | -50 | 2.85 | 1.1 | 0.06 | 74 | 5.79 | 1.4 | 0.14 |
| IAD23 | 52.73 | -7.88 | 100723 | 6.49 | 123.47 | 585.80 | 51.69 | 108.07 | 1.5 | 4.12 | 0.6 | 0.09 | Nul | - | Nul | - |
| IAVAL | 51.94 | -10.24 | 110115 | 2.49 | 96.29 | 19.00 | 75.37 | 98.17 | 2.0 | 3.50 | 0.46 | 0.08 | Nul | - | Nul | - |
| P07 | 51.5 | -9.38 | 070928 | 22.01 | 142.67 | 260.00 | 26.50 | 102.80 | 39 | 1.82 | 1.3 | 0.04 | -86 | 1.84 | 1.0 | 0.04 |
| P07 | 51.5 | -9.38 | 080601 | 20.12 | 121.35 | 31.00 | 45.81 | 96.68 | 84 | 5.71 | 0.8 | 0.13 | -84 | 1.79 | 1.1 | 0.04 |
| P07 | 51.5 | -9.38 | 090809 | 33.17 | 137.94 | 292.00 | 26.93 | 90.94 | 50 | 5.00 | 1.0 | 0.12 | -86 | 2.36 | 0.8 | 0.05 |
| P07 | 51.5 | -9.38 | 100103 | -8.80 | 157.35 | 25.00 | 19.09 | 136.05 | 81 | 2.11 | 1.5 | 0.05 | Nul | - | Nul | - |
| DSB | 53.25 | -6.38 | 040725 | -2.43 | 103.98 | 582.10 | 74.91 | 104.03 | -45 | 2.88 | 0.5 | 0.06 | -77 | 3.09 | 1.5 | 0.07 |

| | | | | | | | | | | | | | | | | |
|---|---|---|---|---|---|---|---|---|---|---|---|---|---|---|---|---|
| DSB | 53.25 | -6.38 | 070928 | 22.01 | 142.67 | 260.00 | 29.03 | 100.39 | 45 | 3.29 | 1.2 | 0.07 | 81 | 1.23 | 0.7 | 0.02 |
| DSB | 53.25 | -6.38 | 080509 | 12.52 | 143.18 | 76.00 | 31.66 | 109.50 | Nul | - | Nul | - | 51 | 1.15 | 1.2 | 0.02 |
| VAL | 51.94 | -10.24 | 040503 | -37.69 | -73.41 | 21.00 | 227.08 | 104.86 | 25 | 2.83 | 1.0 | 0.06 | -25 | 2.30 | 1.1 | 0.05 |
| VAL | 51.93 | -10.24 | 070928 | 22.01 | 142.67 | 260.00 | 25.66 | 102.64 | Nul | - | Nul | - | 44 | 1.63 | 1.0 | 0.03 |
| VAL | 51.93 | -10.24 | 090812 | 32.82 | 140.40 | 53.00 | 24.40 | 91.76 | 0 | 4.60 | 0.8 | 0.11 | 38 | 0.97 | 1.3 | 0.02 |
| VAL | 51.93 | -10.24 | 090930 | -0.72 | 99.87 | 81.00 | 74.39 | 102.87 | Nul | - | Nul | - | 2 | 1.91 | 0.7 | 0.04 |
| VAL | 51.93 | -10.24 | 100117 | -57.66 | -65.88 | 5.00 | 210.26 | 118.32 | 85 | 4.14 | 1.9 | 0.10 | Nul | - | Nul | - |
| VAL | 51.93 | -10.24 | 100723 | 6.49 | 123.47 | 585.80 | 49.72 | 109.70 | Nul | - | Nul | - | 56 | 3.54 | 1.1 | 0.08 |

The majority of SKS and SKKS pairs comes from events in eastern Asia, within the backazimuth range ~19-76$^0$, located in the Java Trench, Philippines plate boundary and Mariana Trench (Fig. 7.14) that sample the lower-most mantle beneath the northwestern part of the Eurasian plate. Marked discrepancies between SKS and SKKS splitting for the same event/station pairs are also identified for a small group of events from South America, within the backazimuth range 210-233$^0$, with CMB pierce points near the triple junction among the Azores fault zone (AFZ), the Mid-Atlantic ridge and the Reykjanes ridge (Fig. 7.14).

Fig. 7.18 shows the exit points from the CMB for the east Asian events. The anomalous SKS (blue circles: C1 and D1) and corresponding SKKS (blue circles: C2 and D2) measurements in the backazimuth range from ~30- 60$^0$ each show fairly uniform fast polarization directions within each group (Fig. 7.18), but the SKS fast polarizations are slightly different from those of SKKS measurements.

In the backazimuth range from ~30- 60$^0$, additionally we found that the anomalous SKS fast polarization directions (blue circles: C1 and D1) and the corresponding SKKS (blue circles: C2 and D2) are parallel to the direction of plate motion at the East Asia (Figs. 7.18 and 7.20). For the Fig. 7.20, Plate Motion Calculator (UNAVCO[2]) is used. This observation may allow a possible correlation between seismic anisotropy related to the flow field of the mantle flow and direction of tectonic plate motion at the Earth's surface (e.g., *Jadamec and Billen*, 2010). On the other hand, the determined SKS fast directions (E1) in the backazimuth range from ~19 to 30$^0$ exhibit strong scatter in polarization directions, as do the corresponding SKKS (E2) fast polarization directions. These observations require further data to progress the interpretation.

In contrast to the East Asian pair cluster, the number of pairs from the SA cluster is very few (Fig. 7.19). The splitting pairs from the South American event cluster sample the lowermost mantle beneath the region of the Azores triple (Fig. 7.19). Two out of 4 the observed SKS fast polarizations from the SA cluster show nearly NW-SE fast directions. Although a clear variation between the SKS and corresponding SKKS fast polarization directions has been observed, much importance cannot be attached to results from this small number of pairs.

[2]http://www.sps.unavco.org

Furthermore, the SKS results (A1) in the backazimuth range from ~60 to $76^0$ show that the fast polarization directions are relatively uniform and they indicate nearly NE-SW orientations while the corresponding SKKS (A2) in this backazimuth range exhibit that the fast polarization directions are roughly NE-SW orientations (Fig. 7.18).

In this study, discrepant SKS-SKKS splitting at broadband stations in Ireland has been observed, for the first time. Although these observations may be sufficient to suggest anisotropy in the D" , further measurements are necessary to confirm the results and resolve in detail the lower mantle or D" anisotropy. The SKS/SKKS pairs will now be used (section 7.3.2) to compare the waveform splitting of SKS and SKKS in an attempt to further investigate lower mantle anisotropy.

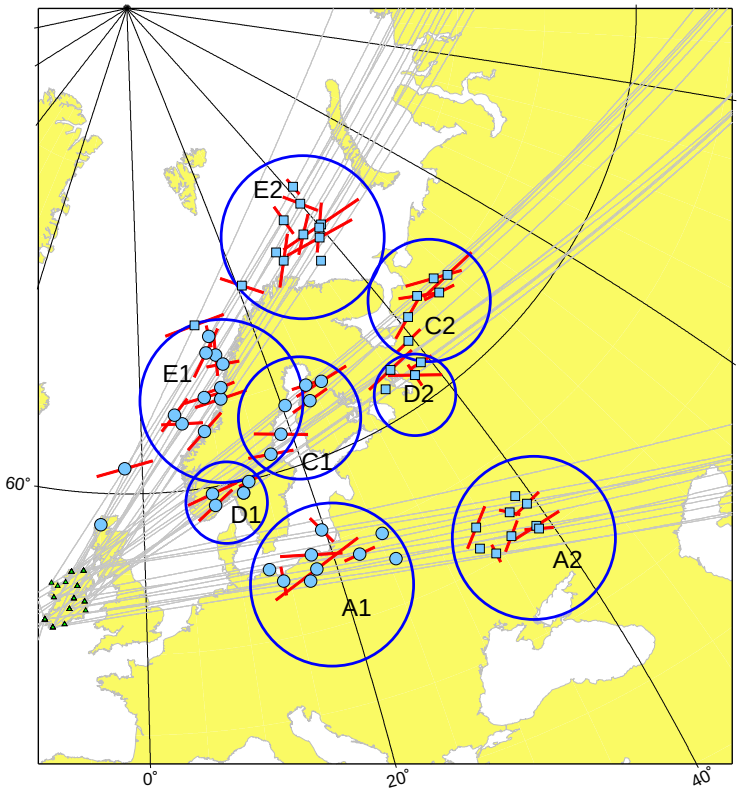



Figure 7.18.: Location map of exit points for SKS (circle) and SKKS (squares) phases from the Core-Mantle Boundary (CMB) for the selected anomalous pairs coming from localized groups of events in the East Asia. Splitting parameters for anomalous pairs are plotted at the CMB. Each individual splitting measurement from the pairs is represented by a solid red segment whose length is proportional to $\delta$t; the direction of the solid segment represents the azimuth of the fast direction $\phi$.

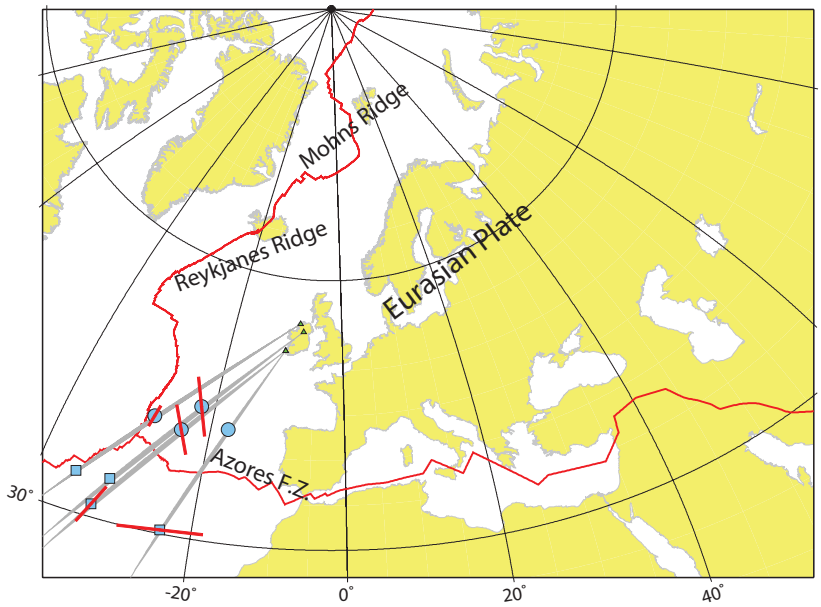



Figure 7.19.: Location map of exit points for SKS (circle) and SKKS (squares) phases from the Core-Mantle Boundary (CMB) for the selected anomalous pairs coming from events in the South America. The parameters for anomalous pairs are plotted at the CMB. The symbols and plotting conventions used are the same as in Fig. 7.18.

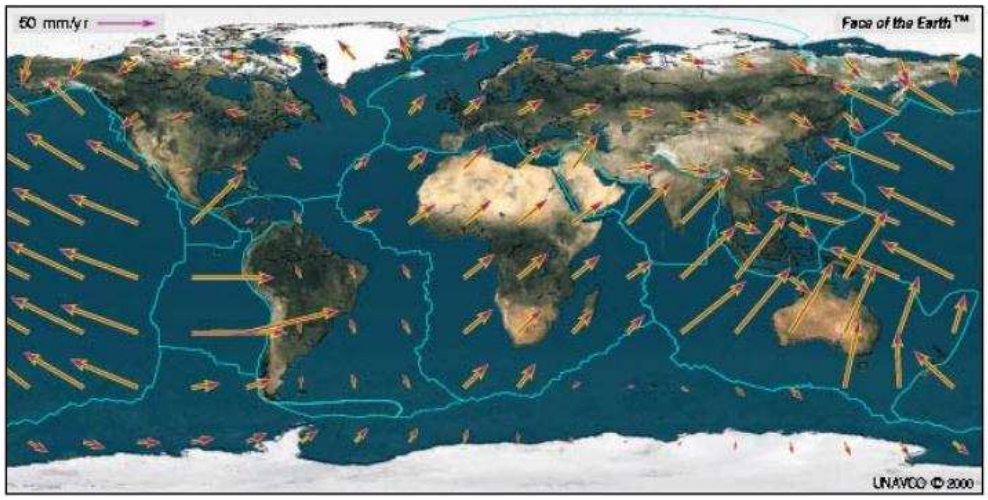



Figure 7.20.: General plate motions on a global scale. Length of arrows indicates rate of movement of that part of the plate. Map is taken from IRIS.

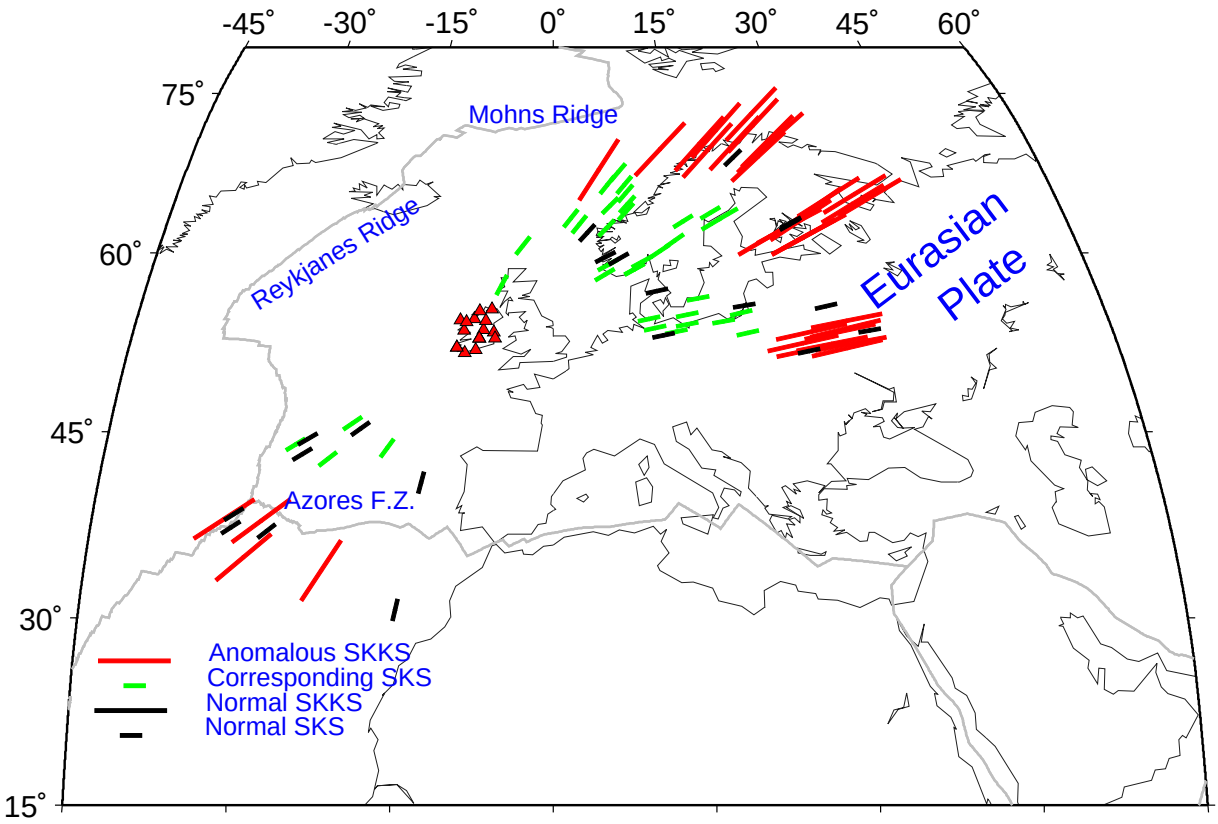



Figure 7.21.: D" paths for the final selected SKS-SKKS pairs. Anomalous pairs are highlighted in colour.

### 7.3.2. Comparison of SKS-SKKS waveform splitting

In this part of the study, we investigated seismic anisotropy in the lower mantle by comparing the waveform splitting of SKS and SKKS found in the same seismogram. The phases have very similar ray paths in the upper mantle, but different ones in the lower mantle. Moreover, as they have the same back-azimuth, it is hence not necessary to consider the effect of multiple anisotropic layers. However, if there is a noticeable difference in splitting between the two, it indicates the presence of anisotropy or dipping structures in the lower mantle. The approach is simply that if the main source for SKS and SKKS splitting is completely located in the upper mantle, the ratios of energy on the radial to transverse component of the SKS and SKKS waveforms for any station-event pair should be equal. Therefore, if the amplitudes of the SKS and SKKS phases differ, the deviations are likely related to lower mantle anisotropy (e.g., *Niu and Perez*, 2004).

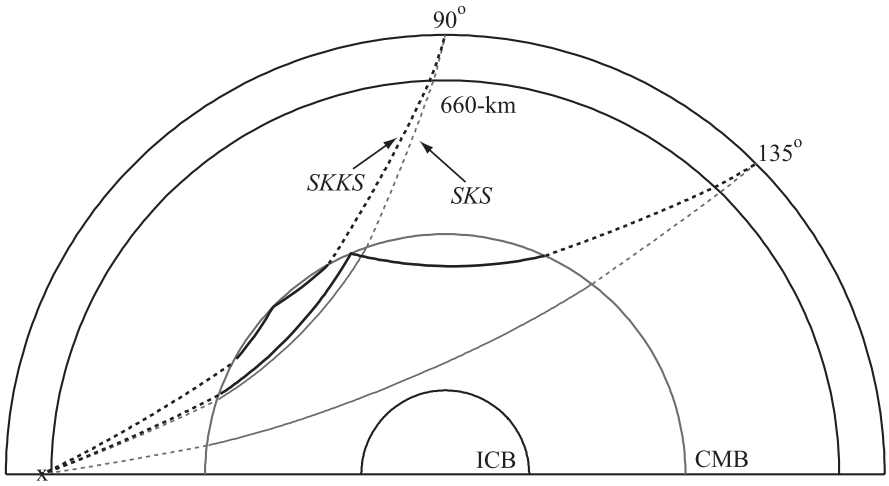



Figure 7.22.: SKS and SKKS ray paths at the distances of 90-135$^0$ based on IASP91 (*Kennett and Engdahl*, 1991). P- and S-wave rays segments are shown by solid and dashed lines, respectively. Note that the two have almost identical ray paths in the upper mantle. Thus similar splitting behavior is expected if the lower mantle is isotropic. Taken from *Niu and Perez* (2004).

A total of 46 SKS and SKKS pairs, recorded at 16 different stations, were used. The ratios were calculated by measuring picked peak amplitudes of the SKS and SKKS arrivals on both the radial and transverse components. The criteria used in data selection are described in section 7.3.1. The results are shown in Fig. 7.23 where $SKS_R$, $SKS_T$, $SKKS_R$ and $SKKS_T$ are the measured amplitudes of the indicated phase of the radial and transverse components, respectively. The transverse-to-radial ratio is generally less than 0.5 for both SKS and SKKS phases (Fig. 7.23a and b). There is an approximately positive correlation between the $SKS_T/SKS_R$ and $SKKS_T/SKKS_R$ ratios (Fig. 7.23c).

To reveal the existence of transverse anisotropy or anomalous dipping structures in some part of the lower mantle or D" (*Iidaka and Niu*, 1998), this approach seems feasible, as observed in our case. However, our results to be confirmed should be supported with additional data that will be available in the future.

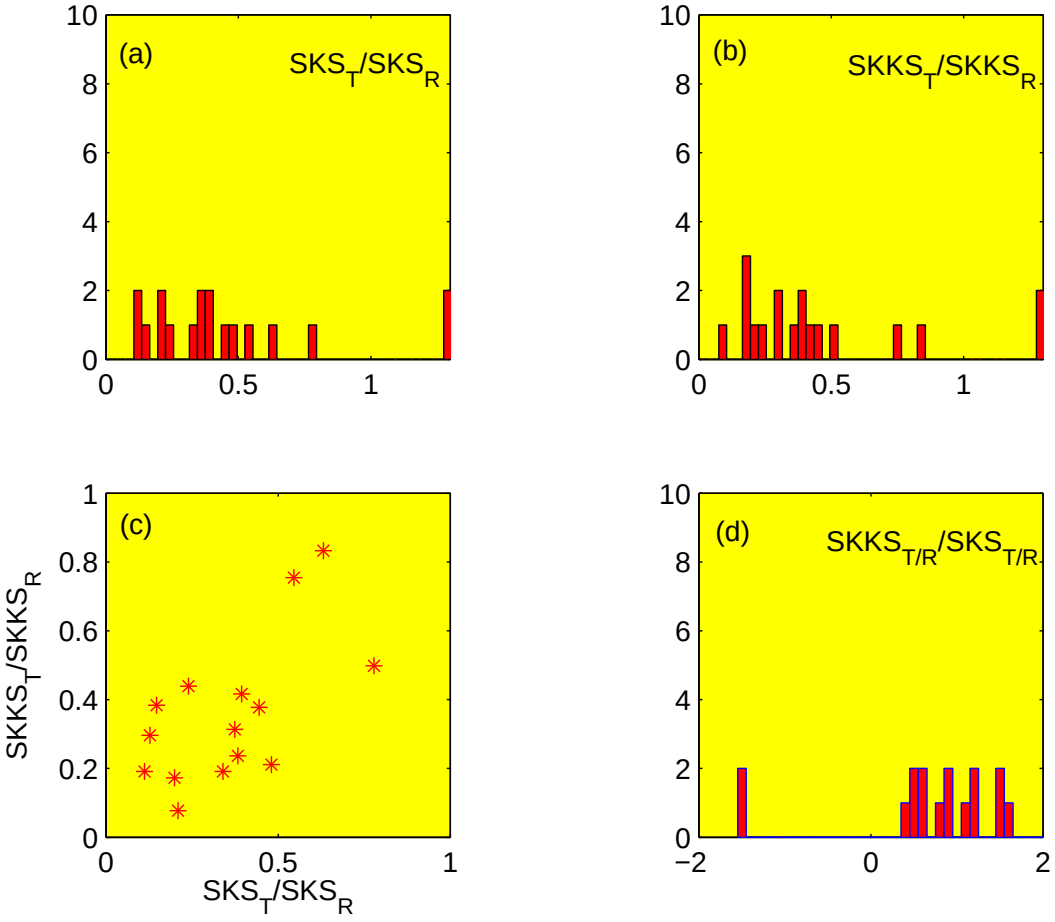



Figure 7.23.: Histograms of the amplitude ratios $SKS_T/SKS_R$ and $SKKS_T/SKKS_R$ are shown in (a) and (b), respectively. (c) $SKKS_T/SKKS_R$ is plotted against $SKS_T/SKS_R$. (d) Histogram of the relative ratio of $SKKS_T/SKKS_R$ and $SKS_T/SKS_R$, plotted on logarithmic scale.

### 7.3.3. The estimation of the depth of anisotropy using spatial coherency of shear-waves plitting parameters

In addition to the techniques already described to estimate the depth of anisotropy, the program AnisDep has also been used (*Gao et al.*, 2010; *Liu and Gao*, 2011; *Gao and Liu*, 2012). This method searches for the optimal depth by computing a spatial variation factor. The program was tested using synthetic and real data from the Afar Depression and adjacent areas (*Gao et al.*, 2010; *Liu and Gao*, 2011). The procedure starts with computing the geographic distribution

of the ray-piercing points at a series of assumed depths of anisotropy ranging from the surface to the maximum possible depth of anisotropy, based on the IASP91 Earth model (*Kennett and Engdahl*, 1991). A study area is first divided into *dx* by *dy* square degree blocks at each assumed depth of anisotropy. Dx=$0.1^0$ and a distance of $0.05^0$ between the centre of neighboring blocks are used for the synthetic and real data tests. Then, for the depth range of 0-400 km, the variation factors $F_{\delta t}$ for $\delta$t and $F_{\phi}$ for $\phi$ are calculated using

$$A = \frac{1}{M_i - 1} \sum_{j=1}^{M_i} (\delta t_{ij} - ave(\delta t_i))^2 \tag{7.4}$$

$$F_{\delta t} = 1/N \sum_{i=1}^{N} A^{1/2} \tag{7.5}$$

and

$$B = \frac{-1}{2} \ln(R_i) \tag{7.6}$$

$$F_{\phi} = \frac{1}{N} \sum_{i=1}^{N} \sqrt{B} \tag{7.7}$$

where

$$p1 = \frac{1}{M_i} \sum_{j=1}^{M_i} cos(2\phi_{ij}) \tag{7.8}$$

$$p2 = \frac{1}{M_i} \sum_{j=1}^{M_i} sin(2\phi_{ij}) \tag{7.9}$$

$$R_i^2 = p1^2 + p2^2. \tag{7.10}$$

$N$ is the number of blocks, $M_i$ is the number of measurements for the $i$-th block, $\phi_{ij}$ and $\delta t_{ij}$ are the $j$-th fast direction and splitting delay-time measurement in the $i$-th block, and $\delta t_i$ is the average $\delta$t over all the measurements in block $i$. $F_{\delta t}$ is the mean simple standard deviation (STD), and $F_{\phi}$ is the mean circular STD (*Fisher*, 1993) over all the blocks. Finally, the variation factor, $F_v^i$, for the $i$-th block as dimensionless weighted sum of $F_{\phi}^i$ and $F_{\delta t}^i$, i.e.,

$$F_v^i = w_\phi F_\phi^i + w_{\delta t} F_{\delta t}^i \tag{7.11}$$

where $w_\phi$ and $w_{\delta t}$ are the weighting factor for the $\phi$ and $\delta$t measurements, respectively (for detailed information on the program see *Liu and Gao*, 2011; *Gao and Liu*, 2012). This approach was applied to 298 pairs of splitting measurements obtained at the Irish stations in order to estimate the depth of anisotropy.

From the results (Fig. 7.24), it is estimated that the optimal depth of the source of anisotropy is about 150 km, i.e., in the lithosphere. This observation is very consistent with the VCD model. Our splitting results from the main clusters reveal a systematic azimuthal dependence of splitting parameters, indicating a two-layer or more layers model of anisotropy. The top layer can be characterized by splitting delay time greater than 0.5 s and nearly E-W fast directions may also be attributed to frozen deformation/Caledonian deformation within the continental lithosphere beneath Ireland. The spatial and azimuthal variations in the lower layer anisotropy can be ideally explained with mantle flow or highly anisotropic minerals in the D” or the deep rooted mantle beneath Ireland.

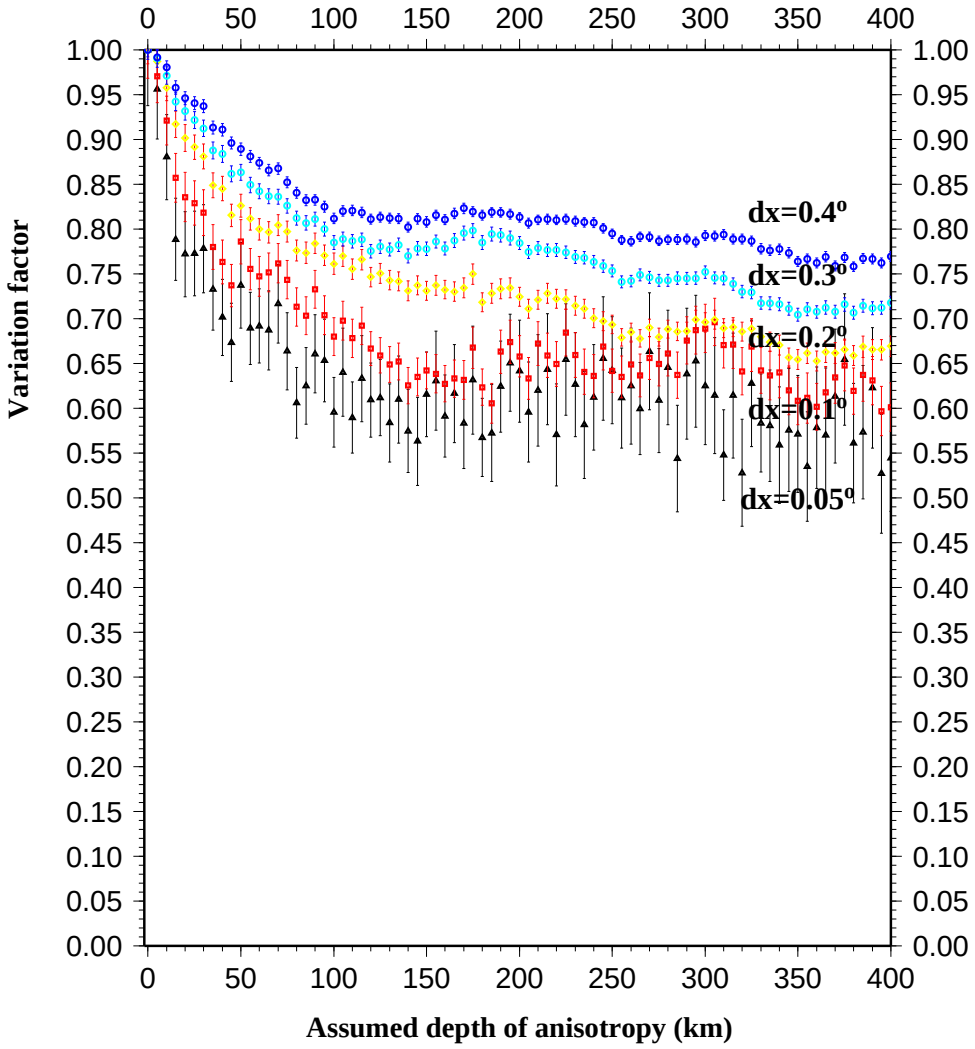



Figure 7.24.: Resulting depth variations of $F_v$ for Ireland using five different block sizes. Spatial variation factors computed using 298 shear-wave splitting measurements at all Irish stations.

# 8. Summary and conclusions

## 8.1. Summary and conclusions

In this study, a total of 42 broad-band seismic stations have been used to investigate seismic anisotropy in the Irish crust, mantle and D" using two methods, shear wave splitting and surface wave tomography, for the first time.

**A) The main results from shear wave splitting observations are:**

1) This study shows that there were two major event clusters: one from East Asia and the other from South America. A considerable change in fast polarisation direction was observed between the results from these two event clusters which have nearly opposite back azimuths. The results indicate that there are fundamentally different origins for the observed anisotropy. In contrast, no significant difference in delay time was found between the two event clusters, and the average delay time is greater than 1 s for both clusters.

2) According to Fresnel zone arguments (*Alsina and Snieder*, 1995), a possible presence of anisotropy below 410 km depth has been revealed by splitting results from two opposite back azimuths at both VAL and DSB. Also, splitting results from the two crossing ray paths from the two event clusters suggest lateral variation of anisotropy should occur above about a depth of 210 km, or below a depth of 660 km (or the D").

3) The averaged fast polarization directions from the East Asian events are approximately aligned with Caledonian/Variscan trends, but with some significant scatter, particularly in central Ireland. However, the averaged fast polarization directions from the South American events

are fairly uniform and show N-S orientations. Although there is no correlation of the observed anisotropy from the South American events with regional tectonic trends, the pattern of the observed anisotropy correlates well with the long axis of the finite strain ellipsoid in mantle convection in the North Atlantic. This means that at regional scale, the seismic anisotropy measured from this cluster is likely to be caused by this mantle flow at a depth of 175 km.

4) Rapid spatial variations in splitting parameters obtained from the East Asian events are observed at stations located in central Ireland. This suggests that the contribution of crustal anisotropy to teleseismic shear wave splitting is quite high and the observed anisotropy beneath central Ireland is probably related to fabrics within deep crustal rocks that preserve a record of deformation during and after the continental collisions.

5) For each cluster, there is no strong correlation between the fast polarisation directions and the present-day plate motions. This suggests that present day plate motions do not strongly influence the observed anisotropy beneath Ireland.

6) At station D23, the measured delay times proportionally increase as a function of incidence angle. This may be an important observation because variations in delay time are more pronounced than polarizations and may be more useful for distinguishing dipping layers. However, it is not easy to make precise interpretations using only this observation.

7) Discrepant SKS-SKKS splitting at broadband stations in Ireland has been observed, for the first time, in particular, from the East Asian events. This could be caused by anisotropy within the D" layer or lower-mantle effects such as CMB boundary topography. In contrast to the results from East Asia, the number of pairs from the South American cluster is very few. Therefore, it is difficult to make any interpretation using such few pairs.

8) In this study the optimal depth of the source of anisotropy has been estimated by using the AnisDep program described by *Liu and Gao* (2011) to be about 150 km, i.e. in the lithosphere. This observation seems consistent with the vertically-coherent deformation (VCD) model (*Silver*, 1996).

**B) The main results from surface wave tomography are:**

1) Strong seismic anisotropy with a NE-SW fast-propagation azimuth in the whole crust of Ireland at periods of 10-20 s has been revealed.

2) The NE-SW trend of the deep-crustal anisotropic fabric is parallel to tectonic trends, in particular the Iapetus Suture Zone, which indicates that suture-parallel flow in the middle and lower crust accommodated the continental collision.

3) The amplitude of azimuthal phase-velocity anisotropy reaches a maximum of 2% at a 15 s period. In contrast, the observed azimuthal anisotropy at periods sampling the Moho and the uppermost mantle (between 25 and 30 s) is very small.

4) For the first time, in this study the results show that the $4\Psi$ terms are required to fit the data, although the $4\Psi$ anisotropic terms are generally considered to be unimportant in Rayleigh wave anisotropy imaging.

5) For the inversion of Ireland-average Love and Rayleigh phase-velocity curves, the VARNET profile (*Hauser et al.*, 2008) as a reference model seems to fit well with the data. From this observation it is apparent that shear velocities $Vs$ in the continental Irish crust, between the upper crust to Moho, which vary from 3.3 to ~4 km/s, are consistent with previous studies (*Van den Berg et al.*, 2005; *Landes et al.*, 2006; *O'Reilly et al.*, 2010). As a consequence, this indicates that the VARNET profile is representative of the whole Irish crust.

6) The shear velocity in the upper crust to Moho slightly increases as a function of depth. Drastic variations in shear-speed structure of the Irish crust are not observed. This means that the Irish crust is fairly uniform with velocities of 3.3 to nearly 4 km/s. This observation reflects the moderate crustal thickness and radially anisotropic variations.

7) The Ireland-average radial anisotropy in the crust and uppermost mantle is slightly higher than the global average; it is almost 3%. Variations in the amount of the observed radial anisotropy within the upper crust to lower crust are not large and are very smooth.

8) Radial anisotropy indicative of horizontal fabric in the crust and uppermost mantle ($Vsh > Vsv$) is suggested by the data. This horizontally oriented fabric may develop due to the align-

ment (lattice preferred orientation (LPO) or shape preferred orientation (SPO)) of intrinsically anisotropic minerals in the crust and uppermost mantle. The anisotropic fabrics of the minerals are probably indicative of the patterns of deformation within the preserved crust that is an important record of its tectonic evolution.

## 8.2. Future work

The results obtained from shear wave splitting and surface wave tomography mentioned previously have proved successful in investigating crustal and mantle anisotropy beneath Ireland and in increasing the understanding of anisotropy within the crust, upper mantle beneath Ireland, and in the D" layer. The methods have some limitations, however, as follows:

a) Shear wave splitting measurements provide excellent lateral resolution but poor vertical resolution of particularly polarization anisotropy. This means that splitting measurements have poor depth resolution (e.g., *Long and Silver,* 2009) because anisotropic regions are typically sampled with near-vertical ray paths. The method can yield some of the most direct constraints on mantle flow, but there is a significant problem. That is understanding how to make and interpret splitting measurements correctly and how to relate them properly to mantle flow, is of paramount importance to the study of mantle dynamics.

b) With a single splitting measurement, it is impossible to tell where along the path the anisotropy lies without additional information because the splitting of an SKS/SKKS phase may reflect anisotropy anywhere along the raypath from the CMB to the surface. As a consequence, it is difficult to determine the location, and the degree of the contribution from different origins between the surface and CMB.

c) The azimuthal dependence of the shear-wave splitting results suggests a contribution to the observed anisotropy coming from deeper parts of the mantle. However, the lack of an adequate earthquake distribution limits further investigation using only shear-wave splitting studies.

d) Significant SKS-SKKS splitting discrepancies have been observed in the splitting measurements obtained from the East Asian event cluster. However, nothing much can be said

about the events in the South America because of the limited SKS and SKKS pairs obtained from this cluster. Therefore, more data is required from South America.

e) Rayleigh and Love wave tomography provided robust results for this study. However, they have only allowed detection of anisotropy within the Irish crust. Therefore, additional longer period data is required to investigate seismic anisotropy at deeper depth.

New data and methods are required to further the understanding of anisotropy and S-velocity variations. In the light of the present study, some methods can be suggested:

A) Rayleigh wave and Love wave group velocity maps constructed for each period using the vertical and transverse component of the Green's function estimates from the ambient noise can help to construct a model for Ireland crustal structure.

B) Additional surface wave data can improve the quality of Love wave measurements.

C) The anisotropic P receiver function and S receiver function can help to obtain higher vertical resolution in the top few hundred km of the mantle.

D) Discrepant SKS and SKKS splitting can be supported by the differential S-ScS splitting technique to detect post-perovskite anisotropy in D".

# Bibliography

Aki, K., and K. Kaminuma (1963), Phase velocity in Japan. part I. Love waves from the Aleutian shock of March 9, 1957, *Bulletin of the Earthquake Research Inst.*, *41*, 243–259.

Aki, K., and P. Richards (1980), *Quantitative Seismology: Theory and Methods*, Freeman and Company, New York.

Alsina, D., and R. Snieder (1995), Small-scale sublithospheric continental mantle deformation: constraints from SKS splitting observations, *Geophysical Journal International*, *123*, 431–448.

Anderson, D. L. (1961), Elastic wave propagation in layered anisotropic media, *Journal of Geophysical Research*, *66*, 2953–2963.

Anderson, M., G. Zandt, E. Triep, M. Fouch, and S. Beck (2004), Anisotropy and mantle flow in the Chile-Argentina subduction zone from shear wave splitting analysis, *Geophysical Research Letters*, *31*, 23,608, doi:10.1029/2004GL020906.

Ando, M., Y. Ishikawa, and H. Wada (1980), S-wave anisotropy in the upper mantle under a volcanic area in Japan, *Nature*, *286*, 43–46.

Artemieva, I. M. (2006), Global $1^0x1^0$ thermal model TC1 for the continental lithosphere: Implications for lithosphere secular evolution, *Tectonophysics*, *416*, 245–277.

Babuška, V., and M. Cara (1991), *Seismic anisotropy of the Earth*, 217 pp., Kluwer Academic Publishers.

Backus, G. (1962), Long-wave elastic anisotropy produced by horizontal layering, *Journal of Geophysical Research*, *67*, 4427–4440.

Bamford, S. (1971), An interpretation of first-arrival data from the continental margin refraction experiment, *Geophysical Journal of the Royal Astronomical Society*, *24*, 213–229.

Barruol, G., and H. Kern (1996), Seismic anisotropy and shear-wave splitting in lower-crustal and upper-mantle rocks from the Ivrea Zone–experimental and calculated data, *Physics of the Earth and Planetary Interiors*, *95*, 175–194.

Barruol, G., and D. Mainprice (1993), A quantitative evaluation of the contribution of crustal rocks to the shear-wave splitting of teleseismic SKS waves, *Physics of the Earth and Planetary Interiors*, *78*, 281–300.

Barruol, G., P. G. Silver, and A. Vauchez (1997), Seismic anisotropy in the eastern United States: Deep structure of a complex continental plate, *Journal of Geophysical Research*, *102*, 8329–8348, doi:10.1029/96JB03800.

Bartzsch, S., S. Lebedev, and T. Meier (2011), Resolving the lithosphere-asthenosphere boundary with seismic Rayleigh waves, *Geophysical Journal International*, *186*, 1152–1164.

Bastow, I. D., T. J. Owens, G. Helffrich, and J. H. Knapp (2007), Spatial and temporal constraints on sources of seismic anisotropy: Evidence from the Scottish Highlands, *Geophysical Research Letters*, *34*, L05,305, doi:10.1029/2006GL028911.

Behn, M., G. Hirth, and P. Keleman (2007), Trench-parallel anisotropy produced by foundering of arc lower crust, *Science*, *317*, 108–111.

Belonoshko, A., N. Skorodumova, A. Rosengren, and B. Johansson (2008), Elastic anisotropy of Earth's inner core, *Science*, *319*, 797–800., doi:10.1126/science.1150302.

Birch, F. (1961), The velocity of compressional waves in rocks to 10 kilobars, parts 2, *Journal of Geophysical Research*, *66*, 2199–2224.

Bjarnason, I. T., P. G. Silver, G. Rumpker, and S. C. Solomon (2002), Shear wave splitting across the Iceland hot spot: Results from the ICEMELT experiment, *Journal of Geophysical Research*, *107(B12)*, 2382, doi:10.1029/2001JB000916.

Boore, D. M. (1969), Effect of higher mode contamination on measured Love wave phase velocities, *Journal of Geophysical Research*, *74*, 6612–6616.

Bormann, P., G. Grnthal, R. Kind, and H. Montag (1996), Upper mantle anisotropy beneath Central Europe from SKS wave splitting: Effects of absolute plate motion and lithosphere - asthenosphere boundary topography, *Journal of Geodynamics*, *22*(1), 11–32.

Boschi, L., and A. Dziewonski (1999), "High" and "low" resolution images of the Earth's mantle: Implications of different approaches to tomographic modeling, *Journal of Geophysical Research*, *104*, 25,567–25,594.

Bowman, J., and M. Ando (1987), Shear wave splitting in the upper-mantle wedge above the Tonga subduction zone, *Geophysical Journal of the Royal Astronomical Society*, *88*, 25–41.

Brechner, S., K. Klinge, F. Krüger, and T. Plenefisch (1998), Backazimuthal variations of splitting parameters of teleseismic SKS phases observed at the broadband stations in Germany, *Pure and Applied Geophysics*, *151*, 305 – 331.

Brown, C., and J. P. Whelan (1995), Terrane boundaries in Ireland inferred from the Irish magnetotelluric profile and other geophysical data, *Journal of the Geological Society, London*, *152*(3), 523–534.

Buchbinder, G. G. R. (1985), Shear-wave splitting and anisotropy in the Charlevoix Seismic Zone, Quebec, *Geophysical Research Letters*, *12*, 425–428.

Bullen, K. (1949), Compressibility-pressure hypothesis and the Earth's interior, *Monthly Notices of the Royal Astronomical Society*, *5*, 355–368.

Bunge, H.-P., and M. Richards (1996), The origin of long-wavelength structure in mantle convection: effects of plate motions and viscosity stratification, *Geophysical Research Letters*, *23*, 2987–2990.

Bush, I., and S. Crampin (1991), Paris basin VSPs: Case history establishing combinations of matrix- and crack anisotropy from modelling shear wavefields near point singularities, *Geophysical Journal International*, *107*, 433–447.

Cheng, C., L. Chen, H. Yao, M. Jiang, and B. Wang (2013), Distinct variations of crustal shear wave velocity structure and radial anisotropy beneath the North China Craton and tectonic implications, *Gondwana Research*, *23*, 25–38.

Chevrot, S. (2000), Multichannel analysis of shear wave splitting, *Journal of Geophysical Research*, *105*, 21,579–21,590.

Chew, D. M. (2009), Grampian Orogeny, in *The Geology of Ireland*, edited by C. H. Holland and I. S. Sanders, pp. 69–93, Dunedin Academic Press, Edinburgh, U. K.

Chew, D. M., and C. J. Stillman (2009), Late Caledonian Orogeny and magmatism, in *The Geology of Ireland*, edited by C. H. Holland and I. S. Sanders, pp. 143–174, Dunedin Academic Press, Edinburgh, U. K.

Christensen, N. I. (1996), Poisson's ratio and crustal seismology, *Journal of Geophysical Research*, *101*, 3139–3156, doi:10.1029/95JB03446.

Christensen, N. I., and W. D. Mooney (1995), Seismic velocity structure and composition of the continental crust: A global view, *Journal of Geophysical Research*, *100*, 9761–9788.

Conliffe, J., D. Selby, S. Porter, and M. Feely (2010), Re-Os molybdenite dates from Ballachulish and Kilmeford Igneous Complexes (Scottish Highlands): Age constraints for late Caledonian magmatism, *Journal of the Geological Society, London*, *167*, 297–302.

Conrad, C. P., M. D. Behn, and P. G. Silver (2007), Global mantle flow and the development of seismic anisotropy: Differences between the oceanic and continental upper mantle, *Journal of Geophysical Research*, *112*, B07,317, doi:10.1029/2006JB004608.

Cooper, M. A., D. Collins, M. Ford, F. X. Murphy, P. M. Trayner, and M. O'Sullivan (1986), Structural style of the Irish Variscides, *Journal of the Geological Society London*, *143*, 53–61.

Crampin, S. (1970), The dispersion of surface waves in multilayered anisotropic media, *Geophysical Journal of the Royal Astronomical Society*, *21*, 387–402.

Crampin, S. (1981), A review of wave motion in anisotropic and cracked elastic-media, *Wave Motion*, *3*, 343–391.

Crampin, S. (1989), Suggestion for a consistent terminology for seismic anisotropy, *Geophysical Prospecting*, *37*, 753–770.

Crampin, S. (1993a), A review of the effects of crack geometry on wave propagation through aligned cracks, *Canadian Journal of Exploration Geophysics*, *29*, 3–17.

Crampin, S. (1999a), Calculable fluid-rock interactions, *Journal of the Geological Society, London*, *156*, 501–514.

Crampin, S., and J. H. Lovell (1991), A decade of shear-wave splitting in the Earth's crust: what does it mean? what use can we make of it? and what should we do next?, *Geophysical Journal International*, *107*, 387–407.

Crampin, S., and S. S. Chastin (2003), A review of shear-wave splitting in the crack-critical crust, *Geophysical Journal International*, *155*, 221–240.

Crampin, S., E. Chesnokov, and R. Hipkin (1984), Seismic anisotropy - the state of the art ii, in proc. 1st int. workshop on seismic anisotropy, suzdahl, 1982, eds:S. Crampin and R.G. Hipkin and E.M. Chesnokov, *Geophysical Journal of the Royal Astronomical Society*, *76*, 1–16.

Currie, C. A., J. F. Cassidy, R. D. Hyndman, and M. G. Bostock (2004), Shear wave anisotropy beneath the Cascadia subduction zone and western North American craton, *Geophysical Journal International*, *157*, 341–353, doi:10.1111/j.1365-246X.2004.02175.x.

Curtis, A., J. Trampert, R. Snieder, and B. Dost (1998), Eurasian fundamental mode surface wave phase velocities and their relationship with tectonic structures, *Journal of Geophysical Research*, *103*, 26,919–26,947.

Dahlen, F. (1972), Elastic velocity anisotropy in the presence of an anisotropic initial stress, *Bulletin of the Seismological Society of America*, *62*, 1183–1193.

Daly, J. S., and R. van den Berg (2004), Ion microprobe U-Pb zircon evidence from lower crustal xenoliths for Palaeozoic crust formation and crustal development within the Caledonian suture zone in central Ireland, *Geological Society of America Abstract Programs*, *36(5)*, 48.

Darbyshire, F., and S. Lebedev (2009), Rayleigh wave phase-velocity heterogeneity and multilayered azimuthal anisotropy of the Superior Craton, Ontario, *Geophysical Journal International*, *176*, 215–234, doi:10.1111/j.1365-246X.2008.03982.x.

Debayle, E., and B. L. N. Kennett (2000), The Australian continental upper mantle: Structure and deformation inferred from surface waves, *Journal of Geophysical Research*, *105*(B11), 25,423–25,450.

Debayle, E., B. Kennett, and K. Priestley (2005), Global azimuthal seismic anisotropy and the unique plate motion deformation of Australia, *Nature*, *433*, 509–512, doi:10.1038/nature03247.

Deschamps, F., S. Lebedev, T. Meier, and J. Trampert (2008), Impacts of non-plane waves on two-station measurements of phase velocities, *Geophysical Journal International*, *173*, 827–843, doi:10.1111/j.1365-246X.2008.03751.x.

Dewey, J., and M. Mange (1999), Petrography of Ordovician and Silurian sediments in the western Irish Caledonides: Tracers of a short-lived Ordovician continent-arc collision orogeny and the evolution of the Laurentian Appalachian-Caledonian margin, in *Continental Tectonics*, vol. 164, edited by M. Niocaill and P. Ryan, pp. 55–107, Geological Society London, Special Publications.

Dewey, J. M., and R. M. Shackleton (1984), A model for the evolution of the Grampian tract in the early Caledonides and Appalachians., *Nature*, *312*, 115–121.

Do, V. C., P. Readman, B. M. O'Reilly, and M. Landes (2006), Shear-wave splitting observations across southwest Ireland, *Geophysical Research Letters*, *33*, L03,309, doi:10.1029/2005GL024496.

Duclos, M., M. Savage, A. Tommasi, and K. Gledhill (2005), Mantle tectonics beneath New Zealand inferred from SKS splitting and petrophysics, *Geophysical Journal International*, *163(2)*, 760–774.

Dziewonski, A. M., and D. L. Anderson (1981), Preliminary reference Earth model, *Physics of the Earth and Planetary Interiors*, *25*, 297–356, doi:10.1016/0031-9201(81)90046-7.

Ekstrom, G. (2001), Mapping azimuthal anisotropy of intermediate-period surface waves (abstract), *Eos, Transactions American Geophysical Union*, *82(47)*, doi:AbstractS51E-06.

Endrun, B., T. Meier, S. Lebedev, M. Bohnhoff, G. Stravrakakis, and H. Harjes (2008), S velocity structure and radial anisotropy in the Aegean region from surface wave dispersion, *Geophysical Journal International*, *174*, 593–616.

Endrun, B., S. Lebedev, T. Meier, C. Tirel, and W. Friederich (2011), Complex layered deformation within the Aegean crust and mantle revealed by seismic anisotropy, *Nature Geoscience*, *4*, 203–207, doi:10.1038/ngeo1065.

Evangelidis, C., W. Liang, N. S. Melis, and K. I. Konstantinou (2011), Shear wave anisotropy

beneath the Aegean inferred from SKS splitting observations, *Journal of Geophysical Research, 116*, B04,314, doi:10.1029/2010JB007884.

Evans, M. S., J.-M. Kendall, and R. J. Willemann (2006), Automated SKS splitting and upper-mantle anisotropy beneath Canadian seismic stations, *Geophysical Journal International*, *165*, 931–942, doi:10.1111/j.1365-246X.2006.02973.x.

Evans, R. (1984), Anisotropy: A pervasive feature of fault zones?, *Geophysical Journal of the Royal Astronomical Society*, *76*, 157–63, doi:10.1111/j.1365-246X.1984.tb05031.x.

Fisher, N. (1993), *Statistical Analysis of Circular Data*, Cambridge University Press, London.

Flesch, L., W. E. Holt, P. G. Silver, M. Stephenson, C. Y. Wang, and W. W. Chan (2005), Constraining the extend of crust-mantle coupling in central Asia using GPS, geologic, and shear wave splitting data, *Earth and Planetary Science Letters*, *238 (1-2)*, 248–268.

Ford, M. (1987), Practical application of the sequential balancing technique: an example of the Irish Variscides, *Journal of the Geological Society London*, *144*, 885–891.

Ford, M., S. Klemperer, and P. Ryan (1992), Deep structure of southern Ireland: a new geological synthesis using BIRPS deep reflection profiling, *Journal of the Geological Society, London*, *149*(6), 915–922.

Forsyth, D. W. (1975), The early structural evolution and anisotropy of the oceanic upper mantle, *Geophysical Journal of the Royal Astronomical Society*, *43*, 103–162.

Fouch, M., and S. Rondenay (2006), Seismic anisotropy beneath stable continental interiors, *Physics of the Earth and Planetary Interiors*, *158*, 292–320.

Fouch, M. J., and K. M. Fischer (1998), Shear wave anisotropy in the Mariana subduction zone, *Geophysical Research Letters*, *25*, 1221–1224, doi:10.1029/98GL00650.

Fouch, M. J., P. G. Silver, D. R. Bell, and J. N. Lee (2004), Small-scale variations in seismic anisotropy near Kimberley, South Africa, *Geophysical Journal International*, *157*, 764–774, doi:10.1111/j.1365-246X.2004.02234.x.

Friederich, W., and Z. X. Huang (1996), Evidence for upper mantle anisotropy beneath southern Germany from Love and Rayleigh wave dispersion, *Geophysical Research Letters*, *23 (10)*, 1135–1138.

Friederich, W., S. Hunzinger, and E. Wielandt (2000), A note on the interpretation of seismic surface waves over three-dimensional structures, *Geophysical Journal International*, *143*, 335–339, doi:10.1046/j.1365-246X.2000.01241.x.

Fukao, Y. (1984), Evidence from Core-Reflected Shear Waves for Anisotropy in the Earth's Mantle, *Nature*, *309*, 695–698, doi:10.1038/309695a0.

Gaherty, J. (2004), A surface wave analysis of seismic anisotropy beneath eastern North America, *Geophysical Journal International*, *158*, 1053–1066.

Gamble, J., R. J. Wysoczanski, and I. Meighan (1999), Constraints on the age of British Tertiary Volcanic Province from ion microprobe U-Pb (SHRIMP) ages for acid igneous rocks from NE Ireland, *Journal of the Geological Society, London*, *156*, 291–299.

Gao, S. S., and K. H. Liu (2012), Anisdep: A FORTRAN program for the estimation of the depth of anisotropy using spatial coherency of shear-wave splitting parameters, *Computers and Geosciences*, doi:10.1016/j.cageo.2012.01.020.

Gao, S. S., K. H. Liu, and M. G. Abdelsalam (2010), Seismic anisotropy beneath the Afar Depression and adjacent areas: Implications for mantle flow, *Journal of Geophysical Research*, *115*, B12,330, doi:10.1029/2009JB007141.

Gao, Y., P. Wang, S. Zheng, M. Wang, Y. Chen, and H. Zhou (1998), Temporal changes in shear-wave splitting at an isolated swarm of small earthquakes in 1992 near Dongfang, Hainan Island, southern China, *Geophysical Journal International*, *135*, 102–112.

Garnero, E. J., M. M. Moore, T. Lay, and M. J. Fouch (2004), Isotropy or weak vertical transverse isotropy in D" beneath the Atlantic Ocean, *Journal of Geophysical Research (Solid Earth)*, *109*, B08,308, doi:10.1029/2004JB003004.

Gillet, P. (1995), *Mineral physics, mantle mineralogy and mantle dynamics*, vol. 320 série IIa, C.R. Académie des Sciences.

Godfrey, N. J., N. I. Christensen, and D. A. Okaya (2000), Anisotropy of schists: Contribution of crustal anisotropy to active source seismic experiments and shear wave splitting observations, *Journal of Geophysical Research*, *105*, 27,991–28,008, doi:10.1029/2000JB900286.

Graham, J. R. (2001), Variscan Structures, in *The Geology of Ireland* , edited by C. Holland, pp. 313–330, Dunedin Academic Press Ltd., Edinburgh, U.K.

Greve, S., and M. Savage (2009), Modelling seismic anisotropy variations across the Hikurangi subduction margin, New Zealand, *Physics of the Earth and Planetary Interiors*, *285*, 16–26.

Gripp, A. E., and R. G. Gordon (1990), Current plate velocities relative to the hotspots incorporating the NUVEL-1 global plate motion model, *Geophysical Research Letters*, *17*(8), 1109–1112.

Hall, C., K. Fischer, E. Parmentier, and D. Blackman (2000), The influence of plate motions on three-dimensional back arc mantle flow and shear wave splitting, *Journal of Geophysical Research*, *105*, 28,009–28,034.

Hall, S. A., J.-M. Kendall, and M. van der Baan (2004), Some comments on the effects of lower-mantle anisotropy on SKS and SKKS phases, *Physics of the Earth and Planetary Interiors*, *146*, 469–481, doi:10.1016/j.pepi.2004.05.002.

Hatzfeld, D., E. Karagianni, I. Kassaras, A. Kiratzi, E. Louvari, H. Lyon-Caen, K. Makropoulos, P. Papadimitriou, G. Bock, and K. Priestley (2001), Shear wave anisotropy in the upper mantle beneath the Aegean related to internal deformation, *Journal of Geophysical Research*, *106*, 30,737–30,753.

Hauser, F., B. M. O'Reilly, P. W. Readman, J. S. Daly, and R. van den Berg (2008), Constraints on crustal structure and composition within a continental suture zone in the Irish Caledonides from shear wave wideangle reflection data and lower crustal xenoliths, *Geophysical Journal International*, *175*, 1254–1272, doi:10.1111/j.1365-246X.2008.03945.x.

Helffrich, G. (1995), Lithospheric deformation inferred from teleseismic shear wave splitting observations in the United Kingdom, *Journal of Geophysical Research*, *100*(B9), 18,195–18,204.

Hess, H. H. (1964), Seismic anisotropy of the uppermost mantle under oceans, *Nature*, *203*, 629–631.

Hodgson, J. (2001), A seismic and gravity study of the Leinster Granite: SE Ireland, Ph.D. thesis, National University of Ireland, University College Dublin, unpublished.

Holbrook, W., D. Gajewski, A. Krammer, and C. Prodehl (1988), An interpretation of the wide-angle compressional and shear wave data in southwest Germany: Poisson's ratio and petrological implications, *Journal of Geophysical Research*, *93*, 12,081–12,106.

Holland, C. H. (2001), *The Geology of Ireland*, Dunedin Academic Press Ltd., Edinburgh.

Hudson, J. (1982), Overall properties of a cracked solid, *Mathematical Proceedings of the Cambridge Philosophical Society*, *88*, 371–384.

Hutchison, A. R., and G. Oliver (1998), Garnet provenance studies, juxtaposition of Laurentian marginal terranes and timing of the Grampian Orogeny in Scotland, *Journal of the Geological Society, London.*, *155*, 541–550.

Iidaka, T., and F. Niu (1998), Evidence for an anisotropic lower mantle beneath eastern Asia: Comparison of shear-wave splitting data of SKS and P660s, *Geophysical Research Letters*, *25*, 675–678.

Ismaïl, W. B., and D. Mainprice (1998), An olivine fabric database: an overview of upper mantle fabrics and seismic anisotropy, *Tectonophysics*, *296*, 145–157.

Jacob, A., W. Kaminski, T. Murphy, W. Phillips, and C. Prodehl (1985), A crustal model for a NE-SW profile through Ireland, *Tectonophysics*, *113*, 75–103.

Jadamec, M., and M. I. Billen (2010), Reconciling surface plate motions with rapid three-dimensional mantle flow around a slab edge, *Nature*, *465*, 338–341, doi:10.1038/nature09053.

James, D. E., and M. Assumpçao (1996), Tectonic implications of S-wave anisotropy beneath SE Brazil, *Geophysical Journal International*, *126*, 1–10.

Jones, A. G., D. Snyder, S. Hanmer, I. Asudeh, D. White, D. Eaton, and G. Clarke (2002), Magnetotelluric and teleseismic study across the Snowbird Tectonic Zone, Canadian Shield: A Neoarchean mantle suture ?, *Geophysical Research Letters*, *29*(17).

Jones, S. M., N. White, and B. Lovell (2001), Cenozoic and Cretaceous transient uplift in the Porcupine Basin and its relationship to a mantle plume, in *The Petroleum Exploration of Ireland's Offshore Basins*, vol. 188, edited by P. M. Shannon, P. D. W. Haughton, and D. V. Corcoran, pp. 145–360, Geological Society, London, Special Publication, London, U.K.

Jung, H., and S. Karato (2001), Water-induced fabric transitions in olivine, *Science*, *293*, 1460–1463.

Jung, H., I. Katayama, Z. Jiang, T. Hiraga, and S. Karato (2006), Effects of water and stress on the lattice preferred orientation in olivine, *Tectonophysics*, *421*, 1–22.

Kaneshima, S., and P. G. Silver (1992), A search for source side mantle anisotropy, *Geophysical Research Letters*, *19*, 1049–1052.

Karato, S. (2008), *Deformation of Earth Materials: Introduction to the Rheology of the Solid Earth*, 462. pp., Cambridge University Press, Cambridge, U.K.

Karato, S., and P. Wu (1993), Rheology of the upper mantle: a synthesis., *Science*, *260*, 771–778.

Karato, S.-I., S. Zhang, and H.-R. Wenk (1995), Superplasticity in the Earth's lower mantle: Evidence from seismic anisotropy and rock physics, *Science*, *270*, 458–461.

Katayama, I., and S. Karato (2006), Effects of temperature on the B- to C- type fabric transition in olivine, *Physics of the Earth and Planetary Interiors*, *157*, 33–45.

Katayama, I., S. Karato, and M. Brandon (2005), Evidence of high water content in the deep upper mantle inferred from deformation micro-structures, *Geology*, *33*, 613–616.

Kendall, J., S. Pilidou, D. Keir, I. Bastow, G. Stuart, and A. Ayele (2006), Mantle upwellings, melt migration and the rifting of Africa: insights from seismic anisotropy, in *The Afar volcanic province within the East African Rift System*, vol. 259, edited by G. Yirgu, C. J. Ebinger, and P. K. H. Maguire, pp. 55–72, Geological Society, London, Special Publications.

Kendall, J.-M., and P. Silver (1998), Constraints from seismic anisotropy on the nature of the lowermost mantle, *Nature*, *381*, 409–412.

Kennett, B. L. N., and E. R. Engdahl (1991), Traveltimes for Global Earthquake Location and Phase Identification, *Geophysical Journal International*, *105*, 429–465.

Kern, H., and J. M. Tubia (1993), Pressure and temperature dependence of P- and S-wave velocities, seismic anisotropy and density of sheared rocks from the Sierra Alpujata massif (Ronda peridotites, Southern Spain), *Earth and Planetary Science Letters*, *119*, 191–205, doi:10.1016/0012-821X(93)90016-3.

Klemperer, S. L., P. D. Ryan, and D. B. Snyder (1991), A deep seismic reflection transect across the Irish Caledonides, *Journal of the Geological Society, London*, *148*, 149–164.

Kneller, E., P. E. van Keken, I. Katayama, and S. Karato (2007), Stress, strain, and b-type olivine

fabric in the fore-arc mantle: sensitivity tests using high-resolution steady-state subduction zone models, *Journal of Geophysical Research*, *112*, B04,406, doi:10.1029/2006JB004544.

Lambert, R., and W. McKerrow (1976), The Grampian Orogeny, *Scottish Journal of Geology*, *12*, 271–292.

Landes, M., C. Prodehl, F. Hauser, and A. W. B. Jacob (2000), VARNET-96: Influence of Variscan and Caledonian orogenies on crustal structure in SW Ireland, *Geophysical Journal International*, *140*(3), 660–676.

Landes, M., J. R. R. Ritter, V. C. Do, P. W. Readman, and B. M. O'Reilly (2004), Passive Teleseismic Experiment Explores the Deep Subsurface of Southern Ireland, *EOS Transactions American Geophysical Union*, *85*(36), 337–340, doi:10.1029/2004EO360002.

Landes, M., J. R. R. Ritter, P. W. Readman, and B. M. O'Reilly (2005), A review of the Irish crustal structure and signatures from the Caledonian and Variscan Orogenies, *Terra Nova*, *17*(2), 111–120.

Landes, M., J. R. R. Ritter, B. M. O'Reilly, P. W. Readman, and V. C. Do (2006), A N-S receiver function profile across the Variscides and Caledonides in SW Ireland, *Geophysical Journal International*, *166*, 814–824, doi:10.1111/j.1365-246X.2006.03052.x.

Landes, M., J. Ritter, and P. Readman (2007), Proto-Iceland plume caused thinning of Irish lithosphere, *Earth and Planetary Science Letters*, *255*, 32–40, doi:10.1016/j.epsl.2006.12.003.

Laske, G., and G. Masters (1996), Constraints on global phase velocity maps from long-period polarization data, *Journal of Geophysical Research*, *101*, 16,059–16,075.

Lay, T., and E. J. Garnero (2007), Reconciling the post-perovskite phase with seismological observations of lowermost mantle structure, in *Post-Perovskite: The Last Mantle Phase Change*, *Geophysical Monograph Series*, vol. 174, edited by K. H. et al., pp. 129–153, American Geophysical Union, Washington, D. C.

Lay, T., and T. Wallace (1995), *Modern Global Seismology*, Academic Press, London.

Lay, T., Q. Williams, E. Garnero, L. Kellogg, and M. Wysession (1998), Seismic wave anisotropy in the D" region and its implications, in The Core-Mantle Boundary region, in *Geodynamic Series*, vol. 28M, edited by G. et al., pp. 299–318, American Geophysical Union, Washington, D. C.

Lay, T., J. Hernlund, and B. Buffett (2008), Core-mantle boundary heat flux, *Nature Geoscience*, *1*, 25–32.

Lebedev, S., and R. D. van der Hilst (2008), Global upper-mantle tomography with the automated multimode inversion of surface and S-wave forms, *Geophysical Journal International*, *173*, 505–518, doi:10.1111/j.1365-246X.2008.03721.x.

Lebedev, S., T. Meier, and R. D. van der Hilst (2006), Asthenospheric flow and origin of volcanism in the Baikal Rift area, *Earth and Planetary Science Letters*, *249*, 415–424.

Lebedev, S., J. Boonen, and J. Trampert (2009), Seismic structure of precambrian lithosphere: New constraints from broadband surface-wave dispersion, *Lithos, Special Issue* "*Continental Lithospheric Mantle: the Petro-Geophysical Approach*", *109*, 96–111.

Lebedev, S., J. M.-C. Adam, and T. Meier (2013), Mapping the moho with seismic surface waves: A review, resolution analysis, and recommended inversion strategies. invited review, *Tectonophysics*, "*Moho*" *special issue*, *609*, 377–394.

Leven, J., I. Jackson, and A. Ringwood (1981), Upper mantle seismic anisotropy and lithospheric decoupling, *Nature*, *289*, 234–239.

Levin, V., W. Menke, and A. Lerner-Lam (1996), Shear-wave splitting in Appalachians and Urals: A case for multilayered anisotropy, *Geophysical Journal International*, *126*, 593–603.

Levin, V., W. Menke, and J. Park (1999), Shear-wave splitting in Appalachians and Urals: a case for multilayered anisotropy, *Journal of Geophysical Research*, *104*, 17,975–17,994.

Levshin, A. L., M. H. Ritzwoller, M. P. Barmin, A. Villasenor, and C. A. Padgett (2001), New constraints on the Arctic crust and uppermost mantle: Surface wave group velocities, Pn and Sn, *Physics of the Earth and Planetary Interiors*, *123*, 185–204.

Li, A., and R. S. Detrick (2003), Azimuthal anisotropy and phase velocity beneath Iceland: Implications for plume-ridge interaction, *Earth and Planetary Science Letters*, *214*, 153–165.

Liu, K., and S. Gao (2011), Estimation of the depth of anisotropy using spatial coherency of shear-waves plitting parameters, *Bulletin of the Seismological Society of America*, *101(5)*, doi:10.1785/0120100258.

Long, M. (2009), Complex anisotropy in D" beneath the eastern Pacific from SKS-SKKS splitting discrepancies, *Earth and Planetary Science Letters*, *283*, 181–189.

Long, M., and T. Becker (2010), Mantle dynamics and seismic anisotropy, *Earth and Planetary Science Letters, Frontiers*, *297*, 341–354.

Long, M., and P. Silver (2008), The subduction zone flow field from seismic anisotropy: A global view., *Science*, *319*, 315–318.

Long, M., and P. G. Silver (2009), Shear wave splitting and mantle anisotropy: measurements, interpretations, and new directions, *Surveys in Geophysics*, *30*, 407–461.

Lowe, C., and A. W. B. Jacob (1989), A north-south seismic profile across the Caledonian Suture zone in Ireland, *Tectonophysics*, *168*, 297–318.

Mainprice, D. (2007), Seismic anisotropy of the deep Earth from a mineral and rock physics perspective, in *Treatise on Geophysics*, vol. 2, edited by G. Schubert, pp. 437–492, Elsevier, Oxford, U.K.

Mainprice, D., and P. G. Silver (1993), Interpretation of SKS-waves using samples from the subcontinental lithosphere, *Physics of the Earth and Planetary Interiors*, *78*, 257–280.

Mainprice, D., G. Barruol, and W. B. Ismaïl (2000), The Seismic Anisotropy of the Earth's Mantle: From Single Crystal to Polycrystal, in *Earth's Deep Interior, Mineral Physics and Tomography from the atomic to the global scale*, *Geophysical Monograph Series*, vol. 117, edited by S. Karato, A. M. Forte, R. C. Liebermann, G. Masters, and L. Stixrude, pp. 237–264.

Mainprice, D., A. Tommasi, H. Couvy, P. Cordier, and D. Frost (2005), Pressure sensitivity of olivine slip systems and seismic anisotropy of the Earth's upper mantle, *Nature*, *233*, 731–733, doi:10.1038/nature03266.

Makris, J., R. Egloff, A. Jacob, P. Mohr, T. Murphy, and P. Ryan (1988), Continental crust under the southern Porcupine Seabight west of Ireland, *Earth and Planetary Science Letters*, *89*, 387–397.

Marquart, G., H. Schmeling, and O. $\hat{C}$adek (2007), Dynamic models for mantle flow and seismic anisotropy in the North Atlantic region and comparison with observations, *Geochemistry, Geophysics, Geosystems*, *8*, Q02,008, doi:10.1029/2006GC001359.

Masson, F., A. B. W. Jacob, C. Prodehl, P. W. Readman, P. M. Shannon, A. Schulze, and U. Enderle (1998), A wide-angle seismic traverse through the Variscan of southwest Ireland, *Geophysical Journal International*, *134*(3), 689–705.

Masson, F., F. Hauser, and A. W. B. Jacob (1999), The lithospheric trace of the Iapetus Suture in SW Ireland from teleseismic data, *Tectonophysics*, *302*, 83–89.

Mattatall, L., and M. Fouch (2007), Small-scale variations in SKS splitting near Parkfield, California, *Transactions American Geophysical Union*, *88*, Fall meeting Suppl, abstract T53C–0.

Matte, P. (1986), Tectonics and plate tectonic model for the Variscan belt in Europe, *Tectonophysics*, *126*, 329–374.

Maupin, V., and J. Park (2007), Theory and Observations-Wave Propagation in Anisotropic

Media, in *Treatise in Geophysics*, edited by E.-i.-C. Gerald Schubert, pp. 289–321, Elsevier, Amsterdam.

Maupin, V., E. J. Garnero, T. Lay, and M. J. Fouch (2005), Azimuthal anisotropy in the D" layer beneath the Caribbean, *Journal of Geophysical Research (Solid Earth)*, *110*, B08, 301, doi:10.1029/2004JB003506.

McKerrow, W. S., C. M. Niocaill, and J. F. Dewey (2000), The Caledonian Orogeny redefined, *Journal of the Geological Society, London*, *157*, 1149–1154.

Meade, C., P. G. Silver, and S. Kaneshima (1995), Laboratory and seismological observations of lower mantle isotropy, *Geophysical Research Letters*, *22*, 1293–1296.

Meier, T., K. Dietrich, B. Stckhert, and H. P. Harjes (2004), One dimensional models of shear wave velocity for the eastern Mediterranean obtained from the inversion of Rayleigh wave phase velocities and tectonic implications, *Geophysical Journal International*, *156*, 45–58, doi:10.1111/j.1365-246X.2004.02121.x.

Meissner, R. (1996), Faults and folds, fact and fiction, *Tectonophysics*, *264*, 278–283.

Meissner, R., W. Rabbel, and H. Kern (2006), Seismic lamination and anisotropy of the Lower Continental Crust, *Tectonophysics*, *416*, 81–99.

Menke, W., and D. Abbott (1990), *Geophysical Theory*, Columbia University Press, Irvington, New York.

Menke, W., and V. Levin (2003), The cross-convolution method for interpreting SKS splitting observations, with application to one and two-layer anisotropic Earth models, *Geophysical Journal International*, *154 (2)*, 379–392.

Menke, W., B. Brandsdottir, S. Jakobsdottir, and R. Stefansson (1994), Seismic anisotropy in the crust at the mid-Atlantic plate boundary in south-west Iceland, *Geophysical Journal International*, *119*, 783–790.

Molnar, P., and H. Lyon-Caen (1988), Some simple physical aspects of the support, structure, and evolution of mountain belts, *Processes in continental lithospheric deformation: Geological Society of America Special Paper*, *218*, 197–207.

Montagner, J., and H. Nataf (1988), Vectorial tomography. I. Theory, *Geophysical Journal of the Royal Astronomical Society*, *94*, 295–307.

Montagner, J.-P. (1994), Can Seismology tell us anything about convection in the mantle?, *Reviews of Geophysics*, *32*(2), 115–137.

Montagner, J. P., and B. Kennett (1996), How to reconcile body-wave and normal-mode reference earth models, *Geophysical Journal International*, *125*, 229–248.

Montagner, J.-P., and H.-C. Nataf (1986), A simple method for inverting the azimuthal anisotropy of surface waves, *Journal of Geophysical Research*, *91*, 511–520.

Montagner, J. P., and T. Tanimoto (1991), Global upper mantle tomography of seismic velocities and anisotropies, *Journal of Geophysical Research*, *96*, 20,337–20,351.

Montagner, J.-P., D.-A. Griot-Pommera, and J. Lavé (2000), How to relate body wave and surface wave anisotropy?, *Journal of Geophysical Research*, *105*, 19,015–19,028, doi:10.1029/2000JB900015.

Moore, M. M., E. J. Garnero, T. Lay, and Q. Williams (2004), Shear wave splitting and waveform complexity for lowermost mantle structures with low-velocity lamellae and transverse isotropy, *Journal of Geophysical Research (Solid Earth)*, *109*, BO2319, doi:10.1029/2003JB002546.

Nakajima, J., and A. Hasegawa (2004), Shear-wave polarization anisotropy and subduction-induced flow in the mantle wedge of northeastern Japan, *Earth and Planetary Science Letters*, *225*, 365–377.

Naylor, D., and P. Shannon (1982), *The Geology of Offshore Ireland and West Britain*, Graham-Trotman, London, U.K.

Naylor, D., and P. M. Shannon (2011), *Petroleum Geology of Ireland*, 262 pp., Dunedin Academic Press, Edinburgh, U.K.

Nicolas, A., and N. I. Christensen (1987), Formation of anisotropy in upper mantle peridotites -A review, in *Composition structure and dynamics of the lithosphere asthenosphere systems*, edited by K. Fuchs and C. Froideveaux, pp. 111–123, American Geophysical Union, Washington D.C.

Nicolas, A., and J. Poirier (1976), *Crystalline Plasticity and Solid State Flow in Metamorphic Rocks*, Wiley, New York.

Niu, F., and A. M. Perez (2004), Seismic anisotropy in the lower mantle: A comparison of waveform splitting of SKS and SKKS, *Geophysical Research Letters*, *31*, 24,612–+, doi: 10.1029/2004GL021196.

Nolet, G. (1990), Partitioned waveform inversion and two-dimensional structure under the network of autonomously recording seismographs, *Geophysical Journal International*, *95*, 8499–8512.

Nolet, G. (1993), Imaging the upper mantle with partitioned non-linear waveform inversion, in *Seismic tomography: theory and practice*, edited by H. Iyer and K. Hirahara, Chapman and Hall, London.

Nolet, G., S. Grand, and B. Kennett (1994), Seismic heterogeneity in the upper mantle, *Journal of Geophysical Research*, *99*, 23,753–23,766.

Nowacki, A., J. Wookey, and J.-M. Kendall (2010), Deformation of the lowermost mantle from seismic anisotropy, *Nature*, *467*, 1091–1094, doi:10.1038/nature09507.

Nye, J. F. (1972), *Physical Properties of crystals. Their representation by tensors and matrixes,*, Oxford University Press.

Officer, C. (1974), *Introduction to Theoretical Geophysics*, Springer, New York.

Oganov, A., R. Martonak, A. Laio, P. Raiteri, and M. Parrinello (2005), Anisotropy of Earth's D" layer and stacking faults in the $MgSiO_3$ post-perovskite phase, *Nature, 438 (7071)*, 1142–1144.

O'Reilly, B., P. Shannon, and U. Vogt (1991), Seismic studies in the North Celtic Sea Basin: implications for basin development, *Journal of the Geological Society, London*, *148*, 191–195.

O'Reilly, B., F. Hauser, A. Jacob, P. Shannon, J. Makris, and U. Vogt (1995), The transition between the Erris and the Rockall basins: New evidence from wide-angle seismic data, *Tectonophysics*, *241*, 143–163.

O'Reilly, B. M., and P. W. Readman (2003), Regional Mesozoic basin development along the Irish continental margins: evidence from regional gravity studies, *European Geophysical Society (EGS)-American Geophysical Union (AGU) -European Union of Geosciences (EUG), Joint Assembly*, *1*.

O'Reilly, B. M., P. W. Readman, and T. Murphy (1996), The gravity signature of Caledonian and Variscan tectonics in Ireland, *Physics and Chemistry of the Earth, 21(4)*, 299–304.

O'Reilly, B. M., F. Hauser, C. Ravaut, P. M. Shannon, and P. W. Readman (2006), Crustal thinning, mantle exhumation and serpentinization in the Porcupine Basin, offshore Ireland: Evidence from wide-angle seismic data, *Journal of the Geological Society, London, 163*, 775–787, doi:10.1144/0016-76492005-079.

O'Reilly, B. M., F. Hauser, and P. W. Readman (2010), The fine-scale structure of upper continental lithosphere from seismic waveform methods: Insights into Phanerozoic crustal forma-

tion processes, *Geophysical Journal International*, *180*, 101–124, doi:10.1111/j.1365-246X.2009.04420.x.

O'Reilly, B. M., F. Hauser, and P. W. Readman (2012), The fine-scale seismic structure of the upper lithosphere within accreted Caledonian lithosphere: implications for the origins of the Newer Granites, *Journal of the Geological Society, London*, *169*, 561–573, doi:10.1144/0016-76492011-128.

Özalaybey, S., and M. K. Savage (1995), Shear-wave splitting beneath western United States in relation to plate tectonics, *Journal of Geophysical Research*, *100*, 18,135–18,150, doi:10.1029/95JB00715.

Paige, C., and M. A. Saunders (1982), Lsqr: An algorithm for sparse linear equations and sparse least squares, *Association for Computing Machinery. Transactions on Mathematical Software*, *8*, 43–71, doi:10.1145/355984.355989.

Pedersen, H. A. (2006), Impacts of non-plane waves on two-station measurements of phase velocities, *Geophysical Journal International*, *165*, 279–287, doi:10.1111/j.1365-246X.2006.02893.x.

Phillips, W. E. A., C. J. Stillman, and T. Murphy (1976), A Caledonian plate tectonic model, *Journal of the Geological Society, London*, *132*(6), 579–609.

Pilidou, S., K. Priestley, E. Debayle, and O. Gudmundsson (2005), Rayleigh wave tomography in the North Atlantic: high resolution images of the Iceland, Azores and Eifel mantle plumes, *Lithos*, *79*, 453–474.

Plomerova, J., J. Sileny, and V. Babuska (1996), Joint interpretation of upper-mantle anisotropy based on teleseismic P-travel time delays and inversion of shear-wave splitting parameters, *Physics of the Earth and Planetary Interiors*, *95*, 293–309.

Plomerova, J., U. Achauer, V. Babuska, and L. Vecsey (2007), Upper mantle beneath the Eger

Rift (Central Europe): plume or asthenosphere upwelling, *Geophysical Journal International*, *169*, 675–682.

Polat, G., S. Lebedev, P. Readman, B. O'Reilly, and F. Hauser (2012), Anisotropic Rayleigh-wave tomography of Irelands crust: implications for crustal accretion and evolution within the Caledonian Orogen, *Geophysical Research Letters*, *39*, L04,302, doi:10.1029/2012GL051014.

Postma, G. (1955), Wave propagation in a stratified medium, *Geophysics*, *20*, 780–806.

Rao, C. K., A. Jones, and M. Moorkamp (2007), The geometry of the Iapetus Suture Zone in central Ireland deduced from a magnetotelluric study, *Physics of the Earth and Planetary Interiors*, *160(1-2)*, 134–141.

Readman, P. W., B. M. O'Reilly, and T. Murphy (1997), Gravity gradients and upper-crustal tectonic fabrics, Ireland, *Journal of the Geological Society, London*, *154*(5), 817–828.

Restivo, A., and G. Helffrich (1999), Teleseismic shear wave splitting measurements in noisy environments, *Geophysical Journal International*, *137*, 821–830.

Restivo, A., G. Helffrich, and J.-M. Kendall (1998), Core mantle boundary heterogeneities inferred from anomalous SKS and SKKS splitting, *EOS: Transactions American Geophysical Union*, *79*, F617.

Rickers, F., A. Fichtner, and J. Trampert (2013), The Iceland-Jan Mayen plume system and its impact on mantle dynamics in the North Atlantic region: Evidence from full-waveform inversion, *Earth and Planetary Science Letters*, *367*, 39–51.

Rider, M. H. (1974), The Namurian of west County Clare, *Proceedings of the Royal Irish Academy*, *74B*, 125–143.

Robertson, J., and D. Corrigan (1983), Radiation patterns of a shear-wave vibrator in near-surface shale, *Geophysics*, *48*, 19–26.

Rudnick, R. L., and D. Fountain (1995), Nature and composition of the continental crust: a lower crustal perspective, *Reviews of Geophysics*, *33*, 267–309.

Russo, R. M., and P. G. Silver (1994), Trench-parallel flow benearth the Nazca plate from seismic anisotropy, *Science*, *263*, 1105–1111.

Sanderson, D. J. (1984), Structural variation across the northern margin of the Variscides in NW Europe, in *Variscan Tectonics of the North Atlantic Region*, vol. 14, edited by D. H. Hutton and D. J. Sanderson, pp. 149–165, Geological Society, London, Special Publication.

Sandvol, E., and J. Ni (1997), Deep azimuthal seismic anisotropy in the southern Kurile and Japan subduction zones, *Journal of Geophysical Research*, *102(B5)*, 9911–9922.

Sandvol, E., N. Turkelli, E. Zor, R. Gok, T. Bekler, C. Gurbuz, D. Seber, and M. Barazangi (2003), Shear wave splitting in a young continent-continent collision: An example from Eastern Turkey, *Geophysical Research Letters*, *30*, NO. 24, 8041, doi:10.1029/2003GL017390.

Savage, M. K. (1999), Seismic anisotropy and mantle deformation: What have we learned from shear wave splitting?, *Reviews of Geophysics*, *37*, 65–106, doi:10.1029/98RG02075.

Scarrow, J. (2000), Major element records of variable plume involvement in the North Atlantic province Tertiary flood basalts, *Journal of Petrology*, *41*, 1155–1176.

Sevastopulo, G. D. (1981), Lower Carboniferous and Upper Carboniferous, in *A Geology of Ireland*, edited by C. Holland, pp. 147–187, Scottish Academic Press, Edinburgh.

Sevastopulo, G. D., and P. N. W. Jackson (2009), Carboniferous: Mississippian-Tournaisian and Viséan, in *The Geology of Ireland*, edited by C. Holland and I. S. Sanders, pp. 215–268, Scottish Academic Press, Edinburgh.

Shannon, P. M. (1991), The development of Irish offshore sedimentary basins, *Journal of the Geological Society, London*, *148*, 181–189.

Shearer, M. (1999), *Introduction to Seismology*, Cambridge University Press.,pp, 260.

Sileny, J., and J. Plomerova (1996), Inversion of shear-wave splitting parameters to retrieve three-dimensional orientation of anisotropy in continental lithosphere, *Physics of the Earth and Planetary Interiors*, *95*, 277–292.

Silveira, G., and E. Stutzmann (2002), Anisotropic tomography of the Atlantic Ocean, *Physics of the Earth and Planetary Interiors*, *132*, 237–248.

Silver, P. G. (1996), Seismic Anisotropy Beneath the Continents: Probing the Depths of Geology, *Annual Review of Earth and Planetary Sciences*, *24*, 385–432, doi:10.1146/annurev.earth.24.1.385.

Silver, P. G., and W. W. Chan (1988), Implications for continental structure and evolution from seismic anisotropy, *Nature*, *335*, 34–39.

Silver, P. G., and W. W. Chan (1991), Shear wave splitting and subcontinental mantle deformation, *Journal of Geophysical Research*, *96*(B10), 16,429–16,454.

Silver, P. G., and W. E. Holt (2002), The mantle flow field beneath western north Africa, *Science*, *295*, 1054–1057.

Silver, P. G., and M. K. Savage (1994), The interpretation of shear-wave splitting parameters in the presence of two anisotropic layers, *Geophysical Journal International*, *119*, 949–963.

Skemer, P., I. Katayama, and S. Karato (2006), Deformation fabrics of a peridotite from Cima di Gagnone, central Alps, Switzerland: evidence of deformation under water-rich condition at low temperatures, *Contributions to Mineralogy and Petrology*, *152*, 43–51.

Slater, C., S. Crampin, L. Brodov, and V. Kuznetsov (1993), Observations of anisotropic cusps in transversely isotropic clay, *Canadian Journal of Exploration Geophysics*, *29*, 216–226.

Smith, G., D. Wiens, K. Fischer, L. Dorman, S. Webb, and J. Hildebrand (2001), A complex pattern of mantle flow in the Lau Backarc, *Science*, *292*, 713–716.

Smith, M., and F. A. Dahlen (1973), The azimuthal dependence of Love and Rayleigh wave propagation in a slightly anisotropic medium, *Journal of Geophysical Research*, *78*, 3321–3333, doi:10.1029/JB078i017p03321.

Sodoudi, F., R. Kind, D. Hatzfeld, K. Priestley, W. Hanka, K. Wylegalla, G. Stavrakakis, A. Vafidis, H.-P. Harjes, and M. Bohnhoff (2006), Lithospheric structure of the Aegean obtained from P and S receiver functions, *Journal of Geophysical Research*, *111*, B12,307, doi:10.1029/2005JB003932.

Soper, N., R. Strachan, R. Holdsworht, R. Gayer, and R. Greiling (1992), Sinistral transpression and the Silurian closure of the Iapetus, *Journal of the Geological Society, London*, *149*, 871–880.

Soper, N. J., and N. H. Woodcock (1990), Silurian collision and sediment dispersal patterns in southern Britain, *Geological Magazine*, *127*, 527–542.

Stammler, K. (1993), Seismic Handler - Programmable multichannel data handler for interactive and automatic processing of seismological analyses, *Computer and Geosciences*, *2*, 135–140.

Stein, S., and M. Wysession (2003), *An Introduction to Seismology, Earthquakes and Earth Structure*, Blackwell Publishing.

Stevenson, D. (1987), Limits on lateral density and velocity variations in the Earth's outer core, *Geophysical Journal of the Royal Astronomical Society*, *88*, 311–319.

Stone, P., P. Green, and T.M.Williams (1997), Relationship of source and drainage geochemistry in the British Paratectonic Caledonides: an exploratory regional assessment, *Transactions of the Institution of Mining and Metallurgy*, *106*, B79–B84.

Teanby, N., J.-M. Kendall, R. H. Jones, and O. Barkved (2004), FAST TRACK PAPER: Stress-induced temporal variations in seismic anisotropy observed in microseismic data, *Geophysical Journal International*, *156*, 459–466, doi:10.1111/j.1365-246X.2004.02212.x.

Tommasi, A., A. Vauchez, and R. Russo (1996), Seismic anisotropy in ocean basins: Resistive drag of the sublithospheric mantle?, *Geophysical Research Letters*, *23*, 2991–2994, doi:10.1029/96GL02891.

Torsvik, T. H. (2001), Cretaceous Tertiary geodynamics: A North Atlantic exercise, *Geophysical Journal International*, *146*, 850–866.

Trampert, J., and J.-J. Leveque (1990), Simultaneous iterative reconstruction technique: Physical interpretation based on the generalized least squares solution, *Journal of Geophysical Research*, *95*, 12,553–12,559.

Trampert, J., and J. H. Woodhouse (2003), Global anisotropic phase velocity maps for fundamental mode surface waves between 40 and 150 s, *Geophysical Journal International*, *154*, 154–165, doi:10.1046/j.1365-246X.2003.01952.x.

Van den Berg, R., J. S. Daly, and M. Salisbury (2005), Seismic velocities of granulite-facies xenoliths from Central Ireland: implications for lower crustal composition and anisotropy, *Tectonophysics*, *407*, 81–99.

van Staal, C. R., J. Dewey, C. MacNiocaill, and W. S. McKerrow (1998), Cambrian-Silurian tectonic evolution of the northern Appalachians and British Caledonides: history of a complex, west and southwest Pacific-type segment of Iapetus, in *the Past is the Key to the Present*, vol. 143, edited by D. Blundell and A. C. Scott, pp. 198–242, Geological Society, London, Special Publication.

Vecsey, L., J. Plomerova, and V. Babuska (2008), Shear-wave splitting measurements-problems and solutions, *Tectonophysics*, *462*, 178–196.

Vinnik, L., L. Makeyeva, A. Milev, and A. Usenko (1992), Global patterns of azimuthal anisotropy and deformations in the continental mantle, *Geophysical Journal International*, *111 (3)*, 433–447.

Vinnik, L., B. Romanowicz, Y. L. Stunff, and L. Makeyeva (1995a), Seismic anisotropy in the D" layer, *Geophysical Research Letters*, *22*, 1657–1660.

Vinnik, L. P., R. Kind, G. L. Kosarev, and L. I. Makeyeva (1989), Azimuthal anisotropy in the lithosphere from observations of long-period S-waves, *Geophysical Journal International*, *99*, 549–559.

Voigt, W. (1928), *Lehrbuch der Kristallphysik*, B.G. Tubner, Leipzig.

Wahr, J., and D. de Vries (1989), The possibility of lateral structure inside the core and its implications for nutation and Earth tide observations, *Geophysical Journal International*, *99*, 511–519.

Ware, P. D., and J. P. Turner (2002), Sonic velocity analysis of the Tertiary denudation of the Irish Sea basin , in *Exhumation of the North Atlantic Margin: Timing, Mechanisms and Implications for Petroleum Exploration*, vol. 196, edited by A. G. Dor'e, pp. 355–370, Geological Society, London, Special Publications.

Wawerzinek, B., J. Ritter, M. Jordan, and M. Landes (2008), An upper mantle upwelling underneath Ireland revealed from non-linear tomography, *Geophysical Journal International*, *175 (1)*, 253–268.

Wenk, H.-R. (1985), *Preferred Orientation in Deformed Metals and Rocks: An Introduction to Modern Texture Analysis*, Academic Press, Orlando.

Wentzcovitch, R., T. Tsuchiya, and J. Tsuchiya (2006), $MgSiO_3$ postperovskite at D" conditions, *Proceedings of the National Academy of Sciences of the United States of America*, *103 (3)*, 543–546.

White, R. (1989), Magmatism at rift zones: the generation of volcanic continental margins and flood basalts, *Journal of Geophysical Research*, *94*, 7685–7729.

Wild, P., and S. Crampin (1991), The range of effects of azimuthal isotropy and EDA-anisotropy in sedimentary basins, in *Proc. 4th Int. Workshop on Seismic Anisotropy, 1990*, vol. 107, edited by J. Lovell and S. Crampin, pp. 513–529, Geophysical Journal International, Edinburgh.

Windley, B. (1995), *The Evolving Continents, 3rd edn*, 168–224 pp., Wiley, Chichester, UK.

Wolfe, C. J., and S. C. Solomon (1998), Upper mantle anisotropy beneath the MELT region of the East Pacific Rise: Shear-wave splitting measurements and implications for mantle flow, *Science, 280*, 1230–1232.

Woodcock, N. H., and R. A. Strachan (2000), *Geological History of Britain and Ireland*, chap. The Caledonian Orogeny: a multiple plate collision, pp. 187–206, Blackwell Science.

Woodcock, N. H., M. A. Awan, T. E. Johnson, A. H. Mackie, and R. D. A. Smith (1988), Acadian tectonics of Wales during Avalonia-Laurentia Convergence, *Tectonics, 7 (3)*, 483–495, doi:10.1029/TC007i003p00483.

Woodward, R., and G. Masters (1991), Global upper mantle structure from long-period differential travel-times, *Journal of Geophysical Research, 96*, 6351–6377.

Wookey, J., J.-M. Kendall, and G. Barruol (2002), Mid-mantle deformation inferred from seismic anisotropy, *Nature*, (415), 777–780.

Wookey, J., J.-M. Kendall, and G. Rümpker (2005a), Lowermost mantle anisotropy beneath the north Pacific from differential S-ScS splitting, *Geophysical Journal International, 161*, 829–838, doi:10.1111/j.1365-246X.2005.02623.x.

Wookey, J., S. Stackhouse, J.-M. Kendall, J. P. Brodholt, and G. D. Price (2005b), Efficacy of the post-perovskite phase as an explanation of lowermost mantle seismic properties, *Nature*, (438), 1004–1008.

Xue, M., and R. M. Allen (2005), Asthenospheric channeling of the Icelandic upwelling: Evidence from seismic anisotropy , *Earth and Planetary Science Letters*, *235*, 167–182, doi: 10.1016/j.epsl.2005.03.017.

Yang, X., and K. M. Fischer (1994), Constraints on North Atlantic upper mantle anisotropy from S and SS phases, *Geophysical Research Letters*, *21*, 309–312.

Yang, X., K. M. Fischer, and G. A. Abers (1995), Seismic anisotropy beneath the Shumagin Islands segment of the Aleutian-Alaska subduction zone, *Journal of Geophysical Research*, *100*, 18,165–18,178, doi:10.1029/95JB01425.

Zhang, X., H. Paulssen, S. Lebedev, and T. Meier (2007), Surface wave tomography of the Gulf of California, *Geophysical Research Letters*, *34 (L15305)*, doi:10.1029/2007GL030631.

# A. Glossary, annotation and symmetry system in seismic anisotropy

## A.1. Glossary

Below is summary of seismic anisotropy related terms and symbols used in this study.

| Term | Symbol | Description |
|---|---|---|
| Azimuthal anisotropy | | The variation of speed for a given wave type as a function of the azimuth of the propagation direction. |
| Azimuthal isotropy | | Type of anisotropy where there is no variation of properties with azimuth in the horizontal plane. This is the result of hexagonal symmetry with a vertical axis of symmetry. Referred to as transverse isotropy when used as a spatial orientation. |
| Back azimuth | $\phi_{baz}(^0)$ | The angle measured between the geographic north and the direction to the source. |
| Birefringence | | The phenomenon by which one component of a transverse wave travelling through an anisotropic medium is faster than the orthogonal component. When observed for acoustic (seismic shear) waves, it is commonly called shear wave splitting. |
| Crystal Preferred Orientation | CPO | See LPO. |
| D” | | The layer, approximately 250 km thick at the base of the mantle, just above the outer core. |
| Delay time | $\delta t(s)$ | Time separation between fast and slow components of split shear waves. |

| | | |
|---|---|---|
| Diffusion creep | | Deformation caused by diffusive mass transport across the crystal lattice or along grain boundaries. It results in an isotropic rock fabric. |
| Dislocation creep | | Deformation caused by the motion of crystalline dislocations within grains, which results in preferred mineral orientation. |
| Double refraction | | See Birefringence. |
| Effective anisotropy | | See Shaped Preferred Orientation. |
| Fast direction | $\phi$ | (1) The direction in a medium which results in the fastest velocity for a given wave type or fastest polarisations of the S wave, or (2) the horizontal component of the fast direction. With some symmetry systems the fast directions will differ for P and S waves. |
| Fresnel zone | | The region surrounding the ray path in which the material properties of the region affect the waveform. Also referred to as the maximum lateral seismic resolution. The Fresnel zone radius is proportional to the period and length of the ray path. |
| Hexagonal symmetry | | Symmetry with a single axis of sixfold rotation. The seismic properties of hexagonally symmetric systems are identical to those of cylindrical symmetry, in which properties in the plane perpendicular to the symmetry axis are independent of direction. |
| Intrinsic anisotropy | | The difference between the maximum and minimum velocities in a medium. |
| Isotropy | | In a uniform isotropic rock all planes are planes of symmetry and the elastic properties are the same in all directions. |
| Lattice Preferred Orientation | LPO | Non-random orientation of crystals produced by dislocation glide. See also dislocation creep. |
| Lehmann discontinuity | | A seismic discontinuity at about 200 km depth where transition from dislocation creep to diffusion creep may occur. |
| Love wave | | Horizontally polarised surface wave. |
| Triclinic | | Adjective for material with full, general anisotropy with 21 elastic constants. Triclinic may have no plane of symmetry and/or no symmetry. |
| Monoclinic symmetry | | Symmetry with only one plane of symmetry. |

| | | |
|---|---|---|
| Null measurement | | A measurement that detects no splitting on a shear wave. Such measurements suggest either that the medium is isotropic or that the initial polarisation was parallel to the fast or slow direction of anisotropy for that propagation direction. |
| Orthorhombic symmetry | | Symmetry with three mutually orthogonal planes of symmetry. |
| Particle motion diagram | | See Polarisation diagram. |
| Percent anisotropy | $ks$(%) | Velocity differences between the two quasi-S waves in a given propagation direction, or the degree of intrinsic anisotropy of a material. |
| Polarisation | | Direction of particle motion in a wave, where $\phi_{ini}$ is polarisation of initial P and S waves before entering anisotropic media, and $\phi$ is fast polarisation after passing through an anisotropic medium; $\phi$ is usually measured in the horizontal plane. |
| Polarisation anisotropy | | The property that wave speed differs for shear or surface waves of different polarisations travelling along the same direction. |
| Polarisation diagram | | A two-dimensional diagram in which two components of a seismogram are plotted against each other. As time increases, the figure traces out a pattern that is linear if there is no phase shift between the two components (no splitting) and elliptical if a phase shift exists. |
| Quasi P S wave | qP, qS | qP, qS1, and qS2 waves are the three quasi-body waves propagating in every direction of phase propagation in an anisotropic solid. "Quasi-" refers to when the polarisation is not exactly radial or transverse. qSl- is the faster and qS2- the slower split shear-wave. The three waves propagating with the same direction of phase propagation have mutually orthogonal polarisations. Note that the displacement of qP waves is usually within one or two degrees of the direction of the ray path for anisotropy less than about 10%. |
| Radial anisotropy | | Hexagonal anisotropy with a vertical symmetry axis. |
| Radial component | R-comp | A horizontal component, rotated to being parallel to the earthquake-station back azimuth. |
| Rayleigh waves | | Surface waves polarised in a vertical plane. |

| | | |
|---|---|---|
| Sagittal plane | | The vertical plane containing an observing station and a seismic source. |
| SH wave | SH | A shear wave vibrating in the horizontal plane. |
| Shear wave splitting | | Acoustic birefringence. |
| Shear wave window | | The cone of incidence angles that are sufficiently close to vertical so that particle motion for an isotropic Earth is expected to be linear. |
| Structural frame | XYZ | Usually used in describing mineral orientations or velocity measurements in rock samples; it is defined by the foliation plane and lineation direction. |
| SV wave | SV | A shear wave vibrating in the sagittal plane. |
| Shaped Preferred Orientation | SPO | Alignment of isotropic material layers. SPO can only be detected by seismic signals of wavelengths larger than the spacing of the layers. |
| Symmetry plane | | A plane in which the elastic properties have reflection symmetry. |
| Transverse anisotropy | | Anisotropy with hexagonal symmetry. |
| Transverse component | T-comp | The horizontal component that is perpendicular to the radial component. |
| Transverse isotropy | | Often reserved for cases in which the symmetry axis is vertical. See azimuthal isotropy. |
| TTI | | Hexagonal symmetry with tilted symmetry axis. |
| VTI | | See Transverse isotropy. |

## A.2. Anisotropic symmetry systems

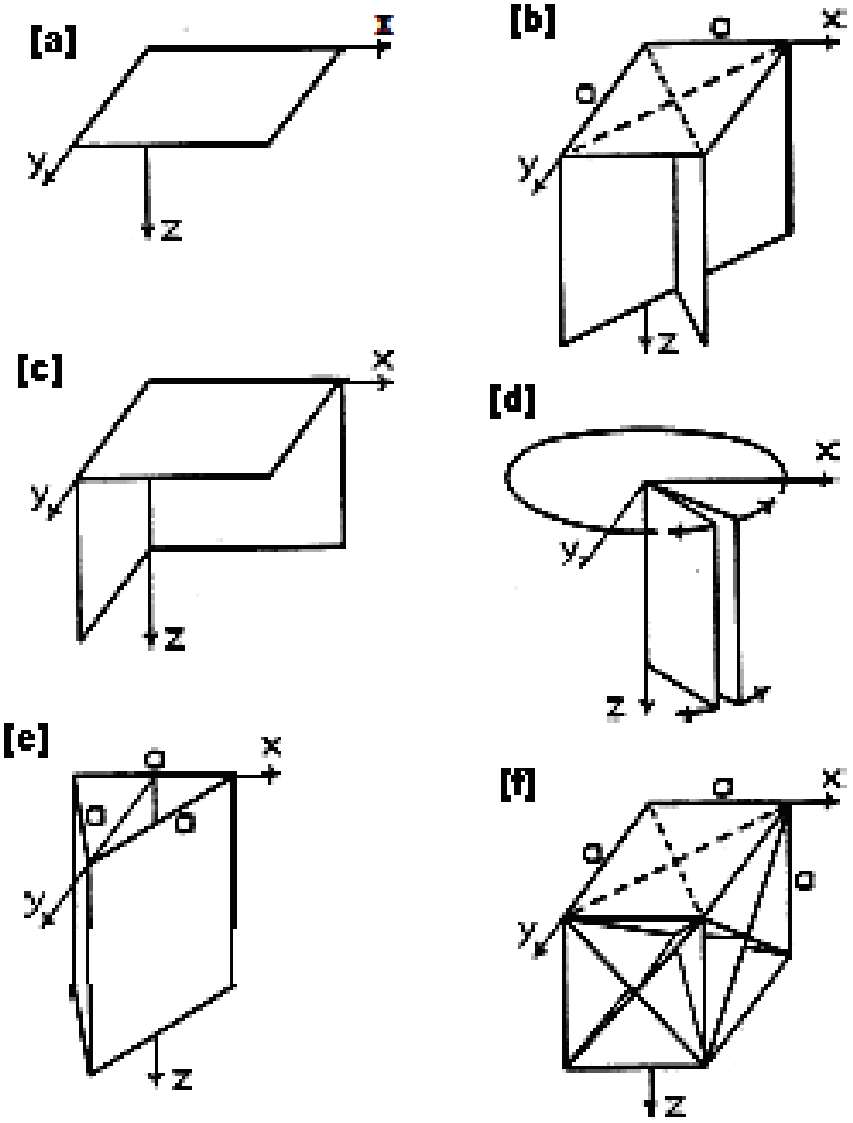



Figure A.1.: Summary of common symmetry systems (from *Crampin*, 1989). (a) Monoclinic, (b) Tetragonal, (c) Orthorhombic, (d) Hexagonal, (e) Trigonal, (f) Cubic.

# A.3. Elastic stiffness tensor

Stiffness tensors, $c_{ijkl}$ are derived from the general form of Hooke's law, which relates the stress to the strain, in a homogeneous system and written as followed: $\sigma_{ij} = c_{ijkl}\epsilon_{kl}$, where $\sigma_{ij}$ and $\epsilon_{kl}$ are stress and strain tensors, respectively. The symmetries of $\sigma_{ij}$ and $\epsilon_{kl}$ which lead to $c_{ijkl} = c_{jikl} = c_{ijlk} = c_{klij}$ usually help to reduce the number of independent components of $c_{ijkl}$ from 81 to 21. The number of independent elastic constants required to fully describe the stiffness tensor depends on the symmetry systems. Higher symmetries require less independent constants. The stiffness tensor of a material can be written in four or two suffix notations as follows:

## A.3.1. Notation

- Four suffix tensor notation

$$\begin{pmatrix} c_{1111} & c_{1122} & c_{1133} & c_{1123} & c_{1131} & c_{1112} \\ c_{2211} & c_{2222} & c_{2233} & c_{2223} & c_{2231} & c_{2212} \\ c_{3311} & c_{3322} & c_{3333} & c_{3323} & c_{3331} & c_{3312} \\ c_{2311} & c_{2322} & c_{2333} & c_{2323} & c_{2331} & c_{2312} \\ c_{3111} & c_{3122} & c_{3133} & c_{3123} & c_{3131} & c_{3112} \\ c_{1211} & c_{1222} & c_{1233} & c_{1223} & c_{1231} & c_{1212} \end{pmatrix} \tag{A.1}$$

- Two suffix matrix notation

$$\begin{pmatrix} c_{11} & c_{12} & c_{13} & c_{14} & c_{15} & c_{16} \\ c_{21} & c_{22} & c_{23} & c_{24} & c_{25} & c_{26} \\ c_{31} & c_{32} & c_{33} & c_{34} & c_{35} & c_{36} \\ c_{41} & c_{42} & c_{43} & c_{44} & c_{45} & c_{46} \\ c_{51} & c_{52} & c_{53} & c_{54} & c_{55} & c_{56} \\ c_{61} & c_{62} & c_{63} & c_{64} & c_{65} & c_{66} \end{pmatrix} \tag{A.2}$$

### A.3.2. Isotropic case

For isotropic materials and minerals, e.g. garnet, the matrix form of the elastic tensor is:

$$\begin{pmatrix} \lambda+2\mu & \lambda & \lambda & 0 & 0 & 0 \\ \lambda & \lambda+2\mu & \lambda & 0 & 0 & 0 \\ \lambda & \lambda & \lambda+2\mu & 0 & 0 & 0 \\ 0 & 0 & 0 & \mu & 0 & 0 \\ 0 & 0 & 0 & 0 & \mu & 0 \\ 0 & 0 & 0 & 0 & 0 & \mu \end{pmatrix} \tag{A.3}$$

where $\lambda$ and $\mu$ are Lamé's constants which are related to P-wave velocity $\alpha$, S-wave velocity $\beta$, and the density of the medium $\rho$ as follows:

$$\lambda = \rho(\alpha^2 - 2\beta^2) \tag{A.4}$$

$$\mu = \rho\beta^2 \tag{A.5}$$

For special case of fluid-filled cracks in an isotropic medium, the corresponding stiffness matrix is:

$$\begin{pmatrix} \lambda+2\mu & \lambda & \lambda & 0 & 0 & 0 \\ \lambda & \lambda+2\mu & \lambda & 0 & 0 & 0 \\ \lambda & \lambda & \lambda+2\mu & 0 & 0 & 0 \\ 0 & 0 & 0 & \mu & 0 & 0 \\ 0 & 0 & 0 & 0 & \mu(1-\epsilon) & 0 \\ 0 & 0 & 0 & 0 & 0 & \mu(1-\epsilon) \end{pmatrix} \tag{A.6}$$

where $\epsilon = Na^3/V$ is the crack density of the medium, $N$ is the number of cracks in a volume of rock $V$ and $a$ is the radii of the cracks (*Babuška and Cara*, 1991).

### A.3.3. Orthorhombic case

The orthorhombic symmetry system has three perpendicular axes of symmetry and nine independent elastic constants. Examples of orthorhombic symmetry systems are mantle minerals such as olivine, orthopyroxenes and mantle xenoliths composed of these minerals.

The stiffness tensor for orthorhombic symmetry is written in four suffix and two suffix notations as follows:

Four suffix tensor notation:

$$\begin{pmatrix} c_{1111} & c_{1122} & c_{1133} & 0 & 0 & 0 \\ c_{1122} & c_{2222} & c_{2233} & 0 & 0 & 0 \\ c_{1133} & c_{2233} & c_{3333} & 0 & 0 & 0 \\ 0 & 0 & 0 & c_{2323} & 0 & 0 \\ 0 & 0 & 0 & 0 & c_{3131} & 0 \\ 0 & 0 & 0 & 0 & 0 & c_{1212} \end{pmatrix} \tag{A.7}$$

Two suffix matrix notation:

$$\begin{pmatrix} c_{11} & c_{12} & c_{13} & 0 & 0 & 0 \\ c_{12} & c_{22} & c_{23} & 0 & 0 & 0 \\ c_{13} & c_{23} & c_{33} & 0 & 0 & 0 \\ 0 & 0 & 0 & c_{44} & 0 & 0 \\ 0 & 0 & 0 & 0 & c_{55} & 0 \\ 0 & 0 & 0 & 0 & 0 & c_{66} \end{pmatrix} \tag{A.8}$$

### A.3.4. Hexagonal case

Hexagonal symmetry system has five independent elastic constants. Typical hexagonal systems in the case of anisotropic studies are mica minerals, sedimentary layering and aligned parallel cracks. Hexagonal symmetry may be referred to as transverse isotropy or TI (see A.1). Transverse isotropy with a vertical symmetry axis (VTI) is referred to as radial anisotropy. Transverse

isotropy with a tilted symmetry axis is referred to as TTI (see A.1).

Also note that for hexagonal symmetry: $c_{1212} = (c_{1111} - c_{1122})/2$.

The stiffness tensor for hexagonal symmetry is written in four suffix, two suffix and Love notations as follows:

Four suffix notation:

$$\begin{pmatrix} c_{1111} & c_{1111}-2c_{1122} & c_{1133} & 0 & 0 & 0 \\ c_{1111}-2c_{1122} & c_{1111} & c_{1133} & 0 & 0 & 0 \\ c_{1133} & c_{1133} & c_{3333} & 0 & 0 & 0 \\ 0 & 0 & 0 & c_{2323} & 0 & 0 \\ 0 & 0 & 0 & 0 & c_{2323} & 0 \\ 0 & 0 & 0 & 0 & 0 & c_{1212} \end{pmatrix} \tag{A.9}$$

Two suffix notation:

$$\begin{pmatrix} c_{11} & c_{11}-2c_{66} & c_{13} & 0 & 0 & 0 \\ c_{11}-2c_{66} & c_{11} & c_{13} & 0 & 0 & 0 \\ c_{13} & c_{13} & c_{33} & 0 & 0 & 0 \\ 0 & 0 & 0 & c_{44} & 0 & 0 \\ 0 & 0 & 0 & 0 & c_{44} & 0 \\ 0 & 0 & 0 & 0 & 0 & c_{66} \end{pmatrix} \tag{A.10}$$

Love notation:

$$\begin{pmatrix} A & A-2N & F & 0 & 0 & 0 \\ A-2N & A & F & 0 & 0 & 0 \\ F & F & C & 0 & 0 & 0 \\ 0 & 0 & 0 & L & 0 & 0 \\ 0 & 0 & 0 & 0 & L & 0 \\ 0 & 0 & 0 & 0 & 0 & N \end{pmatrix} \tag{A.11}$$

In laboratory petrophysical measurements which are used to derive stiffness matrices from rock samples, the two compressional wave velocities, one quasi compressional wave velocity, two shear-wave velocities and a density value are usually needed in order to calculate the five independent elastic stiffness constants that can fully describe a transversely isotropic media. The relationships between these parameters are as follows (*Godfrey et al.*, 2000):

$$c_{11} = \rho V_P(90^0)^2 \tag{A.12}$$

$$c_{33} = \rho V_P(0^0)^2 \tag{A.13}$$

$$c_{44} = \rho V_{SV}(0^0)^2 = \rho * V_{SH}(0^0)^2 = \rho * V_{SV}(90^0)^2 \tag{A.14}$$

$$c_{12} = c_{11} - [2\rho V_{SH}(90^0)^2] = c_{11} - 2c_{66} \tag{A.15}$$

$$c_{13} = -c_{44} + [(4\rho^2 V_P(45^0)^4) - (2\rho V_P(45^0)^2)(c_{11} + c_{33} + 2c_{44} + (c_{11} + c_{44})(c_{33} + c_{44})]^{1/2} \tag{A.16}$$

$$c_{66} = \rho V_{SH}(90^0)^2 = [c_{11} - c_{12}]/2 \tag{A.17}$$

where

- $V_P(90^0)$ is the compressional wave propagating perpendicular to the symmetry axis and within the foliation plane.
- $V_P(0^0)$ is the compressional wave propagating parallel to the symmetry axis, hence perpendicular to the foliation plane.
- $V_P(45^0)$ is the quasi compressional wave propagating at $45^0$ to the symmetry axis. $V_P(45^0)$ also corresponds to the average value between $V_P(90^0)$ and $V_P(0^0)$ (*Barruol and Mainprice*, 1993).
- $V_{SH}(0^0)$ is the shear wave propagating parallel to the symmetry axis with particle motion within the foliation plane. For transverse isotropic material, $V_{SH}(0^0) = V_{SV}(0^0) = V_{SV}(90^0)$.

- $V_{SH}(90^0)$ is the shear wave propagating perpendicular to the symmetry axis with particle motion also perpendicular to the symmetry axis within the foliation plane.

# B. List of stations used in this study

| Station | Latitude | Longtitude | Start Date | End date | Remarks |
|---|---|---|---|---|---|
| D01 | 52.80360 | -9.35000 | 18-Nov-2002 | 8-Aug-2005 | – |
| D02 | 52.57884 | -9.10712 | 4-Nov-2002 | 30-Jan-2004 | – |
| D03 | 52.38928 | -9.02120 | 4-Nov-2002 | 06-Sept-2006 | – |
| D04 | 52.19810 | -8.83439 | 5-Nov-2002 | 28-Jan-2004 | – |
| D05 | 51.99039 | -8.74578 | 25-Nov-2002 | 07-Sept-2006 | – |
| D06 | 53.00040 | -8.95040 | 18-Nov-2002 | 08-June-2004 | – |
| D07 | 52.78610 | -8.77280 | 19-Nov-2002 | 29-Jan-2004 | – |
| D08 | 52.52400 | -8.65630 | 07-Nov-2002 | 05-May-2004 | – |
| D09 | 52.37698 | -8.58278 | 7-Nov-2002 | 28-Jan-2004 | – |
| D10 | 52.13735 | -8.41274 | 06-Nov-2002 | 05-May-2004 | – |
| D12 | 52.70950 | -8.42610 | 17-Nov-2002 | 04-Sep-2003 | – |
| D14 | 52.30540 | -8.05850 | 26-Nov-2002 | 19-Sept-2006 | – |
| D15 | 54.06720 | -9.31190 | 01-Aug-2004 | 15-May-2012 | – |
| D16 | 53.35195 | -9.56198 | 14-June-2004 | 16-May-2012 | – |
| D17 | 53.9577 | -8.8387 | 04-Feb-2004 | 16-May-2012 | – |
| D18 | 53.62830 | -8.26060 | 03-Feb-2004 | 05-Dec-2006 | – |
| D21 | 53.22159 | -8.02400 | 27-Feb-2003 | 03-Aug-2005 | – |
| D23 | 52.72600 | -7.87620 | 26-Nov-2002 | 22-Oct-2010 | – |
| D31 | 52.93917 | -6.63982 | 23-May-2003 | 29-Sept-2003 | – |

| | | | | | |
|---|---|---|---|---|---|
| D32 | 55.15433 | -6.67797 | 14-Feb-2006 | – | in operation |
| D33 | 54.18411 | -7.23886 | 20-Jun-2006 | 29-Sept-2012 | – |
| D34 | 55.03577 | -7.96855 | 21-Jun-2006 | – | in operation |
| D35 | 52.24917 | -6.33472 | 03-Aug-2006 | 17-Sept-2007 | – |
| D36 | 52.69608 | -6.21142 | 05-Oct-2006 | 01-March-2007 | – |
| D37 | 53.44983 | -7.48217 | 13-Aug-2008 | 01-July-2011 | – |
| D38 | 51.7981 | -8.2500 | 30-May-2008 | 12-Apr-2011 | – |
| P07 | 51.49609 | -9.37581 | 30-May-2004 | 12-Apr-2011 | – |
| IA001 | 54.2276 | -10.0067 | 20-Oct-2010 | – | in operation |
| IA002 | 54.3529 | -8.5191 | 19-Oct-2010 | – | in operation |
| IA003 | 53.0942 | -7.9202 | 23-Feb-2011 | – | in operation |
| IA004 | 53.1188 | -8.7468 | 06-Apr-2011 | – | in operation |
| IA005 | 52.0786 | -9.1909 | 13-Apr-2011 | – | in operation |
| IA006 | 52.5093 | -8.5304 | 05-May-2011 | – | in operation |
| IA007 | 52.1690 | -7.4403 | 25-May-2011 | – | in operation |
| IA008 | 54.0875 | -6.2644 | 08-June-2011 | 15-Aug-2012 | closed |
| IA009 | 53.8649 | -8.9680 | 12-July-2011 | – | in operation |
| IA010 | 53.6731 | -7.0495 | 20-July-2011 | – | in operation |
| IAD01 | 52.8037 | -9.3501 | 23-Sept-2010 | – | in operation |
| IAD18 | 53.6284 | -8.2613 | 19-Oct-2010 | – | in operation |
| IAD23 | 52.7262 | -7.8772 | 22-Sept-2010 | – | in operation |
| IAD38 | 51.7981 | -8.2500 | 22-Sept-2010 | – | in operation |
| IAP07 | 51.4965 | -9.3764 | 12-Apr-2011 | 27-March-2014 | closed |
| IAVAL | 51.9396 | -10.2444 | 21-Oct-2010 | 11-Jan-2012 | closed |
| DSB | 53.2450 | -6.3755 | 1-Dec-1993 | – | in operation |
| VAL | 51.9370 | -10.2442 | 24-May-1999 | – | in operation |

# C. Summary of data loggers and sensors deployed at ISLE, ISUME and IA stations

A footnote for this table[1]

| Station | Rec. Box | Sensor | Serial No. | Sampling rate and Bandwidth |
|---|---|---|---|---|
| D01 | EDL PR242 | CMG-40T | 4506 | 25 BB |
| D02 | EDL PR2400 | CMG-40T | 4275 | 75 BB |
| D03 | EDL PR2400 | CMG-40T | 4274 | 75 BB |
| D04 | EDL PR242 | CMG-40T | 4276 | 25 BB |
| D05 | EDL PR2400 | CMG-40T | 4311 | 75 BB |
| D06 | EDL PR242 | CMG-40T | 4313 | 25 BB |
| D07 | EDL PR2400 | CMG-40T | 4309 | 75 BB |
| D08 | EDL PR2400 | CMG-40T | 4505 | 75 BB |
| D09 | EDL PR2400 | CMG-40T | 4509 | 75 BB |
| D10 | EDL PR2400 | CMG-40T | 4954 | 75 BB |
| D12 | EDL PR2400 | CMG-40T | 4504 | 75 BB |
| D14 | EDL PR2400 | CMG-40T | 4286 | 75 BB |
| D15 | EDL PR2400 | CMG-40T | 4509 | 75 BB |

[1]EDL-Earth Data limited. G40T seismometers manufacturated by Guralp Systems ltd. Taurus data logger manufactured by Nanometrics Inc. Trillium 12PA seismometers manufactured by Nanometrics Inc.

| | | | | |
|---|---|---|---|---|
| D16 | EDL PR6-24 | CMG-40T | 4313 | 75 BB |
| D18 | EDL PR2400 | CMG-40T | 4509 | 75 BB |
| D21 | EDL PR2400 | CMG-40T | 4290 | 75 BB |
| D23 | EDL PR2400 | CMG-40T | 4312 | 75 BB |
| D31 | EDL PR242 | CMG-40T | 458 | 25 BB |
| D32 | EDL PR6-24 | CMG-40T | 4505 | 25 BB |
| D33 | EDL PR2400 | CMG-40T | 4504 | 75 BB |
| D34 | EDL PR6-24 | CMG-40T | 4290 | 25 BB |
| P07 | EDL PR242 | CMG-40T | 4276 | 25 BB |
| DSB | QT STS-2 | Various | - | 100 BB |
| VAL | EDL | CMG-40T | 4230 | 75 BB |
| IA001 | Taurus data logger | Trillium 120PA | 0888 | 100 |
| IA002 | Taurus data logger | Trillium 120PA | 0810 | 100 |
| IA003 | Taurus data logger | Trillium 120PA | 0880 | 100 |
| IA005 | Taurus data logger | Trillium 120PA | 0885 | 100 |
| IA006 | Taurus data logger | Trillium 120PA | 0882 | 100 |
| IA007 | Taurus data logger | Trillium 120PA | 0849 | 100 |
| IA008 | Taurus data logger | Trillium 120PA | 0879 | 100 |
| IA009 | Taurus data logger | Trillium 120PA | 0823 | 100 |
| IA010 | Taurus data logger | Trillium 120PA | 0881 | 100 |
| IAD01 | Taurus data logger | Trillium 120PA | 0891 | 100 |
| IAD18 | Taurus data logger | Trillium 120PA | 0877 | 100 |
| IAD23 | Taurus data logger | Trillium 120PA | 0844 | 100 |
| IAD38 | Taurus data logger | Trillium 120PA | 0878 | 100 |
| IAP07 | Taurus data logger | Trillium 120PA | 0896 | 100 |
| IAVAL | Taurus data logger | Trillium 120PA | 0797 | 100 |

# D. Complete list of results from shear wave splitting measurements at all Irish stations from 01/01/2003 to 31/09/2011

| Complete list of results from shear wave splitting measurements at all Irish stations from 01/01/2003 to 30/09/2011 | | | | | | | | | | | | | |
|---|---|---|---|---|---|---|---|---|---|---|---|---|---|
| Event parameters | | | | | Splitting Parameters | | | | | | | | |
| Origin time | Lat | Lon | Mb | Depth | Station | $\phi_{baz}$ | $\Delta$ | Phase | Quality | $\delta$t | $\sigma_\delta t$ | $\phi$ | $\sigma_\phi$ |
| | ($^0$) | ($^0$) | | (km) | | ($^0$) | ($^0$) | | | (s) | (s) | ($^0$) | ($^0$) |
| 20 JUN 2003 13:30:41.640 | -30.61 | -71.64 | 6.8 | 33.00 | D01 | 230.64 | 99.16 | SKKS | Low | 0.8 | 0.08 | -15 | 3.36 |
| 20 JUN 2003 13:30:41.640 | -30.61 | -71.64 | 6.8 | 33.00 | D01 | 230.64 | 99.16 | SKS | Low | 1.7 | 0.13 | 23 | 5.66 |
| 25 JUL 2004 14:35:19.000 | -2.43 | 103.98 | 7.3 | 582.10 | D01 | 72.52 | 105.88 | SKS | NULL | - | - | - | - |
| 28 JUL 2004 03:56:28.000 | -0.44 | 133.09 | 6.5 | 13.40 | D01 | 44.27 | 119.17 | SKS | Low | 1.7 | 0.07 | 61 | 2.89 |
| 8 OCT 2004 08:27:53.000 | -10.95 | 162.16 | 6.8 | 36.00 | D01 | 12.44 | 137.70 | SKKS | Low | 1.2 | 0.08 | -56 | 3.40 |
| 21 MAR 2005 12:43:12.000 | -24.73 | -63.51 | 6.4 | 570.10 | D01 | 227.49 | 90.41 | SKKS | Low | 1.8 | 0.17 | -69 | 7.28 |
| 21 MAR 2005 12:43:12.000 | -24.73 | -63.51 | 6.4 | 570.10 | D01 | 227.49 | 90.41 | SKS | Low | 1.3 | 0.13 | 17 | 5.60 |
| 10 APR 2005 17:24:39.000 | -1.59 | 99.72 | 6.4 | 30.00 | D01 | 75.59 | 102.72 | SKS | Low | 0.7 | 0.10 | -69 | 4.19 |
| 20 JUN 2003 13:30:41.640 | -30.61 | -71.64 | 6.8 | 33.00 | D02 | 230.79 | 99.13 | SKKS | Low | 1.9 | 0.09 | -13 | 4.12 |
| 20 JUN 2003 13:30:41.640 | -30.61 | -71.64 | 6.8 | 33.00 | D03 | 230.82 | 99.05 | SKKS | Low | 1.4 | 0.13 | -21 | 5.52 |
| 3 APR 2005 00:59:21.000 | 0.37 | 98.32 | 6.0 | 30.00 | D03 | 75.92 | 100.23 | SKS | Low | 1.2 | 0.16 | 39 | 6.95 |

| | | | | | | | | | | | | | |
|---|---|---|---|---|---|---|---|---|---|---|---|---|---|
| 13 JUN 2005 22:44:33.000 | -19.99 | -69.20 | 7.8 | 115.60 | D03 | 234.69 | 88.96 | SKS | High | 0.8 | 0.05 | 20 | 2.31 |
| 28 JUL 2006 07:40:11.840 | 24.18 | 122.53 | 5.9 | 33.00 | D03 | 43.18 | 92.83 | SKS | Low | 2.2 | 0.14 | -37 | 6.16 |
| 7 AUG 2006 22:18:55.090 | -15.80 | 167.79 | 6.8 | 150.00 | D03 | 5.16 | 143.41 | SKKS | Medium | 1.3 | 0.09 | 36 | 3.90 |
| 25 AUG 2006 00:44:46.160 | -24.40 | -67.03 | 6.6 | 184.00 | D03 | 230.67 | 91.64 | SKS | High | 0.8 | 0.02 | 32 | 0.92 |
| 26 MAY 2003 19:23:27.940 | 2.35 | 128.85 | 7.1 | 31.00 | D04 | 47.92 | 115.00 | SKKS | NULL | - | - | - | - |
| 20 JUN 2003 13:30:41.640 | -30.61 | -71.64 | 6.8 | 33.00 | D05 | 230.98 | 98.93 | SKKS | NULL | - | - | - | - |
| 25 JUL 2004 14:35:19.000 | -2.43 | 103.98 | 7.3 | 582.10 | D05 | 73.25 | 105.77 | SKS | NULL | - | - | - | - |
| 6 SEP 2004 12:42:59.000 | -55.37 | -28.98 | 6.9 | 10.00 | D05 | 192.00 | 108.30 | SKS | Low | 0.7 | 0.09 | 75 | 4.10 |
| 13 MAY 2003 21:21:14.050 | -17.29 | 167.74 | 6.4 | 33.00 | D06 | 5.42 | 144.27 | SKKS | Medium | 1.4 | 0.11 | -30 | 4.90 |
| 26 MAY 2003 19:23:27.940 | 2.35 | 128.85 | 7.1 | 31.00 | D06 | 47.53 | 114.51 | SKKS | Low | 0.8 | 0.08 | -61 | 3.34 |
| 20 JUN 2003 13:30:41.640 | -30.61 | -71.64 | 6.8 | 33.00 | D06 | 230.95 | 99.47 | SKKS | NULL | - | - | - | - |
| 10 MAR 2003 02:09:37.080 | 1.69 | 127.30 | 6.4 | 93.00 | D08 | 49.83 | 114.57 | SKKS | NULL | - | - | - | - |
| 11 NOV 2003 18:48:23.000 | 22.32 | 143.25 | 6.0 | 101.00 | D08 | 26.43 | 101.55 | SKS | Low | 0.5 | 0.10 | -37 | 4.24 |
| 12 NOV 2003 08:26:43.000 | 33.17 | 137.07 | 6.4 | 384.90 | D08 | 28.18 | 89.57 | SKKS | Medium | 0.7 | 0.07 | -4 | 3.26 |
| 26 MAY 2003 19:23:27.940 | 2.35 | 128.85 | 7.1 | 31.00 | D09 | 48.10 | 114.77 | SKS | NULL | - | - | - | - |
| 26 MAY 2003 19:23:27.940 | 2.35 | 128.85 | 7.1 | 31.00 | D10 | 48.35 | 114.85 | SKKS | NULL | - | - | - | - |
| 20 JUN 2003 13:30:41.640 | -30.61 | -71.64 | 6.8 | 33.00 | D10 | 231.24 | 99.18 | SKKS | NULL | - | - | - | - |

| | | | | | | | | | | | | | |
|---|---|---|---|---|---|---|---|---|---|---|---|---|---|
| 26 MAY 2003 19:23:27.940 | 2.35 | 128.85 | 7.1 | 31.00 | D12 | 48.14 | 114.47 | SKKS | NULL | - | - | - | - |
| 25 MAR 2003 02:53:25.030 | -8.29 | 120.74 | 6.5 | 33.00 | D12 | 61.95 | 119.60 | SKS | NULL | - | - | - | - |
| 13 MAY 2003 21:21:14.050 | -17.29 | 167.74 | 6.4 | 33.00 | D12 | 6.32 | 144.53 | SKKS | Low | 0.5 | 0.06 | -17 | 2.60 |
| 20 JUN 2003 13:30:41.640 | -30.61 | -71.64 | 6.8 | 33.00 | D12 | 231.30 | 99.54 | SKKS | Low | 1.8 | 0.07 | -21 | 3.19 |
| 20 JUN 2003 13:30:41.640 | -30.61 | -71.64 | 6.8 | 33.00 | D14 | 231.51 | 99.46 | SKKS | NULL | - | - | - | - |
| 25 JUL 2004 14:35:19.000 | -2.43 | 103.98 | 7.3 | 582.10 | D14 | 73.74 | 105.27 | SKS | NULL | - | - | - | - |
| 13 JUN 2005 22:44:33.000 | -19.99 | -69.20 | 7.8 | 115.60 | D14 | 235.46 | 89.39 | SKS | NULL | - | - | - | - |
| 25 AUG 2006 00:44:46.160 | -24.40 | -67.03 | 6.6 | 184.00 | D14 | 231.42 | 92.04 | SKS | High | 0.9 | 0.04 | 43 | 1.67 |
| 9 MAY 2003 20:26:15.980 | -48.21 | 32.27 | 6.3 | 10.00 | D14 | 153.25 | 105.88 | SKKS | NULL | - | - | - | - |
| 13 MAY 2003 21:21:14.050 | -17.29 | 167.74 | 6.4 | 33.00 | D14 | 6.99 | 144.90 | SKKS | Low | 1.2 | 0.09 | -55 | 3.94 |
| 13 JUN 2005 22:44:33.000 | -19.99 | -69.20 | 7.8 | 115.60 | D15 | 234.45 | 89.79 | SKS | High | 1.1 | 0.04 | -12 | 2.03 |
| 30 APR 2006 19:17:14.980 | -27.02 | -71.02 | 6.7 | 12.00 | D15 | 232.27 | 96.65 | SKS | High | 1.0 | 0.02 | -4 | 1.13 |
| 16 JUL 2006 11:42:41.410 | -28.72 | -72.54 | 6.2 | 10.00 | D15 | 232.52 | 98.80 | SKS | Medium | 1.2 | 0.13 | 2 | 5.55 |
| 27 JUL 2006 11:16:40.370 | 1.71 | 97.15 | 6.3 | 20.00 | D15 | 75.60 | 98.22 | SKS | Low | 0.8 | 0.15 | 26 | 6.23 |
| 25 AUG 2006 00:44:46.160 | -24.40 | -67.03 | 6.6 | 184.00 | D15 | 230.49 | 92.57 | SKS | Medium | 0.7 | 0.07 | 10 | 3.02 |
| 17 OCT 2006 01:25:12.230 | -5.88 | 150.98 | 6.7 | 32.00 | D15 | 25.71 | 129.36 | SKS | Medium | 1.0 | 0.03 | 17 | 1.31 |
| 21 JUL 2007 15:34:52.600 | -22.15 | -65.78 | 6.4 | 289.50 | D15 | 230.60 | 90.05 | SKS | High | 1.0 | 0.04 | 0 | 2.05 |

| | | | | | | | | | | | | | |
|---|---|---|---|---|---|---|---|---|---|---|---|---|---|
| 6 SEP 2007 17:51:26.190 | 24.34 | 122.22 | 6.2 | 53.00 | D15 | 43.08 | 91.46 | SKKS | Low | 1.4 | 0.17 | 82 | 7.15 |
| 6 SEP 2007 17:51:26.190 | 24.34 | 122.22 | 6.2 | 53.00 | D15 | 43.08 | 91.46 | SKS | High | 0.9 | 0.05 | -57 | 2.41 |
| 31 OCT 2007 03:30:15.960 | 18.90 | 145.39 | 7.2 | 207.00 | D15 | 24.66 | 104.15 | SKS | NULL | - | - | - | - |
| 27 NOV 2007 04:26:58.560 | 16.06 | 119.84 | 5.9 | 35.00 | D15 | 48.81 | 97.80 | SKS | Low | 1.6 | 0.08 | -66 | 3.68 |
| 16 NOV 2008 17:02:32.700 | 1.27 | 122.09 | 7.3 | 30.00 | D15 | 53.89 | 111.83 | SKKS | Low | 0.5 | 0.07 | -57 | 3.18 |
| 1 JUN 2008 01:57:23.690 | 20.12 | 121.35 | 6.3 | 31.00 | D15 | 45.67 | 94.85 | SKKS | Medium | 0.9 | 0.07 | -55 | 3.09 |
| 1 JUN 2008 01:57:23.690 | 20.12 | 121.35 | 6.3 | 31.00 | D15 | 45.67 | 94.85 | SKS | NULL | - | - | - | - |
| 7 MAY 2008 16:02:02.600 | 36.18 | 141.54 | 6.2 | 19.00 | D15 | 23.25 | 86.66 | SKS | Medium | 1.2 | 0.10 | -20 | 4.47 |
| 21 MAR 2005 12:43:12.000 | -24.73 | -63.51 | 6.4 | 570.10 | D16 | 227.32 | 90.68 | SKS | NULL | - | - | - | - |
| 13 JUN 2005 22:44:33.000 | -19.99 | -69.20 | 7.8 | 115.60 | D16 | 234.24 | 89.25 | SKS | High | 0.9 | 0.04 | -6 | 2.00 |
| 30 APR 2006 19:17:14.980 | -27.02 | -71.02 | 6.7 | 12.00 | D16 | 232.01 | 96.09 | SKS | Medium | 0.7 | 0.07 | -5 | 3.11 |
| 30 APR 2006 21:40:58.440 | -27.21 | -71.06 | 6.5 | 12.00 | D16 | 231.94 | 96.27 | SKS | Low | 0.7 | 0.23 | 5 | 9.74 |
| 16 MAY 2006 10:39:23.340 | -31.81 | -179.31 | 7.4 | 152.00 | D16 | 336.94 | 157.23 | SKKS | High | 1.1 | 0.05 | 34 | 2.32 |
| 16 MAY 2006 15:28:25.920 | 0.09 | 97.05 | 6.8 | 12.00 | D16 | 76.51 | 99.79 | SKS | NULL | - | - | - | - |
| 7 AUG 2006 22:18:55.090 | -15.80 | 167.79 | 6.8 | 150.00 | D16 | 4.19 | 142.47 | SKKS | Medium | 2.1 | 0.11 | -68 | 4.89 |
| 25 AUG 2006 00:44:46.160 | -24.40 | -67.03 | 6.6 | 184.00 | D16 | 230.27 | 92.00 | SKS | Medium | 0.7 | 0.07 | -3 | 3.01 |

| | | | | | | | | | | | | | |
|---|---|---|---|---|---|---|---|---|---|---|---|---|---|
| 28 SEP 2007 13:38:57.880 | 22.01 | 142.67 | 7.5 | 260.00 | D16 | 26.15 | 101.18 | SKS | NULL | - | - | - | - |
| 31 OCT 2007 03:30:15.960 | 18.90 | 145.39 | 7.2 | 207.00 | D16 | 24.50 | 104.86 | SKS | NULL | - | - | - | - |
| 18 NOV 2007 05:40:12.040 | -22.64 | -66.32 | 6.0 | 246.40 | D16 | 230.60 | 90.16 | SKS | Medium | 1.7 | 0.06 | 15 | 2.78 |
| 1 JUN 2008 01:57:23.690 | 20.12 | 121.35 | 6.3 | 31.00 | D16 | 45.51 | 95.46 | SKS | NULL | - | - | - | - |
| 13 JUL 2008 14:58:33.010 | 21.01 | 121.15 | 6.2 | 14.00 | D16 | 45.27 | 94.59 | SKS | NULL | - | - | - | - |
| 25 FEB 2008 08:36:33.030 | -2.49 | 99.97 | 7.2 | 25.00 | D16 | 75.61 | 103.58 | SKS | Low | 1.8 | 0.12 | 44 | 5.25 |
| 3 MAR 2008 14:11:14.620 | 13.35 | 125.63 | 6.9 | 24.00 | D16 | 44.82 | 103.32 | SKKS | Low | 2.1 | 0.16 | -67 | 6.89 |
| 28 MAR 2008 22:41:32.220 | 20.25 | 121.95 | 5.8 | 10.00 | D16 | 44.95 | 95.60 | SKS | Low | 1.8 | 0.14 | 82 | 6.10 |
| 16 MAR 2010 02:21:57.940 | -36.22 | -73.26 | 6.7 | 18.00 | D16 | 228.58 | 104.83 | SKS | Medium | 0.8 | 0.14 | 83 | 5.82 |
| 26 APR 2010 02:59:51.000 | 22.18 | 123.63 | 6.5 | 14.70 | D16 | 42.68 | 94.58 | SKS | NULL | - | - | - | - |
| 9 MAY 2010 05:59:41.620 | 3.75 | 96.02 | 7.2 | 38.00 | D16 | 75.23 | 96.24 | SKS | Low | 1.3 | 0.12 | 64 | 4.96 |
| 26 MAY 2010 08:53:08.030 | 25.77 | 129.94 | 6.5 | 10.00 | D16 | 35.93 | 93.72 | SKS | NULL | - | - | - | - |
| 31 MAY 2010 10:16:02.390 | 6.95 | 124.00 | 5.9 | 35.00 | D16 | 49.26 | 108.29 | SKKS | Medium | 2.2 | 0.12 | -64 | 4.98 |
| 31 MAY 2010 19:51:45.870 | 11.13 | 93.47 | 6.5 | 112.00 | D16 | 73.01 | 88.81 | SKKS | Medium | 0.8 | 0.10 | 80 | 4.14 |
| 31 MAY 2010 19:51:45.870 | 11.13 | 93.47 | 6.5 | 112.00 | D16 | 73.01 | 88.81 | SKS | NULL | - | - | - | - |
| 12 JUL 2010 00:11:21.250 | -22.15 | -68.22 | 6.3 | 115.00 | D16 | 232.36 | 90.62 | SKS | High | 1.2 | 0.07 | -13 | 3.10 |
| 23 JUL 2010 22:51:12.450 | 6.49 | 123.47 | 7.6 | 585.80 | D16 | 49.98 | 108.46 | SKKS | NULL | - | - | - | - |
| 23 JUL 2010 22:51:12.450 | 6.49 | 123.47 | 7.6 | 585.80 | D16 | 49.98 | 108.46 | SKS | NULL | - | - | - | - |

| | | | | | | | | | | | | | |
|---|---|---|---|---|---|---|---|---|---|---|---|---|---|
| 23 JUL 2010 23:15:10.190 | 6.78 | 123.26 | 7.4 | 640.60 | D16 | 50.03 | 108.11 | SKS | Medium | 0.7 | 0.10 | -59 | 4.38 |
| 1 JAN 2011 09:56:58.120 | -26.80 | -63.14 | 7.0 | 576.80 | D16 | 226.04 | 92.34 | SKS | High | 0.8 | 0.06 | -7 | 2.81 |
| 11 APR 2011 08:16:50.910 | 37.79 | 140.81 | 5.8 | 10.00 | D16 | 23.13 | 85.67 | SKS | NULL | - | - | - | - |
| 16 APR 2011 01:11:10.720 | 25.42 | 123.89 | 5.8 | 134.30 | D16 | 41.05 | 91.78 | SKKS | Low | 2.8 | 0.13 | -69 | 5.46 |
| 16 APR 2011 01:11:10.720 | 25.42 | 123.89 | 5.8 | 134.30 | D16 | 41.05 | 91.78 | SKS | NULL | - | - | - | - |
| 24 APR 2011 23:07:51.490 | -4.59 | 122.77 | 6.1 | 8.00 | D16 | 56.40 | 117.78 | SKKS | Medium | 1.2 | 0.09 | -47 | 3.82 |
| 3 JUN 2011 00:05:00.830 | 37.28 | 143.91 | 6.2 | 14.00 | D16 | 20.91 | 86.85 | SKS | Low | 2.4 | 0.15 | 67 | 6.40 |
| 20 JUN 2011 16:36:01.050 | -21.70 | -68.23 | 6.5 | 127.00 | D16 | 232.59 | 90.25 | SKS | High | 1.2 | 0.03 | 18 | 1.61 |
| 3 MAY 2004 04:36:50.000 | -37.69 | -73.41 | 6.6 | 21.00 | D18 | 228.78 | 106.89 | SKS | Low | 1.9 | 0.08 | 24 | 3.54 |
| 7 SEP 2004 11:53:06.000 | -28.57 | -65.84 | 6.4 | 22.30 | D18 | 228.27 | 95.82 | SKS | NULL | - | - | - | - |
| 14 MAY 2005 05:05:18.000 | 0.59 | 98.46 | 6.8 | 34.00 | D18 | 76.09 | 99.39 | SKS | Low | 1.6 | 0.10 | -31 | 4.24 |
| 5 JUL 2005 01:52:02.000 | 1.82 | 97.08 | 6.7 | 21.00 | D18 | 76.51 | 97.60 | SKS | Low | 1.6 | 0.08 | 89 | 3.51 |
| 4 SEP 2005 23:58:34.000 | 3.00 | 123.07 | 6.0 | 443.90 | D18 | 53.21 | 110.55 | SKKS | Low | 2.5 | 0.11 | 69 | 4.73 |
| 28 JUL 2006 07:40:11.840 | 24.18 | 122.53 | 5.9 | 33.00 | D18 | 43.77 | 91.61 | SKS | Low | 1.9 | 0.18 | -77 | 7.70 |
| 7 AUG 2006 22:18:55.090 | -15.80 | 167.79 | 6.8 | 150.00 | D18 | 6.20 | 142.13 | SKKS | NULL | - | - | - | - |
| 25 AUG 2006 00:44:46.160 | -24.40 | -67.03 | 6.6 | 184.00 | D18 | 231.30 | 92.78 | SKS | Low | 2.1 | 0.13 | 29 | 5.38 |
| 26 MAY 2003 19:23:27.940 | 2.35 | 128.85 | 7.1 | 31.00 | D21 | 48.37 | 113.95 | SKKS | NULL | - | - | - | - |
| 20 JUN 2003 13:30:41.640 | -30.61 | -71.64 | 6.8 | 33.00 | D21 | 231.66 | 100.05 | SKKS | Medium | 1.7 | 0.10 | 15 | 4.19 |

| | | | | | | | | | | | | | |
|---|---|---|---|---|---|---|---|---|---|---|---|---|---|
| 26 MAY 2003 19:23:27.940 | 2.35 | 128.85 | 7.1 | 31.00 | D23 | 48.68 | 114.21 | SKKS | Medium | 0.7 | 0.10 | 72 | 4.20 |
| 26 MAY 2003 19:23:27.940 | 2.35 | 128.85 | 7.1 | 31.00 | D23 | 48.68 | 114.21 | SKS | Low | 0.8 | 0.08 | -84 | 3.63 |
| 20 JUN 2003 13:30:41.640 | -30.61 | -71.64 | 6.8 | 33.00 | D23 | 231.70 | 99.81 | SKKS | High | 1.7 | 0.06 | 44 | 2.87 |
| 25 JUL 2004 14:35:19.000 | -2.43 | 103.98 | 7.3 | 582.10 | D23 | 73.79 | 105.05 | SKS | NULL | - | - | - | - |
| 21 MAR 2005 12:43:12.000 | -24.73 | -63.51 | 6.4 | 570.10 | D23 | 228.65 | 91.03 | SKS | Medium | 0.8 | 0.09 | -18 | 3.86 |
| 16 APR 2005 16:38:03.000 | 1.81 | 97.66 | 6.4 | 31.00 | D23 | 76.47 | 97.93 | SKKS | Low | 1.2 | 0.07 | -36 | 3.30 |
| 16 APR 2005 16:38:03.000 | 1.81 | 97.66 | 6.4 | 31.00 | D23 | 76.47 | 97.93 | SKS | NULL | - | - | - | - |
| 14 MAY 2005 05:05:18.000 | 0.59 | 98.46 | 6.8 | 34.00 | D23 | 76.55 | 99.38 | SKS | NULL | - | - | - | - |
| 13 JUN 2005 22:44:33.000 | -19.99 | -69.20 | 7.8 | 115.60 | D23 | 235.60 | 89.72 | SKS | High | 1.1 | 0.05 | -13 | 2.43 |
| 27 JAN 2006 16:58:53.670 | -5.47 | 128.13 | 7.6 | 397.00 | D23 | 53.54 | 120.72 | SKS | High | 0.5 | 0.07 | 79 | 2.89 |
| 16 JUL 2006 11:42:41.410 | -28.72 | -72.54 | 6.2 | 10.00 | D23 | 233.43 | 98.67 | SKS | Low | 1.7 | 0.16 | 36 | 6.74 |
| 25 AUG 2006 00:44:46.160 | -24.40 | -67.03 | 6.6 | 184.00 | D23 | 231.57 | 92.39 | SKS | High | 1.3 | 0.05 | 36 | 2.44 |
| 28 SEP 2007 13:38:57.880 | 22.01 | 142.67 | 7.5 | 260.00 | D23 | 27.73 | 101.28 | SKS | High | 1.5 | 0.06 | -80 | 2.71 |
| 7 MAY 2008 16:02:02.600 | 36.18 | 141.54 | 6.2 | 19.00 | D23 | 24.33 | 87.54 | SKS | NULL | - | - | - | - |
| 9 MAY 2008 21:51:29.730 | 12.52 | 143.18 | 6.8 | 76.00 | D23 | 30.28 | 110.42 | SKKS | NULL | - | - | - | - |
| 9 MAY 2008 21:51:29.730 | 12.52 | 143.18 | 6.8 | 76.00 | D23 | 30.28 | 110.42 | SKS | NULL | - | - | - | - |
| 11 SEP 2008 00:00:02.700 | 1.88 | 127.36 | 6.6 | 96.00 | D23 | 50.35 | 113.93 | SKKS | Low | 1.9 | 0.12 | -62 | 5.01 |
| 11 SEP 2008 00:00:02.700 | 1.88 | 127.36 | 6.6 | 96.00 | D23 | 50.35 | 113.93 | SKS | NULL | - | - | - | - |

| | | | | | | | | | | | | | |
|---|---|---|---|---|---|---|---|---|---|---|---|---|---|
| 13 JUL 2009 18:05:01.420 | 24.06 | 122.20 | 6.3 | 17.00 | D23 | 44.42 | 92.08 | SKS | High | 1.0 | 0.08 | 71 | 3.49 |
| 9 AUG 2009 10:55:55.110 | 33.17 | 137.94 | 7.1 | 292.00 | D23 | 28.11 | 89.42 | SKS | Low | 1.6 | 0.14 | -84 | 6.16 |
| 12 AUG 2009 22:48:51.420 | 32.82 | 140.40 | 6.6 | 53.00 | D23 | 26.28 | 90.42 | SKKS | Medium | 1.3 | 0.11 | 63 | 4.72 |
| 12 AUG 2009 22:48:51.420 | 32.82 | 140.40 | 6.6 | 53.00 | D23 | 26.28 | 90.42 | SKS | High | 0.8 | 0.08 | 80 | 3.38 |
| 2 SEP 2009 07:55:01.050 | -7.78 | 107.30 | 7.0 | 46.00 | D23 | 74.26 | 111.29 | SKKS | High | 1.1 | 0.06 | 52 | 2.86 |
| 2 SEP 2009 07:55:01.050 | -7.78 | 107.30 | 7.0 | 46.00 | D23 | 74.26 | 111.29 | SKS | NULL | - | - | - | - |
| 18 SEP 2009 18:34:22.140 | 1.75 | 127.19 | 5.8 | 92.70 | D23 | 50.59 | 113.97 | SKS | Low | 1.7 | 0.08 | -13 | 3.70 |
| 30 SEP 2009 10:16:09.250 | -0.72 | 99.87 | 7.6 | 81.00 | D23 | 76.18 | 101.26 | SKKS | High | 0.8 | 0.04 | 52 | 1.90 |
| 30 SEP 2009 10:16:09.250 | -0.72 | 99.87 | 7.6 | 81.00 | D23 | 76.18 | 101.26 | SKS | High | 2.5 | 0.02 | 69 | 0.87 |
| 1 OCT 2009 01:52:27.320 | -2.48 | 101.52 | 6.6 | 9.00 | D23 | 75.87 | 103.65 | SKS | NULL | - | - | - | - |
| 4 OCT 2009 10:58:00.170 | 6.74 | 123.38 | 6.6 | 620.00 | D23 | 51.65 | 107.81 | SKS | High | 1.4 | 0.02 | -29 | 1.17 |
| 10 NOV 2009 02:48:46.790 | 8.08 | 91.90 | 6.0 | 23.00 | D23 | 77.39 | 89.51 | SKS | NULL | - | - | - | - |
| 22 NOV 2009 22:07:48.220 | -39.63 | -74.97 | 5.9 | 7.00 | D23 | 228.70 | 108.75 | SKKS | Low | 1.0 | 0.09 | 28 | 3.76 |
| 27 FEB 2010 06:34:11.530 | -36.12 | -72.90 | 8.8 | 22.90 | D23 | 229.43 | 104.95 | SKKS | Medium | 2.1 | 0.11 | 21 | 4.95 |
| 14 MAR 2010 08:08:03.960 | 37.74 | 141.59 | 6.5 | 32.00 | D23 | 23.81 | 86.07 | SKS | NULL | - | - | - | - |
| 9 MAY 2010 05:59:41.620 | 3.75 | 96.02 | 7.2 | 38.00 | D23 | 76.66 | 95.40 | SKKS | High | 2.2 | 0.08 | 46 | 3.61 |
| 28 JUN 2010 12:07:25.120 | 30.67 | 141.59 | 5.8 | 7.00 | D23 | 25.99 | 92.78 | SKS | Medium | 1.1 | 0.06 | 84 | 2.67 |

| | | | | | | | | | | | | | |
|---|---|---|---|---|---|---|---|---|---|---|---|---|---|
| 23 JUL 2010 22:51:12.450 | 6.49 | 123.47 | 7.6 | 585.80 | D23 | 51.69 | 108.07 | SKKS | High | 1.3 | 0.09 | -55 | 3.96 |
| 23 JUL 2010 22:51:12.450 | 6.49 | 123.47 | 7.6 | 585.80 | D23 | 51.69 | 108.07 | SKS | NULL | - | - | - | - |
| 23 JUL 2010 23:15:10.190 | 6.78 | 123.26 | 7.4 | 640.60 | D23 | 51.74 | 107.72 | SKKS | High | 1.1 | 0.05 | -68 | 2.37 |
| 28 SEP 2007 13:38:57.880 | 22.01 | 142.67 | 7.5 | 260.00 | D32 | 28.60 | 98.80 | SKS | High | 1.2 | 0.01 | 82 | 0.59 |
| 9 MAY 2008 21:51:29.730 | 12.52 | 143.18 | 6.8 | 76.00 | D32 | 31.03 | 107.96 | SKS | High | 1.0 | 0.04 | 84 | 1.84 |
| 9 MAY 2008 21:51:29.730 | 12.52 | 143.18 | 6.8 | 76.00 | D32 | 31.03 | 107.96 | SKKS | Medium | 2.2 | 0.11 | -83 | 4.82 |
| 1 JUN 2008 01:57:23.690 | 20.12 | 121.35 | 6.3 | 31.00 | D32 | 47.83 | 92.99 | SKKS | Medium | 1.6 | 0.09 | -85 | 3.97 |
| 1 JUN 2008 01:57:23.690 | 20.12 | 121.35 | 6.3 | 31.00 | D32 | 47.83 | 92.99 | SKS | High | 1.4 | 0.08 | 84 | 3.60 |
| 13 JUL 2008 14:58:33.010 | 21.01 | 121.15 | 6.2 | 14.00 | D32 | 47.60 | 92.12 | SKKS | Medium | 0.9 | 0.10 | -74 | 4.52 |
| 13 JUL 2009 18:05:01.420 | 24.06 | 122.20 | 6.3 | 17.00 | D32 | 45.37 | 89.85 | SKS | High | 1.4 | 0.07 | -88 | 3.04 |
| 4 OCT 2009 10:58:00.170 | 6.74 | 123.38 | 6.6 | 620.00 | D32 | 52.17 | 105.75 | SKS | Medium | 1.4 | 0.06 | -79 | 2.75 |
| 14 OCT 2009 18:00:21.770 | -14.91 | -174.82 | 6.3 | 10.00 | D32 | 342.45 | 138.80 | SKKS | Medium | 0.9 | 0.09 | -50 | 3.74 |
| 27 FEB 2010 06:34:11.530 | -36.12 | -72.90 | 8.8 | 22.90 | D32 | 230.80 | 107.05 | SKKS | High | 1.3 | 0.08 | 62 | 3.49 |
| 2 MAR 2010 02:51:21.310 | 18.18 | 122.40 | 5.8 | 17.00 | D32 | 47.82 | 95.16 | SKS | NULL | - | - | - | - |
| 4 MAR 2010 22:39:26.530 | -22.23 | -68.33 | 6.4 | 114.00 | D32 | 234.76 | 93.18 | SKKS | Medium | 1.5 | 0.08 | -13 | 3.71 |
| 6 APR 2010 22:15:01.580 | 2.38 | 97.05 | 7.8 | 31.00 | D32 | 77.35 | 95.87 | SKS | NULL | - | - | - | - |
| 26 APR 2010 02:59:51.000 | 22.18 | 123.63 | 6.5 | 14.70 | D32 | 45.02 | 92.11 | SKS | Low | 1.7 | 0.12 | -87 | 5.19 |

| | | | | | | | | | | | | | |
|---|---|---|---|---|---|---|---|---|---|---|---|---|---|
| 8 MAY 2010 03:22:09.650 | -8.09 | 118.26 | 5.9 | 12.00 | D32 | 64.67 | 116.10 | SKS | Medium | 1.4 | 0.07 | 0 | 2.98 |
| 9 MAY 2010 05:59:41.620 | 3.75 | 96.02 | 7.2 | 38.00 | D32 | 77.44 | 94.17 | SKKS | NULL | - | - | - | - |
| 9 MAY 2010 05:59:41.620 | 3.75 | 96.02 | 7.2 | 38.00 | D32 | 77.44 | 94.17 | SKS | NULL | - | - | - | - |
| 31 MAY 2010 19:51:45.870 | 11.13 | 93.47 | 6.5 | 112.00 | D32 | 75.40 | 86.68 | SKS | High | 0.7 | 0.04 | -6 | 1.70 |
| 16 JUN 2010 03:16:27.550 | -2.17 | 136.54 | 7.0 | 18.00 | D32 | 43.35 | 119.36 | SKKS | Low | 1.0 | 0.11 | -87 | 4.79 |
| 12 JUL 2010 00:11:21.250 | -22.15 | -68.22 | 6.3 | 115.00 | D32 | 234.71 | 93.06 | SKKS | NULL | - | - | - | - |
| 12 JUL 2010 00:11:21.250 | -22.15 | -68.22 | 6.3 | 115.00 | D32 | 234.71 | 93.06 | SKS | NULL | - | - | - | - |
| 13 DEC 2010 01:14:42.320 | -6.53 | 155.65 | 6.2 | 135.80 | D32 | 23.01 | 129.49 | SKKS | Low | 1.3 | 0.09 | 78 | 4.11 |
| 13 DEC 2010 01:14:42.320 | -6.53 | 155.65 | 6.2 | 135.80 | D32 | 23.01 | 129.49 | SKS | Low | 1.7 | 0.17 | 87 | 7.10 |
| 20 JUN 2011 16:36:01.050 | -21.70 | -68.23 | 6.5 | 127.00 | D32 | 234.94 | 92.68 | SKS | NULL | - | - | - | - |
| 7 AUG 2006 22:18:55.090 | -15.80 | 167.79 | 6.8 | 150.00 | D33 | 7.70 | 141.50 | SKKS | Medium | 1.6 | 0.11 | 25 | 4.56 |
| 25 AUG 2006 00:44:46.160 | -24.40 | -67.03 | 6.6 | 184.00 | D33 | 232.13 | 93.60 | SKS | High | 0.9 | 0.06 | -19 | 2.66 |
| 17 OCT 2006 01:25:12.230 | -5.88 | 150.98 | 6.7 | 32.00 | D33 | 28.23 | 128.71 | SKKS | Medium | 1.8 | 0.08 | 50 | 3.69 |
| 1 JUN 2008 01:57:23.690 | 20.12 | 121.35 | 6.3 | 31.00 | D33 | 47.41 | 93.89 | SKKS | Medium | 0.8 | 0.07 | -71 | 3.10 |
| 1 JUN 2008 01:57:23.690 | 20.12 | 121.35 | 6.3 | 31.00 | D33 | 47.41 | 93.89 | SKS | High | 1.0 | 0.05 | 78 | 2.08 |

| | | | | | | | | | | | | | |
|---|---|---|---|---|---|---|---|---|---|---|---|---|---|
| 9 AUG 2009 10:55:55.110 | 33.17 | 137.94 | 7.1 | 292.00 | D33 | 28.63 | 87.95 | SKS | High | 1.4 | 0.06 | 49 | 2.65 |
| 24 OCT 2009 14:40:43.720 | -6.13 | 130.38 | 6.9 | 130.00 | D33 | 51.56 | 121.17 | SKKS | High | 1.4 | 0.08 | 81 | 3.35 |
| 24 OCT 2009 14:40:43.720 | -6.13 | 130.38 | 6.9 | 130.00 | D33 | 51.56 | 121.17 | SKS | High | 1.3 | 0.06 | 74 | 2.61 |
| 5 JAN 2010 04:55:38.910 | -58.17 | -14.70 | 6.8 | 10.00 | D33 | 184.26 | 112.16 | SKKS | NULL | - | - | - | - |
| 26 FEB 2010 20:31:26.970 | 25.93 | 128.43 | 7.0 | 25.00 | D33 | 39.02 | 91.53 | SKS | NULL | - | - | - | - |
| 27 FEB 2010 06:34:11.530 | -36.12 | -72.90 | 8.8 | 22.90 | D33 | 230.18 | 106.18 | SKKS | NULL | - | - | - | - |
| 27 FEB 2010 06:34:11.530 | -36.12 | -72.90 | 8.8 | 22.90 | D33 | 230.18 | 106.18 | SKS | Medium | 1.3 | 0.09 | -20 | 3.78 |
| 4 MAR 2010 22:39:26.530 | -22.23 | -68.33 | 6.4 | 114.00 | D33 | 234.27 | 92.35 | SKS | NULL | - | - | - | - |
| 16 MAR 2010 02:21:57.940 | -36.22 | -73.26 | 6.7 | 18.00 | D33 | 230.38 | 106.42 | SKS | NULL | - | - | - | - |
| 22 MAR 2010 19:58:14.900 | 18.47 | 120.74 | 5.9 | 47.60 | D33 | 48.69 | 95.08 | SKKS | Medium | 1.4 | 0.09 | -13 | 3.98 |
| 6 APR 2010 22:15:01.580 | 2.38 | 97.05 | 7.8 | 31.00 | D33 | 76.99 | 96.40 | SKS | NULL | - | - | - | - |
| 26 APR 2010 02:59:51.000 | 22.18 | 123.63 | 6.5 | 14.70 | D33 | 44.58 | 93.03 | SKS | Medium | 1.1 | 0.10 | -51 | 4.38 |
| 16 MAY 2010 00:33:06.350 | 0.51 | 124.66 | 5.8 | 123.00 | D33 | 53.77 | 112.66 | SKS | Medium | 1.0 | 0.07 | 6 | 3.24 |
| 12 JUL 2010 00:11:21.250 | -22.15 | -68.22 | 6.3 | 115.00 | D33 | 234.22 | 92.23 | SKKS | NULL | - | - | - | - |
| 12 JUL 2010 00:11:21.250 | -22.15 | -68.22 | 6.3 | 115.00 | D33 | 234.22 | 92.23 | SKS | NULL | - | - | - | - |
| 14 JUL 2010 08:32:21.490 | -38.07 | -73.31 | 6.6 | 22.00 | D33 | 229.33 | 107.97 | SKS | Medium | 1.0 | 0.13 | -4 | 5.63 |

| | | | | | | | | | | | | | |
|---|---|---|---|---|---|---|---|---|---|---|---|---|---|
| 21 AUG 2010 05:42:52.880 | 2.22 | 96.72 | 6.0 | 24.00 | D33 | 77.35 | 96.35 | SKS | NULL | - | - | - | - |
| 30 NOV 2010 03:24:41.600 | 28.36 | 139.15 | 6.8 | 486.70 | D33 | 29.24 | 92.82 | SKS | NULL | - | - | - | - |
| 21 DEC 2010 17:19:40.660 | 26.90 | 143.70 | 7.4 | 14.00 | D33 | 25.83 | 95.43 | SKS | NULL | - | - | - | - |
| 22 DEC 2010 21:49:38.790 | 26.81 | 143.60 | 6.4 | 10.00 | D33 | 25.94 | 95.50 | SKS | NULL | - | - | - | - |
| 27 JUL 2006 11:16:40.370 | 1.71 | 97.15 | 6.3 | 20.00 | D34 | 76.58 | 97.23 | SKS | NULL | - | - | - | - |
| 7 AUG 2006 22:18:55.090 | -15.80 | 167.79 | 6.8 | 150.00 | D34 | 6.46 | 140.71 | SKKS | Medium | 0.9 | 0.07 | 64 | 3.22 |
| 25 AUG 2006 00:44:46.160 | -24.40 | -67.03 | 6.6 | 184.00 | D34 | 231.60 | 93.79 | SKS | High | 2.0 | 0.03 | 42 | 1.52 |
| 8 AUG 2007 17:04:57.840 | -5.93 | 107.68 | 6.1 | 291.20 | D34 | 71.90 | 109.37 | SKS | NULL | - | - | - | - |
| 13 SEP 2007 03:35:28.720 | -2.13 | 99.63 | 7.0 | 22.00 | D34 | 76.67 | 101.78 | SKKS | Low | 1.9 | 0.12 | 59 | 5.35 |
| 28 SEP 2007 13:38:57.880 | 22.01 | 142.67 | 7.5 | 260.00 | D34 | 27.45 | 99.26 | SKS | High | 1.4 | 0.03 | -78 | 1.30 |
| 9 MAY 2008 21:51:29.730 | 12.52 | 143.18 | 6.8 | 76.00 | D34 | 29.78 | 108.44 | SKS | NULL | - | - | - | - |
| 1 JUN 2008 01:57:23.690 | 20.12 | 121.35 | 6.3 | 31.00 | D34 | 46.76 | 93.62 | SKKS | High | 1.4 | 0.08 | -59 | 3.40 |
| 1 JUN 2008 01:57:23.690 | 20.12 | 121.35 | 6.3 | 31.00 | D34 | 46.76 | 93.62 | SKS | High | 0.7 | 0.03 | -84 | 1.62 |
| 8 JUL 2008 09:13:07.460 | -15.99 | -71.75 | 6.2 | 123.00 | D34 | 239.66 | 88.81 | SKS | Medium | 1.3 | 0.04 | 42 | 1.95 |
| 13 JUL 2008 14:58:33.010 | 21.01 | 121.15 | 6.2 | 14.00 | D34 | 46.53 | 92.74 | SKKS | High | 0.7 | 0.03 | 80 | 1.49 |
| 11 SEP 2008 00:00:02.700 | 1.88 | 127.36 | 6.6 | 96.00 | D34 | 49.50 | 112.49 | SKKS | Low | 1.8 | 0.14 | -83 | 6.04 |
| 13 JUL 2009 18:05:01.420 | 24.06 | 122.20 | 6.3 | 17.00 | D34 | 44.31 | 90.46 | SKS | NULL | - | - | - | - |

| | | | | | | | | | | | | | |
|---|---|---|---|---|---|---|---|---|---|---|---|---|---|
| 5 AUG 2009 00:17:58.820 | 24.23 | 125.10 | 6.1 | 25.00 | D34 | 41.85 | 91.44 | SKS | Medium | 1.7 | 0.09 | -70 | 4.01 |
| 12 AUG 2009 22:48:51.420 | 32.82 | 140.40 | 6.6 | 53.00 | D34 | 26.22 | 88.37 | SKS | High | 0.6 | 0.02 | -87 | 1.20 |
| 2 SEP 2009 07:55:01.050 | -7.78 | 107.30 | 7.0 | 46.00 | D34 | 73.33 | 110.70 | SKKS | NULL | - | - | - | - |
| 2 SEP 2009 07:55:01.050 | -7.78 | 107.30 | 7.0 | 46.00 | D34 | 73.33 | 110.70 | SKS | NULL | - | - | - | - |
| 18 SEP 2009 06:23:53.490 | 12.62 | 120.43 | 5.9 | 12.00 | D34 | 50.95 | 99.88 | SKS | Medium | 0.9 | 0.09 | 75 | 4.02 |
| 30 SEP 2009 10:16:09.250 | -0.72 | 99.87 | 7.6 | 81.00 | D34 | 75.67 | 100.75 | SKKS | NULL | - | - | - | - |
| 30 SEP 2009 10:16:09.250 | -0.72 | 99.87 | 7.6 | 81.00 | D34 | 75.67 | 100.75 | SKS | High | 0.8 | 0.03 | -27 | 1.36 |
| 1 OCT 2009 01:52:27.320 | -2.48 | 101.52 | 6.6 | 9.00 | D34 | 75.26 | 103.13 | SKS | Medium | 0.9 | 0.10 | -44 | 4.37 |
| 4 OCT 2009 10:58:00.170 | 6.74 | 123.38 | 6.6 | 620.00 | D34 | 51.01 | 106.40 | SKS | High | 0.7 | 0.05 | 83 | 2.12 |
| 24 OCT 2009 14:40:43.720 | -6.13 | 130.38 | 6.9 | 130.00 | D34 | 50.41 | 120.96 | SKS | NULL | - | - | - | - |
| 30 OCT 2009 07:03:39.120 | 29.22 | 129.78 | 6.8 | 34.00 | D34 | 36.01 | 88.59 | SKS | Low | 1.4 | 0.17 | 87 | 7.20 |
| 10 NOV 2009 02:48:46.790 | 8.08 | 91.90 | 6.0 | 23.00 | D34 | 77.34 | 89.05 | SKS | High | 0.8 | 0.03 | 30 | 1.57 |
| 13 NOV 2009 03:05:57.220 | -19.39 | -70.32 | 6.5 | 27.00 | D34 | 236.75 | 91.02 | SKS | NULL | - | - | - | - |
| 14 NOV 2009 19:44:29.930 | -22.97 | -66.64 | 6.2 | 220.40 | D34 | 232.00 | 92.37 | SKS | Low | 1.6 | 0.14 | 17 | 5.98 |
| 9 DEC 2009 09:46:03.300 | -22.15 | 170.96 | 6.4 | 45.00 | D34 | 1.83 | 147.15 | SKKS | Medium | 2.3 | 0.10 | 53 | 4.24 |
| 15 FEB 2010 21:51:47.790 | -7.22 | 128.72 | 6.2 | 126.00 | D34 | 52.70 | 121.18 | SKS | NULL | - | - | - | - |
| 15-FEB 2010 21:51:47.790 | -7.22 | 128.72 | 6.2 | 126.00 | D34 | 52.70 | 121.18 | SKKS | NULL | - | - | - | - |
| 26-FEB 2010 20:31:26.970 | 25.93 | 128.43 | 7.0 | 25.00 | D34 | 38.40 | 91.13 | SKS | High | 1.3 | 0.05 | 68 | 2.30 |

| | | | | | | | | | | | | | |
|---|---|---|---|---|---|---|---|---|---|---|---|---|---|
| 27 FEB 2010 06:34:11.530 | -36.12 | -72.90 | 8.8 | 22.90 | D34 | 229.86 | 106.40 | SKKS | NULL | - | - | - | - |
| 4 MAR 2010 22:39:26.530 | -22.23 | -68.33 | 6.4 | 114.00 | D34 | 233.72 | 92.51 | SKS | High | 0.9 | 0.06 | 34 | 2.85 |
| 14 MAR 2010 08:08:03.960 | 37.74 | 141.59 | 6.5 | 32.00 | D34 | 23.82 | 83.97 | SKS | Low | 1.9 | 0.17 | -12 | 7.40 |
| 16 MAR 2010 02:21:57.940 | -36.22 | -73.26 | 6.7 | 18.00 | D34 | 230.06 | 106.64 | SKS | Medium | 0.8 | 0.07 | 77 | 3.01 |
| 26 MAR 2010 14:52:07.230 | -27.95 | -70.82 | 6.3 | 42.00 | D34 | 232.76 | 98.56 | SKS | Low | 1.5 | 0.09 | -80 | 3.93 |
| 6 APR 2010 22:15:01.580 | 2.38 | 97.05 | 7.8 | 31.00 | D34 | 76.29 | 96.62 | SKS | High | 0.8 | 0.04 | -30 | 1.66 |
| 26 APR 2010 02:59:51.000 | 22.18 | 123.63 | 6.5 | 14.70 | D34 | 43.94 | 92.71 | SKS | NULL | - | - | - | - |
| 9 MAY 2010 05:59:41.620 | 3.75 | 96.02 | 7.2 | 38.00 | D34 | 76.38 | 94.92 | SKKS | NULL | - | - | - | - |
| 31 MAY 2010 19:51:45.870 | 11.13 | 93.47 | 6.5 | 112.00 | D34 | 74.34 | 87.43 | SKS | NULL | - | - | - | - |
| 12 JUL 2010 00:11:21.250 | -22.15 | -68.22 | 6.3 | 115.00 | D34 | 233.67 | 92.39 | SKKS | NULL | - | - | - | - |
| 12 JUL 2010 00:11:21.250 | -22.15 | -68.22 | 6.3 | 115.00 | D34 | 233.67 | 92.39 | SKS | High | 0.5 | 0.04 | 13 | 1.89 |
| 18 JUL 2010 13:04:09.410 | -5.97 | 150.43 | 6.9 | 28.00 | D34 | 27.73 | 128.08 | SKS | Medium | 0.7 | 0.05 | 87 | 2.32 |
| 23 JUL 2010 22:51:12.450 | 6.49 | 123.47 | 7.6 | 585.80 | D34 | 51.04 | 106.67 | SKKS | Low | 0.5 | 0.09 | -86 | 4.11 |
| 23 JUL 2010 22:51:12.450 | 6.49 | 123.47 | 7.6 | 585.80 | D34 | 51.04 | 106.67 | SKS | Medium | 1.3 | 0.08 | -64 | 3.71 |
| 23 JUL 2010 23:15:10.190 | 6.78 | 123.26 | 7.4 | 640.60 | D34 | 51.10 | 106.32 | SKS | Medium | 0.7 | 0.10 | 84 | 4.32 |
| 16 AUG 2010 03:30:53.310 | -17.76 | 65.65 | 6.3 | 9.80 | D34 | 113.33 | 95.34 | SKKS | NULL | - | - | - | - |
| 21 AUG 2010 05:42:52.880 | 2.22 | 96.72 | 6.0 | 24.00 | D34 | 76.65 | 96.57 | SKKS | Low | 1.7 | 0.11 | -46 | 4.93 |
| 21 DEC 2010 14:07:48.290 | 2.71 | 95.89 | 5.9 | 21.00 | D34 | 77.06 | 95.70 | SKKS | NULL | - | - | - | - |

| | | | | | | | | | | | | | |
|---|---|---|---|---|---|---|---|---|---|---|---|---|---|
| 1 JAN 2011 09:56:58.120 | -26.80 | -63.14 | 7.0 | 576.80 | D34 | 227.36 | 94.18 | SKS | Medium | 1.3 | 0.08 | 2 | 3.61 |
| 25 AUG 2006 00:44:46.160 | -24.40 | -67.03 | 6.6 | 184.00 | D35 | 232.75 | 92.85 | SKS | NULL | - | - | - | - |
| 17 OCT 2006 01:25:12.230 | -5.88 | 150.98 | 6.7 | 32.00 | D35 | 30.12 | 130.13 | SKKS | Low | 0.8 | 0.12 | -14 | 5.32 |
| 21 JUL 2007 15:34:52.600 | -22.15 | -65.78 | 6.4 | 289.50 | D36 | 233.07 | 90.67 | SKS | NULL | - | - | - | - |
| 12 SEP 2007 23:49:03.720 | -2.62 | 100.84 | 7.9 | 35.00 | D36 | 77.90 | 102.38 | SKKS | NULL | - | - | - | - |
| 28 SEP 2007 13:38:57.880 | 22.01 | 142.67 | 7.5 | 260.00 | D36 | 29.23 | 100.83 | SKKS | Medium | 1.8 | 0.07 | -80 | 2.95 |
| 28 SEP 2007 13:38:57.880 | 22.01 | 142.67 | 7.5 | 260.00 | D36 | 29.23 | 100.83 | SKS | High | 1.3 | 0.07 | 84 | 2.93 |
| 4 OCT 2007 12:40:31.130 | 2.54 | 92.90 | 6.2 | 35.00 | D36 | 81.22 | 93.52 | SKS | High | 0.9 | 0.05 | 48 | 2.07 |
| 14 NOV 2009 19:44:29.930 | -22.97 | -66.64 | 6.2 | 220.40 | D37 | 232.34 | 91.62 | SKS | NULL | - | - | - | - |
| 22 NOV 2009 22:07:48.220 | -39.63 | -74.97 | 5.9 | 7.00 | D37 | 229.14 | 109.41 | SKS | Low | 1.7 | 0.12 | 74 | 4.97 |
| 31 DEC 2009 09:23:24.010 | -59.40 | -150.98 | 6.0 | 10.00 | D37 | 238.79 | 159.15 | SKKS | High | 0.6 | 0.07 | 13 | 2.98 |
| 5 JAN 2010 12:15:32.210 | -9.02 | 157.55 | 6.8 | 15.40 | D37 | 20.80 | 134.07 | SKKS | Low | 0.7 | 0.13 | 65 | 5.74 |
| 17 JAN 2010 12:00:01.080 | -57.66 | -65.88 | 6.3 | 5.00 | D37 | 212.09 | 120.49 | SKKS | Low | 1.0 | 0.20 | 58 | 8.56 |
| 26 FEB 2010 20:31:26.970 | 25.93 | 128.43 | 7.0 | 25.00 | D37 | 38.83 | 92.19 | SKKS | High | 0.8 | 0.04 | -43 | 1.93 |
| 27 FEB 2010 06:34:11.530 | -36.12 | -72.90 | 8.8 | 22.90 | D37 | 229.85 | 105.60 | SKKS | Low | 1.3 | 0.13 | -19 | 5.76 |
| 11 MAR 2010 14:39:43.950 | -34.29 | -71.89 | 6.9 | 11.00 | D37 | 230.21 | 103.62 | SKS | Medium | 1.3 | 0.08 | 39 | 3.47 |
| 2 APR 2010 22:58:07.560 | -36.23 | -72.88 | 6.0 | 24.00 | D37 | 229.78 | 105.68 | SKKS | Low | 0.9 | 0.16 | 17 | 6.82 |
| 26 APR 2010 02:59:51.000 | 22.18 | 123.63 | 6.5 | 14.70 | D37 | 44.41 | 93.65 | SKS | Medium | 1.2 | 0.11 | 78 | 4.65 |

| | | | | | | | | | | | | | |
|---|---|---|---|---|---|---|---|---|---|---|---|---|---|
| 3 MAY 2010 23:09:44.790 | -38.07 | -73.45 | 6.3 | 19.00 | D37 | 229.08 | 107.45 | SKS | High | 0.6 | 0.05 | 17 | 2.45 |
| 6 MAY 2010 02:42:47.940 | -18.06 | -70.55 | 6.2 | 37.00 | D37 | 238.02 | 89.38 | SKS | NULL | - | - | - | - |
| 9 MAY 2010 05:59:41.620 | 3.75 | 96.02 | 7.2 | 38.00 | D37 | 76.92 | 95.01 | SKKS | Medium | 1.1 | 0.09 | -82 | 3.94 |
| 9 MAY 2010 05:59:41.620 | 3.75 | 96.02 | 7.2 | 38.00 | D37 | 76.92 | 95.01 | SKS | Medium | 0.8 | 0.13 | 85 | 5.55 |
| 31 MAY 2010 19:51:45.870 | 11.13 | 93.47 | 6.5 | 112.00 | D37 | 74.67 | 87.58 | SKS | High | 1.2 | 0.02 | 85 | 1.19 |
| 12 JUL 2010 00:11:21.250 | -22.15 | -68.22 | 6.3 | 115.00 | D37 | 234.01 | 91.68 | SKS | Medium | 0.9 | 0.10 | 41 | 4.37 |
| 14 JUL 2010 15:05:50.400 | -38.22 | -73.23 | 5.8 | 35.00 | D37 | 228.84 | 107.47 | SKKS | NULL | - | - | - | - |
| 14 JUL 2010 15:05:50.400 | -38.22 | -73.23 | 5.8 | 35.00 | D37 | 228.84 | 107.47 | SKS | NULL | - | - | - | - |
| 23 JUL 2010 22:51:12.450 | 6.49 | 123.47 | 7.6 | 585.80 | D37 | 51.87 | 107.43 | SKKS | Medium | 0.6 | 0.08 | -85 | 3.40 |
| 23 JUL 2010 22:51:12.450 | 6.49 | 123.47 | 7.6 | 585.80 | D37 | 51.87 | 107.43 | SKS | High | 0.5 | 0.05 | 76 | 2.23 |
| 23 JUL 2010 23:15:10.190 | 6.78 | 123.26 | 7.4 | 640.60 | D37 | 51.92 | 107.08 | SKS | NULL | - | - | - | - |
| 25 OCT 2010 12:05:28.930 | -0.07 | 125.06 | 5.8 | 37.00 | D37 | 53.71 | 113.92 | SKKS | NULL | - | - | - | - |
| 22 DEC 2010 21:49:38.790 | 26.81 | 143.60 | 6.4 | 10.00 | D37 | 25.77 | 96.22 | SKKS | Medium | 0.9 | 0.12 | -28 | 5.26 |
| 22 DEC 2010 21:49:38.790 | 26.81 | 143.60 | 6.4 | 10.00 | D37 | 25.77 | 96.22 | SKS | Medium | 1.0 | 0.10 | 8 | 4.16 |
| 1 JAN 2011 09:56:58.120 | -26.80 | -63.14 | 7.0 | 576.80 | D37 | 227.66 | 93.32 | SKS | Medium | 0.8 | 0.14 | 17 | 5.89 |
| 15 FEB 2011 13:33:53.180 | -2.50 | 121.48 | 6.1 | 16.20 | D37 | 58.42 | 114.23 | SKS | Low | 0.8 | 0.07 | -8 | 3.12 |
| 11 MAR 2011 15:13:15.090 | 36.00 | 141.80 | 6.3 | 23.70 | D37 | 24.50 | 87.02 | SKS | Medium | 1.4 | 0.12 | -23 | 5.21 |
| 6 APR 2011 14:01:43.340 | 1.62 | 97.10 | 6.0 | 25.30 | D37 | 77.28 | 97.36 | SKS | Medium | 0.9 | 0.04 | 68 | 1.78 |

| | | | | | | | | | | | | | |
|---|---|---|---|---|---|---|---|---|---|---|---|---|---|
| 24 APR 2011 23:07:51.490 | -4.59 | 122.77 | 6.1 | 8.00 | D37 | 58.36 | 116.67 | SKS | NULL | - | - | - | - |
| 3 JUN 2011 00:05:00.830 | 37.28 | 143.91 | 6.2 | 14.00 | D37 | 22.50 | 86.30 | SKS | Medium | 1.1 | 0.12 | -50 | 5.32 |
| 20 JUN 2011 16:36:01.050 | -21.70 | -68.23 | 6.5 | 127.00 | D37 | 234.25 | 91.31 | SKS | High | 0.8 | 0.06 | 5 | 2.53 |
| 28 SEP 2009 19:22:57.140 | 27.93 | 127.82 | 5.8 | 9.00 | D38 | 37.89 | 91.75 | SKKS | Low | 1.4 | 0.10 | 16 | 4.48 |
| 28 SEP 2009 19:22:57.140 | 27.93 | 127.82 | 5.8 | 9.00 | D38 | 37.89 | 91.75 | SKS | Low | 1.3 | 0.13 | -77 | 5.74 |
| 13 NOV 2009 07:27:13.360 | -17.92 | -64.10 | 5.8 | 608.00 | D38 | 232.30 | 84.70 | SKS | Low | 1.8 | 0.16 | 22 | 6.74 |
| 14 MAR 2010 08:08:03.960 | 37.74 | 141.59 | 6.5 | 32.00 | D38 | 23.50 | 87.01 | SKS | NULL | - | - | - | - |
| 26 MAR 2010 14:52:07.230 | -27.95 | -70.82 | 6.3 | 42.00 | D38 | 232.20 | 96.45 | SKS | Medium | 1.3 | 0.09 | 28 | 4.05 |
| 26 APR 2010 02:59:51.000 | 22.18 | 123.63 | 6.5 | 14.70 | D38 | 43.86 | 95.17 | SKKS | Medium | 1.2 | 0.08 | 70 | 3.59 |
| 26 APR 2010 02:59:51.000 | 22.18 | 123.63 | 6.5 | 14.70 | D38 | 43.86 | 95.17 | SKS | Medium | 1.3 | 0.06 | -71 | 2.65 |
| 31 MAY 2010 19:51:45.870 | 11.13 | 93.47 | 6.5 | 112.00 | D38 | 74.01 | 88.48 | SKKS | Medium | 0.7 | 0.12 | -61 | 5.13 |
| 31 MAY 2010 19:51:45.870 | 11.13 | 93.47 | 6.5 | 112.00 | D38 | 74.01 | 88.48 | SKS | NULL | - | - | - | - |
| 12 JUL 2010 00:11:21.250 | -22.15 | -68.22 | 6.3 | 115.00 | D38 | 233.38 | 90.32 | SKS | NULL | - | - | - | - |
| 14 JUL 2010 08:32:21.490 | -38.07 | -73.31 | 6.6 | 22.00 | D38 | 228.10 | 105.94 | SKS | Medium | 1.1 | 0.08 | -23 | 3.68 |
| 22 OCT 2010 19:31:37.560 | -20.88 | -68.37 | 5.8 | 132.20 | D38 | 234.18 | 89.33 | SKS | NULL | - | - | - | - |
| 2 DEC 2010 03:12:09.820 | -6.00 | 149.98 | 6.6 | 33.00 | IA001 | 26.08 | 129.26 | SKKS | High | 1.1 | 0.06 | -50 | 2.85 |

| | | | | | | | | | | | | | |
|---|---|---|---|---|---|---|---|---|---|---|---|---|---|
| 2 DEC 2010 03:12:09.820 | -6.00 | 149.98 | 6.6 | 33.00 | IA001 | 26.08 | 129.26 | SKS | Medium | 1.4 | 0.14 | 74 | 5.79 |
| 1 JAN 2011 09:56:58.120 | -26.80 | -63.14 | 7.0 | 576.80 | IA001 | 225.71 | 92.76 | SKS | Medium | 1.4 | 0.12 | -5 | 4.97 |
| 22 OCT 2010 19:31:37.560 | -20.88 | -68.37 | 5.8 | 132.20 | IA002 | 233.97 | 90.71 | SKS | NULL | - | - | - | - |
| 21 DEC 2010 17:19:40.660 | 26.90 | 143.70 | 7.4 | 14.00 | IA002 | 24.72 | 95.60 | SKS | High | 0.64 | 0.04 | 0.9 | 1.91 |
| 22 DEC 2010 21:49:38.790 | 26.81 | 143.60 | 6.4 | 10.00 | IA002 | 24.83 | 95.67 | SKKS | Medium | 0.45 | 0.10 | 2.1 | 4.17 |
| 22 DEC 2010 21:49:38.790 | 26.81 | 143.60 | 6.4 | 10.00 | IA002 | 24.83 | 95.67 | SKS | High | 0.53 | 0.03 | 0.7 | 1.43 |
| 1 JAN 2011 09:56:58.120 | -26.80 | -63.14 | 7.0 | 576.80 | IA002 | 226.89 | 93.48 | SKS | High | 1.6 | 0.03 | 38 | 1.45 |
| 6 MAR 2011 12:31:59.780 | -18.02 | -69.36 | 6.3 | 118.00 | IA003 | 236.73 | 88.33 | SKS | Medium | 1.4 | 0.08 | 4 | 3.61 |
| 11 MAR 2011 11:46:42.500 | 36.00 | 141.17 | 5.8 | 17.70 | IA003 | 24.64 | 87.29 | SKS | High | 0.54 | 0.08 | 0.4 | 3.70 |
| 12 MAR 2011 13:15:41.650 | 37.25 | 141.16 | 6.2 | 38.00 | IA003 | 24.27 | 86.11 | SKS | Medium | 0.59 | 0.09 | 0.8 | 3.86 |
| 12 MAR 2011 22:12:46.270 | 37.68 | 141.89 | 5.9 | 16.00 | IA003 | 23.58 | 85.88 | SKS | NULL | - | - | - | - |
| 20 MAR 2011 08:26:10.730 | 19.00 | 121.24 | 6.0 | 35.00 | IA003 | 47.52 | 95.87 | SKS | Medium | 0.52 | 0.09 | 2.9 | 3.85 |
| 22 MAR 2011 07:18:45.380 | 37.24 | 144.00 | 6.5 | 11.00 | IA003 | 22.10 | 86.79 | SKS | Low | 0.44 | 0.14 | 1.7 | 6.15 |
| 27 MAR 2011 22:23:58.800 | 38.42 | 142.01 | 6.2 | 19.00 | IA003 | 23.26 | 85.21 | SKS | Low | 0.73 | 0.23 | 0.9 | 9.77 |
| 17 APR 2011 01:58:49.310 | -27.60 | -63.20 | 5.9 | 556.60 | IA003 | 226.96 | 93.60 | SKKS | Low | 0.67 | 0.19 | 4.4 | 8.25 |
| 17 APR 2011 01:58:49.310 | -27.60 | -63.20 | 5.9 | 556.60 | IA003 | 226.96 | 93.60 | SKS | Low | 0.58 | 0.16 | 1.7 | 6.91 |
| 8 OCT 2010 05:43:07.630 | 2.83 | 128.23 | 6.1 | 116.00 | IAD01 | 47.58 | 114.12 | SKKS | Low | 1.8 | 0.24 | 30 | 10.1 |

| | | | | | | | | | | | | | |
|---|---|---|---|---|---|---|---|---|---|---|---|---|---|
| 14 MAR 2011 06:12:36.060 | 37.78 | 142.46 | 6.1 | 14.00 | IAD01 | 22.03 | 86.51 | SKS | Medium | 0.5 | 0.10 | 0.7 | 4.32 |
| 27 MAR 2011 22:23:58.800 | 38.42 | 142.01 | 6.2 | 19.00 | IAD01 | 22.18 | 85.81 | SKS | High | 0.34 | 0.04 | 1.7 | 1.72 |
| 29 MAR 2011 10:54:33.200 | 37.40 | 142.29 | 6.1 | 15.00 | IAD01 | 22.26 | 86.84 | SKS | High | 0.44 | 0.03 | 0.8 | 1.39 |
| 1 JAN 2011 09:56:58.120 | -26.80 | -63.14 | 7.0 | 576.80 | IAD18 | 227.06 | 93.09 | SKS | High | 0.8 | 0.05 | 6 | 2.21 |
| 12 JUL 2010 00:11:21.250 | -22.15 | -68.22 | 6.3 | 115.00 | IAD23 | 233.68 | 91.06 | SKS | Medium | 0.41 | 0.06 | 1.0 | 2.78 |
| 23 JUL 2010 22:51:12.450 | 6.49 | 123.47 | 7.6 | 585.80 | IAD23 | 51.69 | 108.07 | SKKS | Medium | 0.6 | 0.09 | 1.5 | 4.12 |
| 23 JUL 2010 22:51:12.450 | 6.49 | 123.47 | 7.6 | 585.80 | IAD23 | 51.69 | 108.07 | SKS | NULL | - | - | - | - |
| 8 DEC 2010 05:24:35.260 | -56.41 | -25.74 | 6.3 | 29.40 | IAD23 | 190.44 | 109.76 | SKS | Medium | 1.5 | 0.13 | 44 | 5.66 |
| 22 OCT 2010 19:31:37.560 | -20.88 | -68.37 | 5.8 | 132.20 | IAD38 | 234.18 | 89.33 | SKS | NULL | - | - | - | - |
| 1 JAN 2011 09:56:58.120 | -26.80 | -63.14 | 7.0 | 576.80 | IAD38 | 227.01 | 91.85 | SKS | NULL | - | - | - | - |
| 27 MAR 2011 22:23:58.800 | 38.42 | 142.01 | 6.2 | 19.00 | IAD38 | 22.98 | 86.48 | SKS | NULL | - | - | - | - |
| 7 APR 2011 14:32:43.290 | 38.28 | 141.59 | 7.1 | 42.00 | IAD38 | 23.34 | 86.51 | SKS | Medium | 1.0 | 0.05 | 81 | 2.09 |
| 22 DEC 2010 21:49:38.790 | 26.81 | 143.60 | 6.4 | 10.00 | IAVAL | 23.46 | 98.30 | SKS | Low | 0.51 | 0.16 | 1.7 | 6.69 |
| 1 JAN 2011 09:56:58.120 | -26.80 | -63.14 | 7.0 | 576.80 | IAVAL | 225.47 | 91.05 | SKS | Medium | 1.1 | 0.11 | -28 | 4.57 |
| 15 JAN 2011 11:23:53.220 | 2.49 | 96.29 | 5.8 | 19.00 | IAVAL | 75.37 | 98.17 | SKKS | Medium | 0.46 | 0.08 | 2.0 | 3.50 |
| 15 JAN 2011 11:23:53.220 | 2.49 | 96.29 | 5.8 | 19.00 | IAVAL | 75.37 | 98.17 | SKS | NULL | - | - | - | - |

| | | | | | | | | | | | | | |
|---|---|---|---|---|---|---|---|---|---|---|---|---|---|
| 30 APR 2006 21:40:58.440 | -27.21 | -71.06 | 6.5 | 12.00 | P07 | 231.93 | 95.21 | SKS | Low | 0.3 | 0.09 | 9 | 3.97 |
| 25 AUG 2006 00:44:46.160 | -24.40 | -67.03 | 6.6 | 184.00 | P07 | 230.38 | 90.90 | SKS | NULL | - | - | - | - |
| 6 SEP 2007 17:51:26.190 | 24.34 | 122.22 | 6.2 | 53.00 | P07 | 43.10 | 93.36 | SKS | High | 1.5 | 0.05 | 64 | 2.38 |
| 28 SEP 2007 13:38:57.880 | 22.01 | 142.67 | 7.5 | 260.00 | P07 | 26.50 | 102.80 | SKKS | High | 1.3 | 0.04 | 39 | 1.82 |
| 28 SEP 2007 13:38:57.880 | 22.01 | 142.67 | 7.5 | 260.00 | P07 | 26.50 | 102.80 | SKS | High | 1.0 | 0.04 | -86 | 1.84 |
| 1 JUN 2008 01:57:23.690 | 20.12 | 121.35 | 6.3 | 31.00 | P07 | 45.81 | 96.68 | SKKS | Medium | 0.8 | 0.13 | 84 | 5.71 |
| 1 JUN 2008 01:57:23.690 | 20.12 | 121.35 | 6.3 | 31.00 | P07 | 45.81 | 96.68 | SKS | High | 1.1 | 0.04 | -84 | 1.79 |
| 8 JUL 2008 09:13:07.460 | -15.99 | -71.75 | 6.2 | 123.00 | P07 | 238.65 | 86.26 | SKS | NULL | - | - | - | - |
| 13 JUL 2009 18:05:01.420 | 24.06 | 122.20 | 6.3 | 17.00 | P07 | 43.25 | 93.61 | SKS | Low | 1.2 | 0.21 | 70 | 8.84 |
| 9 AUG 2009 10:55:55.110 | 33.17 | 137.94 | 7.1 | 292.00 | P07 | 26.93 | 90.94 | SKKS | Medium | 1.0 | 0.12 | 50 | 5.00 |
| 9 AUG 2009 10:55:55.110 | 33.17 | 137.94 | 7.1 | 292.00 | P07 | 26.93 | 90.94 | SKS | High | 0.8 | 0.05 | -86 | 2.36 |
| 12 AUG 2009 22:48:51.420 | 32.82 | 140.40 | 6.6 | 53.00 | P07 | 25.10 | 91.93 | SKS | High | 0.7 | 0.03 | 71 | 1.62 |
| 30 SEP 2009 10:16:09.250 | -0.72 | 99.87 | 7.6 | 81.00 | P07 | 75.20 | 102.46 | SKKS | NULL | - | - | - | - |
| 30 SEP 2009 10:16:09.250 | -0.72 | 99.87 | 7.6 | 81.00 | P07 | 75.20 | 102.46 | SKS | NULL | - | - | - | - |
| 30 OCT 2009 07:03:39.120 | 29.22 | 129.78 | 6.8 | 34.00 | P07 | 34.89 | 91.97 | SKS | NULL | - | - | - | - |
| 8 NOV 2009 19:41:43.360 | -8.21 | 118.63 | 6.6 | 18.00 | P07 | 63.60 | 119.45 | SKKS | Medium | 1.5 | 0.11 | -59 | 4.71 |
| 10 NOV 2009 02:48:46.790 | 8.08 | 91.90 | 6.0 | 23.00 | P07 | 76.21 | 90.69 | SKS | High | 1.1 | 0.09 | -62 | 3.76 |
| 19 DEC 2009 13:02:15.570 | 23.80 | 121.61 | 6.4 | 43.00 | P07 | 43.86 | 93.58 | SKKS | NULL | - | - | - | - |

| | | | | | | | | | | | | | |
|---|---|---|---|---|---|---|---|---|---|---|---|---|---|
| 23 DEC 2009 01:11:58.200 | -1.43 | 99.39 | 6.0 | 19.00 | P07 | 76.03 | 102.74 | SKKS | NULL | - | - | - | - |
| 3 JAN 2010 22:36:27.960 | -8.80 | 157.35 | 7.1 | 25.00 | P07 | 19.09 | 136.05 | SKKS | High | 1.5 | 0.05 | 81 | 2.11 |
| 3 JAN 2010 22:36:27.960 | -8.80 | 157.35 | 7.1 | 25.00 | P07 | 19.09 | 136.05 | SKS | NULL | - | - | - | - |
| 27 FEB 2010 06:34:11.530 | -36.12 | -72.90 | 8.8 | 22.90 | P07 | 228.17 | 103.44 | SKKS | NULL | - | - | - | - |
| 14 MAR 2010 08:08:03.960 | 37.74 | 141.59 | 6.5 | 32.00 | P07 | 22.65 | 87.57 | SKS | NULL | - | - | - | - |
| 26 APR 2010 02:59:51.000 | 22.18 | 123.63 | 6.5 | 14.70 | P07 | 42.95 | 95.87 | SKS | Medium | 0.7 | 0.09 | 85 | 3.74 |
| 3 MAY 2010 23:09:44.790 | -38.07 | -73.45 | 6.3 | 19.00 | P07 | 227.38 | 105.28 | SKKS | High | 1.0 | 0.04 | 61 | 1.85 |
| 6 MAY 2010 02:42:47.940 | -18.06 | -70.55 | 6.2 | 37.00 | P07 | 236.55 | 87.35 | SKS | Medium | 1.0 | 0.07 | 17 | 3.13 |
| 9 MAY 2010 05:59:41.620 | 3.75 | 96.02 | 7.2 | 38.00 | P07 | 75.58 | 96.60 | SKKS | NULL | - | - | - | - |
| 26 MAY 2003 23:13:29.000 | 6.76 | 123.71 | 6.9 | 565.80 | DSB | 52.58 | 106.91 | SKS | Medium | 0.9 | 0.08 | -70 | 3.53 |
| 20 JUN 2003 13:30:41.000 | -30.61 | -71.64 | 6.8 | 33.00 | DSB | 232.87 | 100.84 | SKKS | Medium | 1.7 | 0.08 | -27 | 3.38 |
| 25 JUL 2003 09:37:45.000 | -1.53 | 149.69 | 6.4 | 24.00 | DSB | 29.58 | 124.77 | SKS | Medium | 0.8 | 0.10 | 75 | 4.29 |
| 25 JUL 2004 14:35:19.000 | -2.43 | 103.98 | 7.3 | 582.10 | DSB | 74.91 | 104.03 | SKKS | Medium | 0.5 | 0.06 | -45 | 2.88 |
| 25 JUL 2004 14:35:19.000 | -2.43 | 103.98 | 7.3 | 582.10 | DSB | 74.91 | 104.03 | SKS | Medium | 1.5 | 0.07 | -77 | 3.09 |
| 7 SEP 2004 11:53:06.000 | -28.57 | -65.84 | 6.4 | 22.30 | DSB | 229.67 | 96.41 | SKS | Medium | 1.2 | 0.08 | -14 | 3.66 |
| 16 FEB 2005 20:27:52.000 | -36.32 | -16.56 | 6.6 | 10.00 | DSB | 188.21 | 89.63 | SKS | Low | 2.1 | 0.13 | -21 | 5.42 |

| | | | | | | | | | | | | | |
|---|---|---|---|---|---|---|---|---|---|---|---|---|---|
| 21 MAR 2005 12:43:12.000 | -24.73 | -63.51 | 6.4 | 570.10 | DSB | 229.85 | 92.05 | SKS | Medium | 1.5 | 0.08 | -24 | 3.53 |
| 12 JUN 2005 19:26:24.000 | -56.29 | -27.08 | 6.0 | 94.10 | DSB | 192.15 | 110.49 | SKKS | NULL | - | - | - | - |
| 13 JUN 2005 22:44:33.000 | -19.99 | -69.20 | 7.8 | 115.60 | DSB | 236.80 | 90.77 | SKS | High | 1.7 | 0.02 | -19 | 1.05 |
| 17 NOV 2005 19:26:56.000 | -22.32 | -67.89 | 6.9 | 162.60 | DSB | 234.53 | 92.08 | SKS | NULL | - | - | - | - |
| 2 FEB 2006 12:48:43.440 | -17.75 | -178.39 | 6.7 | 597.50 | DSB | 346.97 | 144.03 | SKKS | High | 0.6 | 0.04 | -75 | 1.96 |
| 16 JUL 2006 11:42:41.410 | -28.72 | -72.54 | 6.2 | 10.00 | DSB | 234.60 | 99.71 | SKS | High | 2.0 | 0.04 | -24 | 1.71 |
| 25 AUG 2006 00:44:46.160 | -24.40 | -67.03 | 6.6 | 184.00 | DSB | 232.76 | 93.43 | SKS | High | 0.5 | 0.03 | -1 | 1.43 |
| 1 SEP 2006 10:18:51.600 | -6.76 | 155.51 | 6.8 | 38.00 | DSB | 24.29 | 131.36 | SKKS | Medium | 1.3 | 0.12 | 83 | 5.18 |
| 21 JUL 2007 15:34:52.600 | -22.15 | -65.78 | 6.4 | 289.50 | DSB | 232.95 | 90.92 | SKS | High | 0.9 | 0.03 | -18 | 1.62 |
| 1 AUG 2007 17:08:51.400 | -15.60 | 167.68 | 7.2 | 120.00 | DSB | 9.36 | 142.14 | SKKS | Medium | 1.6 | 0.12 | 77 | 5.12 |
| 6 SEP 2007 17:51:26.190 | 24.34 | 122.22 | 6.2 | 53.00 | DSB | 45.48 | 90.82 | SKS | High | 1.2 | 0.06 | 58 | 2.70 |
| 28 SEP 2007 13:38:57.880 | 22.01 | 142.67 | 7.5 | 260.00 | DSB | 29.03 | 100.39 | SKKS | Medium | 1.2 | 0.07 | 45 | 3.29 |
| 28 SEP 2007 13:38:57.880 | 22.01 | 142.67 | 7.5 | 260.00 | DSB | 29.03 | 100.39 | SKS | High | 0.7 | 0.02 | 81 | 1.23 |
| 18 NOV 2007 05:40:12.040 | -22.64 | -66.32 | 6.0 | 246.40 | DSB | 233.13 | 91.60 | SKS | Medium | 1.2 | 0.08 | 35 | 3.52 |
| 9 MAY 2008 21:51:29.730 | 12.52 | 143.18 | 6.8 | 76.00 | DSB | 31.66 | 109.50 | SKS | High | 1.2 | 0.02 | 51 | 1.15 |
| 9 MAY 2008 21:51:29.730 | 12.52 | 143.18 | 6.8 | 76.00 | DSB | 31.66 | 109.50 | SKKS | NULL | - | - | - | - |

| | | | | | | | | | | | | | |
|---|---|---|---|---|---|---|---|---|---|---|---|---|---|
| 8 JUL 2008 09:13:07.460 | -15.99 | -71.75 | 6.2 | 123.00 | DSB | 240.99 | 88.73 | SKS | Low | 0.7 | 0.15 | 33 | 6.47 |
| 13 JUL 2008 14:58:33.010 | 21.01 | 121.15 | 6.2 | 14.00 | DSB | 47.92 | 93.27 | SKKS | High | 1.3 | 0.04 | -72 | 1.87 |
| 11 SEP 2008 00:00:02.700 | 1.88 | 127.36 | 6.6 | 96.00 | DSB | 51.62 | 112.90 | SKKS | Low | 1.7 | 0.13 | -85 | 5.57 |
| 16 NOV 2008 17:02:32.700 | 1.27 | 122.09 | 7.3 | 30.00 | DSB | 56.90 | 110.86 | SKS | Low | 1.5 | 0.12 | -82 | 5.24 |
| 3 JAN 2009 22:33:40.290 | -0.69 | 133.30 | 7.4 | 23.00 | DSB | 47.06 | 117.89 | SKKS | Low | 2.0 | 0.24 | -86 | 9.98 |
| 14 NOV 2009 19:44:29.930 | -22.97 | -66.64 | 6.2 | 220.40 | DSB | 233.21 | 92.03 | SKS | NULL | - | - | - | - |
| 19 DEC 2009 13:02:15.570 | 23.80 | 121.61 | 6.4 | 43.00 | DSB | 46.23 | 91.04 | SKS | Low | 1.8 | 0.17 | -88 | 7.28 |
| 7 FEB 2010 06:10:00.230 | 23.49 | 123.61 | 6.3 | 21.00 | DSB | 44.74 | 92.17 | SKS | NULL | - | - | - | - |
| 27 FEB 2010 06:34:11.530 | -36.12 | -72.90 | 8.8 | 22.90 | DSB | 230.58 | 105.98 | SKKS | High | 1.2 | 0.06 | -24 | 2.48 |
| 14 MAR 2010 08:08:03.960 | 37.74 | 141.59 | 6.5 | 32.00 | DSB | 24.96 | 85.22 | SKS | NULL | - | - | - | - |
| 6 APR 2010 22:15:01.580 | 2.38 | 97.05 | 7.8 | 31.00 | DSB | 77.79 | 96.11 | SKS | High | 0.6 | 0.06 | -88 | 2.54 |
| 6 MAY 2010 02:42:47.940 | -18.06 | -70.55 | 6.2 | 37.00 | DSB | 238.91 | 89.84 | SKS | NULL | - | - | - | - |
| 9 MAY 2010 05:59:41.620 | 3.75 | 96.02 | 7.2 | 38.00 | DSB | 77.83 | 94.41 | SKKS | Low | 0.9 | 0.12 | -80 | 5.00 |
| 9 MAY 2010 05:59:41.620 | 3.75 | 96.02 | 7.2 | 38.00 | DSB | 77.83 | 94.41 | SKS | NULL | - | - | - | - |
| 31 MAY 2010 19:51:45.870 | 11.13 | 93.47 | 6.5 | 112.00 | DSB | 75.54 | 86.99 | SKS | High | 0.9 | 0.03 | -83 | 1.48 |
| 12 JUL 2010 00:11:21.250 | -22.15 | -68.22 | 6.3 | 115.00 | DSB | 234.88 | 92.10 | SKS | High | 1.1 | 0.05 | -16 | 2.39 |
| 23 JUL 2010 22:51:12.450 | 6.49 | 123.47 | 7.6 | 585.80 | DSB | 52.94 | 107.03 | SKS | Medium | 0.9 | 0.09 | -80 | 3.90 |
| 23 JUL 2010 23:15:10.190 | 6.78 | 123.26 | 7.4 | 640.60 | DSB | 52.98 | 106.68 | SKS | Low | 0.9 | 0.17 | -86 | 7.13 |

| | | | | | | | | | | | | | |
|---|---|---|---|---|---|---|---|---|---|---|---|---|---|
| 26 MAY 2003 19:23:27.000 | 2.35 | 128.85 | 7.0 | 31.00 | VAL | 46.62 | 115.82 | SKKS | NULL | - | - | - | - |
| 20 JUN 2003 13:30:41.000 | -30.61 | -71.64 | 6.8 | 33.00 | VAL | 229.88 | 98.18 | SKKS | NULL | - | - | - | - |
| 3 MAY 2004 04:36:50.000 | -37.69 | -73.41 | 6.6 | 21.00 | VAL | 227.08 | 104.86 | SKKS | High | 1.0 | 0.06 | 25 | 2.83 |
| 3 MAY 2004 04:36:50.000 | -37.69 | -73.41 | 6.6 | 21.00 | VAL | 227.08 | 104.86 | SKS | Medium | 1.1 | 0.05 | -25 | 2.30 |
| 25 JUL 2004 14:35:19.000 | -2.43 | 103.98 | 7.3 | 582.10 | VAL | 72.01 | 106.67 | SKS | NULL | - | - | - | - |
| 6 SEP 2004 12:42:59.000 | -55.37 | -28.98 | 6.9 | 10.00 | VAL | 191.12 | 108.06 | SKS | NULL | - | - | - | - |
| 6 SEP 2004 12:42:59.000 | -55.37 | -28.98 | 6.9 | 10.00 | VAL | 191.12 | 108.06 | SKKS | NULL | - | - | - | - |
| 7 SEP 2004 11:53:06.000 | -28.57 | -65.84 | 6.4 | 22.30 | VAL | 226.66 | 93.78 | SKS | High | 0.9 | 0.06 | -11 | 2.60 |
| 26 OCT 2004 20:48:10.000 | -57.07 | -24.83 | 6.0 | 10.00 | VAL | 188.38 | 109.30 | SKKS | Medium | 0.8 | 0.05 | -8 | 2.16 |
| 21 MAR 2005 12:43:12.000 | -24.73 | -63.51 | 6.4 | 570.10 | VAL | 226.79 | 89.42 | SKS | Low | 1.6 | 0.10 | 25 | 4.21 |
| 10 MAY 2005 01:09:05.000 | -6.23 | 103.14 | 6.3 | 17.00 | VAL | 75.08 | 109.20 | SKKS | Low | 1.8 | 0.12 | -47 | 5.35 |
| 12 JUN 2005 19:26:24.000 | -56.29 | -27.08 | 6.0 | 94.10 | VAL | 189.82 | 108.75 | SKKS | Medium | 1.2 | 0.10 | 0 | 4.31 |
| 17 NOV 2005 19:26:56.000 | -22.32 | -67.89 | 6.9 | 162.60 | VAL | 231.47 | 89.41 | SKS | NULL | - | - | - | - |
| 16 MAY 2006 10:39:23.340 | -31.81 | -179.31 | 7.4 | 152.00 | VAL | 334.03 | 158.35 | SKKS | Medium | 1.2 | 0.10 | 46 | 4.20 |
| 16 MAY 2006 15:28:25.920 | 0.09 | 97.05 | 6.8 | 12.00 | VAL | 76.20 | 100.53 | SKS | NULL | - | - | - | - |
| 7 AUG 2006 22:18:55.090 | -15.80 | 167.79 | 6.8 | 150.00 | VAL | 3.22 | 143.92 | SKKS | Medium | 0.8 | 0.08 | 11 | 3.34 |

| | | | | | | | | | | | | | |
|---|---|---|---|---|---|---|---|---|---|---|---|---|---|
| 25 AUG 2006 00:44:46.160 | -24.40 | -67.03 | 6.6 | 184.00 | VAL | 229.71 | 90.77 | SKS | NULL | - | - | - | - |
| 17 OCT 2006 01:25:12.230 | -5.88 | 150.98 | 6.7 | 32.00 | VAL | 25.32 | 131.54 | SKKS | NULL | - | - | - | - |
| 21 JUL 2007 15:34:52.600 | -22.15 | -65.78 | 6.4 | 289.50 | VAL | 229.88 | 88.25 | SKS | High | 0.5 | 0.04 | 5 | 1.85 |
| 28 SEP 2007 13:38:57.880 | 22.01 | 142.67 | 7.5 | 260.00 | VAL | 25.66 | 102.64 | SKKS | NULL | - | - | - | - |
| 28 SEP 2007 13:38:57.880 | 22.01 | 142.67 | 7.5 | 260.00 | VAL | 25.66 | 102.64 | SKS | High | 1.0 | 0.03 | 44 | 1.63 |
| 1 JUN 2008 01:57:23.690 | 20.12 | 121.35 | 6.3 | 31.00 | VAL | 45.05 | 96.76 | SKS | High | 0.5 | 0.02 | 67 | 1.21 |
| 13 JUL 2008 14:58:33.010 | 21.01 | 121.15 | 6.2 | 14.00 | VAL | 44.80 | 95.89 | SKS | NULL | - | - | - | - |
| 13 JUL 2009 18:05:01.420 | 24.06 | 122.20 | 6.3 | 17.00 | VAL | 42.53 | 93.65 | SKS | NULL | - | - | - | - |
| 9 AUG 2009 10:55:55.110 | 33.17 | 137.94 | 7.1 | 292.00 | VAL | 26.24 | 90.79 | SKS | High | 1.3 | 0.04 | 41 | 1.77 |
| 12 AUG 2009 22:48:51.420 | 32.82 | 140.40 | 6.6 | 53.00 | VAL | 24.40 | 91.76 | SKKS | Medium | 0.8 | 0.11 | 0 | 4.60 |
| 12 AUG 2009 22:48:51.420 | 32.82 | 140.40 | 6.6 | 53.00 | VAL | 24.40 | 91.76 | SKS | High | 1.3 | 0.02 | 38 | 0.97 |
| 2 SEP 2009 07:55:01.050 | -7.78 | 107.30 | 7.0 | 46.00 | VAL | 72.53 | 112.91 | SKS | NULL | - | - | - | - |
| 30 SEP 2009 10:16:09.250 | -0.72 | 99.87 | 7.6 | 81.00 | VAL | 74.39 | 102.87 | SKKS | NULL | - | - | - | - |
| 30 SEP 2009 10:16:09.250 | -0.72 | 99.87 | 7.6 | 81.00 | VAL | 74.39 | 102.87 | SKS | High | 0.7 | 0.04 | 2 | 1.91 |
| 1 OCT 2009 01:52:27.320 | -2.48 | 101.52 | 6.6 | 9.00 | VAL | 74.10 | 105.26 | SKS | NULL | - | - | - | - |
| 15 OCT 2009 17:48:21.890 | 3.27 | -103.82 | 6.0 | 10.00 | VAL | 274.82 | 89.66 | SKS | Low | 2.0 | 0.06 | -40 | 2.53 |
| 24 OCT 2009 14:40:43.720 | -6.13 | 130.38 | 6.9 | 130.00 | VAL | 49.54 | 124.01 | SKKS | NULL | - | - | - | - |

| | | | | | | | | | | | | | |
|---|---|---|---|---|---|---|---|---|---|---|---|---|---|
| 30 OCT 2009 07:03:39.120 | 29.22 | 129.78 | 6.8 | 34.00 | VAL | 34.19 | 91.92 | SKS | NULL | - | - | - | - |
| 8 NOV 2009 19:41:43.360 | -8.21 | 118.63 | 6.6 | 18.00 | VAL | 62.56 | 119.74 | SKS | Medium | 1.2 | 0.12 | -81 | 5.21 |
| 10 NOV 2009 02:48:46.790 | 8.08 | 91.90 | 6.0 | 23.00 | VAL | 75.52 | 91.11 | SKKS | NULL | - | - | - | - |
| 13 NOV 2009 03:05:57.220 | -19.39 | -70.32 | 6.5 | 27.00 | VAL | 234.94 | 88.15 | SKS | Low | 1.0 | 0.26 | -86 | 10.9 |
| 14 NOV 2009 19:44:29.930 | -22.97 | -66.64 | 6.2 | 220.40 | VAL | 230.15 | 89.36 | SKS | Medium | 1.2 | 0.11 | 17 | 4.69 |
| 17 JAN 2010 12:00:01.080 | -57.66 | -65.88 | 6.3 | 5.00 | VAL | 210.26 | 118.32 | SKKS | Medium | 1.9 | 0.10 | 85 | 4.14 |
| 17 JAN 2010 12:00:01.080 | -57.66 | -65.88 | 6.3 | 5.00 | VAL | 210.26 | 118.32 | SKS | NULL | - | - | - | - |
| 27 FEB 2010 06:34:11.530 | -36.12 | -72.90 | 8.8 | 22.90 | VAL | 227.65 | 103.33 | SKKS | NULL | - | - | - | - |
| 4 MAR 2010 22:39:26.530 | -22.23 | -68.33 | 6.4 | 114.00 | VAL | 231.86 | 89.54 | SKS | High | 1.5 | 0.04 | -16 | 1.90 |
| 26 APR 2010 02:59:51.000 | 22.18 | 123.63 | 6.5 | 14.70 | VAL | 42.20 | 95.91 | SKS | Medium | 1.1 | 0.05 | -55 | 2.10 |
| 9 MAY 2010 05:59:41.620 | 3.75 | 96.02 | 7.2 | 38.00 | VAL | 74.83 | 97.01 | SKKS | Medium | 0.7 | 0.10 | 56 | 4.20 |
| 20 MAY 2010 08:06:28.760 | -39.06 | -92.16 | 5.9 | 10.00 | VAL | 238.38 | 115.15 | SKS | Medium | 1.5 | 0.03 | -12 | 1.42 |
| 31 MAY 2010 19:51:45.870 | 11.13 | 93.47 | 6.5 | 112.00 | VAL | 72.45 | 89.62 | SKS | NULL | - | - | - | - |
| 16 JUN 2010 03:16:27.550 | -2.17 | 136.54 | 7.0 | 18.00 | VAL | 40.84 | 123.18 | SKKS | Medium | 1.4 | 0.13 | 14 | 5.67 |
| 12 JUL 2010 00:11:21.250 | -22.15 | -68.22 | 6.3 | 115.00 | VAL | 231.82 | 89.42 | SKS | High | 0.7 | 0.05 | 34 | 2.37 |
| 23 JUL 2010 22:51:12.450 | 6.49 | 123.47 | 7.6 | 585.80 | VAL | 49.72 | 109.70 | SKKS | NULL | - | - | - | - |
| 23 JUL 2010 22:51:12.450 | 6.49 | 123.47 | 7.6 | 585.80 | VAL | 49.72 | 109.70 | SKS | Medium | 1.1 | 0.08 | 56 | 3.54 |

# E. Summary of results

| Station | Total | SKS | SKKS | High | Medium | Low | Null | $\delta t_{min}$ | $\delta t_{max}$ | $\phi_{min}$ | $\phi_{max}$ |
|---|---|---|---|---|---|---|---|---|---|---|---|
| D01 | 8 | 5 | 3 | - | - | 7 | 1 | 0.7 | 1.8 | -69 | 61 |
| D02 | 1 | - | 1 | - | - | 1 | - | 1.9 | 1.9 | -13 | 13 |
| D03 | 6 | 4 | 2 | 2 | 1 | 3 | - | 0.8 | 2.2 | -37 | 39 |
| D04 | 1 | - | 1 | - | - | - | 1 | - | - | - | - |
| D05 | 3 | 2 | 1 | - | - | 1 | 2 | 0.7 | 0.7 | 75 | 75 |
| D06 | 3 | - | 3 | - | 1 | 1 | 1 | 0.8 | 1.4 | -61 | -30 |
| D08 | 3 | 1 | 2 | - | 1 | 1 | 1 | 0.5 | 0.7 | -37 | -4 |
| D09 | 1 | 1 | - | - | - | - | 1 | - | - | - | - |
| D10 | 2 | - | 2 | - | - | - | 2 | - | - | - | - |
| D12 | 4 | 1 | 3 | - | - | 2 | 2 | 0.5 | 1.8 | -21 | -17 |
| D14 | 6 | 3 | 3 | 1 | - | 1 | 4 | 0.9 | 1.2 | -55 | 43 |
| D15 | 15 | 12 | 3 | 4 | 5 | 4 | 2 | 0.5 | 1.6 | -66 | 82 |
| D16 | 34 | 26 | 8 | 5 | 9 | 7 | 13 | 0.7 | 2.8 | -69 | 82 |
| D18 | 8 | 6 | 2 | - | - | 6 | 2 | 1.6 | 2.5 | -77 | 89 |
| D21 | 2 | - | 2 | - | 1 | - | 1 | 1.7 | 1.7 | 15 | 15 |
| D23 | 38 | 25 | 13 | 14 | 5 | 7 | 12 | 0.5 | 2.5 | -84 | 84 |
| D32 | 24 | 14 | 10 | 6 | 7 | 4 | 7 | 0.7 | 2.2 | -88 | 87 |

| | | | | | | | | | | | |
|---|---|---|---|---|---|---|---|---|---|---|---|
| D33 | 25 | 17 | 8 | 5 | 8 | - | 12 | 0.8 | 1.8 | -71 | 81 |
| D34 | 50 | 34 | 16 | 13 | 11 | 8 | 18 | 0.5 | 2.3 | -87 | 87 |
| D35 | 2 | 1 | 1 | - | - | 1 | 1 | 0.8 | 0.8 | -14 | -14 |
| D36 | 5 | 3 | 2 | 2 | 1 | - | 2 | 0.9 | 1.8 | -80 | 84 |
| D37 | 31 | 20 | 11 | 6 | 12 | 6 | 7 | 0.5 | 1.4 | -85 | 85 |
| D38 | 12 | 9 | 3 | - | 5 | 3 | 4 | 0.7 | 1.8 | -77 | 70 |
| DSB | 41 | 28 | 13 | 13 | 12 | 8 | 8 | 0.5 | 2.1 | -88 | 83 |
| IA001 | 3 | 2 | 1 | 1 | 2 | - | - | 1.1 | 1.4 | -50 | 74 |
| IA002 | 5 | 4 | 1 | 3 | 1 | - | 1 | 0.44 | 1.6 | 0.7 | 38 |
| IA003 | 9 | 8 | 1 | 1 | 3 | 4 | 1 | 0.44 | 1.4 | 0.8 | 4.4 |
| IAD01 | 4 | 3 | 1 | 2 | 1 | 1 | - | 0.34 | 1.8 | 0.7 | 30 |
| IAD18 | 1 | 1 | - | 1 | - | - | - | 0.8 | 0.8 | 6 | 6 |
| IAD23 | 4 | 3 | 1 | - | 3 | - | 1 | 0.4 | 1.5 | 1 | 44 |
| IAD38 | 4 | 4 | - | - | 1 | - | 3 | 1 | 1 | 81 | 81 |
| IAVAL | 4 | 3 | 1 | - | 2 | 1 | 1 | 0.46 | 1.1 | -28 | 2 |
| P07 | 27 | 16 | 11 | 9 | 5 | 2 | 11 | 0.3 | 1.5 | -86 | 85 |
| VAL | 50 | 34 | 16 | 10 | 14 | 4 | 22 | 0.5 | 2 | -86 | 85 |

# F. Averaged shear-wave splitting results

Average splitting parameters were calculated using the program described in Appendix G (the program taken from *Özalaybey and Savage*, 1995).

Table F.1.: Summary of average SKS splitting parameters obtained from medium and high quality measurements at the permanent and temporary seismic stations for all events from the back-azimuth range $0 - 90^0$. $\overline{\delta t}$ and $\overline{\sigma}^2$ is the average delay time and its standard deviation, respectively. $\overline{\phi}$ and $\nu$ is the average fast polarisation and its standard deviation, respectively. Results from stations with only one measurement are also shown. In this case, $\overline{\delta t} \sim \delta t$, $\overline{\sigma}^2 \sim \sigma_{\delta t}$, $\overline{\phi} \sim \phi$ and $\nu \sim \sigma_{\phi}$.

| Station | $\overline{\delta t}$ | $\overline{\sigma}^2$ | $\overline{\phi}$ | $\nu$ | No. events |
|---|---|---|---|---|---|
| D15 | 0.99 | 0.04 | 61 | 23 | 3 |
| D16 | 0.7 | 0.10 | -59 | 4.38 | 1 |
| D23 | 1.61 | 0.25 | 98 | 13 | 7 |
| D32 | 1.11 | 0.10 | 101 | 18 | 7 |
| D33 | 1.16 | 0.08 | 63 | 13 | 5 |
| D34 | 0.90 | 0.08 | 108 | 8 | 14 |
| D36 | 1.04 | 0.13 | 60 | 12 | 2 |
| D37 | 0.98 | 0.09 | 78 | 9 | 8 |
| D38 | 1.3 | 0.06 | -71 | 2.65 | 1 |
| DSB | 0.95 | 0.08 | 81 | 7 | 9 |
| IA001 | 1.4 | 0.14 | 74 | 5.79 | 1 |
| IA002 | 0.58 | 0.08 | 1 | 4 | 2 |

| | | | | | |
|---|---|---|---|---|---|
| IA003 | 0.55 | 0.15 | 1 | 6 | 3 |
| IAD01 | 0.40 | 0.07 | 1 | 3 | 3 |
| IAD38 | 1.0 | 0.05 | 81 | 2.09 | 1 |
| P07 | 0.96 | 0.10 | 87 | 5 | 7 |
| VAL | 0.98 | 0.11 | 50 | 12 | 8 |

Table F.2.: Summary average SKKS splitting parameters obtained from medium and high quality measurements at the permanent and temporary seismic stations for all events from the back-azimuth range $0 - 90^0$. $\overline{\delta t}$ and $\widetilde{\sigma}^2$ is the average delay time and its standard deviation, respectively. $\overline{\phi}$ and $\nu$ is the average fast polarisation and its standard deviation, respectively. Results from stations with only one measurement are also shown. In this case, $\overline{\delta t} \sim \delta t$, $\widetilde{\sigma}^2 \sim \sigma_{\delta t}$, $\overline{\phi} \sim \phi$ and $\nu \sim \sigma_{\phi}$.

| Station | $\overline{\delta t}$ | $\widetilde{\sigma}^2$ | $\overline{\phi}$ | $\nu$ | No. events |
|---|---|---|---|---|---|
| D03 | 1.3 | 0.09 | 36 | 3.90 | 1 |
| D06 | 1.4 | 0.11 | -30 | 4.90 | 1 |
| D08 | 0.7 | 0.07 | -4 | 3.26 | 1 |
| D16 | 1.48 | 0.29 | 111 | 10 | 4 |
| D23 | 1.09 | 0.15 | 70 | 11 | 7 |
| D32 | 1.53 | 0.17 | 99 | 7 | 3 |
| D33 | 0.62 | 0.08 | 90 | 20 | 5 |
| D34 | 0.67 | 0.08 | 81 | 9 | 4 |
| D36 | 1.8 | 0.07 | -80 | 2.95 | 1 |
| D37 | 0.81 | 0.07 | -54 | 10 | 4 |
| D38 | 1.05 | 0.16 | 85 | 16 | 2 |
| DSB | 1.12 | 0.15 | 99 | 13 | 5 |
| IA001 | 1.1 | 0.06 | -50 | 2.85 | 1 |
| IA002 | 0.44454 | 0.10 | 2.1 | 4.17 | 1 |
| IAD23 | 0.59601 | 0.09 | 1.5 | 4.12 | 1 |
| IAVAL | 0.45599 | 0.08 | 2.0 | 3.50 | 1 |

| | | | | | |
|---|---|---|---|---|---|
| P07 | 1.34 | 0.08 | 61 | 11 | 5 |
| VAL | 0.86 | 0.11 | 21 | 11 | 4 |

Table F.3.: Summary average SKS+SKKS splitting parameters obtained from medium and high quality measurements at the permanent and temporary seismic stations for all events from the back-azimuth range $0 - 90^0$. $\overline{\delta t}$ and $\widetilde{\sigma}^2$ is the average delay time and its standard deviation, respectively. $\overline{\phi}$ and $\nu$ is the average fast polarisation and its standard deviation, respectively. Results from stations with only one measurement are also shown. In this case, $\overline{\delta t} \sim \delta t$, $\widetilde{\sigma}^2 \sim \sigma_{\delta t}$, $\overline{\phi} \sim \phi$ and $\nu \sim \sigma_{\phi}$.

| Station | $\overline{\delta t}$ | $\widetilde{\sigma}^2$ | $\overline{\phi}$ | $\nu$ | No. events |
|---|---|---|---|---|---|
| D03 | 1.3 | 0.09 | 36 | 3.90 | 1 |
| D06 | 1.4 | 0.11 | -30 | 4.90 | 1 |
| D08 | 0.7 | 0.07 | -4 | 3.26 | 1 |
| D15 | 0.97 | 0.04 | 71 | 28 | 4 |
| D16 | 1.31 | 0.27 | 113 | 9 | 5 |
| D23 | 1.41 | 0.16 | 88 | 9 | 14 |
| D32 | 1.15 | 0.10 | 101 | 14 | 10 |
| D33 | 1.23 | 0.09 | 74 | 12 | 10 |
| D34 | 0.89 | 0.08 | 96 | 8 | 18 |
| D36 | 1.23 | 0.21 | 70 | 13 | 3 |
| D37 | 0.93 | 0.07 | 92 | 9 | 12 |
| D38 | 1.19 | 0.12 | 99 | 11 | 3 |
| DSB | 0.99 | 0.08 | 86 | 6 | 14 |
| IA001 | 1.15 | 0.08 | 119 | 16 | 2 |
| IA002 | 0.57 | 0.07 | 1 | 4 | 3 |
| IA003 | 0.55 | 0.15 | 1 | 6 | 3 |
| IAD01 | 0.40 | 0.07 | 1 | 3 | 3 |
| IAD23 | 0.59601 | 0.09 | 1.5 | 4.12 | 1 |
| IAD38 | 1.0 | 0.05 | 81 | 2.09 | 1 |

| | | | | | |
|---|---|---|---|---|---|
| IAVAL | 0.45599 | 0.08 | 2.0 | 3.50 | 1 |
| P07 | 1.07 | 0.08 | 79 | 6 | 12 |
| VAL | 0.97 | 0.09 | 47 | 10 | 12 |

Table F.4.: Summary average SKS splitting parameters obtained from medium and high quality measurements at the permanent and temporary seismic stations for all events from the back-azimuth range 180 – 270$^0$. $\overline{\delta t}$ and $\widetilde{\sigma}^2$ is the average delay time and its standard deviation, respectively. $\overline{\phi}$ and $\nu$ is the average fast polarisation and its standard deviation, respectively. Results from stations with only one measurement are also shown. In this case, $\overline{\delta t} \sim \delta t$, $\widetilde{\sigma}^2 \sim \sigma_{\delta t}$, $\overline{\phi} \sim \phi$ and $\nu \sim \sigma_{\phi}$.

| Station | $\overline{\delta t}$ | $\widetilde{\sigma}^2$ | $\overline{\phi}$ | $\nu$ | No. events |
|---|---|---|---|---|---|
| D03 | 0.80 | 0.08 | 28 | 4 | 2 |
| D14 | 0.9 | 0.04 | 43 | 1.67 | 1 |
| D15 | 1.01 | 0.06 | -3 | 3 | 5 |
| D16 | 1.06 | 0.1 | 5 | 6 | 8 |
| D23 | 1.15 | 0.10 | 7 | 14 | 3 |
| D33 | 1.02 | 0.14 | -17 | 6 | 3 |
| D34 | 1.27 | 0.24 | 34 | 8 | 6 |
| D37 | 0.81 | 0.11 | 19 | 6 | 5 |
| D38 | 1.19 | 0.07 | 0.1 | 18 | 2 |
| DSB | 1.21 | 0.19 | -13 | 5 | 8 |
| IA001 | 1.4 | 0.12 | -5 | 4.97 | 1 |
| IA002 | 1.6 | 0.03 | 38 | 1.45 | 1 |
| IA003 | 1.4 | 0.08 | 4 | 3.61 | 1 |
| IAD18 | 0.8 | 0.05 | 6 | 2.21 | 1 |
| IAD23 | 0.60 | 0.29 | 10 | 12 | 2 |
| IAVAL | 1.1 | 0.11 | -28 | 4.57 | 1 |
| P07 | 1.0 | 0.07 | 17 | 3.13 | 1 |
| VAL | 1.11 | 0.15 | -5 | 6 | 7 |

Table F.5.: Summary average SKKS splitting parameters obtained from medium and high quality measurements at the permanent and temporary seismic stations for all events from the back-azimuth range 180 – 270$^0$. $\overline{\delta t}$ and $\widetilde{\sigma}^2$ is the average delay time and its standard deviation, respectively. $\overline{\phi}$ and $\nu$ is the average fast polarisation and its standard deviation, respectively. Results from stations with only one measurement are also shown. In this case, $\overline{\delta t} \sim \delta t$, $\widetilde{\sigma}^2 \sim \sigma_{\delta t}$, $\overline{\phi} \sim \phi$ and $\nu \sim \sigma_{\phi}$.

| Station | $\overline{\delta t}$ | $\widetilde{\sigma}^2$ | $\overline{\phi}$ | $\nu$ | No. events |
|---|---|---|---|---|---|
| D21 | 1.7 | 0.10 | 15 | 4.19 | 1 |
| D23 | 1.79 | 0.16 | 38 | 7 | 2 |
| D32 | 1.40 | 0.07 | 40 | 17 | 2 |
| D37 | 0.6 | 0.07 | 13 | 2.98 | 1 |
| DSB | 1.38 | 0.14 | -25 | 6 | 2 |
| P07 | 1.0 | 0.04 | 61 | 1.85 | 1 |
| VAL | 1.03 | 0.17 | 14 | 15 | 4 |

Table F.6.: Summary average SKS+SKKS splitting parameters obtained from medium and high quality measurements at the permanent and temporary seismic stations for all events from the back-azimuth range 180 – 270$^0$. $\overline{\delta t}$ and $\widetilde{\sigma}^2$ is the average delay time and its standard deviation, respectively. $\overline{\phi}$ and $\nu$ is the average fast polarisation and its standard deviation, respectively. Results from stations with only one measurement are also shown. In this case, $\overline{\delta t} \sim \delta t$, $\widetilde{\sigma}^2 \sim \sigma_{\delta t}$, $\overline{\phi} \sim \phi$ and $\nu \sim \sigma_{\phi}$.

| Station | $\overline{\delta t}$ | $\widetilde{\sigma}^2$ | $\overline{\phi}$ | $\nu$ | No. events |
|---|---|---|---|---|---|
| D03 | 0.80 | 0.08 | 28 | 4 | 2 |
| D14 | 0.9 | 0.04 | 43 | 1.67 | 1 |
| D15 | 1.01 | 0.05 | -3 | 3 | 5 |
| D16 | 1.06 | 0.10 | 5 | 6 | 8 |
| D21 | 1.7 | 0.1 | 15 | 4.19 | 1 |
| D23 | 1.34 | 0.15 | 15 | 12 | 5 |

| | | | | | |
|---|---|---|---|---|---|
| D32 | 1.40 | 0.07 | 27 | 26 | 2 |
| D33 | 1.02 | 0.14 | -17 | 6 | 3 |
| D34 | 1.16 | 0.22 | 34 | 8 | 6 |
| D37 | 0.77 | 0.09 | 18 | 5 | 6 |
| D38 | 1.19 | 0.07 | 0 | 18 | 2 |
| DSB | 1.23 | 0.16 | -15 | 4 | 10 |
| IA001 | 1.4 | 0.12 | -5 | 4.97 | 1 |
| IA002 | 1.6 | 0.03 | 38 | 1.45 | 1 |
| IA003 | 1.4 | 0.08 | 4 | 3.61 | 1 |
| IAD18 | 0.8 | 0.05 | 6 | 2.21 | 1 |
| IAD23 | 0.60 | 0.29 | 10 | 12 | 1 |
| IAVAL | 1.1 | 0.11 | -28 | 4.57 | 1 |
| P07 | 1.00 | 0.02 | 50 | 14 | 2 |
| VAL | 1.09 | 0.11 | -2 | 7 | 11 |

Table F.7.: Summary average SKS+SKKS splitting parameters obtained from medium and high quality measurements at the permanent and temporary seismic stations for all events from the back-azimuth range from 0 – $90^0$ and 180 – $270^0$. $\overline{\delta t}$ and $\widetilde{\sigma}^2$ is the average delay time and its standard deviation, respectively. $\overline{\phi}$ and $\nu$ is the average fast polarisation and its standard deviation, respectively. Results from stations with only one measurement are also shown. In this case, $\overline{\delta t} \sim \delta t$, $\widetilde{\sigma}^2 \sim \sigma_{\delta t}$, $\overline{\phi} \sim \phi$ and $\nu \sim \sigma_{\phi}$.

| Station | $\overline{\delta t}$ | $\widetilde{\sigma}^2$ | $\overline{\phi}$ | $\nu$ | No. events |
|---|---|---|---|---|---|
| D03 | 0.97 | 0.06 | 29 | 4 | 3 |
| D06 | 1.4 | 0.11 | -30 | 4.90 | 1 |
| D08 | 0.7 | 0.07 | -4 | 3.26 | 1 |
| D14 | 0.9 | 0.04 | 43 | 1.67 | 1 |
| D15 | 1.00 | 0.05 | 92 | 25 | 9 |
| D16 | 0.81 | 0.05 | 101 | 19 | 14 |
| D21 | 1.7 | 0.10 | 15 | 4.19 | 1 |

| | | | | | |
|---|---|---|---|---|---|
| D23 | 1.39 | 0.13 | 87 | 10 | 19 |
| D32 | 1.16 | 0.08 | 71 | 12 | 13 |
| D33 | 1.19 | 0.08 | 92 | 14 | 13 |
| D34 | 0.99 | 0.09 | 81 | 8 | 24 |
| D36 | 1.23 | 0.21 | 70 | 13 | 3 |
| D37 | 0.89 | 0.06 | 71 | 10 | 18 |
| D38 | 1.19 | 0.08 | 99 | 17 | 5 |
| DSB | 1.08 | 0.09 | 119 | 9 | 25 |
| IA001 | 1.19 | 0.08 | 131 | 17 | 3 |
| IA002 | 0.94 | 0.25 | 13 | 9 | 4 |
| IA003 | 0.79 | 0.13 | 2 | 5 | 4 |
| IAD01 | 0.41 | 0.07 | 1 | 3 | 3 |
| IAD18 | 0.8 | 0.05 | 6 | 2.21 | 1 |
| IAD23 | 0.60 | 0.21 | 8 | 9 | 3 |
| IAD38 | 1.0 | 0.05 | 81 | 2.09 | 1 |
| IAVAL | 0.68 | 0.22 | -9 | 10 | 1 |
| P07 | 1.06 | 0.07 | 74 | 6 | 14 |
| VAL | 1.03 | 0.07 | 77 | 13 | 24 |

# G. Program to average shear-wave splitting measurements

In this appendix, a program to calculate the weighted mean program for multiple measurements is described. This program is based on the method of *Silver and Chan* (1991). It has been applied separately to splitting measurements of shear-waves coming from South America and East Asia. Complete results of the application of this method for the two event clusters are also summarised in Appendix F.

```
      program sks_mean
c     calculates weighted mean of a set of measurements for
c     measurement file.uncertainty assumed to be 1 sigma
c     allows user to put limits on minimum sd.
c     Also, measurements are ignored
c     if sd on angle is above anglesdmax,
c     set in data statement.
c     Finally, chi-square is computed
c     and the uncertainties are adjusted
c  so that the errors have a normalized chi-square of 1.Note,
c     this is only done if chi-square is greater than 1.
c     if less nothing is done for means near +-90 degrees,
c     can choose an optional interval by
```

```
c     adding 180 to negative measurements
      parameter (ndim=10000, infi=1)
dimension tlag(ndim), tlagsd(ndim), angle(ndim),anglesd(ndim)
      character*132 line,char_ans*1,stn*4
      logical lrot
      data lrot/.false./
      data anglesdmax/22./
c     call sfiles(1,infi)
c     write(*,*)'give minimum values for angle sd and tlag sd'
c     read(*,*)anglemin, tlagmin
      anglemin=5.0
      tlagmin=0.1
      char_ans=' '
      write(*,*)'rotate negative values by 180 ?[n]'
      read(*,'(a)')char_ans
      if(char_ans.eq.'y'.or.char_ans.eq.'Y')then
      lrot=.true.
      endif
      indx=0
c     read,write header
      read(infi,'(a)')line
      write(*,'(a)')line
1     read(infi,'(a)',end=2)line
      write(*,'(a)')line
      indx=indx+1
      read(line,100)stn,angle(indx),anglesd(indx),
     + tlag(indx),tlagsd(indx)
```

```
100  format(7x,a4,10x,f4.0,1x,f4.0,3x,f5.2,5x,f4.2)
     if (stn .eq. '') then
     print *,"Blank line: skipping"
     indx=indx-1
     goto 1
     end if
     write(*,*) angle(indx),anglesd(indx),
    +  tlag(indx),tlagsd(indx)
     if(anglesd(indx).ge.anglesdmax)then
     write(*,*)'angle sd too large, measurement ignored'
     indx=indx-1
     go to 1
     endif
     if(tlagsd(indx).lt.tlagmin)then
     write(*,*)'tlag sd changed from ',tlagsd(indx),
    +  'to tlagmin ',tlagmin
     tlagsd(indx)=tlagmin
     endif
     if(anglesd(indx).lt.anglemin)then
     write(*,*)'angle sd changed from ',anglesd(indx),
    + 'to anglemin ',anglemin
     anglesd(indx)=anglemin
     endif
     if(angle(indx).lt.0.)then
     if(lrot)then
     angle(indx)=angle(indx)+180.
     endif
```

```
      endif
      go to 1
2     continue
      if(indx.eq.0)then
      write(*,*)'no constrained measurements,continue'
      angave=0.
      angavesd=0.
      tlave=0.
      tlavesd=0.
      go to 3
      endif
      call wmean(angle,anglesd,indx,angave,angavesd)
      call wmean(tlag,tlagsd,indx,tlave,tlavesd)
c     compute chi-square
      chi_angle=0.
      chi_tlag=0.
      do i=1,indx
      chi_angle=chi_angle+((angle(i)-angave)/anglesd(i))**2
      chi_tlag=chi_tlag+((tlag(i)-tlave)/tlagsd(i))**2
      enddo
      chi_angle=chi_angle/float(indx)
      chi_tlag=chi_tlag/float(indx)
      write(*,*)'normalized chi_angle,chi_tlag:',
      write(*,*) chi_angle,chi_tlag
c     if chi's are greater than one, normalize, if not, dont
      if(chi_angle.gt.1.0)angavesd=angavesd*sqrt(chi_angle)
      if(chi_angle.gt.1.0)tlavesd=tlavesd*sqrt(chi_tlag)
```

```
3     write(*,100)stn,angave,angavesd,tlave,tlavesd
      stop
      end


ccccccccccccccccccccccccccccccccccccccccccccccccccccccccc
      Subroutine wmean(d,sd,n,ave,avesd)
c     This program computes the mean of N data points (d)
c     with standard deviations (sd)
c     and returns ave and avesd
      dimension d(1),sd(1)
      ave=0.
      sigsum=0.
      do i=1,n
      sd2=sd(i)**2
      ave=ave+d(i)/sd2
      sigsum=sigsum+1./sd2
      enddo
      ave=ave/sigsum
      avesd=sqrt(1./sigsum)
      return
      end
```

# H. List of publications

## H.1. Journals

Polat, G., S. Lebedev, P. W. Readman, B. M. O'Reilly, and F. Hauser (2012), Anisotropic Rayleigh-wave tomography of Ireland's crust: Implications for crustal accretion and evolution within the Caledonian Orogen, *Geophysical Research Letters*, *39*, L04302, doi: 10.1029/2012GL051014.

## H.2. Conference proceedings

Polat, G., P. W. Readman, B. M. O'Reilly, and F. Hauser (2009a), Deep-source anisotropy revealed by shear-wave splitting results from Ireland, *Fall Meeting Abstracts*, American Geophysical Union, San Francisco, USA.

Polat, G., P. W. Readman, B. M. O'Reilly, and F. Hauser (2010b), Deep anisotropy beneath Ireland from shear-wave splitting measurements , *53th Irish Geological Research Meeting Abstract*, Belfast, UK.

Polat, G., S. Lebedev, P. W. Readman, B. M. O'Reilly, and F. Hauser (2010a), Surface Wave Tomography for Ireland, *Postgraduate Research Meeting Abstracts*, British Geophysical Association, Bristol, UK.

Polat, G., S. Lebedev, P. W. Readman, B. M. O'Reilly, and F. Hauser (2010c), Deep-source anisotropy revealed by shear-wave splitting results from Ireland, in *Fall Meeting*

*Abstracts*, American Geophysical Union, San Francisco, USA.

Polat, G.,S. Lebedev, P. W. Readman, B. M. O'Reilly,and F. Hauser (2011a), Surface-Wave Tomography in Ireland , in *54th Irish Geological Research Meeting Abstract*, NUI Galway, Ireland.

Polat, G.,S. Lebedev, P. W. Readman, B. M. O'Reilly,and F. Hauser (2012a), Anisotropic Rayleigh-wave tomography of Irelands crust: Implications for crustal accretion and evolution within the Caledonian Orogeny, *54th Irish Geological Research Meeting Abstract*, UCC Cork, Ireland.

Polat, G.,S. Lebedev, P. W. Readman, B. M. O'Reilly,and F. Hauser (2012b), Anisotropic Rayleigh-wave tomography of Ireland's crust: Implications for crustal accretion and evolution within the Caledonian Orogen, *EGU General Assembly Abstracts*, European Geosciences Union, Vienna, Austria.